Bernhard Lehofer, MSc

Impact of high hydrostatic pressure on the structure and molecular dynamics of low-density lipoprotein particles

DISSERTATION

zur Erlangung des akademischen Grades

Doktor der Naturwissenschaften

eingereicht an der

Technischen Universität Graz

Betreuerin

Assoz. Prof. Univ.-Doz. Dr. Ruth Prassl

Institut für Biophysik
Medizinische Universität Graz

Graz, November 2017

EIDESSTATTLICHE ERKLÄRUNG

Ich erkläre an Eides statt, dass ich die vorliegende Arbeit selbstständig verfasst, andere als die angegebenen Quellen/Hilfsmittel nicht benutzt, und die den benutzten Quellen wörtlich und inhaltlich entnommenen Stellen als solche kenntlich gemacht habe. Das in TUGRAZonline hochgeladene Textdokument ist mit der vorliegenden Dissertation identisch.

Datum

Unterschrift

Abstract

Low-density lipoprotein (LDL) is a physiologically highly important natural nanoparticle and has caught the attention of researchers for decades. It has an essential physiological role as cholesterol carrier in the blood circulation and is the main cholesterol supplier of peripheral tissue. Despite these essential functions, LDL also plays a crucial role in the progression of atherosclerosis, the basis for various cardiovascular diseases.

The LDL particle has a very complex structure and therefore has challenged researchers in elucidating more details about this molecular assembly. Today it is known that LDL has a core-shell structure facilitating the transport of hydrophobic lipids in the aqueous environment of the blood circulation. The core is composed of cholesteryl esters, triglycerides and small amounts of free cholesterol and forms the molecular cargo transported within LDL. This hydrophobic cargo is surrounded by an amphiphilic monolayer of phospholipids and the single protein moiety apolipoprotein B-100 (apoB-100).

The scope of this thesis was to further elucidate molecular details of LDL on a dynamical and structural basis in order to provide new knowledge for the development of novel treatment options for cardiovascular diseases. A novel approach by combining different scattering techniques with high hydrostatic pressure (HHP) equipment was applied to characterize LDL on a molecular basis. It could be shown that pressure is a promising tool and an interesting alternative to the use of temperature.

Quasielastic neutron scattering (QENS) and elastic incoherent neutron scattering (EINS) were used to investigate dynamical aspects of the LDL samples, whereas small-angle X-ray scattering (SAXS) and small-angle neutron scattering (SANS) were used to probe the structure of LDL under HHP conditions. Different physiologically relevant forms of LDL were probed, namely normolipidemic, triglyceride-rich and oxidized species.

It could be shown that motional parameters of different forms of LDL were identical even under HHP conditions, but the proportion of molecular groups participating in the motions was decreased in triglyceride-rich LDL under HHP. Generally, the mean square displacements were reduced for modified forms of LDL under HHP in contrast to normolipidemic LDL, which was not affected in the same way.

The structural studies revealed a pressure-induced phase transition of the lipid core of LDL above the transition temperature, which resembled the low temperature state of the macromolecule. This effect was observed in all investigated forms of LDL. The position of the

lamellae in the lipid core of LDL seems to be a highly conserved feature, which was not altered through HHP. Ab initio modeling of scattering data revealed anisotropic changes of the overall dimensions of LDL as well as a characteristic flattening of the particle at high hydrostatic pressure conditions. Even under high pressure conditions LDL revealed a reversible behavior concerning structural rearrangements.

The knowledge gained in this thesis provides new molecular details about the physiologically highly relevant LDL particle and might support the development of new concepts for the treatment of cardiovascular diseases.

Zusammenfassung

Low Density Lipoprotein (LDL) ist ein physiologisch höchst relevantes, natürlich vorkommendes Nanopartikel und hat die Aufmerksamkeit von Wissenschaftlern seit Jahrzehnten auf sich gezogen. Es trägt eine essentielle Rolle als Cholesterin Transporter in der Blutzirkulation und ist hauptverantwortlich für die Cholesterin Versorgung von peripherem Gewebe. Trotz dieser essentiellen Funktionen, spielt LDL auch eine entscheidende Rolle im Fortschreiten von Atherosklerose, der Basis für viele kardiovaskuläre Erkrankungen.

Das LDL Teilchen besitzt eine sehr komplexe Struktur und hat Wissenschaftler beim Aufklären neuer Details dieses molekularen Konstrukts stets herausgefordert. Heute ist bekannt, dass LDL eine Kern-Schale Struktur aufweist, die den Transport von hydrophoben Lipiden im wässrigen Milieu der Blutzirkulation ermöglicht. Der Kern besteht aus Cholesterinestern, Triglyzeriden und kleinen Mengen an freiem Cholesterin und bildet die molekulare Fracht, die innerhalb des LDL Teilchens transportiert wird. Diese hydrophobe Fracht ist umgeben von einem amphiphilen Monolayer aus Phospholipiden und dem einzigen Proteinanteil Apolipoprotein B-100 (apoB-100).

Das Ziel dieser Arbeit war die weitere Aufklärung molekularer Details von LDL auf dynamischer und struktureller Ebene, um neues Wissen für die Entwicklung neuartiger Behandlungsmöglichkeiten kardiovaskulärer Erkrankungen zu ermöglichen. Ein neuer Ansatz durch die Kombination verschiedenster Streumethoden mit hohem hydrostatischen Druck (HHP) wurde angewandt um LDL auf molekularer Ebene zu charakterisieren. Es konnte gezeigt werden, dass Druck ein vielversprechendes Werkzeug und eine hervorragende Alternative zur Verwendung von Temperatur darstellt.

Quasielastische Neutronenstreuung (QENS) und elastische inkohärente Neutronenstreuung (EINS) wurden verwendet um dynamische Aspekte der LDL Proben zu untersuchen, wohingegen Kleinwinkelröntgenstreuung (SAXS) und Kleinwinkelneutronenstreuung (SANS) verwendet wurden um die Struktur von LDL unter Hochdruckbedingungen zu erforschen. Verschiedene physiologisch relevante Formen von LDL, wie normolipidämische, Triglyzerid-reiche und oxidierte Formen, wurden untersucht.

Es konnte gezeigt werden, dass die Beweglichkeitsparameter von verschiedenen LDL Formen sogar unter Hochdruckbedingungen identisch waren, hingegen hat sich der Anteil an molekularen Gruppen, der in den Bewegungen teilnimmt, in Triglyzerid-reichem LDL unter

Hochdruck verringert. Generell hat sich die mittlere quadratische Auslenkung in modifizierten LDL Formen unter Hochdruck reduziert im Gegensatz zu normolipidämischem LDL, welches nicht auf diese Weise beeinflusst wurde.

Die strukturellen Untersuchungen zeigten einen Druck-induzierten Phasenübergang des LDL Lipidkerns über der Übergangstemperatur, was dem Zustand des Makromoleküls bei niedriger Temperatur gleicht. Dieser Effekt wurde in allen untersuchten Formen von LDL beobachtet. Die Lage der Lamellen im Lipidkern von LDL scheint ein höchst konserviertes Merkmal zu sein, das durch den Einsatz von hohem hydrostatischen Druck nicht verändert wurde. Ab initio Modellierung der Streudaten zeigte sowohl anisotrope Änderungen der Dimensionen von LDL als auch ein charakteristisches Abflachen der Teilchen bei hohem hydrostatischen Druck. Auch unter hohen Druckbedingungen zeigte LDL ein reversibles Verhalten in Bezug auf strukturelle Umordnungen.

Die hier neu gewonnenen Erkenntnisse über die molekularen Details des physiologisch höchst relevanten LDL Teilchens könnten zur Entwicklung neuer Therapieansätze bei der Behandlung kardiovaskulärer Erkrankungen beitragen.

Weine nicht, dass etwas vorbei ist, sondern freue Dich darüber, dass Du es erleben durftest.

(Unbekannt)

Danksagung

Nun ist er also gekommen. Der Zeitpunkt an dem ich auf eine wahnsinnig ereignisreiche, spannende, abwechslungsreiche, bereichernde und viel zu schnell vergangene Zeit zurück blicke. Niemals hätte ich mir gedacht, dass ich so viel lernen und erleben würde, dass mich diese Zeit so bereichern würde und dass es mir so schwer fallen würde den nächsten Schritt zu machen. Doch er ist notwendig und wird mich bestimmt auf neue interessante Wege leiten, von denen ich derzeit noch nicht einmal wage zu träumen. Doch bevor es soweit ist, ist es an der Zeit sich zu bedanken und einen kurzen Blick zurück zu werfen.

Die Zeit, die ich hier am Institut für Biophysik verbringen durfte, war äußerst abwechslungsreich und von vielschichtigen Erfahrungen geprägt. War es nun die Übersiedelung des (Teil-)Institutes vom alten Standort der ÖAW in Messendorf auf die Vorklinik, die uns in eine völlig neue Umgebung mit vielen neuen KollegInnen führte, oder waren es die vielen Forschungsreisen und Konferenzteilnahmen, die es wirklich nie langweilig werden ließen. Es lauerte tatsächlich ständig eine neue Erfahrung an der nächsten Ecke. Und dann folgte im Juni 2017 noch die zweite Übersiedelung des Instituts von der Vorklinik auf den neuen MED CAMPUS, die ich auch noch miterleben durfte und auch noch einige Zeit im ganz neuen Büro verbringen durfte.

Viele besondere Momente werden mir in Erinnerung bleiben: Unter anderem die Nachtschicht am Paul Scherrer Institut mitten im eisigen Dezember, in der ich zu sehr später (bzw. sehr früher) Stunde alleine über den völlig finsteren Campus in Richtung Café schlenderte, um mir noch etwas zu essen zu holen. Und dort im verlassenen Café, als ich mir etwas aus dem Automaten holte, wurde ich vom Nachtwächter, der dort seine Runden drehte, vollkommen überrascht und zu Tode erschreckt. Er hatte seinen Spaß und ich war froh, dass es nur der Nachtwächter war.

Oder die vielen langen Messzeiten an der SAXS Beamline in Triest, wo wir bis in die frühen Morgenstunden Proben untersuchten. Und ich dann den immer fantastischen Ausblick auf das nächtlich beleuchtete Triest genoss, wenn wir von Basovizza in Richtung Triest unterwegs waren um uns ein schönes Lokal fürs Abendessen zu suchen (inklusive einmaligem Besuch im außergewöhnlichen und extra teuren Fischlokal).

Oder die Reisen nach Grenoble, die mich das erste Mal nach Frankreich führten, und mich mit einem außergewöhnlich südländischen Flair überraschten. Die Fahrt mit den „Kugeln“ auf die Bastille war immer wieder ein tolles Erlebnis.
Oder die schönen, gemütlichen Abende bei Judiths Familie zu Hause, die immer eine kleine Entdeckungsreise ins kulinarische und landschaftliche Frankreich waren.
Oder der Konferenzbesuch des 60th Biophysical Society Meeting in Los Angeles, das mich das erste Mal in die USA führte und mich wahnsinnig bereicherte.
Oder die Wanderung mit der gesamten Arbeitsgruppe durch die Klause Deutschlandsberg bis zum Fischerwirt, bei dem ich die beste gebratene Forelle meines ganzen Lebens gegessen habe.
Und und und... ich könnte noch lange so weiter machen.

Niemand kann aber ein Projekt von diesem Ausmaß ohne die Hilfe, Unterstützung und Motivation von KollegInnen, FreundInnen und Familie schaffen. Daher muss an dieser Stelle all jenen gedankt werden, die durch ihre ständige Unterstützung zum Erfolg beigetragen haben.

Allen vorweg möchte ich meiner Betreuerin **Ruth Prassl** danken, dass sie mir die Möglichkeit gegeben hat an diesem Projekt zu arbeiten und ich dadurch die Chance hatte mich in so vielerlei Hinsicht weiter zu entwickeln und Neues zu lernen. Die gemeinsamen Forschungsreisen waren immer eine tolle Erfahrung und haben wirklich Spaß gemacht. Ihre stetige Motivation hat mich immer wieder neue Ziele erreichen lassen. Es war eine wirklich außergewöhnliche Zeit, vielen Dank dafür!
Natürlich wäre das alles nicht möglich gewesen ohne die Unterstützung von einer Vielzahl an KollegInnen. Allen voran möchte ich mich bei **Karin Kornmüller** und **Hanna Lindermuth** für ihre tatkräftige Hilfe im Projekt bedanken, sowie bei meinen restlichen KollegInnen hier am Institut **Christian Hill**, **Christian Mikl**, **Johann Krebs**, **Gebhard Schratter**, **Ivan Vidakovic** und **Angela Steinberger** für die unzähligen lustigen Gespräche, Erlebnisse und Feiern.

Weiters möchte ich mich ganz besonders bei **Judith Peters** bedanken, die gemeinsam mit meiner Betreuerin das Projekt überhaupt erst initiiert hat und damit alles möglich machte. Ich möchte mich bei ihr auch ganz besonders für die hervorragende Zusammenarbeit bedanken, die von Anfang an durch eine optimale Kommunikationsebene geprägt war. Auch

Maksym Golub und **Nicolas Martinez** sei an dieser Stelle gedankt, da sie für mich immer hilfsbereite Ansprechpartner darstellten und am Erfolg des Projektes essentiell beteiligt waren.

Außerdem möchte ich noch **Heinz Amentisch** und seiner Arbeitsgruppe danken, da sie für den Erfolg des Projektes ebenso wichtig waren und uns immer mit Rat und Tat zur Seite standen. Ein Dankeschön an **Manfred Kriechbaum**, **Benedetta Marmiroli** und **Barbara Sartori**, die sich immer besonders für uns engagiert haben wenn wir bei einer Beamzeit am Synchrotron in Triest waren.

Natürlich braucht es aber auch Unterstützung und Motivation von privater Seite. Von ganzem Herzen möchte ich meinen Eltern **Monika und Johann Lehofer** danken, die mich immer in allem unterstützt haben was ich gemacht habe und auch immer an mich glauben. Ich hätte meine Ziele ohne diese bedingungslose Unterstützung nie erreichen können.
Mein allergrößter Dank gilt meinem Partner **Mike Trauntschnig**, der für mich einfach überall und jederzeit die größte Stütze ist, die ich nur haben kann. Ich kann mich wirklich immer auf ihn verlassen und habe immer ein offenes Ohr, das mir zuhört und einen sicheren Ort an dem ich mich wohlfühle.

Ein großes **Dankeschön** an alle!

Contents

Abstract 1
Zusammenfassung 3
Danksagung 6
Contents 9
Abbreviations 12
1. Introduction 14
2. Theoretical Background 16
2.1 Low-density lipoprotein structure and physiological role 16
2.2 Apolipoprotein B-100 20
2.3 Modified forms of LDL 22
2.3.1 Oxidized LDL 23
2.3.2 Triglyceride-rich LDL 25
2.4 High hydrostatic pressure 26
2.5 Effect of high hydrostatic pressure on biological systems 27
2.5.1 Lipid systems 27
2.5.2 Proteins 29
2.5.3 Deep sea organisms 30
2.5.4 High-pressure processing of food 31
2.6 X-rays and neutrons 32
2.7 Basics of scattering 35
2.8 Scattering of X-rays 39
2.9 Scattering of neutrons 39
3. References 42
4. Results Part I 48
Introduction 49
Results 51
TG-LDL dynamics is sensitive to HHP application in contrast to N-LDL dynamics 51
The shape of TG-LDL is modified by high pressure application 54
Discussion 56
Materials and Methods 61
Sample preparation for neutron scattering experiments 61
Elastic and quasi-elastic neutron scattering experiments and data analysis 61

Elastic neutron scattering experiments 62
Quasi-elastic neutron scattering experiments 63
QENS model free analysis approach 64
SANS experiments and data analysis 65
Acknowledgements 66
Author contributions 67
Additional information 67
References 67
Supporting Information 70
5. Results Part II 82
Introduction 83
Experimental details 84
Sample preparation and characterization 84
Neutron scattering experiments 86
Results and Discussion 87
Conclusions 91
Acknowledgements 91
Author contribution statement 91
References 91
6. Results Part III 94
Introduction 95
Results and Discussion 96
High hydrostatic pressure SAXS measurements 96
Reversibility of high pressure effects on LDL samples 102
Model-independent analyses of SAXS data 104
High hydrostatic pressure SANS measurements 113
Model-independent analyses of SANS data 115
Ab initio shape determination of LDL under HHP 119
Conclusion 125
Materials and Methods 127
Ethical statement 127
Isolation, purification and characterization of LDL from human blood plasma 127
Differential Scanning Calorimetry (DSC) 127

In vitro oxidation of LDL 128
Small-angle neutron scattering (SANS) 128
Small-angle X-ray scattering (SAXS) 128
Small-angle scattering data analysis procedures 129
Acknowledgments 130
References 130
7. Results Part IV 134
Introduction 135
Results 136
Discussion 143
Materials and Methods 145
Ethical statement 145
Sample preparation and characterization 145
Differential Scanning Calorimetry (DSC) 146
Small-angle X-ray scattering (SAXS) measurements 146
Electron Microscopy Data Bank (EMDB) data processing 147
Solution scattering simulation of cryoEM 3D models 147
Development of mathematical 3D fitting model 147
Fitting of experimental data and derivation of structural parameters 148
References 148
8. Conclusion and Outlook 150
9. Appendix 154
PyMOL Script Draw_Protein_Dimensions 154
PyMOL Script inertia_tensor 157
10. List of Publications 159
Full Papers 159
Published Abstracts 159
Scientific presentations 160

Abbreviations

apoB-100	Apolipoprotein B-100
b	scattering length
b_e	scattering length of an electron
c	speed of light
CE	Cholesteryl ester
CM	Chylomicrons
cryoEM	cryo-electron microscopy
CVD	Cardiovascular disease
D_2O	Deuterium oxide
DSC	Differential scanning calorimetry
dσ/dΩ	differential scattering cross section
E	energy
EDTA	Ethylenediaminetetraacetic acid
EINS	Elastic incoherent neutron scattering
f(s)	atomic scattering factor
FC	Free cholesterol
FH	Familial hypercholesterolemia
FTIR	Fourier-transform infrared spectroscopy
h	Planck's constant
ħ	Planck's constant, = h/2π
HBV	Hepatitis B virus
HCV	Hepatitis C virus
HDL	High-density lipoprotein
HHP	High hydrostatic pressure
HIV	Human immunodeficiency virus
IDL	Intermediate-density lipoprotein
J	scattered beam flux
J_0	incident beam flux
k	Boltzmann's constant
LDL	Low-density lipoprotein
LDLR	Low-density lipoprotein receptor
MAb	Monoclonal antibody
NaPi	Sodium phosphate buffer
NMR	Nuclear magnetic resonance
p	momentum
P(q)	form factor

$p(r)$	Pair distance distribution function
PL	Phospholipid
q	scattering vector, = 2πs
QENS	Quasielastic neutron scattering
r_e	classical radius of the electron
R_g	Radius of gyration
ROS	Reactive oxygen species
s	scattering vector
S	unit vector in the direction of a ray
$S(q)$	structure factor
S_0	unit vector in the direction of the incident ray
SANS	Small-angle neutron scattering
SAXS	Small-angle X-ray scattering
SDS-PAGE	Sodium dodecyl sulfate - polyacrylamide gel electrophoresis
TG	Triglyceride
T_m	Transition temperature
v	velocity
VLDL	Very low-density lipoprotein
ΔH_{cal}	Calorimetric enthalpy
θ	one-half of the scattering angle
λ	wavelength
ν	frequency
σ_{tot}	total scattering cross section
φ	phase angle of a wave
χ^2	Goodness of fit
Ω	solid angle

1. Introduction

Human low-density lipoprotein (LDL) is one of the most fascinating and also most complex known biological macromolecules. It is responsible for the transport of cholesterol and triglycerides through the human blood circulation to peripheral and extrahepatic tissue. However, it represents only one of several physiologically highly relevant lipoprotein classes next to chylomicrons (CM), very low-density lipoprotein (VLDL), intermediate-density lipoprotein (IDL) and high-density lipoprotein (HDL).[1]

The LDL particle has attracted attention of researchers basically through its eminent role in the progression of atherosclerosis. As a known key player in this chronic inflammatory disease a lot of effort has been made to elucidate the particle's structural features and to understand the pathological mechanism behind LDL accumulation and oxidation.[2]

Because of its very complex structure, which is a combination of several lipid classes and a large protein moiety[3], it has not been possible to get a high resolution crystal structure so far although crystallization and X-ray diffraction have already been successful.[4-5] Unfortunately, the resolution of these diffraction patterns was too low to get detailed structural information. Through the use of small-angle X-ray scattering (SAXS) and small-angle neutron scattering (SANS) a lot of characteristics of the LDL nanoparticle could be revealed, although the assumption of a concentrically ordered lipid core was disproven later on.[6-11] Over the last decade several working groups succeeded in producing low-resolution images of LDL particles through the use of cryo-electron microscopy (cryoEM). From these results it was possible to get valuable structural information about the particle which had been unknown from previous studies. The approximate location of the protein moiety on the particle's surface as well as evidence for a layered organization of the lipid core below the transition temperature (T_m) were derived from several studies.[12-17]

Surprisingly the molecular dynamics of LDL have so far been only marginally investigated and are therefore still not fully understood.[18] These molecular motions are, however, of great importance when it comes to physiological functioning of biological macromolecules and are consequently of great interest for LDL research as well.[19-21]

Temperature is one of the most important thermodynamic variables concerning the physical characterization of biological systems (e.g. lipids, lipid membranes, proteins, etc.). It is used to probe systems under various thermal conditions and to observe occurring changes on a structural or dynamical basis. Temperature is a parameter that can be easily handled and

combined with most biochemical and biophysical methods. Nonetheless there is a major disadvantage of applying temperature as a thermodynamic variable as it will always change the thermal energy state and volume of the investigated system as well.[22]

An emerging alternative for the investigation of biological samples at a molecular level is the application of high hydrostatic pressure (HHP).[23-26] In contrast to temperature HHP does not change the thermal energy of a system, but only influences its volume.[22] Thus, different compressibilities, structural flexibilities or dynamical transitions can be probed. However, the technological combination of HHP with biochemical and biophysical methods is not trivial and has not been established for many standard methods so far. Currently it is possible to combine HHP investigations with methods like light microscopy[27], SAXS[28], SANS[29], quasi-elastic neutron scattering (QENS)[30], elastic incoherent neutron scattering (EINS)[30] and nuclear magnetic resonance (NMR) spectroscopy[31]. The growing field of available techniques as well as the possibility to perform such HHP experiments on large-scale facilities is attracting an ever-growing user community. HHP research has many different fields of applications. The research ranges from studies on lipid phase systems[23] or studies on simple proteins in solution[24] to the investigation of deep sea microbes[26] or the analysis of effects of high pressure food processing[32].

This thesis aims at exploring the very complex LDL nanoparticle with a novel approach through the application of HHP in combination with a multitude of biophysical techniques. In this way the thesis wants to promote the knowledge of both molecular motions and structural details of the LDL particle.

2. Theoretical Background

2.1 Low-density lipoprotein structure and physiological role

Low-density lipoprotein is a highly complex physiological nanoparticle, which plays an important role in the proper functioning of human lipid metabolism[1, 3, 33]. The LDL particle consists of a core-shell structure. The shell comprises a phospholipid (PL) monolayer with polar headgroups pointing to the surface of the particle and hydrophobic tails pointing towards the particle's core. Embedded in this PL monolayer lies a single copy of the amphipathic protein apolipoprotein B-100 (apoB-100). The protein moiety appears to be a very flexible and adaptive system and is of fundamental importance for a proper functioning of LDL[11, 34]. Unesterified free cholesterol (FC) molecules are also present, basically in the shell compartment of the LDL particle[35]. Beneath this shell structure is a hydrophobic lipid core largely comprised of cholesteryl esters (CE) and triglycerides (TG).[33] A schematic depiction of the LDL particle is shown in Figure 1.

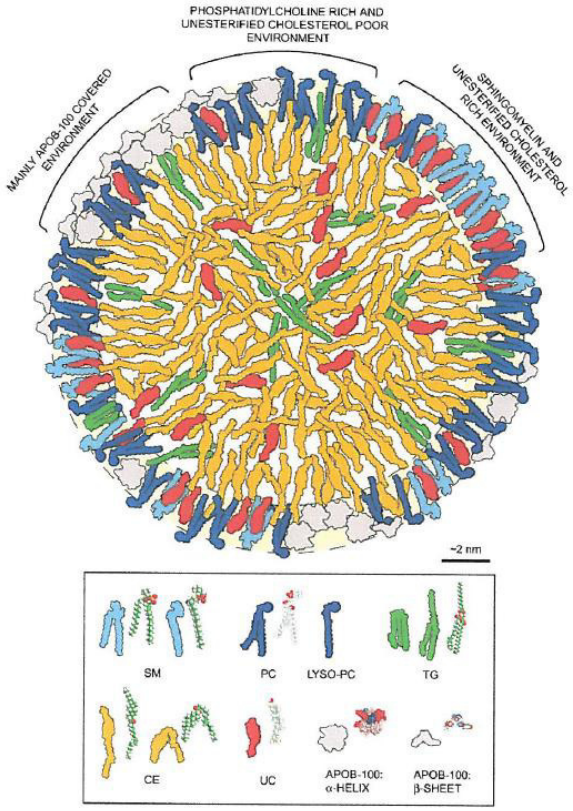

Figure 1: Schematic representation of an average LDL molecule at body temperature. It shows the typical core-shell structure with an interfacial layer in between, where some core lipids penetrate towards the surface. The shell structure is characterized by local nanoenvironments originating from the presence of the protein apoB-100 and different PL species. The depicted particle has a diameter of 20 nm and an average composition of 20% protein, 20% PL, 40% CE, 10% FC and 5% TG. The molecular components are drawn in correct size ratios. Figure was taken from [33].

The LDL particle has an average size of approximately 22 nm. The sole protein component of LDL, namely apoB-100, is built up of 4536 amino acid residues. Moreover the particle harbors in total approximately 3000 lipid molecules. The core is made up of about 170 TG and 1600 CE molecules and the shell monolayer comprises about 700 PL molecules.[33, 36] In addition the LDL particle harbors about 600 unesterified cholesterol molecules, about one-third located in the core and two-thirds located in the shell compartment.[33, 37] A few percent of the core TG and CE molecules also penetrate towards the surface. The main PL components are phosphatidylcholine (about 450 molecules/LDL) and sphingomyelin (about 185 molecules/LDL).[33] Next to the various lipid components LDL also contains small amounts of lipophilic antioxidants like α-tocopherol, γ-tocopherol, carotenoids, oxycarotenoids and ubiquinol-10.[33, 36]

The core structure consists, as already mentioned before, basically of CE molecules and small amounts of TG and FC. The core lipids undergo a phase transition from a completely disordered liquid-like state above T_m, to a highly ordered smectic-like liquid crystal phase below T_m. Transition temperatures are usually found around 25°C or higher. However, the T_m is strongly influenced by the actual core lipid composition. More specifically, it is inversely proportional to the TG/CE ratio and also to increased unsaturation of the core lipid fatty acid chains.[33, 35, 38]

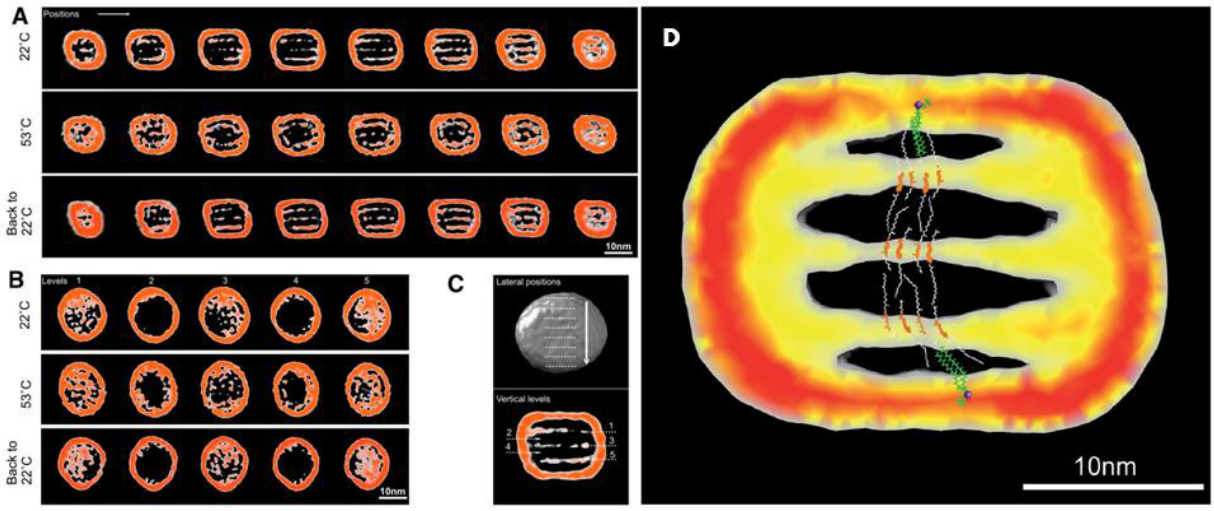

Figure 2: The internal features of reconstructed 3D volumes from cryoEM images are depicted. The LDL used for cryoEM was frozen at different temperatures, namely 22°C (below T_m), 53°C (above T_m) and 22°C after heating. The 3D volumes from the different samples were aligned and sliced. The gray color was contoured at 2σ and the orange color was contoured at 3σ. (A) Slices were made perpendicular to the lipid layers and (B) parallel to the layers. (C) The lateral and vertical positions of the slices are shown. (D) A proposed lipid packing model, where CE molecules (white/orange) and PL molecules (green/purple) are arranged to fit to the reconstructed 3D volume. Depicted is a slice of the LDL structure, where color indicates electron density (red>yellow>gray). Figures were taken and modified from [13, 15].

Figure 2 shows 3D reconstructions from cryoEM investigations on LDL particles. As can be seen from these images LDL has a three-layered internal structure below T_m and gets a disordered core at temperatures above T_m. Based on the electron density distribution of the reconstructed volume a lipid packing model was proposed (see Figure 2D), which suggests CE molecules being arranged in three parallel layers and cholesterol headgroups leading to the characteristic electron dense pattern observed in cryoEM.[12-13, 15]

The structure of LDL is essential for a proper functioning of the particle. Any kind of modifications are believed to have a major impact on inducing processes like aggregation or fusion, which are a prerequisite for the initiation of lipid accumulation. It is a fact that its structure and therefore its physical properties are in a highly dynamical state, which is strongly dependent on the particle's lipid composition as well as the conformation of apoB-100.[33]

The physiological function of LDL is the supply of extrahepatic tissues and cells with cholesterol, which is a crucial building block of biological membranes, steroid hormones or bile acids (see Figure 3).[1]

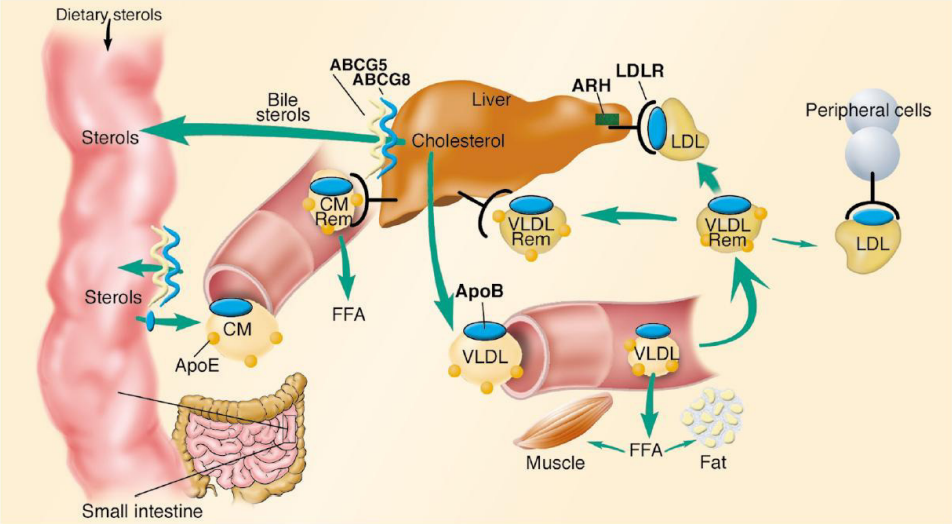

Figure 3: Graphical representation of the human LDL metabolism. Dietary cholesterol and triglycerides are packaged with apolipoproteins in the enterocytes of the small intestine into chylomicrons (CM) which are subsequently secreted into the lymphatic system. The core triglycerides of the circulating CMs are hydrolyzed by lipoprotein lipase (LPL) resulting in free fatty acids (FFA) and chylomicron remnants (CM Rem), which are removed by the liver. Dietary cholesterol has four possible fates once it reaches the liver. It can be esterified and stored as cholesteryl ester in hepatocytes or it is packaged into VLDL and secreted into the plasma. Another possibility is the direct secretion into the bile or a conversion to bile acids precedes the secretion into the bile. ABCG5 and ABCG8 (ATP-binding cassette family G) participate in sterol trafficking into bile. VLDL in the plasma undergoes lipolysis and results in VLDL remnants (VLDL Rem), from which approximately 50% are removed by the liver via the LDL receptor (LDLR). ARH (Autosomal recessive hypercholesterolemia) is a putative adaptor protein involved in LDLR-mediated endocytosis. The remaining fraction matures into LDL particles, the major cholesterol transporter in the blood. An estimated 70% of these LDL is cleared by LDLR in the liver, whereas the remainder is taken up by peripheral cells. Figure was taken from [39].

Cholesterol itself is absolutely insoluble in water, so multicellular organisms developed a cholesterol transport system through esterifying the sterol with long-chain fatty acids and packing these esters within hydrophobic cores of plasma lipoproteins.[1] Responsible for the uptake of LDL from the circulation into cells and for regulating homeostasis of blood cholesterol level is the low-density lipoprotein receptor (LDLR). It is a cell-surface glycoprotein, which binds LDL through apoB-100 and internalizes the ligand by endocytosis via clathrin-coated pits. The release of the ligand in the cell is triggered through the low-pH environment of the endosome.[40-41] The receptor is subsequently returned to the cell surface in a process called receptor recycling and then available for another transport cycle. The internalized LDL particle is degraded in the lysosome and delivers basic building blocks (e.g. cholesterol, amino acids) for further cell processes (see Figure 4).[40]

The LDLR was originally identified by Brown & Goldstein in 1973 during their search for the molecular cause of familial hypercholesterolemia (FH).[1] This is one of the most common inborn metabolic disorders and is caused through a loss-of-function of the gene encoding the LDLR.

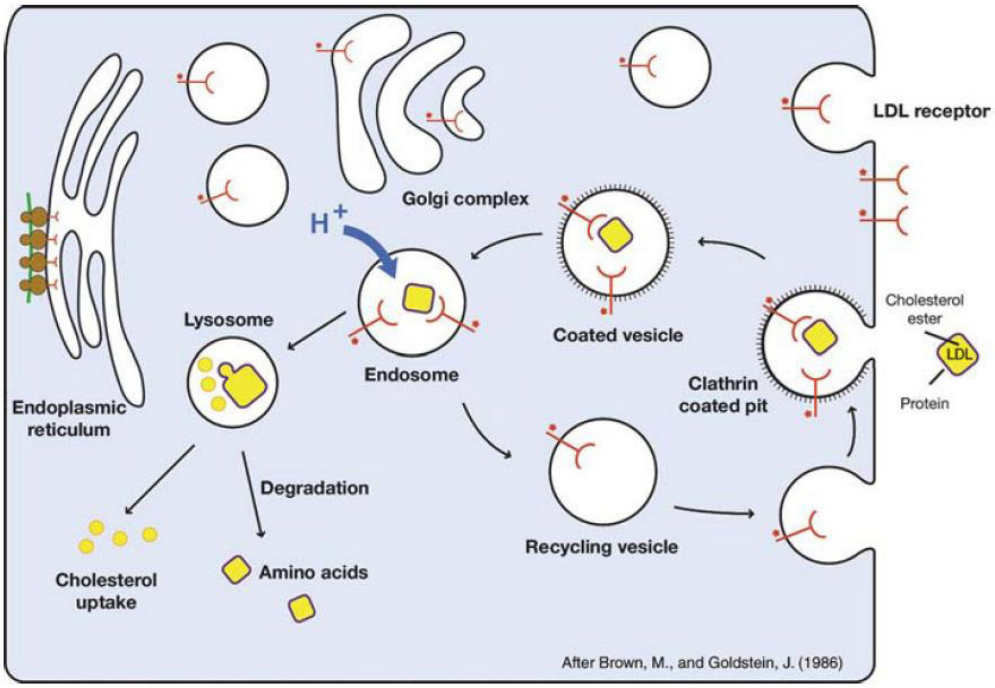

Figure 4: Schematic representation of LDL uptake into a cell through the LDLR. The entry of the LDL-LDLR complex occurs through clathrin-coated pits. In the low-pH environment of the endosome the LDLR dissociates from LDL and is subsequently recycled to the cell surface in a process called receptor recycling. The LDL is degraded in the lysosome into its basic building blocks, which are then further processed by the cell. Figure was taken from [40].

2.2 Apolipoprotein B-100

Apolipoproteins are in general a class of amphiphilic proteins that consist of hydrophilic and hydrophobic regions to enable an interaction of the protein moiety with both the lipids of the lipoprotein particle and the surrounding aqueous environment. With these properties they act as detergents responsible for solubilization but also structural stabilization of the particles. The apolipoproteins can be divided into two major groups, namely the nonexchangeable (apoB-48 and apoB-100) and exchangeable (apoA-I, apoA-II, apoA-IV, apoC-I, apoC-II, apoC-III and apoE) ones. Exchangeable lipoproteins are water-soluble, whereas apoB-100 is highly insoluble in aqueous environments.[42]

As already mentioned in the first chapter, apoB-100 is the only apolipoprotein present in LDL.[43-45] ApoB-100 remains with the lipoprotein particle throughout its whole metabolism.[46] Based on the primary sequence of apoB-100 a secondary structure model was predicted and the so-called pentapartite model was developed. The pentapartite nomenclature is NH_2-$\beta\alpha_1$-β_1-α_2-β_2-α_3-COOH (see Figure 5A).[11, 42]

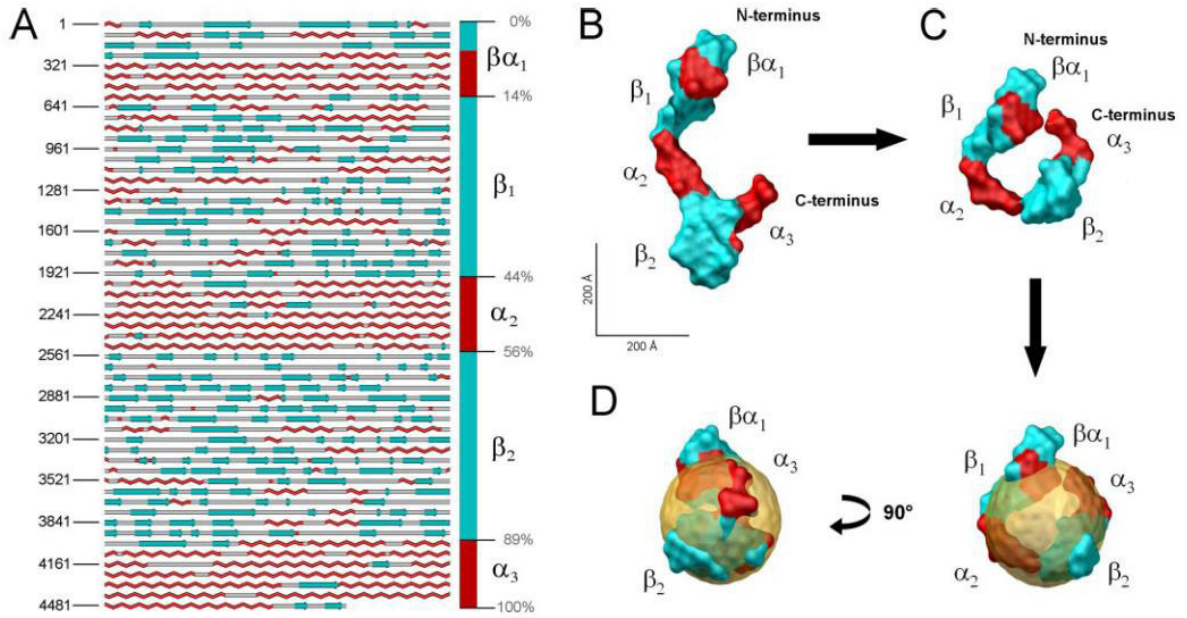

Figure 5: (A) Prediction of the secondary structure of apoB-100 based on the complete amino acid sequence. α-helical structures shown in red, β-sheet structures shown in blue, random coil and structures with low prediction confidence shown in gray. Assignment of the different parts made according to the pentapartite model[42]. (B) Averaged envelope shape of the reconstructed 3D ab initio model from detergent-solubilized apoB-100. The averaged model was created from 10 independent DAMMIN models[47] using the program DAMAVER[48]. The compartments of the pentapartite model were assigned onto the 3D shape according to a homology model[49]. (C) Hypothetical bend of the 3D model for a spatial arrangement of apoB-100 in LDL. (D) Additional simulation of a 250 Å sphere (shown in yellow) representing the lipid components. Figure was taken from [11].

It is based on analyses that suggest that apoB-100 contains four consecutive domains alternatively enriched in amphipathic α-helices or amphipathic β-sheets. The $\beta\alpha_1$ domain is a globular composite, which is built up of both α-helical and β-sheet secondary structures. It is supposed to play a significant role in lipid accumulation during the co-translational assembly of the prenascent triglyceride-rich lipoprotein particles (Lipid pocket model).[42] Moreover the $\beta\alpha_1$ domain has sequence and amphipathic motif homologies with lamprey lipovitellin.[42, 50]

The β-domains form amphipathic β-sheets, which are supposed to fulfill three different functions in apoB-100. First, they are assumed to participate in lipid accumulation in prenascent lipoprotein particles. Second, a direct contact of the hydrophobic parts of the amphipathic β sheets with the neutral lipid core is suggested and third, they are supposed to have an influence on overall LDL particle diameter.[42, 51]

The amphipathic helices of the α_2 and α_3 domains are assumed to represent reversible lipid-associating domains.[51-52] It is anticipated that one function of the helices is to modulate the surface pressure changes that occur during particle size variations.[42]

Analyses of the morphology of detergent-solubilized apoB-100 have shown that it is a flexible elongated protein with alternating thick and thin regions.[11, 34] Various orientations (curved and elongated) in electron microscopic investigations as well as an elongated ab initio shape model from a SANS study confirm the presence of flexible linker regions within the sequence of apoB-100 (see Figure 5B and C).[11, 34] The reconstructed ab initio model including a hypothetical bend was fitted to a simulated 250 Å sphere (representing the lipid components of LDL) to show a possible location of the apoB-100.[11] Another approach to get a more detailed picture of the apoB-100 location within the particle was the application of monoclonal antibodies (MAb). Through Immuno-electron cryo-microscopy the approximate location of several epitopes of apoB-100 could be identified on the particle (see Figure 6).[14, 53]

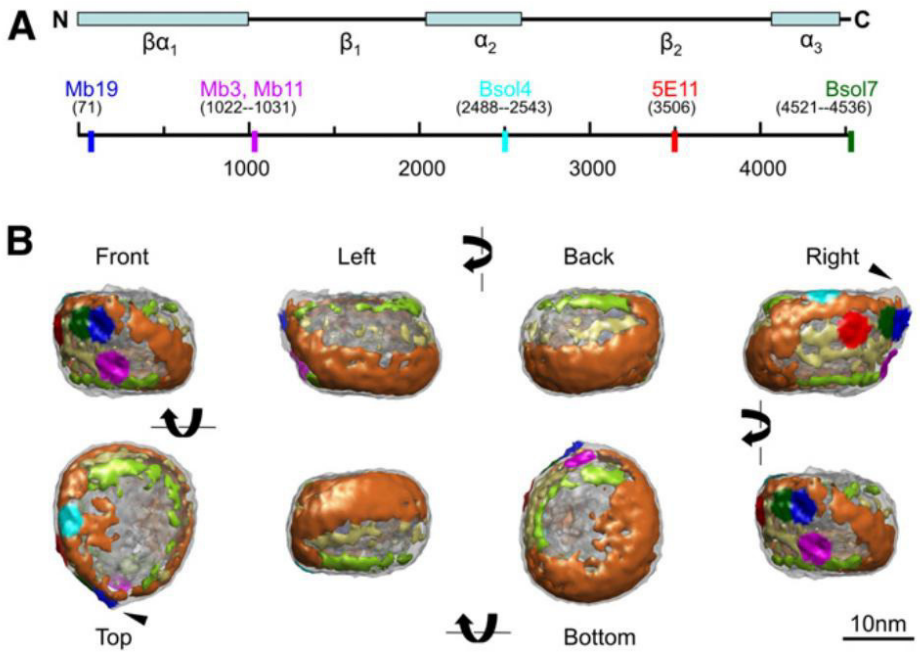

Figure 6: (A) Monoclonal antibody (MAb) binding sites shown in the primary sequence of apoB-100. The first line shows the pentapartite model prediction while the second line shows the exact epitope binding sites of MAbs color-coded and with the epitope residue number in brackets. (B) The high density distribution on the LDL surface from cryoEM reconstructions is shown in combination with the MAb binding sites (color-coded from A). The high density regions are separated into three distinct parts, i.e. the backbone of the high-density region (orange), the rims of the discoidal shaped particle (green) and the densities on the side wall of the LDL (yellow). Figure was taken from [14].

The receptor-binding domain of apoB-100 was identified through site-directed mutagenesis. The physiologically most important ligand for the LDL receptor is LDL, but also other lipoproteins, which contain multiple copies of apoE (e.g. β-migrating forms of VLDL or certain IDL and HDL forms) bind to the LDLR.[40] A possible interacting region, sometimes called site B, has high similarity with the receptor-binding domain of apoE. Experiments with a synthetic peptide (apoB 3345-3381) showed the importance of this region for LDL receptor binding and internalization.[54] The mutagenesis of site B clearly confirmed this domain as the site of interaction with the receptor.[40, 55-56]

2.3 Modified forms of LDL

Modified forms of LDL are often involved in the progression of pathological conditions. They are a well-known key player in the development of cardiovascular diseases (CVD), especially oxidized LDL and small dense triglyceride-rich LDL, which are both highly atherogenic. Therefore the investigation of these modified forms of LDL is of great interest for further pathophysiological considerations.[2, 57]

2.3.1 Oxidized LDL

Atherosclerosis, a progressive disease, is characterized by the accumulation of lipids and fibrous elements in the large arteries. The onset of the disease is supposed to happen through lesion initiation in the arterial wall. This initiation is partly determined by hemodynamic forces on endothelial cells (fluid shear stress), but also by other physical factors. Through these processes the permeability of the endothelial barrier is increased, which in turn leads to retention of LDL and other apoB lipoproteins in the intima of the vessel through interaction with matrix components. In the intima LDL undergoes oxidative modification due to the reaction with reactive oxygen species (ROS). Minimally oxidized LDL stimulates the overlying endothelial cells to recruit monocytes to the vessel wall and also inhibits the production of NO, a mediator of vasodilation. Highly oxidized LDL is formed through the combined action of ROS and different enzymes such as sphingomyelinase (SMase), secretory phospholipase 2 ($sPLA_2$) or myeloperoxidase (MPO) and subsequently aggregates in the intima. These highly oxidized LDL aggregates are recognized by macrophage scavenger receptors (e.g. SR-A, CD36, CD68) and lead to foam cell formation, which is the term for cholesterol-engorged macrophages. Scavenger receptor expression is in turn mediated by cytokines (e.g. TNF-α, IFN-γ) (see Figure 7).[2]

Macrophages secrete apoE, which may inhibit the formation of foam cells through the export of cholesterol to HDL. The accumulation of foam cells in the intima and their subsequent apoptosis/necrosis leads to a growing mass of extracellular lipids and other cell debris and therefore to the formation of fibrous plaques (see Figure 7). A possible rupture and erosion of the lesion can lead to an acute occlusion of a blood vessel through the formation of a thrombus or blood clot leading to myocardial infarction or stroke.[2]

To study the characteristics of oxidized LDL particles, various methods have been developed to simulate oxidation conditions *in vitro*. The most widespread procedure is the *in vitro* oxidation of LDL using transition metal ions (typically Cu^{2+}).[36, 58-59] The LDL peroxidation process can be monitored by continuous spectrophotometric observation at a wavelength of 234 nm. This method is based on the recording of the production of peroxidized polyunsaturated fatty acids (PUFAs), which contain conjugated dienes absorbing with a maximum at about 234 nm.[59] The measured lipid peroxidation profile can be divided in three characteristic sections. The sigmoidal curve contains a 'lag phase', which is a period of relatively slow peroxidation due to the consumption of incorporated antioxidants. The lag phase is followed by a period of uninhibited peroxidation named propagation phase. The

third phase, the so-called decomposition phase, is the terminal phase where most of the fatty acids have been oxidized and the rate of the decomposition of conjugated dienes exceeds the rate of their formation. Therefore the absorption at 234 nm decreases.[60-61]

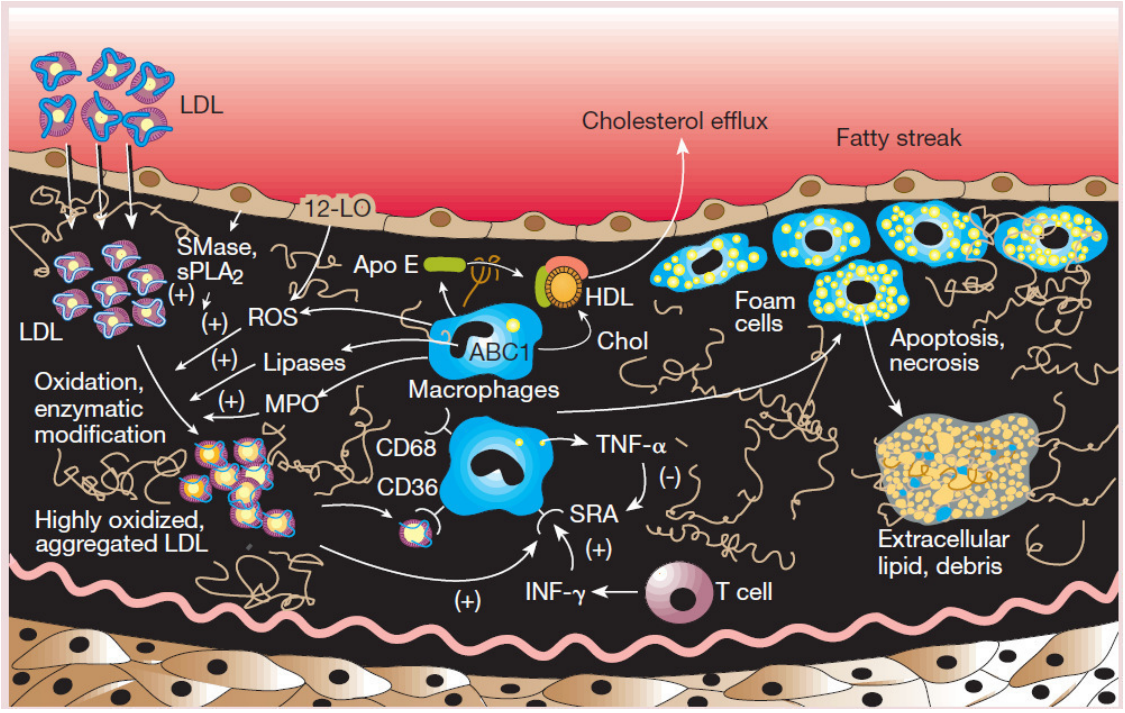

Figure 7: Schematic representation of the intima of a vessel wall (black). The upper cell layer represents endothelial cells separating the intima from the blood stream, whereas the lower layer represents smooth muscle cells from the media. LDL particles penetrating the endothelial cell layer are oxidized by the action of reactive oxygen species (ROS), sphingomyelinase (SMase), secretory phospholipase 2 ($sPLA_2$), myeloperoxidase (MPO) and other lipases. These highly oxidized LDL particles aggregate and are taken up by macrophages through different receptors (SRA, CD36, CD68). The expression of these receptors is in turn regulated through cytokines like tumor necrosis factor-α (TNF-α) and interferon-γ (INF-γ). Cholesterol-engorged macrophages are called foam cells and accumulate in the intima. The apoptosis or necrosis of these foam cells leaves behind extracellular lipids and other cell debris, which leads to the formation of so-called fatty streaks (plaques). Figure was taken from [2].

So far it has been shown that apoB-100 is highly sensitive to oxidation and showed a significant loss of thermal stability already at early stages of oxidation.[38] The changes at early stages of oxidation are predominantly located in the β-sheet regions.[62] However, the core lipid components preserve their structural integrity for a prolonged period of time. This means that the lamellar organization in the core remains at least partially structured even after 18 hours of oxidation.[38, 63] Further, it could be shown that the lag phase was negatively correlated with temperature (higher temperature lead to shorter lag time) and is also dependent on the order/disorder transition of the core lipids.[64] Moreover it has been found that size polydispersity increases with ongoing oxidation, however, the overall structure of the lipoprotein was still similar to that of the native particle.[9, 63]

2.3.2 Triglyceride-rich LDL

Another important group of modified LDL particles are small dense triglyceride-rich LDLs associated with a condition called hypertriglyceridemia. This disease is characterized by high blood levels of triglycerides, one of the most abundant lipid molecules in most organisms. Profound changes in the core and surface domains of LDL have been found in patients with hypertriglyceridemia. With increasing TG levels in plasma, core CEs are depleted and replaced by TG molecules in LDL.[65] Therefore LDL TG content is a predictable function of plasma TG level.[66] This alteration of the particle core in turn influences the melting transition temperature, which decreases with increasing TG content.[66]

Furthermore an altered cell-uptake in cultured cells could be shown. More precisely, a reduced uptake of LDL from hypertriglyceridemic patients in fibroblasts was observed, whereas the uptake by HepG2 cells increased with LDL TG content.[66-68] The different uptake of normal LDL compared to triglyceride-rich LDL in cells may come from effects on the tertiary structure of apoB-100 or its environment due to the increased TG level in the core. The induced changes alter the apoB-100 affinity towards the LDLR resulting in increased uptake by HepG2 cells and reduced uptake by fibroblasts.[66]

Structural investigations showed that at body temperature the cores were isotropic liquids for both normal and triglyceride-rich LDL. Circular dichroism spectra could not detect differences in the secondary structure of normal and triglyceride-rich LDL.[66] CryoEM studies indicate that normal LDL has a discoid shape regardless of its physical state, whereas triglyceride-rich LDL does not have a discoid shape but a more spherical shape. Consequently TG content plays a role in determining the shape of LDL.[69] Another cryoEM study also observed triglyceride-rich LDL as spherical particles without the characteristic striations in the core, however, the core-melted normal LDL showed a similar structure in this case. It was suggested that freezing the LDL core to a smectic lamellar phase imposes structural constraints that force the particle to change its shape from a sphere without striations to an ellipsoid with lamellae.[68]

2.4 High hydrostatic pressure

The physical quantity pressure *P* is defined as the force applied perpendicular to the surface of an object per unit area on which that force is exerted.

$$P = \frac{F}{A} \tag{1}$$

where *F* is the applied force and *A* is the area of the contacted surface.[70]

The SI-unit for pressure is 1 Pascal [Pa] = 1 N/m² = 10^{-5} bar. Pressure is always distributed to solid boundaries or across sections of fluid perpendicular to these boundaries or sections at every point. Pressure is a fundamental thermodynamic variable and intrinsically tied to volume. The pressure at any given point of a static (non-moving) fluid is called hydrostatic pressure.[70] The application of high hydrostatic pressure is a powerful method, which enables the tuning of a system's volume in a controllable and reversible way. Thereby it is possible to study the properties of a system under HHP. A huge variety of effects such as structural, dynamical, electronic or other phase transitions can be observed. HHP methods are applied in multiple scientific disciplines like in physics, chemistry, geosciences or biology. Through the appearance of miniature, safe high-pressure equipment it became possible to use such tools also in standard laboratories. The potential combination with other techniques further disseminated the application of HHP.[71]

Pressure-generation methods can be divided into three categories: (1) Hydraulic techniques for the compression of fluids used for pressures up to 1.4 GPa (14,000 bar). Hydraulic techniques are methods where either the sample is a fluid itself or the pressure-transmitting medium is a fluid. Such techniques are applied to large volumes of fluid (> 1 mm³).[72] These hydraulic methods were applied in the experiments carried out within the scope of this thesis. The pressure applied in the subsequent experiments was in the range of up to 350 MPa (3,500 bar). (2) The compression of large-volume solid samples (> 1 mm³) in the range from 2 to 20-30 GPa (20,000 to 200,000-300,000 bar). Those techniques are mainly applied for materials science and geophysical studies. (3) Diamond-anvil cells (DAC), which are used to pressurize samples in a volume range several orders of magnitude smaller than the before mentioned categories.[72]

When working with high pressure equipment there is, however, an inevitable risk, which is caused by the potential energy stored in such a system. Through the compression of fluid contents, energy is stored in the system and the possibility of this energy being converted to kinetic energy is present. This energy can be transferred to components of the pressure

system and might cause injury in case of failure. Therefore, it is very important to know limitations of the applied material to avoid any damage or failure. The amount of energy stored in the system is a crucial factor, as fluids (like water or hydraulic oil) are compressed by about 10 % for pressures of 300-400 MPa (3-4 kbar) and about 25 % for pressures of about 1 GPa (10 kbar). The corresponding stored energies are of the order 0.5 kJ mol^{-1} $kbar^{-1}$. Compared to this value a gas such as helium stores energies of 2000 kJ mol^{-1} $kbar^{-1}$. This makes clear that greater precautions against failure or damage have to be taken when high pressure is applied to gases than liquids and to large volume systems than small ones. To be prepared for a safe working environment means using good engineering and operating techniques which lead to reliable systems.[72]

2.5 Effect of high hydrostatic pressure on biological systems

The basic fields of application for HHP research have commonly been investigations of inorganic material such as solid matter, crystalline material, polymers, metals, alloys, and also liquids. However, with the development of more diverse sample holders and sample environments as well as the combination of HHP with various analytical techniques (Infrared and Raman spectroscopy, X-ray and neutron scattering, NMR, microscopy, etc.) the research areas have expanded to include new fields of application, especially biological systems. To date research of biological systems has primarily focused on four major fields, namely lipid systems (biomembrane mimetics), proteins (enzymes), deep sea organisms and the effect of HHP on food production processes.[73]

A key-concept underlying all pressure effects is Le Châtelier's principle, which says that any reaction or physical transformation of a system that leads to a reduction in volume will be favored at high pressure.[73] Biochemical effects such as denaturation of proteins, lipid phase changes or biomolecular interactions also obey this rule. It has been observed that at a given temperature a pressure increase leads to lowered entropy of a system and therefore pressure is considered to have the opposite effects to temperature.

2.5.1 Lipid systems

Lipids and bio-membrane assemblies undoubtedly belong to the most important biological structures. Their abundant presence in living organisms is explained by the many important functions lipid membranes fulfill in nature. They occur in all kinds of cells as plasma membranes, membranes of cell organelles or in vesicles. Membranes maintain the integrity

of cells and are responsible for compartmentalization. It is known that lipid bilayers and lipid-protein assemblies are the most pressure sensitive parts of cells and pressure has a major effect on these mesostructures. Lipids are amphiphilic molecules and self-assemble according to their preferred curvature and due to effects such as the interplay between curvature, elastic stress and chain packing frustration. They form a variety of so-called type I (normal) and type II (inverse) lyotropic liquid crystalline phases (e.g. lamellar L_α, two-dimensional hexagonal H_I/H_{II} or inverse bicontinuous cubic phases Q_{II}^G, Q_{II}^D, Q_{II}^P).[23, 74]

The general effect of pressure on any kind of system is the reduction in volume of that corresponding system, which is also true for lipid mesophases.[74-75] Effects of HHP are a reduction in hydrocarbon chain motion and an increase in chain ordering. Another effect is a reduction of the cross-sectional area of the lipid hydrocarbon tail region, whereas the cross-section of the lipid head group is less sensitive to pressure. Due to these effects increasing pressure will tend to increase the positive curvature of a lipid monolayer. However, for type II (inverse) systems the increasing pressure will cause a reduction of the negative curvature.[74-76]

Besides that, the lattice parameters are influenced by HHP. Due to the chain ordering the lattice parameters of flat bilayers increase, however, this effect might be offset to a certain degree by isotropic compression of the water incorporated between the bilayers in the whole mesophase. In inverse systems the negative curvature is reduced through the reduction of chain cross-section, which leads to swelling of the hydrophilic surface and a significant increase of the lattice parameters. The emerging packing frustration within the mesophase increases as well and therefore limits the swelling at a certain stage.[74, 76-77]

Furthermore phase changes induced by HHP are possible if it is energetically favorable. For type I systems this means that phase changes to structures with a larger interfacial curvature is favorable (e.g. lamellar to hexagonal H_I). For type II systems this means that a negative curvature has to become more positive (e.g. hexagonal H_{II} to lamellar). HHP can also induce phase transitions like for lamellar bilayers, which undergo a transition from fluid to gel structure.[23, 74, 78]

For lipid-protein assemblies the pressure stability increases with protein concentration, which is ascribed to attractive protein-lipid headgroup interactions. However, pressure-induced changes in the physical state of the membrane have an impact on large integral and peripheral proteins. At several kbar when the bilayer is ordered by pressure the membrane proteins stop functioning and integral/peripheral proteins are detached from the membrane

through weakening of the protein-lipid interactions. But for those relatively complex lipid-protein complexes so far only a few studies exist.[23, 74]

It has to be mentioned that the effect of increasing pressure on the structure of lipids and lipid assemblies is similar to the effect of decreasing temperature. Phase transitions, which can be induced by a decrease in temperature, can be triggered by an increase in pressure.[74, 76]

2.5.2 Proteins

The utilization of HHP has the advantage that its perturbation of the sample (and the macromolecules in the sample) solely depends on the volume change of the system. Therefore also proteins favor states of a smaller specific volume.[24] In general, the effects of pressure on proteins are reversible and only rarely lead to aggregation or changes in the covalent structure of the molecule.[79-80]

Several effects lead to the observed partial or complete unfolding and therefore net volume change of the proteins: (1) the disruption of non-covalent bonds including salt bridges (electrostatic interactions) or hydrophobic interactions, (2) changes in protein hydration e.g. through the hydration of newly exposed nonpolar & polar residues, and (3) conformational changes e.g. the loss of free volume due to packing defects in the folded state. The overall volume change is largely a result of the disappearance of solvent-inaccessible voids in the protein structure.[79-80] The total specific volume reduction of a protein upon unfolding is in the range of 0.5 - 1.0 % and so relatively small.[24]

Further effects that influence protein conformational changes are the compressibility of hydrogen-bonds and changes in the torsional angles and helix orientations within a given structure.[24] Due to these and aforementioned effects on non-covalent bonds pressure basically influences the quaternary and tertiary structure of a protein and leads to their complete disruption, whereas the secondary structure (at least partly) remains.[24] Most small monomeric proteins unfold reversibly at 4 – 8 kbar, while oligomeric proteins and multiprotein assemblies often already dissociate at 1 – 2 kbar.[80] There are indications that the conformation of a protein denatured by pressure is more compact than that of a protein denatured by temperature or chemical agents. Moreover, it is assumed that they resemble ‘molten-globule’-type structures, which makes the application of pressure even more appealing for the thermodynamic investigation of the folding process.[80]

Another aspect of HHP is the modification of protein overall and local dynamics. It could be shown in neutron scattering experiments that the dynamics of lysozyme were influenced by pressure even if the protein stayed in its native conformation. The intrinsic dynamics are slowed down at HHP and therefore suggest a confinement effect most probably through a different packing of hydration water molecules and an immobilization of protons.[81]

2.5.3 Deep sea organisms

Organisms on planet Earth are exposed to a huge variety of pressures. In particular organisms in the deep sea face a harsh environment concerning temperature and pressure conditions. The pressure increases about 10 MPa km^{-1} and hence results in a maximum pressure value of approximately 100 MPa at the deepest point currently known, i.e. the Mariana Trench (11,000 m depth).[73, 82] The average pressure value in the ocean is 38 MPa (3,800 m depth), where almost no light reaches the sea floor and the temperature is around 2°C. For a long time this harsh environment has been assumed to be inhospitable for organisms, however, today it is known as one of the richest biological environments. Especially the investigation of black smokers (hydrothermal vents) with temperatures of up to 120°C has shown a huge diversity of bacteria and archaea living in the deep sea.[73, 82] Most of them are obligate piezophiles, which means that they cannot grow at atmospheric pressure. Different studies suggested 120 MPa as the upper pressure limit for microorganisms to survive.[83-84] However, different laboratory studies revealed that most microorganisms are killed at pressures of 200-600 MPa.[85] This finding also led to the development of a technique called “pascalization”, which is an alternative to thermal pasteurization for food preservation (discussed in 2.5.4).[73, 86]

At a molecular level it is known that proteins and nucleic acids only elastically change under pressure, but lipid membranes and intermolecular interactions are strongly affected.[87] Pressure induces the solubilization of membrane proteins and the permeabilization of the outer membrane in Gram-negative bacteria.[88-89] Piezophilic microorganisms are known to adapt and change the ratio of saturated to unsaturated lipids in their membranes. A higher portion of unsaturated lipids leads to a higher fluidity.[23] Another pressure-induced effect is a conformational change of the ribosome, which halts protein synthesis. It is known that organisms under such conditions upregulate the expression of stress-induced proteins.[90]

So far, no specific pressure-induced cellular response could be identified; it rather seems to be a wide range of responses as a result of high pressure conditions.[73, 85, 91]

2.5.4 High-pressure processing of food

High-pressure processing is a novel non-thermal method for food preservation and is therefore an alternative to thermal processes (such as thermal sterilization or pasteurization) while maintaining taste, texture and the natural nutritional characteristics. This kind of technique has been applied in food industry since the 1990s. Usually these processes work in a pressure range from 100-800 MPa, strongly depending on the food product and objective.[32, 92-93]

Technologically the process is isostatic (pressure is transmitted uniformly and instantly) and adiabatic (no variation in temperature).[32] Such a high-pressure system consists of a high-pressure vessel and its pressure-generation system, a temperature-control system and material-handling system. The food products should be packaged in a flexible packaging. They are loaded into the high pressure chamber and after this the vessel is sealed. Then the vessel is filled with the pressure-transmitting fluid (typically water, glycol solutions, silicone oil, ethanol solutions or inert gases) and pressure is applied. For most applications the food products are held for 3-5 min at 600 MPa. After pressure treatment the products are removed and stored conventionally.[92]

The basic principle of HHP processing is the extension of shelf-life and the increase food safety through the inactivation of microbial population. The extent of this effect is dependent on many interacting factors: type and number of microorganisms, the magnitude and duration of HHP application, the process temperature and the composition of the suspension media or food.[92]

HHP does not alter the low-energy, covalent bonds, which have low compressibility and do not break within the ranges of pressures applied in food processing.[32] Consequently the primary structures of molecules like proteins or fatty acids remain intact. However, ionic bonds, hydrophobic interactions or hydrogen bonds are disrupted and so the secondary, tertiary or quaternary structure of complex organized components (such as proteins or membranes) is destroyed. The global consequences for the product are diverse, as certain enzymes might be inhibited, which can have an overall effect on the product's properties. Small molecules such as vitamins, amino acids, flavor molecules and other low-molecular weight compounds are hardly affected and so the organoleptic and nutritional properties are only slightly modified.[32] Cell death of foodborne microorganisms occurs due to a multitude of damages in different parts of the cell and when those damages exceed the cell's ability to repair.[32] The cell membrane is the main target of HHP, which basically causes

a permeability modification and functionality disruption. It is known that Gram-positive bacteria are more resistant to pressure than Gram-negative bacteria, molds or yeasts. The double-layered PLs that are present in the lipid membranes are packed tightly during the compression and promote a transition to a gel state. During decompression the double-layer structure is lost, which leads to pore formation. Moreover, the contact of membrane attached enzymes is loosened and leakage of intracellular constituents through the permeabilized membrane is possible.[32, 92] HHP has a higher destructive effect the more complex the organisms get (prokaryotes are usually more resistant than eukaryotes). The multiple effects of protein denaturation, lipid phase changes, and enzyme inactivation contribute to the destruction of cell morphology, genetic mechanisms, and biochemical processes and therefore inactivation of foodborne microorganisms.[32]

2.6 X-rays and neutrons

First of all it has to be stated that there is a great deal of similarity between the theoretical backgrounds of X-ray and neutron scattering. Both methods are applied to study the structure of matter at different levels of complexity. However, as the two methods were historically developed in different time periods and from different groups of scientists the applied terminologies often differ although they describe the same phenomena. The aim of this chapter is to give an overview of both scattering theories and to emphasize both similarities and differences. [94-95]

X-rays are electromagnetic waves that range from a wavelength spectrum of 10^{2} to 10^{-2} Å. X-rays cover a broad range of applications and are commonly used for molecular characterization of condensed matter in scientific research. Those X-rays used for the characterization of material are generally in a wavelength range of 0.5 – 2.5 Å. This is the wavelength range, which is of the same order of magnitude as most interatomic distances. Usually the characteristic emission spectrum of a copper (Cu) anode is used when a lab source (X-ray tube) is applied. A rotating Cu anode emits X-ray radiation after bombardment through high-energy electrons. This spectrum contains the characteristic Cu *Kα* line with a wavelength of 1.5418 Å. Occasionally the *Kα* line from a molybdenum (Mo) target with a wavelength of 0.7107 Å is used as an alternative. These typical wavelengths can certainly also be applied when synchrotron radiation is used. A synchrotron is a large-scale facility and a cyclic particle accelerator, which produces electromagnetic radiation for the use in experimental stations (so-called beamlines). The synchrotron usually contains a linear

accelerator (LINAC) and a full energy booster, which are responsible for the acceleration of electrons to their final energy before they are injected to the storage ring. The synchrotron radiation is produced when the travelling electrons are deflected from their trajectories in magnetic fields. For this reason bending magnets are installed in the storage ring and deflect the circulating electrons from their path to yield the electromagnetic radiation for the beamlines. The broad spectrum of a synchrotron source is filtered with a monochromator to provide the desired wavelength. X-rays propagate with the speed of light c = 2.998 x 10^8 m/s and are related to the wavelength λ and the frequency ν by

$$\lambda = \frac{c}{\nu} \tag{1}$$

and also exhibit a wave-particle duality similar to light. Some properties of X-rays are better described when they are assumed to be a stream of photons and others when they are assumed to be a wave. A photon is characterized by its energy E and momentum p, whereas a wave is described by its wavelength λ and frequency ν. These physical quantities are related to each other by

$$E = h\nu \tag{2}$$

and

$$p = \frac{h}{\lambda} \tag{3}$$

where h is Planck's constant (= 6.626 x 10^{-34} J s). Equation (3) is the so-called *de Broglie relation*. A photon does not have a mass or an electrical charge and the shorter its wavelength the higher its energy. For the characteristic Cu *Kα* and Mo *Kα* radiation, the energy of a photon is 8.04 and 17.44 keV, respectively. [94-95]

The neutron is an uncharged elementary particle which possesses a mass (m = 1.675 x 10^{-24} g) and a spin (1/2). Its kinetic energy E and momentum p are

$$E = \frac{1}{2}mv^2 \tag{4}$$

and

$$p = mv \tag{5}$$

where v is its velocity.[94-95]

The conventional source for neutrons for scientific purposes is a research reactor. These nuclear reactors serve primarily as a neutron source and are not used for electricity production or heat generation (non-power reactors). They have the same working principle

but need far less fuel and therefore produce far less fission products compared to power reactors. Examples of European research reactors are the Institut Laue-Langevin ILL (Grenoble, France) and the FRM II at TU München (Garching, Germany). Although research reactors are still the main source of neutrons, the so-called spallation neutron sources gain in importance. Spallation sources use a high-powered proton accelerator, which focuses an intense beam of protons onto a target, generally tantalum (Ta) or tungsten (W). This target produces free neutrons through occurring spallation processes. Examples for European spallation sources are the ISIS neutron source (Oxfordshire, United Kingdom) and the SINQ at the Paul Scherrer Institut (Villigen, Switzerland).

Whether the neutrons are produced from a nuclear fission reaction in a reactor or through the bombardment of a heavy metal in a spallation source, they are emitted with a very high velocity and have to be moderated for neutron scattering experiments in any case. This is done through multiple collisions of the produced neutrons in the moderating material. For cold neutrons they pass through liquid deuterium maintained at around 25 K. For thermal neutrons the moderating material is heavy water (D_2O, deuterium oxide) at around 330 K. Hot neutrons are produced with a hot graphite at around 2000 K. After a sufficient number of collisions the neutrons reach a "gas" like state with the approximate temperature of the moderator. Their velocity curve follows a Maxwell-Boltzmann distribution of a gas in equilibrium, given by

$$f(v) = 4\pi \left(\frac{m}{2\pi\, kT}\right)^{\frac{3}{2}} v^2 \exp\left(-\frac{1}{2} mv^2/kT\right) \tag{6}$$

where *f(v) dv* is the fraction of gas molecules with velocities between *v* and *v + dv*, *k* is Boltzmann's constant (1.381 x 10^{-23} J/K) and *T* is the temperature.[94] Neutrons also possess a wave-like behavior with their wavelength λ given by the *de Broglie equation*

$$\lambda = \frac{h}{p} = \frac{h}{mv} \tag{7}$$

comparable to X-rays. Table 1 shows values of *v*, *E* and λ for three typical moderator temperatures. Again the typical wavelengths, like for X-rays, are of the order of 1 Å and can therefore be applied for the investigation of structure at an atomic level.[94]

Table 1: Comparison of typical values of velocity *v*, energy *E* and wavelength λ of neutrons from cold, thermal, and hot sources (taken from [94])

	Cold	Thermal	Hot
T (K)	25	330	2000
v (m/s)	642	2333	5743
E (meV)	2.16	28.4	172
λ (Å)	6.16	1.696	0.689

As already mentioned before, neutrons and X-rays exhibit a lot of common properties including their scattering behavior. This also implies that the theoretical tools and experimental techniques can be applied to both X-ray scattering and neutron scattering. However, there are some important differences, which will be pointed out in the following, making the two techniques complementary to each other. Due to this complementarity the two methods are often applied together to combine the gained information.[94]

One of the most significant differences between X-ray photons and neutrons concerns the energies of the particles. As mentioned before, X-ray photons have energies of around 10 keV, whereas a thermal neutron exhibits a kinetic energy in the order of 10 meV. At ambient temperature the energy associated with motions of atoms, arising from vibrational, rotational or translational motions is around 20 meV. In the case that an X-ray photon is scattered by an atom and energy is exchanged in this process, the energy of the photon is scarcely affected. On the other hand, when a neutron is scattered inelastically its energy is modified to an extent which can be measured and interpreted accordingly. This inelastic scattering of neutrons is a very useful method to investigate the motions of atoms and represents a clear example for the different applications of X-rays and neutrons in some techniques.[94]

2.7 Basics of scattering

First, we have a closer look to the terms flux, scattering cross section and intensity. The term flux is generally used to describe the strength of a beam of radiation. Depending on the kind of radiation and the theoretical perspective the flux *J* has several definitions. In the case of a plane wave with parallel rays emitted from the source, *J* is defined as the amount of energy

transmitted per unit area per second. In the case of a stream of particles, *J* is better described by the particle flux, namely the number of photons or neutrons passing through a unit area per second. In the case of a spherical wave, where the radiation is emitted or scattered by a point source, the flux *J* is defined as the amount of energy per second through a unit solid angle rather than a unit area. Therefore, the flux *J* becomes independent of the distance R from the source of radiation to the respective observation point. The same is true for a particle stream emitted from a point source, where *J* is described as the number of photons or neutrons per second per solid angle.[94-95]

In case a sample is hit by an incident plane wave with flux J_0, the result is a scattered spherical wave that propagates in all directions. The aim of an experiment is to measure flux *J* of the scattered wave as a function of the scattering direction and to interpret the results to get information about the investigated sample. Under exactly defined experimental conditions the scattered flux *J* will proportionally increase or decrease with the incident flux J_0. Therefore, the actual experimental aim is to measure the ratio of J/J_0 as a function of the scattering direction. As J_0 represents a plane wave, whereas *J* represents a spherical wave, the relation J/J_0 has the dimension of area per solid angle. In the neutron scattering community the ratio J/J_0 is invariably known as the differential scattering cross section.[94-95]

$$\frac{d\sigma}{d\Omega} \equiv \frac{J}{J_0} \tag{8}$$

In particle language this would mean that the differential scattering cross section is the probability that a photon or neutron impinging on a sample is scattered into a unit solid angle in the given direction. Integrating the differential scattering cross section over the whole solid angle Ω gives the total scattering cross section σ_{tot}. The total scattering cross section is therefore

$$\sigma_{tot} = \frac{total\ number\ of\ particles\ scattered\ in\ all\ directions\ per\ second}{flux\ of\ the\ incident\ beam} \tag{9}$$

and has dimension of area, as the word *cross section* implies.[94-95]

Experimentally the flux *J* of the scattered beam is measured as a function of the scattering angle. The flux *J* may be converted to the differential scattering cross section if the incident flux J_0 is known. Otherwise, *J* is simply recorded in arbitrary units (e.g. counts per second). The term intensity, however, has been used especially by the X-ray scattering community to name both the flux *J* and the differential scattering cross section J/J_0.[94]

The diffraction of X-rays and neutrons is a combination of two consecutive phenomena: (1) X-rays are scattered by individual electrons or neutrons are scattered by individual nuclei

and (2) these scattered waves interfere with each other to result in a measurable scattering pattern caused by constructive or destructive interference. It is basically because of this interference that fluxes vary with different directions. The information of flux as a function of direction is the basic data, which is interpreted to obtain information about the examined sample.[94]

Strictly speaking the term scattering must only be used to describe phenomenon (1) and the term diffraction for a combination of phenomena (1) and (2). However, the term diffraction is commonly used for crystalline materials or matter with some other kind of regular order. Then the scattered beam concentrates in a number of sharply defined directions to result in a diffraction pattern. On the contrary the term scattering is used when the scattering pattern is diffuse and mainly in the small-angle region.[94]

Phenomenon (1), namely scattering, must be discussed for X-rays and neutrons separately because of the difference of nature of the radiation and their different interaction mechanisms with matter. However, the interference effects are exactly the same and can therefore be discussed as a single phenomenon. The theories for the interpretation of diffraction of X-rays and neutrons are equally applicable for both radiation types.[94]

Figure 8 shows a plane incident wave (emanating from an X-ray or neutron source) propagating in the direction of unit vector S_0, which is subsequently scattered by two particles located at the points O and P. A detector is located in direction of the scattered unit vector S at a distance far from the actual scattering event. If the scattered waves are coherent and no phase change occurs through the scattering process, then the phase difference $\Delta\varphi$ of the two waves (scattered from O and P) is only dependent on the path length difference δ between the two rays.[94-95]

$$\Delta\varphi = \frac{2\pi\delta}{\lambda} \tag{10}$$

Defining the relative positions of O and P with the vector r, we get QP = $S_0 \cdot r$ and OR = $S \cdot r$, and the phase difference is

$$\Delta\varphi = \frac{2\pi}{\lambda}\,(S_0 \cdot r - S \cdot r) = -2\pi s \cdot r \tag{11}$$

where s is defined as

$$s = \frac{S - S_0}{\lambda} \tag{12}$$

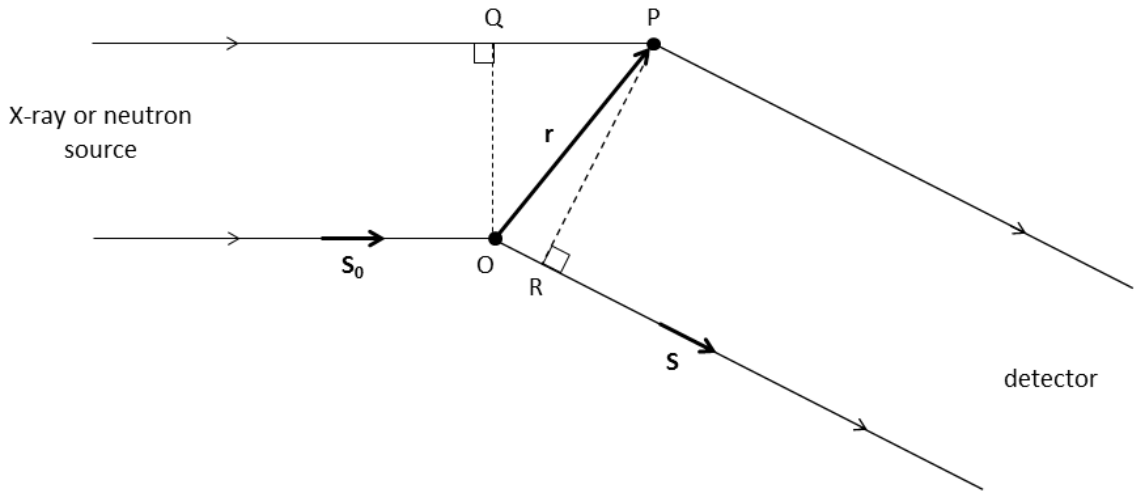

Figure 8: Schematic representation of an incident plane wave scattered by two points (O and P) and the resulting geometry of the path length difference. Figure was reproduced from [94].

The vector *s* is defined as the scattering vector and completely describes the scattering geometry, namely the incident and scattered beam directions and the wavelength. Its magnitude is related to the scattering angle 2θ by

$$|s| = s = \frac{2\,sin\theta}{\lambda} \tag{13}$$

Frequently the quantity *q* is defined as the scattering vector instead of *s*, which is related to *s* by

$$q = 2\pi s \tag{14}$$

The vector *q* can also be defined as

$$q = k - k_0 \tag{15}$$

where $k_0 = 2\pi S_0/\lambda$ and $k = 2\pi S/\lambda$ are the wave vectors characterizing the incident and scattered radiation.[94-95]

The scattering vector *q* is sometimes also referred to as the momentum transfer vector. When equation (12) is written as

$$\hbar q = hs = \frac{h}{\lambda}S - \frac{h}{\lambda}S_0 \tag{16}$$

where ħ ≡ h/2π, it can be seen that it represents the change in the momentum that occurs from the incident photon or neutron to the scattered one. Thus the momentum transferred from the radiation to the scattering particle is equal to *q* when measured in units of *ħ* and equal to *s* when measured in units of *h*.[94-95]

2.8 Scattering of X-rays

The kind of interaction of a stream of particles with a sample will depend on whether the incoming probe has a charge, a spin or incident energy. X-ray photons do not have a charge but, as an electromagnetic wave, they consist of oscillating electric and magnetic fields, which interact with the charge of orbital electrons in the sample. X-rays penetrate matter more easily compared to free electrons, which are electrostatically repelled by the orbital electrons of the atoms in the sample and are therefore prevented from penetrating the sample by more than a small fraction of a micrometer. In contrast X-rays can pass through a few millimeters of aluminum.[94-95]

The X-rays as electromagnetic radiation interact with the electrical charges in matter. If an electron is irradiated with a beam of X-rays the electromagnetic field of the beam induces an oscillation of the electron. The alternating acceleration of the oscillating electron in turn induces the emission of electromagnetic radiation of the same frequency propagating in all directions. The total scattering cross section of an electron is

$$\sigma_e = \frac{8}{3}\pi r_e^2 \tag{17}$$

which has a numerical value of 6.65 x 10^{-29} m² = 0.665 barn (1 barn = 10^{-28} m², classical radius of the electron r_e = 2.818 x 10^{-15} m). The cross section σ_e is independent of the polarization state of the incident X-rays. The scattered beam flux is proportional to 1/m². Atomic nuclei are of much higher mass compared to electrons therefore the scattering of X-rays from atomic nuclei is extremely small and can be safely neglected. Consequently the scattering of X-rays from matter entirely results from the scattering of electrons around atomic nuclei.[94-95]

2.9 Scattering of neutrons

The scattering of neutrons results from an interaction between the incoming neutrons and the nuclei in the sample through nuclear forces. The efficacy of neutron scattering by a certain nucleus is expressed through the scattering length *b* or in other words the differential scattering cross section, which is

$$\frac{d\sigma}{d\Omega} = b^2 \tag{18}$$

The scattering length *b* is independent of the wavelength λ of the incoming neutrons. For a particular nucleus the interaction depends on the spin state of the neutron-nucleus system. The neutron has a spin 1/2, the nucleus might have a nonzero spin *i*, which results in a

neutron-nucleus system spin of $i + 1/2$ or $i - 1/2$ with the associated scattering length values b^+ or b^-. If the nucleus has zero spin then the neutron-nucleus system spin is 1/2 and there is only one value of the scattering length. Generally, the value b refers to a case where the atom is bound to a matrix (e.g. polymers or condensed matter in general) in contrast to atoms that are free to recoil (e.g. gases). In this case the free-atom scattering length is slightly different to the bound-atom scattering length.[94-95]

The strength of the neutron-nucleus interaction basically depends on details of the nuclear structure and is not related to atomic number in a simple way. The scattering length b can vary greatly among elements with similar atomic number or mass and even among isotopes of the same element. This is in clear contrast to X-rays, where the interaction with an atom depends primarily on its number of electrons. Therefore the atomic scattering factor f(s) for X-rays increases linearly with atomic number.[94-95]

The radius of an atomic nucleus is very small, but the range of nuclear forces that interact with the neutrons is even smaller (10^{-14} to 10^{-15} m). This means that the size scale of the scattering event is several orders of magnitude smaller than the wavelength of the incoming neutrons. Consequently, the scattering of neutrons is spherically symmetric and the value of b does not change with the scattering angle. This is in contrast to X-rays, where the equivalent value to b is the product of the scattering length b_e of a single electron and the atomic scattering factor f(s). This atomic scattering factor f(s) decreases with increasing s, because atomic electron clouds are in the same size range as the incoming X-ray wavelength and thus rays scattered from different parts of the electron cloud experience a phase difference that increases with 2θ.[94]

The atomic scattering factors f(s) for X-rays are calculated from the theoretical electron density distributions in atoms, whereas for neutrons the scattering cross sections are determined experimentally, as not enough details about the exact nuclear forces are understood to calculate the corresponding values.[94-95]

Neutron scattering is in many aspects complementary to X-ray scattering and therefore the techniques are often used in combination with each other. As already mentioned, the neutron cross section varies randomly among different elements, whereas the X-ray atomic scattering factor f(s) increases simultaneously with the atomic number. This fact can constitute a major advantage in certain cases but on the other hand can be a disadvantage as well. For instance, the scattering of X-rays from heavy atoms (with a high atomic number and therefore a high electron density) can often overwhelm the scattering from the rest of

the molecule, especially from lighter atoms. Nonetheless, it is exactly this characteristic behavior, which is used for solving the phase problem in crystal structure analysis. Hydrogen, however, is almost invisible to X-rays, even if the rest of the molecule only contains light atoms such as carbon or oxygen. So it is almost impossible to determine the positions of hydrogens by X-ray analysis. This issue can be addressed by using neutron scattering, as hydrogens are highly visible by neutrons. Moreover, the difference in scattering cross section between hydrogen and deuterium is of major importance as those isotopes may be exchanged mutually in molecules but exhibit substantial differences in scattering behavior. Through this exchange, also called deuterium labeling, it is possible to make certain parts of molecules selectively “visible” without altering their thermodynamic properties.[94-95]

3. References

1. Brown, M. S.; Goldstein, J. L., A receptor-mediated pathway for cholesterol homeostasis. *Science* **1986,** *232* (4746), 34-47.

2. Lusis, A. J., Atherosclerosis. *Nature* **2000,** *407* (6801), 233-241.

3. Prassl, R.; Laggner, P., Molecular structure of low density lipoprotein: current status and future challenges. *Eur. Biophys. J.* **2009,** *38* (2), 145-58.

4. Prassl, R.; Chapman, J. M.; Nigon, F.; Sara, M.; Eschenburg, S.; Betzel, C.; Saxena, A.; Laggner, P., Crystallization and preliminary x-ray analysis of a low density lipoprotein from human plasma. *J. Biol. Chem.* **1996,** *271* (46), 28731-28733.

5. Ritter, S.; Frey, I.; Diederichs, K.; Grathwohl, D.; Keul, J.; Baumstark, M. W., Crystallization and preliminary X-ray diffraction data of two different human low-density lipoprotein (LDL) subfractions. *Proteins-Structure Function and Genetics* **1997,** *28* (2), 293-297.

6. Laggner, P.; Kostner, G. M.; Rakusch, U.; Worcester, D., Neutron small angle scattering on selectively deuterated human plasma low density lipoproteins. The location of polar phospholipid headgroups. *J. Biol. Chem.* **1981,** *256* (22), 11832-9.

7. Laggner, P.; Kostner, G. M.; Degovics, G.; Worcester, D. L., Structure of the cholesteryl ester core of human plasma low density lipoproteins: selective deuteration and neutron small-angle scattering. *Proc. Natl. Acad. Sci. U. S. A.* **1984,** *81* (14), 4389-93.

8. Meyer, D. F.; Mayans, M. O.; Groot, P. H.; Suckling, K. E.; Bruckdorfer, K. R.; Perkins, S. J., Time-course studies by neutron solution scattering and biochemical assays of the aggregation of human low-density lipoprotein during Cu(2+)-induced oxidation. *Biochem. J.* **1995,** *310 (Pt 2)*, 417-26.

9. Meyer, D. F.; Nealis, A. S.; MacPhee, C. H.; Groot, P. H. E.; Suckling, K. E.; Bruckdorfer, K. R.; Perkins, S. J., Time-course studies by synchrotron X-ray solution scattering of the structure of human low-density lipoprotein during Cu2+-induced oxidation in relation to changes in lipid composition. *Biochem. J.* **1996,** *319*, 217-227.

10. Prassl, R.; Pregetter, M.; Amenitsch, H.; Kriechbaum, M.; Schwarzenbacher, R.; Chapman, J. M.; Laggner, P., Low density lipoproteins as circulating fast temperature sensors. *PLoS One* **2008,** *3* (12), e4079.

11. Johs, A.; Hammel, M.; Waldner, I.; May, R. P.; Laggner, P.; Prassl, R., Modular structure of solubilized human apolipoprotein B-100. Low resolution model revealed by small angle neutron scattering. *J. Biol. Chem.* **2006,** *281* (28), 19732-9.

12. Orlova, E. V.; Sherman, M. B.; Chiu, W.; Mowri, H.; Smith, L. C.; Gotto, A. M., Jr., Three-dimensional structure of low density lipoproteins by electron cryomicroscopy. *Proc. Natl. Acad. Sci. U. S. A.* **1999,** *96* (15), 8420-5.

13. Liu, Y.; Atkinson, D., Enhancing the contrast of ApoB to locate the surface components in the 3D density map of human LDL. *J. Mol. Biol.* **2011,** *405* (1), 274-83.

14. Liu, Y.; Atkinson, D., Immuno-electron cryo-microscopy imaging reveals a looped topology of apoB at the surface of human LDL. *J. Lipid Res.* **2011,** *52* (6), 1111-6.

15. Liu, Y.; Luo, D.; Atkinson, D., Human LDL core cholesterol ester packing: three-dimensional image reconstruction and SAXS simulation studies. *J. Lipid Res.* **2011,** *52* (2), 256-62.

16. Ren, G.; Rudenko, G.; Ludtke, S. J.; Deisenhofer, J.; Chiu, W.; Pownall, H. J., Model of human low-density lipoprotein and bound receptor based on cryoEM. *Proc. Natl. Acad. Sci. U. S. A.* **2010,** *107* (3), 1059-64.

17. Kumar, V.; Butcher, S. J.; Oorni, K.; Engelhardt, P.; Heikkonen, J.; Kaski, K.; Ala-Korpela, M.; Kovanen, P. T., Three-dimensional cryoEM reconstruction of native LDL particles to 16A resolution at physiological body temperature. *PLoS One* **2011,** *6* (5), e18841.

18. Mikl, C.; Peters, J.; Trapp, M.; Kornmueller, K.; Schneider, W. J.; Prassl, R., Softness of atherogenic lipoproteins: a comparison of very low density lipoprotein (VLDL) and low density lipoprotein (LDL) using elastic incoherent neutron scattering (EINS). *J. Am. Chem. Soc.* **2011,** *133* (34), 13213-5.

19. Doster, W.; Cusack, S.; Petry, W., Dynamical transition of myoglobin revealed by inelastic neutron scattering. *Nature* **1989,** *337* (6209), 754-6.

20. Smith, J. C., Protein dynamics: comparison of simulations with inelastic neutron scattering experiments. *Q. Rev. Biophys.* **1991,** *24* (3), 227-91.

21. Zaccai, G., How Soft Is a Protein? A Protein Dynamics Force Constant Measured by Neutron Scattering. *Science* **2000,** *288* (5471), 1604-1607.

22. Lassalle, M. W.; Yamada, H.; Akasaka, K., The pressure-temperature free energy-landscape of staphylococcal nuclease monitored by H-1 NMR. *J. Mol. Biol.* **2000,** *298* (2), 293-302.

23. Winter, R.; Jeworrek, C., Effect of pressure on membranes. *Soft Matter* **2009,** *5* (17), 3157.

24. Silva, J. L.; Foguel, D.; Royer, C. A., Pressure provides new insights into protein folding, dynamics and structure. *Trends Biochem. Sci.* **2001,** *26* (10), 612-618.

25. Kulkarni, C. V.; Ces, O.; Templer, R. H.; Seddon, J. M., Pressure effects on a protein-lipid model membrane. *Soft Matter* **2013,** *9* (28), 6525-6531.

26. Peters, J.; Martinez, N.; Michoud, G.; Cario, A.; Franzetti, B.; Oger, P.; Jebbar, M., Deep Sea Microbes Probed by Incoherent Neutron Scattering Under High Hydrostatic Pressure. *Z. Phys. Chem.* **2014,** *228* (10-12).

27. Nishiyama, M., High-Pressure Microscopy for Studying Molecular Motors. *Subcell. Biochem.* **2015,** *72*, 593-611.

28. Pressl, K.; Kriechbaum, M.; Steinhart, M.; Laggner, P., High pressure cell for small-and wide-angle x-ray scattering. *Rev. Sci. Instrum.* **1997,** *68* (12), 4588-4592.

29. Kohlbrecher, J.; Bollhalder, A.; Vavrin, R.; Meier, G., A high pressure cell for small angle neutron scattering up to 500 MPa in combination with light scattering to investigate liquid samples. *Rev. Sci. Instrum.* **2007,** *78* (12), 125101.

30. Peters, J.; Trapp, M.; Hughes, D.; Rowe, S.; Deme, B.; Laborier, J. L.; Payre, C.; Gonzales, J. P.; Baudoin, S.; Belkhier, N.; Lelievre-Berna, E., High hydrostatic pressure equipment for neutron scattering studies of samples in solutions. *High Pressure Research* **2012,** *32* (1), 97-102.

31. Winter, R., High Pressure NMR Studies on Lyotropic Lipid Mesophases and Model Biomembranes. In *Annual Reports on NMR Spectroscopy*, Academic Press: 2003; Vol. Volume 50, pp 163-200.

32. Rendueles, E.; Omer, M. K.; Alvseike, O.; Alonso-Calleja, C.; Capita, R.; Prieto, M., Microbiological food safety assessment of high hydrostatic pressure processing: A review. *LWT-Food Sci. Technol.* **2011,** *44* (5), 1251-1260.

33. Hevonoja, T.; Pentikainen, M. O.; Hyvonen, M. T.; Kovanen, P. T.; Ala-Korpela, M., Structure of low density lipoprotein (LDL) particles: Basis for understanding molecular changes in modified LDL. *BBA-Mol. Cell. Biol. Lipids* **2000,** *1488* (3), 189-210.

34. Gantz, D. L.; Walsh, M. T.; Small, D. M., Morphology of sodium deoxycholate-solubilized apolipoprotein B-100 using negative stain and vitreous ice electron microscopy. *J. Lipid Res.* **2000,** *41* (9), 1464-1472.

35. Pregetter, M.; Prassl, R.; Schuster, B.; Kriechbaum, M.; Nigon, F.; Chapman, J.; Laggner, P., Microphase separation in low density lipoproteins - Evidence for a fluid triglyceride core below the lipid melting transition. *J. Biol. Chem.* **1999,** *274* (3), 1334-1341.

36. Esterbauer, H.; Gebicki, J.; Puhl, H.; Jurgens, G., The role of lipid peroxidation and antioxidants in oxidative modification of LDL. *Free Radic. Biol. Med.* **1992,** *13* (4), 341-90.

37. Lund-Katz, S.; Phillips, M. C., Packing of cholesterol molecules in human low-density lipoprotein. *Biochemistry* **1986,** *25* (7), 1562-8.

38. Prassl, R.; Schuster, B.; Laggner, P.; Flamant, C.; Nigon, F.; Chapman, M. J., Thermal stability of apolipoprotein B100 in low-density lipoprotein is disrupted at early stages of oxidation while neutral lipid core organization is conserved. *Biochemistry* **1998,** *37* (3), 938-44.

39. Rader, D. J.; Cohen, J.; Hobbs, H. H., Monogenic hypercholesterolemia: new insights in pathogenesis and treatment. *J. Clin. Invest.* **2003,** *111* (12), 1795-1803.

40. Jeon, H.; Blacklow, S. C., Structure and physiologic function of the low-density lipoprotein receptor. *Annu. Rev. Biochem.* **2005,** *74*, 535-62.

41. Rudenko, G.; Henry, L.; Henderson, K.; Ichtchenko, K.; Brown, M. S.; Goldstein, J. L.; Deisenhofer, J., Structure of the LDL receptor extracellular domain at endosomal pH. *Science* **2002,** *298* (5602), 2353-2358.

42. Segrest, J. P.; Jones, M. K.; De Loof, H.; Dashti, N., Structure of apolipoprotein B-100 in low density lipoproteins. *J. Lipid Res.* **2001,** *42* (9), 1346-1367.

43. Knott, T. J.; Pease, R. J.; Powell, L. M.; Wallis, S. C.; Rall, S. C., Jr.; Innerarity, T. L.; Blackhart, B.; Taylor, W. H.; Marcel, Y.; Milne, R.; et al., Complete protein sequence and identification of structural domains of human apolipoprotein B. *Nature* **1986,** *323* (6090), 734-8.

44. Cladaras, C.; Hadzopoulou-Cladaras, M.; Nolte, R. T.; Atkinson, D.; Zannis, V. I., The complete sequence and structural analysis of human apolipoprotein B-100: relationship between apoB-100 and apoB-48 forms. *EMBO J.* **1986,** *5* (13), 3495-507.

45. Chen, S. H.; Yang, C. Y.; Chen, P. F.; Setzer, D.; Tanimura, M.; Li, W. H.; Gotto, A. M., Jr.; Chan, L., The complete cDNA and amino acid sequence of human apolipoprotein B-100. *J. Biol. Chem.* **1986,** *261* (28), 12918-21.

46. Kane, J. P., Apolipoprotein B: structural and metabolic heterogeneity. *Annu. Rev. Physiol.* **1983,** *45*, 637-50.

47. Svergun, D. I., Restoring low resolution structure of biological macromolecules from solution scattering using simulated annealing. *Biophys. J.* **1999,** *76* (6), 2879-86.

48. Volkov, V. V.; Svergun, D. I., Uniqueness of ab initio shape determination in small-angle scattering. *J. Appl. Crystallogr.* **2003,** *36*, 860-864.

49. Richardson, P. E.; Manchekar, M.; Dashti, N.; Jones, M. K.; Beigneux, A.; Young, S. G.; Harvey, S. C.; Segrest, J. P., Assembly of lipoprotein particles containing apolipoprotein-B: Structural model for the nascent lipoprotein particle. *Biophys. J.* **2005,** *88* (4), 2789-2800.

50. Segrest, J. P.; Jones, M. K.; Dashti, N., N-terminal domain of apolipoprotein B has structural homology to lipovitellin and microsomal triglyceride transfer protein: a "lipid pocket" model for self-assembly of apoB-containing lipoprotein particles. *J. Lipid Res.* **1999,** *40* (8), 1401-1416.

51. Pan, L.; Segrest, J. P., Computational studies of plasma lipoprotein lipids. *Biochim. Biophys. Acta* **2016,** *1858* (10), 2401-20.

52. Wang, L.; Walsh, M. T.; Small, D. M., Apolipoprotein B is conformationally flexible but anchored at a triolein/water interface: a possible model for lipoprotein surfaces. *Proc. Natl. Acad. Sci. U. S. A.* **2006,** *103* (18), 6871-6.

53. Chatterton, J. E.; Phillips, M. L.; Curtiss, L. K.; Milne, R.; Fruchart, J. C.; Schumaker, V. N., Immunoelectron microscopy of low density lipoproteins yields a ribbon and bow model for the conformation of apolipoprotein B on the lipoprotein surface. *J. Lipid Res.* **1995,** *36* (9), 2027-37.

54. Yang, C. Y.; Chen, S. H.; Gianturco, S. H.; Bradley, W. A.; Sparrow, J. T.; Tanimura, M.; Li, W. H.; Sparrow, D. A.; DeLoof, H.; Rosseneu, M.; et al., Sequence, structure, receptor-binding domains and internal repeats of human apolipoprotein B-100. *Nature* **1986,** *323* (6090), 738-42.

55. Boren, J.; Lee, I.; Zhu, W. M.; Arnold, K.; Taylor, S.; Innerarity, T. L., Identification of the low density lipoprotein receptor-binding site in apolipoprotein B100 and the modulation of its binding activity by the carboxyl terminus in familial defective apo-B100. *J. Clin. Invest.* **1998,** *101* (5), 1084-1093.

56. Boren, J.; Olin, K.; Lee, I.; Chait, A.; Wight, T. N.; Innerarity, T. L., Identification of the principal proteoglycan-binding site in LDL - A single-point mutation in apo-B100 severely affects proteoglycan interaction without affecting LDL receptor binding. *J. Clin. Invest.* **1998,** *101* (12), 2658-2664.

57. Reiner, Z., Hypertriglyceridaemia and risk of coronary artery disease. *Nat. Rev. Cardiol.* **2017,** *advance online publication*.

58. Jayaraman, S.; Gantz, D. L.; Gursky, O., Effects of oxidation on the structure and stability of human low-density lipoprotein. *Biochemistry* **2007,** *46* (19), 5790-5797.

59. Pinchuk, I.; Lichtenberg, D., Analysis of the kinetics of lipid peroxidation in terms of characteristic time-points. *Chem. Phys. Lipids* **2014,** *178*, 63-76.

60. Pinchuk, I.; Lichtenberg, D., The effect of compartmentalization on the kinetics of transition metal ions-induced lipoprotein peroxidation. *Chem. Phys. Lipids* **2016,** *195*, 39-46.

61. Esterbauer, H.; Dieber-Rotheneder, M.; Waeg, G.; Striegl, G.; Jurgens, G., Biochemical, structural, and functional properties of oxidized low-density lipoprotein. *Chem. Res. Toxicol.* **1990,** *3* (2), 77-92.

62. Krisko, A.; Stjepanovic, G.; Pifat, G.; Ruysschaert, J. M.; Goormaghtigh, E., Detection of apolipoprotein B100 early conformational changes during oxidation. *Biochim. Biophys. Acta* **2007,** *1768* (11), 2923-30.

63. Oliveira, C. L.; Santos, P. R.; Monteiro, A. M.; Figueiredo Neto, A. M., Effect of oxidation on the structure of human low- and high-density lipoproteins. *Biophys. J.* **2014,** *106* (12), 2595-605.

64. Schuster, B.; Prassl, R.; Nigon, F.; Chapman, M. J.; Laggner, P., Core lipid structure is a major determinant of the oxidative resistance of low density lipoprotein. *Proc. Natl. Acad. Sci. U. S. A.* **1995,** *92* (7), 2509-13.

65. Deckelbaum, R. J.; Granot, E.; Oschry, Y.; Rose, L.; Eisenberg, S., Plasma triglyceride determines structure-composition in low and high density lipoproteins. *Arteriosclerosis* **1984,** *4* (3), 225-31.

66. McKeone, B. J.; Patsch, J. R.; Pownall, H. J., Plasma triglycerides determine low density lipoprotein composition, physical properties, and cell-specific binding in cultured cells. *J. Clin. Invest.* **1993,** *91* (5), 1926-33.

67. Galeano, N. F.; Milne, R.; Marcel, Y. L.; Walsh, M. T.; Levy, E.; Ngu'yen, T. D.; Gleeson, A.; Arad, Y.; Witte, L.; Al-Haideri, M.; Rumsey, S. C.; Deckelbaum, R. J.; et al., Apoprotein B structure and receptor recognition of triglyceride-rich low density lipoprotein (LDL) is modified in small LDL but not in triglyceride-rich LDL of normal size. *J. Biol. Chem.* **1994,** *269* (1), 511-9.

68. Sherman, M. B.; Orlova, E. V.; Decker, G. L.; Chiu, W.; Pownall, H. J., Structure of triglyceride-rich human low-density lipoproteins according to cryoelectron microscopy. *Biochemistry* **2003,** *42* (50), 14988-93.

69. Coronado-Gray, A.; van Antwerpen, R., Lipid composition influences the shape of human low density lipoprotein in vitreous ice. *Lipids* **2005,** *40* (5), 495-500.

70. Halliday, D.; Resnick, R.; Walker, J., *Halliday Physik*. Wiley-VCH: Berlin, 2009; Vol. 2, p 1483.

71. Eremets, M. I., *High Pressure Experimental Methods*. Oxford University Press Inc.: United States, New York, 1996; p 390.

72. *High-pressure Techniques in Chemistry and Physics*. Oxford University Press Inc.: United States, New York, 1997; p 388.

73. Meersman, F.; McMillan, P. F., High hydrostatic pressure: a probing tool and a necessary parameter in biophysical chemistry. *Chem. Commun.* **2014,** *50* (7), 766-775.

74. Brooks, N. J., Pressure effects on lipids and bio-membrane assemblies. *IUCrJ* **2014,** *1* (Pt 6), 470-7.

75. Brooks, N. J.; Ces, O.; Templer, R. H.; Seddon, J. M., Pressure effects on lipid membrane structure and dynamics. *Chem. Phys. Lipids* **2011,** *164* (2), 89-98.

76. Barriga, H. M. G.; Law, R. V.; Seddon, J. M.; Ces, O.; Brooks, N. J., The effect of hydrostatic pressure on model membrane domain composition and lateral compressibility. *PCCP* **2016,** *18* (1), 149-155.

77. Yaghmur, A.; Kriechbaum, M.; Amenitsch, H.; Steinhart, M.; Laggner, P.; Rappolt, M., Effects of pressure and temperature on the self-assembled fully hydrated nanostructures of monoolein-oil systems. *Langmuir* **2010,** *26* (2), 1177-85.

78. Potekhin, S. A.; Senin, A. A.; Abdurakhmanov, N. N.; Khusainova, R. S., High pressure effect on the main transition from the ripple gel P-beta ' phase to the liquid crystal (L-alpha) phase in dipalmitoylphosphatidylcholine. Microcalorimetric study. *Biochimica Et Biophysica Acta-Biomembranes* **2008,** *1778* (11), 2588-2593.

79. Schroer, M. A.; Paulus, M.; Jeworrek, C.; Krywka, C.; Schmacke, S.; Zhai, Y.; Wieland, D. C. F.; Sahle, C. J.; Chimenti, M.; Royer, C. A.; Garcia-Moreno, B.; Tolan, M.; Winter, R., High-Pressure SAXS Study of Folded and Unfolded Ensembles of Proteins. *Biophys. J.* **2010,** *99* (10), 3430-3437.

80. Winter, R., Synchrotron X-ray and neutron small-angle scattering of lyotropic lipid mesophases, model biomembranes and proteins in solution at high pressure. *Biochimica Et Biophysica Acta-Protein Structure and Molecular Enzymology* **2002,** *1595* (1-2), 160-184.

81. Ortore, M. G.; Spinozzi, F.; Mariani, P.; Paciaroni, A.; Barbosa, L. R.; Amenitsch, H.; Steinhart, M.; Ollivier, J.; Russo, D., Combining structure and dynamics: non-denaturing high-pressure effect on lysozyme in solution. *J R Soc Interface* **2009,** *6 Suppl 5*, S619-34.

82. Lutz, R. A.; Falkowski, P. G., A Dive to Challenger Deep. *Science* **2012,** *336* (6079), 301-302.

83. Yayanos, A. A.; Dietz, A. S.; Van Boxtel, R., Obligately barophilic bacterium from the Mariana trench. *Proc. Natl. Acad. Sci. U. S. A.* **1981,** *78* (8), 5212-5.

84. Kato, C.; Li, L.; Nogi, Y.; Nakamura, Y.; Tamaoka, J.; Horikoshi, K., Extremely barophilic bacteria isolated from the Mariana Trench, Challenger Deep, at a depth of 11,000 meters. *Appl. Environ. Microbiol.* **1998,** *64* (4), 1510-1513.

85. Vanlint, D.; Rutten, N.; Michiels, C. W.; Aertsen, A., Emergence and Stability of High-Pressure Resistance in Different Food-Borne Pathogens. *Appl. Environ. Microbiol.* **2012,** *78* (9), 3234-3241.

86. Aertsen, A.; Meersman, F.; Hendrickx, M. E. G.; Vogel, R. F.; Michiels, C. W., Biotechnology under high pressure: applications and implications. *Trends Biotechnol.* **2009,** *27* (7), 434-441.

87. Meersman, F.; Daniel, I.; Bartlett, D. H.; Winter, R.; Hazael, R.; McMillan, P. F., High-Pressure Biochemistry and Biophysics. In *Carbon in Earth*, Hazen, R. M.; Jones, A. P.; Baross, J. A., Eds. Mineralogical Soc Amer: Chantilly, 2013; Vol. 75, pp 607-648.

88. Ritz, M.; Freulet, M.; Orange, N.; Federighi, M., Effects of high hydrostatic pressure on membrane proteins of Salmonella typhimurium. *Int. J. Food Microbiol.* **2000,** *55* (1-3), 115-119.

89. Ganzle, M. G.; Vogel, R. F., On-line fluorescence determination of pressure mediated outer membrane damage in Escherichia coli. *Syst. Appl. Microbiol.* **2001,** *24* (4), 477-485.

90. Pavlovic, M.; Hormann, S.; Vogel, R. F.; Ehrmann, M. A., Transcriptional response reveals translation machinery as target for high pressure in Lactobacillus sanfranciscensis. *Arch. Microbiol.* **2005,** *184* (1), 11-17.

91. Hormann, S.; Scheyhing, C.; Behr, J.; Pavlovic, M.; Ehrmann, M.; Vogel, R. F., Comparative proteome approach to characterize the high-pressure stress response of Lactobacillus sanfranciscensis DSM 20451. *Proteomics* **2006,** *6* (6), 1878-1885.

92. Yordanov, D. G.; Angelova, G. V., High pressure processing for foods preserving. *Biotechnology & Biotechnological Equipment* **2010,** *24* (3), 1940-1945.

93. Huang, H. W.; Wu, S. J.; Lu, J. K.; Shyu, Y. T.; Wang, C. Y., Current status and future trends of high-pressure processing in food industry. *Food Control* **2017,** *72*, 1-8.

94. Roe, R. J., *Methods of X-Ray and Neutron Scattering in Polymer Science*. Oxford University Press: New York, Oxford, 2000; p 331.

95. Sivia, D. S., *Elementary Scattering Theory - For X-ray and neutron users*. Oxford University Press Inc., New York: United States, 2011; p 201.

4. Results Part I

The first results chapter presents the experimental findings of the comparison between a normolipidemic and a triglyceride-rich LDL from a dynamical and structural perspective. Through the application of different neutron scattering techniques it was possible to show the effects of pressure on the behavior of these two different types of LDL.

High hydrostatic pressure specifically affects molecular dynamics and shape of low-density lipoprotein particles

M. Golub[1,2,§], B. Lehofer[3,§], N. Martinez[1,2,†], J. Ollivier[2], J. Kohlbrecher[4], R. Prassl[3], J. Peters[2,5,*]

[1] Univ. Grenoble Alpes, IBS, F-38000 Grenoble, France
[2] Institut Laue Langevin, F-38000 Grenoble, France
[3] Institute of Biophysics, Medical University of Graz, A-8010 Graz, Austria
[4] Paul-Scherrer-Institut, CH-5232 Villigen, Switzerland
[5] Univ. Grenoble Alpes, LiPhy, F-38044 Grenoble, France

**Corresponding author: Judith Peters, Université Grenoble Alpes, LiPhy, CS 10090, 38044 Grenoble, telephone: +33 4 76 20 75 60, fax : +33 4 76 48 39 06, email:peters@ill.fr*

Abstract

Lipid composition of human low-density lipoprotein (LDL) and its physicochemical characteristics are relevant for proper functioning of lipid transport in the blood circulation. To explore dynamical and structural features of LDL particles with either a normal or a triglyceride-rich lipid composition we combined coherent and incoherent neutron scattering methods. The investigations were carried out under high hydrostatic pressure (HHP), which is a versatile tool to study the physicochemical behavior of biomolecules in solution at a molecular level. Within both neutron techniques we applied HHP to probe the shape and degree of freedom of the possible motions (within the time windows of 15 and 100 ps) and consequently the flexibility of LDL particles. We found that HHP does not change the types of motion in LDL, but influences the portion of motions participating. Contrary to our assumption that lipoprotein particles, like membranes, are highly sensitive to pressure we determined that LDL copes surprisingly well with high pressure conditions, although the lipid composition, particularly the triglyceride content of the particles, impacts the molecular dynamics and shape arrangement of LDL under pressure.

† Present address: SPrAM UMR 5819 CEA-CNRS-UJF Grenoble 1, France
§ These authors contributed equally to this work.

Published in: *Scientific Reports* **2017**, *7*, 46034.

DOI: 10.1038/srep46034

Introduction

Human plasma lipoproteins are macromolecular assemblies of lipids and proteins, which function as lipid transporter in blood circulation. Lipoproteins have shown a distinct dynamical behavior as function of temperature[1], which is very similar to membranes, and we assume that lipoprotein particles, like membranes, are highly sensitive to pressure as well. Thus, the conception of a dynamic landscape for lipoprotein species under high hydrostatic pressure (HHP), similar to natural membranes, is very appealing, but has never been evidenced before. Here we report for the first time on the application of HHP on human plasma low-density lipoprotein (LDL), whose main function is the transportation of cholesterol from the liver to peripheral tissue. We applied HHP to compare the dynamical behavior of LDL particles with a healthy normolipidemic composition (N-LDL) to a triglyceride-rich form of LDL (TG-LDL), which mimics pathologically modified LDL. The chemical compositions of LDL particles are well described in the literature[2-5]. Each particle (Figure 1) consists of a complex combination of lipids and a single copy of a protein, termed apolipoprotein B100 (apoB-100). LDL has a hydrophobic core and an amphiphilic shell. The core basically harbors cholesteryl esters, triglycerides and parts of the unesterified cholesterol. The shell consists of a phospholipid monolayer, unesterified cholesterol and the amphipathic apoB-100 molecule wrapped around the surface[6]. It is well known that lipoproteins play a key role in atherosclerosis, which is a dynamic and progressive inflammatory disease that promotes lipid deposition in the arteries[7,8]. Moreover, the lipid composition of the LDL core becomes modified in case of certain diseases such as *hyperlipidemia*, where LDL is enriched with cholesterol or triglycerides[8,9]. Such variations in the lipid core composition may influence the overall particle size and the molecular arrangement of surface components[10], however, little is known how the particles compensate for changes in the surface area and surface pressure depending on the chemical composition of the core lipids[11].

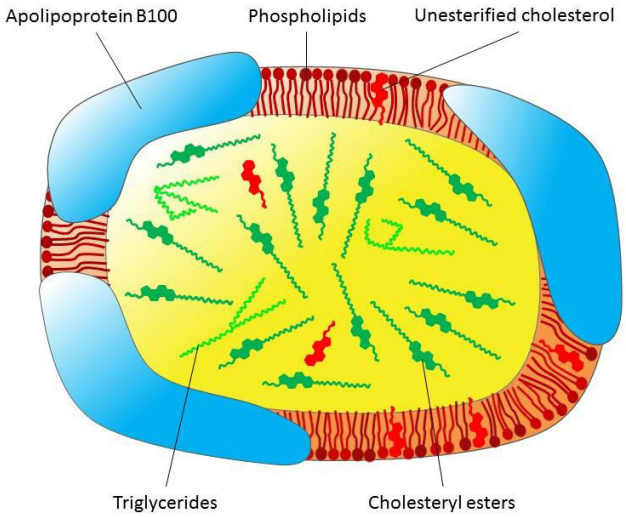

Figure 1: Scheme of an LDL particle including the various components.

Pressure is a thermodynamic variable which, besides temperature, enables to investigate physical parameters of macromolecules, and to explore dynamical and structural properties of supramolecular assemblies. The choice to use HHP instead of temperature is based on the following considerations: about 30 years ago, researchers found that not only the structure of a protein is mandatory for its functioning, but also its dynamics[12,13]. However, temperature variations influence the thermal energy and the volume of a system through the thermal expansion factor simultaneously, which makes it difficult to separate these two effects. On the contrary, pressure affects only the volume of the investigated system and therefore induces controlled changes of intermolecular distances[14]. Pressure gives access to the partial molar volume, a parameter intimately related to structure and dynamics of biomolecules. As biological systems might be in different conformational sub-states according to their free energy[15], this latter quantity determines the degree of freedom of the possible motions and consequently the flexibility of the sample.

To probe the molecular dynamics of LDL in the ps-ns time range we used elastic incoherent neutron scattering (EINS) and quasi-elastic neutron scattering (QENS). As hydrogens are typically homogeneously distributed in biological systems, their motions provide averaged information about molecular movements at atomic scale, which can be determined for different pressure values. The hydrogen contribution is dominating the spectra, since the incoherent neutron cross section (NCS) of hydrogen is much larger than the NCS of any other atom present in biological objects[16]. In addition to the dynamical investigations, we used small-angle neutron scattering (SANS), which is one of the most suitable techniques to answer structural questions of biomolecules in solution, since it furnishes information on

shape, domain organization and molecular interactions[17-20]. The results of these techniques have been combined to gain a general picture of LDL dynamics and structure under high hydrostatic pressure.

All experiments were carried out at body temperature (310 K), which is a temperature above the phase transition temperature of the lipids, and covered the pressure range from 20 to 3000 bar to determine molecular motions and structural remodelling upon HHP. The maximum pressure was far beyond pressure values found on Earth, but the idea was to highlight effects which are hardly distinguishable at lower pressure. QENS data allowed to assign motions to different dynamical populations, associated to specific molecules or molecular groups within LDL. To perform the studies, we took advantage of the HHP equipment developed specifically for biological samples in solution at two different neutron scattering facilities. Our data suggest that an interplay between structural flexibility of the particles and intrinsic molecular dynamics of lipids and proteins partially compensates for variations in the chemical composition of the particles, even at extreme external stress conditions.

Results

TG-LDL dynamics is sensitive to HHP application in contrast to N-LDL dynamics

QENS data analysis was performed through a "model free" approach (see Materials and Methods) by taking into account three distinct relaxation processes. It allowed to distinguish motions of different dynamical sub-groups, called populations in the following, which are associated with specific molecules such as lipids or certain molecular groups within LDL. A scenario which motion corresponds to which kind of population is suggested. Representative data of the global fit at a constant Q-value are shown in Figure 2a (data from the neutron time-of-flight spectrometer IN5) and in the Electronic Supplementary Information (ESI) in Figure S1, which contains all TG-LDL data and fits from the neutron time-of-flight spectrometers IN5 and IN6 including residuals. For N-LDL the curves are virtually the same. To extract more precise information on the type of motion the full width half maxima (FWHM) Γ_n of the Lorentzian curves as function of Q^2 were determined[21] (Figure 2b and ESI Table S1).

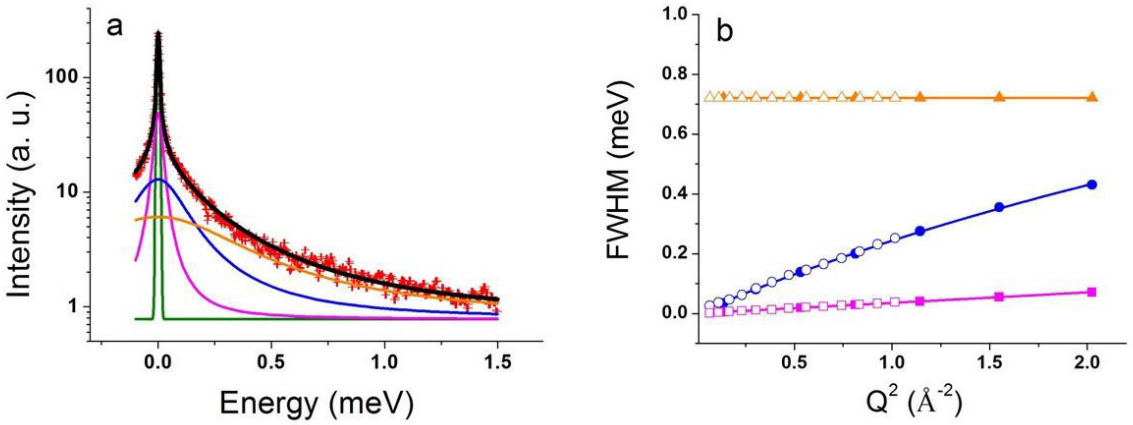

Figure 2: QENS data and fits. Logarithmic plot of a typical QENS spectrum (IN5) of N-LDL at 310 K and 20 bar measured at Q=1.00 Å^{-1} (red points) and quasi-elastic contributions determined by the fit: the green line corresponds to the elastic contribution, the magenta, blue and orange lines to Lorentzian functions. The black line shows the final fit (a); FWHM values of the three Lorentzian distributions as function of Q^2 obtained from IN5 (smaller Q-range, open symbols) and IN6 (full symbols) and their fits according to a translational diffusive model (magenta points), a jump-diffusion model (blue points) and a rotational diffusive model (orange points). The estimated error is ± 2 on the last given digit (b).

First, we analysed the data for the low pressure point (20 bar). The elastic contribution and the Lorentzian functions are shown in Figure 2a. On IN5 we distinguished a sharp peak (magenta line), which was too narrow to be resolved on IN6 due to the lower energy resolution. The Q-dependence of the corresponding FWHM (see Figure 2b) showed a translational motion for this population of particles with the diffusion coefficient of D_T = 0.11*10^{-5} cm^2/s. The second quasi-elastic contribution (blue line) was well resolved on both spectrometers. It corresponded to fast motions in the range of 2 to 15 ps. In particular, the analysis of the IN6 data at high Q values allowed us to detect a change of the FWHM's behavior from a linear to an asymptotic slope at Q^2 values above 1.3 Å^{-2} (see Figure 2b). Thus, the Q-dependence of the FWHM could successfully be ascribed to a jump diffusion model with a diffusion coefficient of D_{JD} = 2.1*10^{-5} cm^2/s; the residence time τ was found to be equal to 1.7 ps. The last and broadest quasi-elastic peak (orange line) could be resolved in the spectra obtained at the neutron spectrometer IN6. According to our analysis, its FWHM remained constant at all Q values, what corresponds to a rotational motion, and was determined to be $\Gamma_{rotation}$ = 0.72 meV (Figure 2b). The parameters extracted from the FWHM were identical for N-LDL and TG-LDL at 20 bar and are summarized in Table 1. We concluded that the structural differences between the two forms of LDL did not lead to any significant changes in their dynamics (on the ps time scale) at low pressure.

The situation changes, however, in case of HHP applied to the same samples. Analysis of the QENS data recorded at HHP (3000 bar) revealed no change in the dynamics of N-LDL (see Figure 3a), whereas a significant difference for TG-LDL was found: the elastic part became much more pronounced, that is to say that some of its components were slowed down by pressure in this sample due to volume reduction, while the shape of the quasi-elastic broadening was not affected (see Figure 3b). This indicates that HHP affects the elastic intensity extracted from QENS data and the Mean Square Displacements (MSD), which can be extracted from EINS measurements (Figure 4a and ESI, Figure S2 and Table S2), but not the quasi-elastic broadening given in Table 1, which remains identical at high pressure.

Table 1: Parameters extracted from the global fits of the QENS curves. The parameters were identical for N-LDL and TG-LDL samples at low (20 bar) and high hydrostatic pressure (3000 bar).

D_T	0.11 ± 0.02 $(10^{-5}$ cm^2/s)
D_{JD}	2.1 ± 0.1 $(10^{-5}$ cm^2/s)
τ	1.7 ± 0.1 (ps)
$\Gamma_{rotation}$	0.72 ± 0.05 (meV)

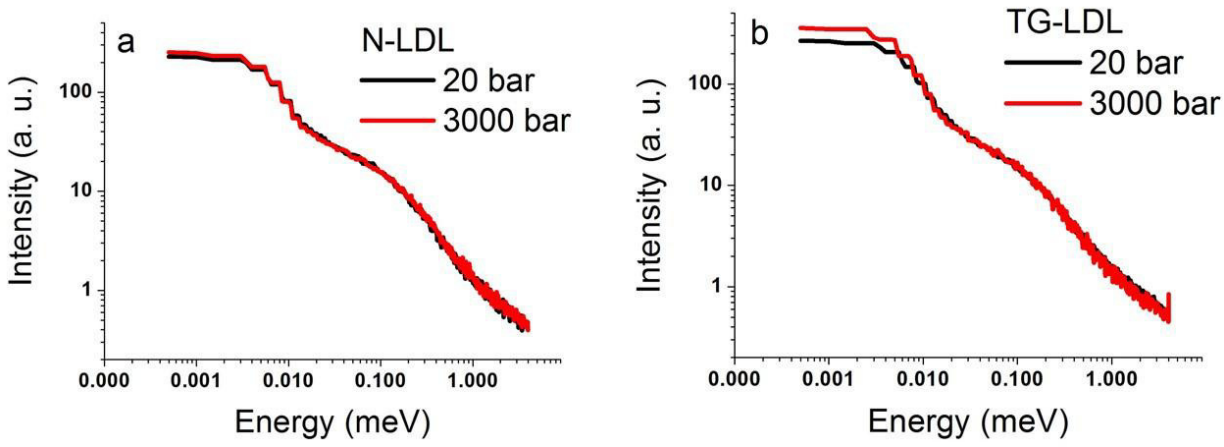

Figure 3: Double-logarithmic plot of QENS spectra taken on IN5. Pressure effect on N-LDL at Q=1.00 Å^{-1} measured at 20 bar (black curve) and at 3000 bar (red curve) (a), same for TG-LDL (b).

The EINS results shown in Figure 4a represent MSD values extracted from data taken on the thermal backscattering spectrometer IN13. This spectrometer has the same energy resolution as chosen on the time-of-flight spectrometer IN5, therefore the results are fully comparable. We found that the MSD of N-LDL are equal within error bars, whereas those of TG-LDL differ significantly between the two pressure points, being much lower at 3000 bar. The elastic intensities extracted from QENS data (Figure 4b and ESI, Table S3) support the

same conclusion, as no difference was found at 20 bar (Figure S2), but the values for TG-LDL at 3000 bar lie significantly above those of N-LDL. The value of the elastic intensities at highest Q-value is indicative of the proportion of immobile particles, which was determined to be about 13% for N-LDL and 23% for TG-LDL.

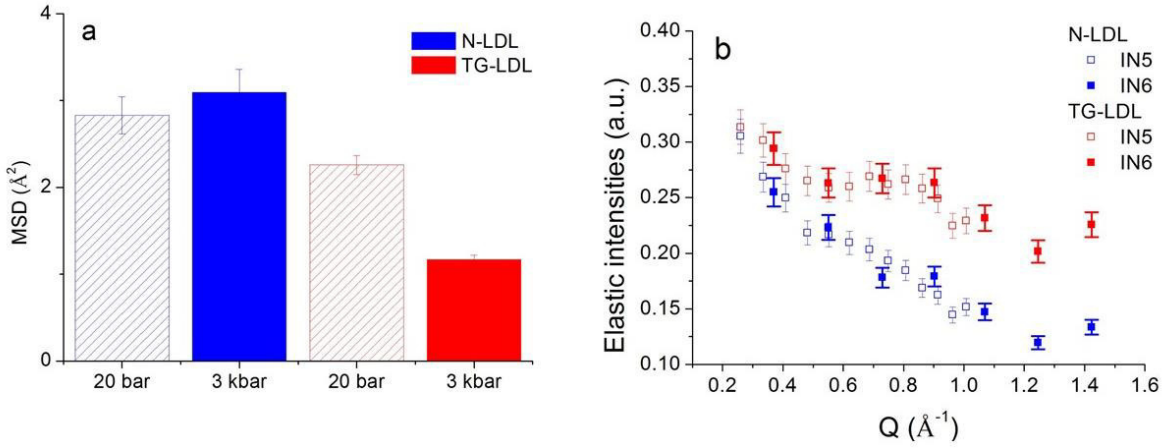

Figure 4: Comparison of the MSD values extracted from elastic data taken on IN13 for both samples at 20 and 3000 bar and 310 K (a). Elastic intensities extracted from QENS data as function of Q: N-LDL (blue) and TG-LDL (red) at 3000 bar. All data were measured at 310 K on IN5 and IN6 (b).

The shape of TG-LDL is modified by high pressure application

To study whether HHP has an effect on the overall structural features of LDL particles we measured SANS. We started the measurements at 600 bar, as no differences were seen between 1 and 600 bar, and we will call this point hereafter “low pressure”. The Guinier region in the SANS curves indicates that both N-LDL and TG-LDL were rather monomeric systems at the two pressure values shown here (600 and 3000 bar). The radius of gyration was approximately 78 Å for both samples, which is in good agreement with previous studies[22,23]. The SANS curves were quite similar for all types of LDL nanoparticles under different pressure conditions, in the sense that all of them had a characteristic peak at the Q-position of 0.060 $Å^{-1}$ (Figure 5). Such a peak position in the reciprocal space is indicative for a characteristic radius of the system under study, which is of about 105 Å here in agreement with the radius of LDL particles of about 100 Å. The access to the internal structure of an LDL nanoparticle was limited due to missing contrast between shell and core as no deuterated lipids were incorporated.

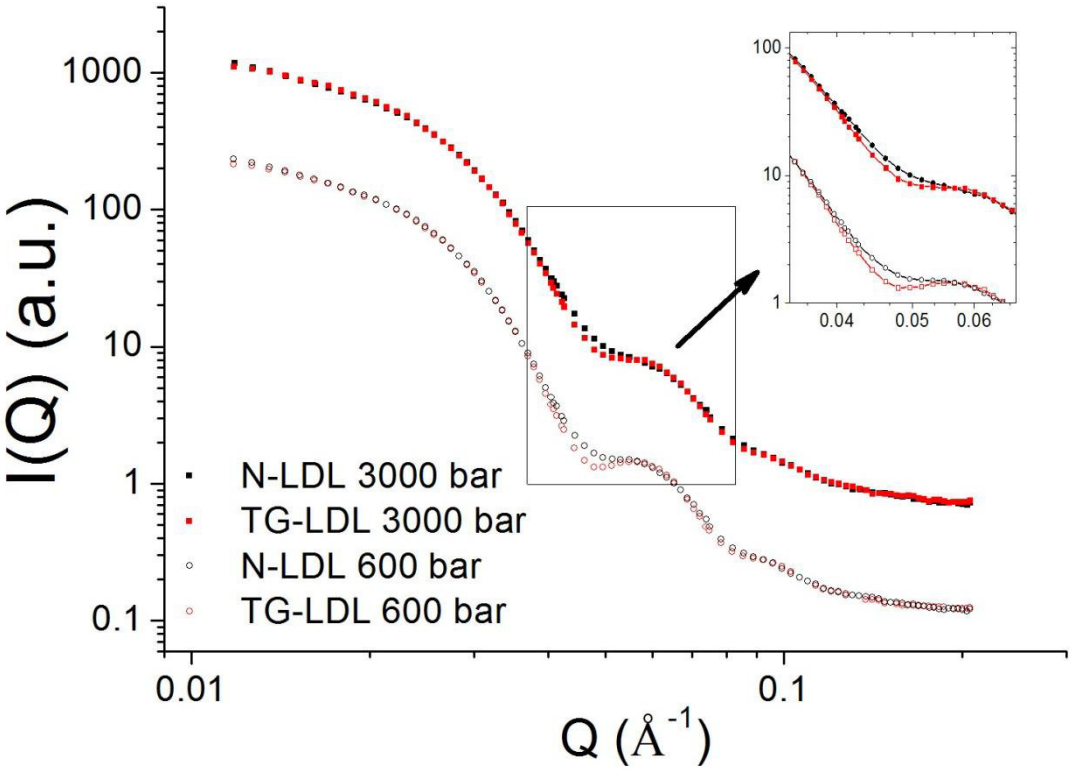

Figure 5: SANS curves of N-LDL and TG-LDL measured at 600 and 3000 bar and at 313 K.

To fit the overall structure of LDL particles we used an ellipsoidal model to extract the radius of gyration and the three radii of the ellipsoid (R_1-R_3) as presented in Figure 6a. The fit indicates that the shape of N-LDL at low pressure is slightly more elongated compared to the shape of TG-LDL (see Figure 6b and ESI Table S4). Still, the difference in the overall structure was rather small at low pressure. This is in good agreement with the QENS data, where the difference in the dynamics was also negligible at low pressure.

With increasing pressure, the shape of the SANS curve changed. For instance, the peak around Q = 0.060 Å^{-1} became less pronounced at high pressure (Figure 5). According to our fits of the SANS curves (Figure 6b), the smallest radius R_3 of the ellipsoid decreased from 76.8 Å at 600 bar to 71.5 Å at 3000 bar for N-LDL and from 82.2 Å at 600 bar to 77.2 Å at 3000 bar for TG-LDL (separate graphs for the individual radii are shown in ESI Figure S3). Most interestingly, the largest radius R_1 decreased for N-LDL and increased for TG-LDL, so that the shape of the TG-LDL at high pressure resembled much more the shape of N-LDL. The radius R_2 and the radius of gyration were only slightly affected by pressure.

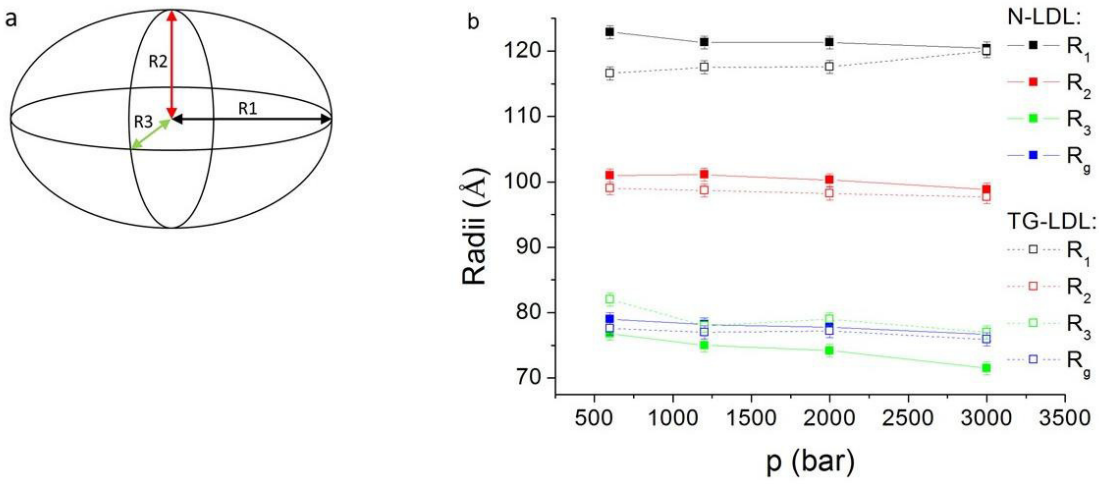

Figure 6: Schematic representation of the fitted ellipsoidal model with the three axes R_1, R_2 and R_3 (a). Fitted radii of a triaxial ellipsoid extracted from the SANS curves. The continuous lines correspond to N-LDL, the dashed lines to TG-LDL (b).

Discussion

Analysis of the QENS data revealed three dynamical contributions reflected by the presence of three Lorentzian functions, each describing a distinct relaxation process to fit the spectra. Each function was related to a certain motion or dynamic behavior of the investigated system. The challenge to interpret QENS results of a sample that has never been studied before consists in identifying the kind of motions and to which population they belong to, and, in the present case, to investigate how they are influenced by pressure application. We compared the obtained dynamical parameters with other results in the literature and suggest corresponding motions according to the composition of the sample to get a better picture of the functioning of the biomolecule.

First, we calculated the hydrogen content of the different components of the samples (see Table 2) to get information about their corresponding scattering contribution and consequently about the ratios of the components which participate to the different motions. Second, we determined the normalised spectral weights of the scattering contributions of the different populations (see Figure 7) for both instruments and pressures.

Table 2: ^{1}H-content (wt%) of the different components of LDL. The average ^{1}H-content of the single components was calculated by using the chemical formulas and molecular masses. The relative composition of fatty acid residues in phospholipids, cholesteryl esters and triglycerides[24] was considered. For the calculation of the ^{1}H-content in the QENS samples the actual chemical composition was taken from Table S5.

Component	QENS	
	N-LDL	TG-LDL
Protein	14.1	12.7
Phospholipids	22.5	20.2
Unesterified cholesterol	9.2	6.7
Cholesteryl esters	49.0	48.1
Triglycerides	5.2	12.2

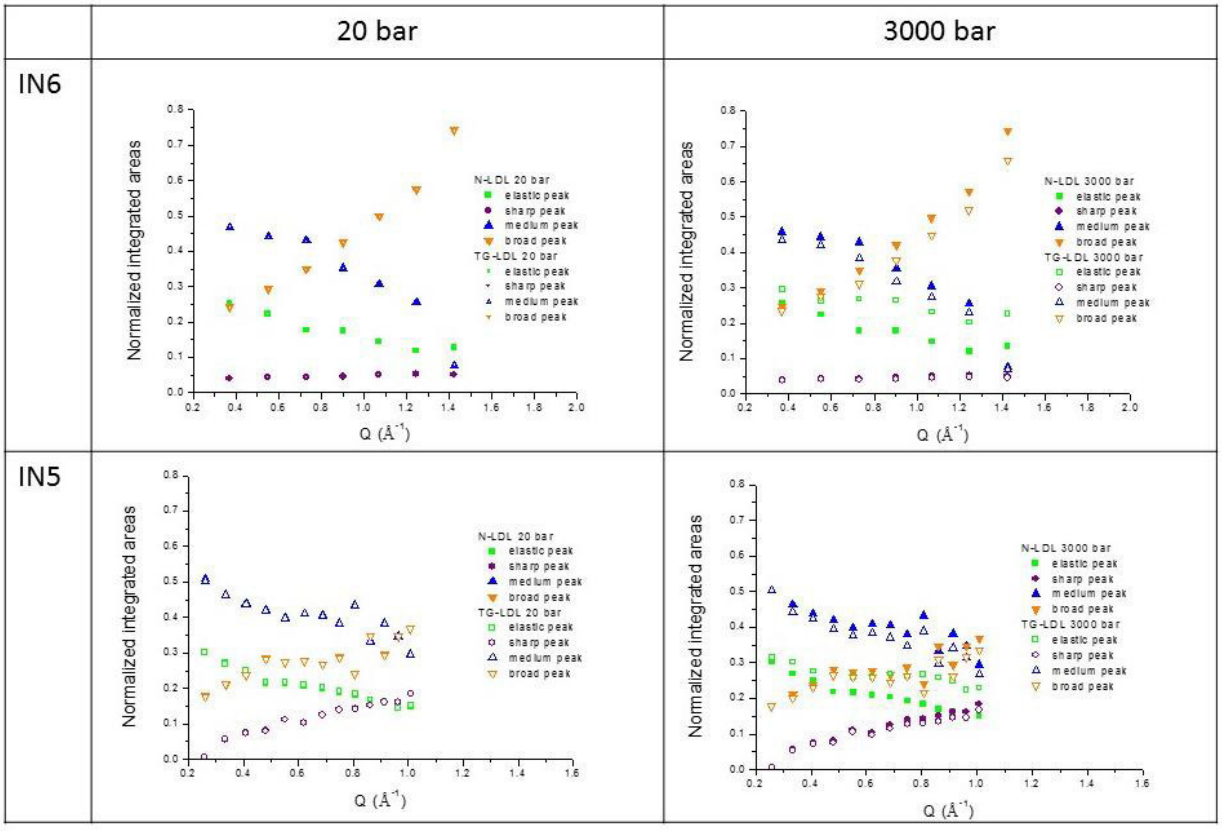

Figure 7: Spectral weights or Q dependence of the integrated areas of the elastic peak and the Lorentzian functions on IN5 and IN6 for both pressure values. For 20 bar the data points are almost completely superposed.

The spectral weights represent the Q-dependence of the integrated areas of the elastic peak and the Lorentzian functions and are indicative for the contribution of the corresponding population at a given Q value (see Figure 7). However, the total spectral weight corresponding to a certain part of the sample has to be Q-independent. Indeed, the

contributions from the medium and broad peak and from the elastic and sharp peak appear pairwise highly correlated as they are almost symmetric with respect to an average line, what indicates that they could belong to the same population, which executes two motions simultaneously.

Without extensive contrast variation using partly and/or fully deuterated components it is not possible to assign more precisely the different motions in such complex systems as are lipoproteins. However, we evaluated that an exchange of a hydrogenated lipid population with a deuterated one would be too small to lead to significant contrast variation of these components and to permit a more precise assignment of the motions. On the other hand, several kinds of lipids were already investigated by neutron scattering methods, for instance DMPC, POPC[25], DOPS and DOPC[26]. They showed up at least two different motions which resulted in characteristics of the same order of magnitude as those found in the present work, that is to say a jump diffusion coefficient of about 2.0×10^{-5} cm^2/s together with a residence time of about 1 ps and another translational diffusion coefficient, associated to a centre-of-mass diffusion of the lipids, which is 10 – 20 times smaller. Without going into details to which part of the lipids such motions can be precisely assigned here, we emphasize that diffusional or confined motions of this order of magnitude exist in lipids at temperatures around 310 K and that we can refine these in the analysis performed. In addition, different kind of lipids behave differently and their motions are highly dependent on the presence of cholesterol[27,28]. It is however not possible to distinguish all movements of such a highly complex system, but we present a serious proposition to describe LDL under HHP which includes both dynamical and structural effects.

The other relaxation process is associated with rotational diffusion according to the form of the FWHM $\Gamma_{rotation}$, which has a width of 0.72 meV very similar to values found in deep sea prokaryotes[29] or in neural tissue[30]. Fast rotational diffusion could originate from different locations in the sample, for instance from protons in CH_2 groups within lipids and the apoB-100 protein. It is thus representative for typical motions in the sample, which can be seen in the time window of the spectrometer. Surprisingly, all these movements are not much influenced by pressure application. However, the proportion of particles participating to these motions changes. In the present case, the dynamical populations are almost constant for both samples in spite of pressure application, but the proportion of the elastic peak is enhanced for TG-LDL, in compliance with the EINS and elastic intensities' results, at the expense of the population undergoing rotational diffusion (by about 7%). Therefore, some of

the slowest detected motions, corresponding to the local movements within the TG-LDL particle, are slowed down by HHP and become finally undetectable by QENS.

Consequently, our results indicate that the dynamic landscape of LDL includes motions of lipids and rotational diffusion of smaller molecular sub-groups as for instance CH_2 groups. Indeed, nearly 80 % of LDL are lipids and cholesterol (see Table 2), but their motions can be influenced by the presence of the protein. As shown recently by Knoll et al.[26], proteins can render lipids more flexible or in contrary reduce the dynamics of parts of them due to more or less confinement compared to the pure system. According to the QENS analysis we could not detect any changes of the quasi-elastic motions neither among the samples nor with the measured pressure points, but the proportion of particles participating to the dynamics has been found to be different.

The observation that the geometry of the motion changes, with a reduction in the typical confinement size in TG-LDL, could be expected according to Le Chatelier's principle, saying that compression by HHP will favor a volume reduction and thus lead to reduced dynamics. This behavior was also reflected in the structural data, as shown by SANS. N-LDL appeared slightly elongated and had a discoid shape at the lowest pressure point, whereas TG-LDL was more spherical at the same conditions. Similar characteristics for normolipidemic and triglyceride-rich LDL particles have already been shown with cryo-electron microscopy before[31,32]. At HHP we found that the N-LDL particles did not change their overall shape and stayed in an ellipsoidal conformation. However, the TG-LDL particles adapted their shape from a more spherical to a more elongated form similar to N-LDL (see Figure 8). In both samples the particle partial molar volume decreased and the surface-to-volume ratio increased with pressure, but the changes were less pronounced for TG-LDL, which on the other hand became deformed. The surface-to-volume ratio change in LDL could be due to differences in the compressibility between shell and core. Other reasons could be a pressure dependent conformational change of the apolipoprotein, which could become more stretched or flat by pressure to cover a larger surface area. Another effect could be a possible lipid phase change induced by pressure or a different equilibrium of unesterified cholesterol between the core and the phospholipid membrane, which could also lead to a different increase in surface-to-volume ratio. We speculate that a combination of several effects might occur. Such variation due to the protein moiety would be in compliance with the dynamical findings which point towards a higher pressure sensitivity of fast local motions within the apoB-100 protein or CH_2 subgroups.

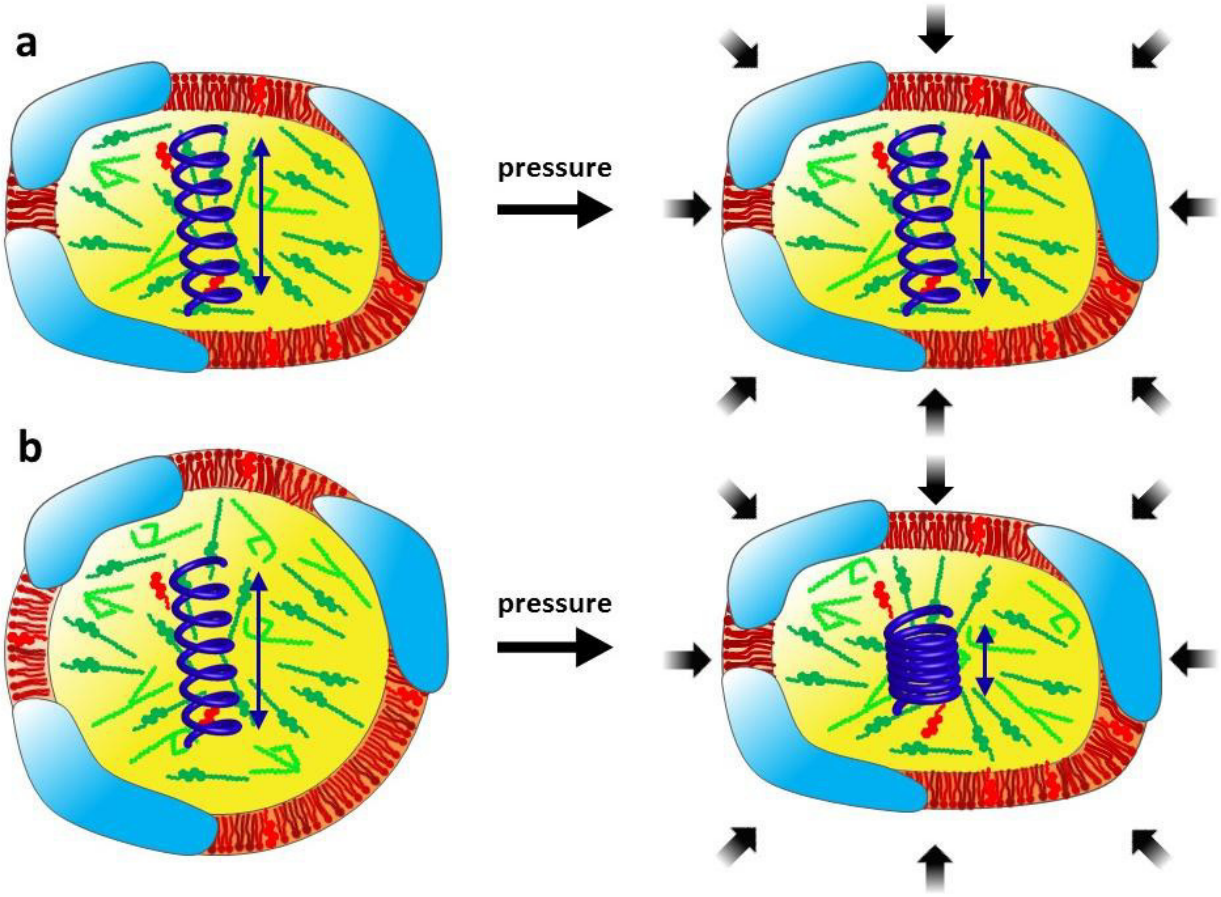

Figure 8: Sketch of the effect of high hydrostatic pressure on LDL particles (caption see Figure 1); N-LDL (a) and TG-LDL (b). The blue spring symbolizes the altered dynamics within the particle.

Taken together, the N-LDL, representing the normolipidemic healthy system seemed to cope much better with the externally increased pressure stress than TG-LDL, which mimicked the hypertriglyceridemic form associated to pathological health conditions. The distinctions in the dynamics between N-LDL and TG-LDL became clearly visible at HHP: TG-LDL showed a lower MSD value indicative for the reduced flexibility of motions and increased stiffness. At low pressure TG-LDL particles were rather spherical but approached the ellipsoidal morphology of N-LDL at high hydrostatic pressure.

It could be shown that especially the apoB-100 protein anchored in an artificial lipid interface is highly flexible under surface pressure and can cope for vast structural changes of the surface layer. Parts of the apoB-100 can be pushed off the surface during compression and readsorb when the surface expands[33]. Moreover, the whole protein structure has a very flexible nature as seen in a low-resolution reconstruction of a SANS study of detergent solubilized apoB-100[19]. The intrinsic mobility of apoB-100 is certainly of major importance when it comes to structural adaptation. The influence of a TG-rich lipid core composition on LDL shape, as shown by cryo-electron microscopy[32], is also reflected in the dynamic behavior

of LDL as shown by our results. We suggest that the structural adaptation of LDL with a TG-rich core is facilitated by the highly flexible apoB-100.

In conclusion, our results indicate that LDL particles withstand HHP quite well, however, a TG-rich core lipid composition seems to have an impact on the molecular dynamics of LDL particles under pressure.

Materials and Methods

Sample preparation for neutron scattering experiments

LDL was isolated from human blood plasma by applying a multiple-step density gradient ultracentrifugation[1]. Blood plasma was obtained from the Department of Blood Group Serology and Transfusion Medicine of the University Hospital Graz (Graz, Austria) after written informed consent, according to a protocol approved by the Institutional Review Board of the Medical University of Graz. The blood plasma was free of pathogens (HBV, HCV, HIV). The isolated LDL was extensively dialyzed against buffer (10 mM NaPi, 0.1 % EDTA, pH 7.4), concentrated with Amicon Ultra-15 centrifugal filter units (cut-off 100 kDa) and characterized for its protein and lipid composition. Sample purity was checked with SDS-PAGE. Chemical compositions and measured concentrations of normolipidemic N-LDL and triglyceride-rich TG-LDL are given in the ESI, Table S5 and Table S6.

Elastic and quasi-elastic neutron scattering experiments and data analysis

LDL samples were measured at a constant temperature of 310 K, at 20 and 3000 bar. The samples were in solution to ensure a homogeneous transmission of hydrostatic pressure and to highlight the single particle dynamics. For the dynamical high pressure experiments, we took advantage of equipment developed and validated within the last years at the neutron scattering facility Institut Laue Langevin (ILL, Grenoble, France) for measurements of samples in solution[34]. We used the time-of-flight spectrometers IN5[35] and IN6[36] as well as the thermal backscattering spectrometer IN13[37] at the ILL which permitted to combine elastic and quasi-elastic scattering investigations and to use two different time windows to identify various types of motions at the atomic scale. The instrumental energy resolutions were determined by a vanadium measurement, which is a completely incoherent scatterer, to be about 0.01 meV for IN5 and IN13 and 0.075 meV for IN6, corresponding to time windows of about 100 ps and 15 ps, respectively. The shorter time scale of IN6 permits to identify fast

motions, whereas the longer time scale of IN5 and IN13 allows to see slower motions arising from the lipids and other local motions. We are summarising the instrumental characteristics of IN5, IN6 and IN13 in the ESI Table S7.

In order to quantify the contribution of the solvent, measurements of LDL in buffer and pure buffer (10 mM NaPi, 0.1 % EDTA, pH 7.4 in D_2O) were carried out separately. All measurements were performed at 20 bar and 3000 bar. Transmission values were measured on IN13. We got 89.0 % for the empty cell transmission, 82.7 % for the buffer and 74.4 and 77.0 % for the N-LDL and TG-LDL samples, respectively. Each sample spectrum was corrected with respect to the incoming flux. Both the sample and the buffer were first corrected for the empty cell contribution by taking into account their respective absorptions, then the buffer was subtracted from the sample in a second step. The spectra were then normalized using the LAMP software available at ILL[38]. Absorption correction was based on the correction formula of Paalman-Pings[39]. To reduce the sample volume and to avoid multiple scattering, we included a cylindrical aluminum insert of 3 cm height and 4 mm diameter into the inner hollow volume of 6 mm diameter of the sample cell. Moreover, we used a cadmium mask limiting the region irradiated by the neutron beam to the height of 3 cm containing the aluminum insert, although the total height of the sample volume was about 5 cm. When increasing the pressure, more LDL particles were pushed into the beam, but we estimated the increase to a few percent, only, as most of the sample volume was outside the beam.

Elastic neutron scattering experiments

Elastic incoherent neutron scattering (EINS) data were collected on the thermal backscattering spectrometer IN13. In a first approximation, the Gaussian approximation[40], which assumes that the distribution of the atoms around their average position follows a Gaussian distribution, the scattered intensity is given by the dynamic structure factor at zero energy exchange

$$S_{el}(Q,\omega = 0 \pm \Delta E) \approx S_0 \exp\left(-\frac{1}{3}\left\langle u^2 \right\rangle Q^2 \right), \qquad (1)$$

where $\langle u^2 \rangle$ are the average atomic mean square displacements (MSD). ω and Q are the energy and momentum exchanged between the neutron and an atomic nucleus of the sample in units of $\hbar$, respectively, and ΔE is the half width half maximum (HWHM) of the instrumental energy resolution. For $Q \rightarrow 0$, the approximation is strictly valid, and it holds up

to $\langle u^2 \rangle Q^2 \approx 1$ [41]. The MSD can be obtained for each pressure value by the slope of the semi-logarithmic plot of the incoherent scattering function through

$$\left\langle u^2 \right\rangle \approx -3 \frac{d \ln S_{el}(q, \omega \pm \Delta E)}{dQ^2}. \quad (2)$$

The MSD values are a measure for the flexibility of the biological system at a given condition of temperature or pressure[42].

Quasi-elastic neutron scattering experiments

Quasi-elastic neutron scattering (QENS), which accounts for small energy exchanges between neutron and target, can be described by the incoherent double-differential cross section[21]:

$$\frac{\delta^2 \sigma}{\delta \Omega \delta \omega} = \frac{|k_1|}{|k_0|} b_{inc}^2 S_{inc}(Q, \omega), \quad (3)$$

where k_0 and k_1 are the wave vectors of the incident and scattered neutron, respectively. b_{inc} is the incoherent scattering length and $S_{inc}(Q,\omega)$ is the incoherent scattering function. In a real experiment, only the experimental scattering function S_{exp} is accessible which contains the instrumental resolution function $R(Q,\omega)$:

$$S_{\exp}(Q, \omega) = R(Q, \omega) \otimes S_{inc}(Q, \omega). \quad (4)$$

To get an idea about $S_{inc}(Q,\omega)$, which is the theoretical model function describing the dynamics of the sample, neutron spectra have therefore to be deconvoluted by the experimentally obtained resolution function. To describe the scattering function, the following generic equation is applied:

$$S_{theo}(Q, \omega) \propto \exp[-\left\langle u^2 \right\rangle Q^2 / 3] * \left\{ A_0(Q) \delta(\omega) + \sum_n A_n(Q) L_n(\Gamma_n, \omega) + S_{in}(Q, \omega) \right\}, \quad (5)$$

that contains the sum of three main contributions: 1) a factor proportional to δ(ω)– corresponding to the elastic component when no energy is exchanged; 2) the quasi-elastic contribution is represented by a sum of Lorentzian-shaped components $L_n(\Gamma_n,\omega)$, where Γ_n is the full-width at half maximum (FWHM); and 3) the inelastic part $S_{in}(Q,\omega)$, corresponding to collective low-frequency vibrational motions. The term $e^{-\left\langle u^2 \right\rangle Q^2/3}$ is the Debye-Waller factor

characterized by the vibrational MSD $\langle u^2 \rangle$. The Q-dependent amplitudes $A_0(Q)$ and $A_n(Q)$ in equation (5) denote the elastic and the quasi-elastic incoherent structure factors (EISF and QISF), respectively. One can show[21] that the EISF $A_0(Q)$ is given by the elastic intensity divided by the sum of elastic and quasi-elastic intensities at $t \rightarrow \infty$ and it is indicative of the geometry of the diffusional process. Generally, if only long-range diffusive motions were present, it vanishes except for Q = 0. For the exclusive rotational diffusion of a particle, the EISF is unity at Q = 0 and falls to a minimum at a Q value which is inversely related to the radius of gyration of the rotating particle and directly related to the proportion of particles seen as immobile. In the present case, we have different motional contributions, which are treated additively.

QENS model free analysis approach

To fit the QENS spectra by such a model scattering function a couple of approximations are applied after verification that they are well fulfilled for the two instruments: 1) the resolution function $R(Q,\omega)$ is assumed to have a Gaussian shape; and 2) inelastic contributions can be neglected within the energy transfer ranges considered here. Therefore, each spectrum was fitted by a sum of an elastic Gaussian function contribution and several Voigt functions, which were representing the convolution of a Lorentzian function with the Gaussian resolution peak.

Theoretically, the sum over the Lorentzian contributions in eq. (5) goes to infinity, but in practice the sum has to be limited to the minimum number of contributions which describe the data reasonably well and permit a physical interpretation of the results. Therefore, it was necessary to make a preliminary analysis in order to figure out the number of independent quasi-elastic contributions contained in the QENS spectra through an inverse Fourier Transformation of the scattering function $S(Q,\omega)$ to the intermediate scattering function I(Q,t). Such approach permits to plot the spectra obtained on IN5 and IN6 on the same graphics and to verify how many relaxation processes are necessary to describe the whole curve[43] (see ESI Figure S4, at Q = 0.73 $Å^{-1}$). The spectra originating from the two instruments show a discrepancy in the two overlapping regions. We thus determined three distinct relaxation processes to describe the QENS spectra in a satisfactory way.

QENS data analysis as presented here, as to say without any further assumption about the composition of the sample and the detected motions, is commonly called a “model free” approach. As mentioned above we determined three distinct relaxation processes to be

taken into account, which were more or less well resolved on both instruments. Therefore, we used the data of IN5 and IN6 simultaneously for a global fit with Origin (http://www.originlab.com/) to gain in precision. IN5 and IN6 do not only differ in energy resolution, but also in the so-called dynamical ranges, that is in the accessible Q-ranges. The only Q-values existing on both instruments are (0.33, 0.55, 0.74, 0.91 and 1.0) $Å^{-1}$ (cf. Figure 2b and Figure 4b), so we started by fitting them first for the two data sets simultaneously. In a second step, we fitted the intermediate Q-values of IN5 and the higher Q-values of IN6 to get consistent results. This is what we call a global fit.

The FWHM Γ_n of the Lorentzian curves as function of Q^2 provided more precise information on the type of motion[21]. If some particles were performing Brownian motion without any restriction in space, the corresponding FWHM would present a linear increase with Q^2 crossing the origin at $Q \rightarrow 0$ and obeying the relation $\Gamma_T = D_T Q^2$. If there were interactions between particles, the FWHM would start with a very similar slope at low Q^2, but would flatten to a constant value at high Q^2 [44]. Such behavior is characteristic for jump-diffusion, where the particles perform a translational diffusive motion for a short time with a diffusion coefficient D_{JD} and then vibrate at their position for a certain time τ, called residence time, after which they perform another jump. Rotational diffusion corresponds typically to a FWHM which is constant in Q. To the best of our knowledge LDL particles have never been studied by QENS, thus we applied the model free approach, as no information was available about motions which could be distinguished, and used models (free Brownian diffusion[44], jump diffusion[45] and rotational diffusion[21]) for the fits of the FWHM of the Lorentzian curves.

SANS experiments and data analysis

SANS experiments were performed on the SANS-II beamline[46] at the Paul-Scherrer-Institute (PSI, Villigen, Switzerland) as function of pressure in the range from 20 bar to 3000 bar. For N-LDL we could not observe significant changes in the SANS curves below 600 bar (see ESI Figure S5), therefore 600 bar were taken as starting point.

High pressure equipment specifically developed for SANS experiments was used[47]. The sample thickness was fixed and did not change with pressure (less than 10 μm, which corresponds to a 1% variation in path length and, thus, in transmission). To get access to the broad Q-range of 0.006 to 0.12 $Å^{-1}$ corresponding best to structural dimensions contained in the LDL particles in the reciprocal space, the data was collected at three different sample-detector distances. We also re-measured our samples after HHP application to check for

denaturation. The curves were fully reproducible and the samples were still clear and did not show any turbidity. All measurements were performed in D_2O buffer (10 mM NaPi, 0.1 % EDTA, pH 7.4 in D_2O).

The radius of gyration R_g, which is a measure for the moment of inertia of LDL, was evaluated according to the Guinier approximation[48] from the experimental scattering curves:

$$I(Q) \approx I(0)e^{(-Q^2R_g^2/3)} \quad , \qquad (6)$$

which is valid for small Q values such that $Q*R_g < 1.5$. Here I(0) is the forward scattering intensity, which is a shape independent function of the total scattering power of the sample.

For further analysis, we used the master formula of SANS for a diluted solution of monodisperse particles:

$$\frac{d\sigma(Q)}{d\Omega(Q)} = n\Delta\rho^2V^2F(Q)S(Q)\,, \qquad (7)$$

where n is the number of particles, Δρ is the difference in scattering length density between the particles and the solvent and V is the volume of the particles. F(Q) is the form factor, which is a function of the averaged shape and the averaged size of the scattering particles. The effective structure factor is called S(Q) and for diluted solutions with no interacting particles equal to 1. The scattering intensity pattern was simulated by the SASView software developed at NIST[49]. In our approximation, the scattering contributions of LDL nanoparticles were modelled as the intensity profile of a triaxial ellipsoid[50]. In this analysis we did some approximations: 1) the average scattering length density of the LDL nanoparticle was taken as about 3.7 10^{-6} $Å^{-2}$ [51]; 2) the polydispersity in radius was assumed to be the same for N-LDL and TG-LDL samples and accounts for about 10-15%.

Acknowledgements

This work has been supported by the Austrian Science Fund (FWF Project No. I 1109-N28 to R. P.) and by the Agence Nationale de la Recherche (ANR; project number ANR-12-ISV5-0002-01 LDLPRESS to J.P.). We are gratefully acknowledging the help of M.M. Koza for the measurement on IN6 and the ILL for allocation of beam time. The work is partially based on experiments performed at the Swiss spallation neutron source SINQ, Paul Scherrer Institute, Villigen, Switzerland. The work benefitted from SasView software, originally developed by the DANSE project under NSF award DMR-0520547.

Author contributions

J.P. and R.P. proposed experiments. B.L. prepared samples. N.M., B.L., J.O., J.K., R.P. and J.P. performed neutron experiments. M.G. and J.P. analyzed neutron data and M.G., J.P., B.L. and R.P. wrote the manuscript, with input from all authors.

Additional information

Electronic Supplementary Information accompanies this paper at http://www.nature.com/srep.
Competing financial interests: The authors declare no competing financial interests.

References

1. Mikl, C. et al., Softness of Atherogenic Lipoproteins: A Comparison of Very Low Density Lipoprotein (VLDL) and Low Density Lipoprotein (LDL) Using Elastic Incoherent Neutron Scattering (EINS). *J. Am. Chem. Soc.* **133**, 13213 – 13215 (2011).

2. Müller, K., Laggner, P., Glatter, O., and Kostner, G. The structure of human-plasma low-density lipoprotein B. An X-ray small-angle scattering study. *Eur J Biochem.* **82**, 73-90 (1978).

3. Laggner, P., Kostner, G. M., Degovics, G., and Worcester, D. L. Structure of the cholesteryl ester core of human-plasma low-density lipoproteins – Selective deuteration and neutron small-angle scattering. *Proc. Nat. Acad. Sc. USA* **81**, 4389-4393 (1984).

4. Chapman, M. J. et al., Further resolution of the low-density lipoprotein spectrum in normal human-plasma – Physicochemical characteristics of discrete subspecies separated by density gradient ultracentrifugation. *J. Lipid Res.* **29**, 442-458 (1988).

5. Dejager, S., Bruckert, E., and Chapman, M. J. Dense low-density lipoprotein subspecies with diminished oxidative resistance predominate in combined hyperlipidemia. *J. Lipid Res.* **34**, 295-308 (1993).

6. Segrest, J. P., Jones, M. K., De Loof, H., and Dashti, N. Structure of apolipoprotein B-100 in low density lipoproteins. *J. Lipid Res.* **42**, 1346-1367 (2001).

7. Oliveira, C. L., Santos, P. R., Monteiro, A. M., and Figueiredo Neto, A. M. Effect of oxidation on the structure of human low- and high-density lipoproteins. *Biophys. J.* **106**, 2595-605 (2014).

8. Lusis, A. J. Atherosclerosis. *Nature* **407**, 233-241 (2000).

9. Toth, P. P. Triglyceride-rich lipoproteins as a causal factor for cardiovascular disease. *Vasc. Health Risk Manag.* **12**, 171-183 (2016).

10. McNamara, J. R., Small, D. M., Li, Z. L., Schaefer, E. J. Differences in LDL subspecies involve alterations in lipid composition and conformational changes in apolipoprotein B. *J Lipid Res* **37**, 1924-1935 (1996).

11. Liu, Y., Atkinson, D. Enhancing the contrast of ApoB to locate the surface components in the 3D density map of human LDL. *J Mol Biol* **405**, 274-283 (2011).

12. Doster, W., Cusack, S., and Petry, W., Dynamical transition of myoglobin revealed by inelastic neutron scattering. *Nature* **337**, 754 - 756 (1989).

13. Smith, J.C., Protein dynamics: comparison of simulations with inelastic neutron scattering experiments. *Q. Rev. Biophys*. **24**, 227 – 291 (1991).

14. Lassalle, M.W., Yamada, H. and Akasaka, K. The Pressure-temperature Free Energy-landscape of Staphylococcal Nuclease Monitored by ^{1}H NMR. *J. Mol. Biol*. **298**, 293 - 302 (2000).

15. Frauenfelder, H., Parak, F. and Young, R.D. Conformational substates in proteins. *Annu. Rev. Biophys. Biophys. Chem.* **17**, 569 –572 (1988).

16. Sears, V.F. Neutron scattering lengths and cross sections. *Neutron News* **3**, 26–37 (1992).

17. Svergun, D. I., and Koch, M. H. J. Small-angle scattering studies of biological macromolecules in solution. *Reports on Progress in Physics* **66**, 1735-1782 (2003).

18. Petoukhov, M. V., and Svergun, D. I. Analysis of X-ray and neutron scattering from biomacromolecular solutions. *Curr. Opin. Struct. Biol.* **17**, 562-571 (2007).

19. Johs, A. et al., Modular structure of solubilized human apolipoprotein B-100. Low resolution model revealed by small angle neutron scattering. *J. Biol. Chem.* **281**, 19732-19739 (2006).

20. Neylon, C. Small angle neutron and X-ray scattering in structural biology: recent examples from the literature. *European Biophysics Journal with Biophysics Letters **37*** (5), 531-541 (2008).

21. Bée, M. *Quasielastic Neutron Scattering: Principles and Applications in Solid State Chemistry, Biology and Materials Science,* Adam Hilger, Philadelphia, 1988.

22. Laggner, P., Kostner, G. M., Rakusch, U. and Worcester, D. Neutron small angle scattering on selectively deuterated human plasma low density lipoproteins. The location of polar phospholipid headgroups. *J. Biol. Chem.* **256**, 11832-11839 (1981).

23. Meyer, D. F. et al., Time-course studies by neutron solution scattering and biochemical assays of the aggregation of human low-density lipoprotein during Cu(2+)-induced oxidation. *The Biochemical journal* **310**, 417-426 (1995).

24. Sattler, W., Kostner, G. M., Waeg, G. and Esterbauer, H. Oxidation of lipoprotein Lp(a) – a comparison with low-density lipoproteins. *Biochimica et biophysica acta* **1081**, 65-74, (1991).

25. Wanderlingh, U. et al., Multi-component modeling of quasielastic neutron scattering from phospholipid membranes. *J. Chem. Phys.* **140**, 174901 (2014).

26. Knoll, W. et al., Structural and dynamical properties of reconstituted myelin sheaths in the presence of myelin proteins MBP and P2 studied by neutron scattering. *Soft Matter* **10**, 519 – 529 (2014).

27. Vist, M.R., and Davis, J.H., Phase equilibria of cholesterol/dipalmitoylphosphatidylcholine mixtures: deuterium nuclear magnetic resonance and differential scanning calorimetry**.** *Biochemistry* **29**, 451 – 464 (1990).

28. Linseisen, F.M., Thewalt, J.L., Bloom, M., and Bayerl, T.M. 2 H-NMR and DSC study of SEPC-cholesterol mixtures**.** *Chem. Phys. Lipids* **65**, 141 – 149 (1993).

29. Martinez, N. et al., High protein flexibility and reduced hydration water dynamics are key pressure adaptive strategies in prokaryotes. *Sc. Rep.* **6**, 32816. (2016).

30. Natali, F. et al., Water dynamics in neural tissue. *J. Phys. Soc. Jap.* **82**, Suppl. A, SA017 (2013).

31. Coronado-Gray, A., and van Antwerpen, R. Lipid composition influences the shape of human low density lipoprotein in vitreous ice. *Lipids* **40**, 495-500 (2005).

32. Sherman, M. B., Orlova, E. V., Decker, G. L., Chiu, W., and Pownall, H. J. Structure of triglyceride-rich human low-density lipoproteins according to cryoelectron microscopy. *Biochem.* **42**, 14988-14993 (2003).

33. Wang, L., Walsh, M. T. and Small, D. M. Apolipoprotein B is conformationally flexible but anchored at a triolein/water interface: a possible model for lipoprotein surfaces. *Proc Natl Acad Sci U S A* **103**, 6871-6876, (2006).

34. Peters, J., et al., High hydrostatic pressure equipment for neutron scattering studies of samples in solutions, *High Press. Res.* **32**, 97 - 102 (2012).

35. Ollivier, J., Disk-chopper time-of-flight spectrometer (2012), date of access: 22/12//2016, http://www.ill.eu/instruments-support/instruments-groups/instruments/in5

36. Koza, M. M., Cold neutron time-focusing time-of-flight spectrometer (2012), date of access: 22/12/2016, https://www.ill.eu/instruments-support/instruments-groups/instruments/in6/description/instrument-layout/

37. Natali, F. et al., IN13 backscattering spectrometer at ILL: Looking for motions in biological macromolecules and organisms. *Neutron News* **19**, 14–18 (2008).

38. Richard, D., Ferrand, M., and Kearley, G.J. Analysis and visualisation of neutron-scattering data. *J. Neutron Res.* **4**, 33-39 (1996).

39. Paalman, H. H., and Pings, C. J., Numerical evaluation of X-ray absorption factors for cylindrical samples and annular sample cells. *J. Appl. Phys*. **33**, 2635-2639 (1962).

40. Rahman, A., Singwi, K. S., Sjölander, A. Theory of slow neutron scattering by liquids, I. *Phys. Rev.* **126,** 986−996 (1962).

41. Tehei, M., and Zaccai, G. Adaptation to extreme environments: macromolecular dynamics in complex systems. *BBA – Gen Subjects* **1724**, 404–410 (2005).

42. Zaccai, G. How soft is a protein ? *Science* **288**, 1604 – 1607 (2000).

43. Barrett, M. A. et al., Alzheimer's peptide amyloid-β, fragment 22–40, perturbs lipid dynamics. *Soft Matter* **12**, 1444-1451 (2016).

44. Teixeira, J., Bellissent-Funel, M.C., Chen, S.H., and Dianoux, A.J. Experimental determination of the nature of diffusive motions of water molecules at low temperatures. *Phys. Rev. A* **31**, 1913 (1985).

45. Volino, F., and Dianoux, A. J. Neutron incoherent scattering law for diffusion in a potential of spherical symmetry: general formalism and application to diffusion inside a sphere. *Mol. Phys.* **41**, 271 – 279 (1980).

46. Strunz, P., Mortensen, K., and Janssen, S. SANS-II at SINQ: installation of the former Riso-SANS facility. *Phys. B – Cond. Matt.* **350**, E783-E786 (2004).

47. Kohlbrecher, J., Bollhalder, A., Vavrin, R., and Meier, G. A high pressure cell for small angle neutron scattering up to 500 MPa in combination with light scattering to investigate liquid samples. *Rev. Sci. Instrum.* **78**, 125101 (2007).

48. Guinier, A. and Fournet, G. Small Angle Scattering of X-rays, 1955, New York.

49. SasView for Small Angle Scattering Analysis. (18.09.2016) http://www.sasview.org/

50. Kline, S. R. Reduction and analysis of SANS and USANS data using IGOR Pro. *J. Appl. Cryst.* **39**, 895-900 (2006).

51. Fitter, J., Gutberlet, T., and Katsaras, J. (Eds.), *Neutron Scattering in Biology*, Springer, Berlin - Heidelberg, 2006.

Supporting Information

IN5: TG-LDL sample

Q (Å^{-1})	20 bar	3000 bar
0.25	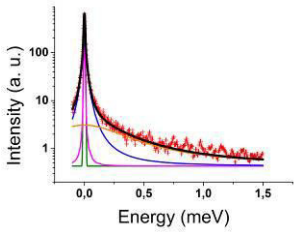	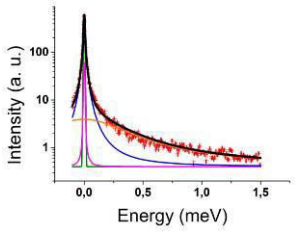
	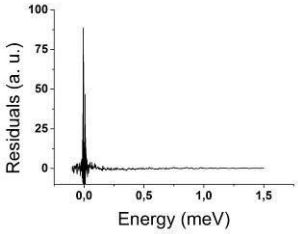	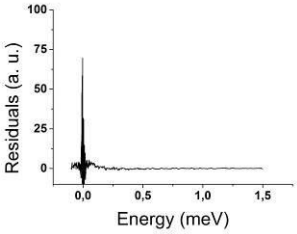
0.33	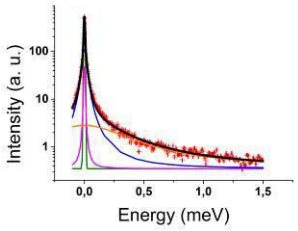	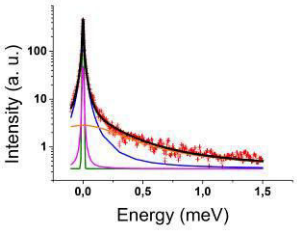
	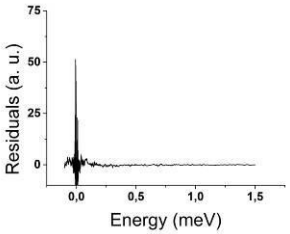	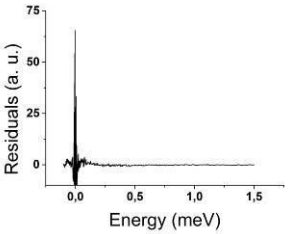
0.40	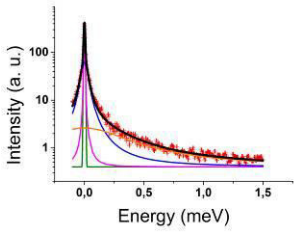	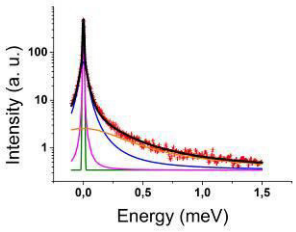
	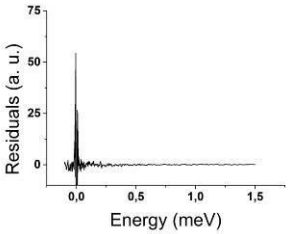	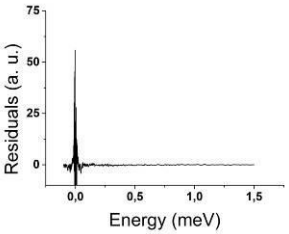
0.48	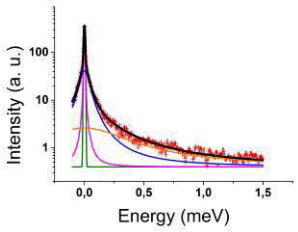	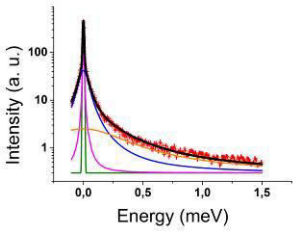

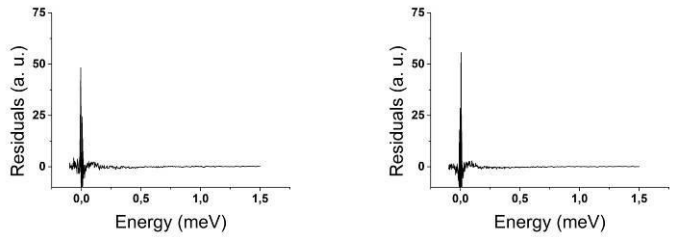
Residuals (a. u.)
Energy (meV)
Residuals (a. u.)
Energy (meV)

0.55

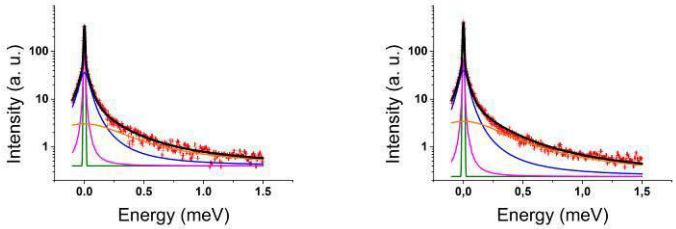
Intensity (a. u.)
Energy (meV)
Intensity (a. u.)
Energy (meV)

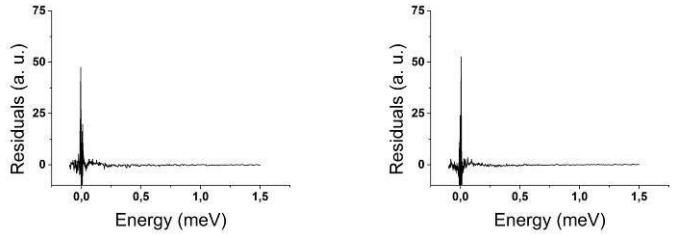
Residuals (a. u.)
Energy (meV)
Residuals (a. u.)
Energy (meV)

0.62

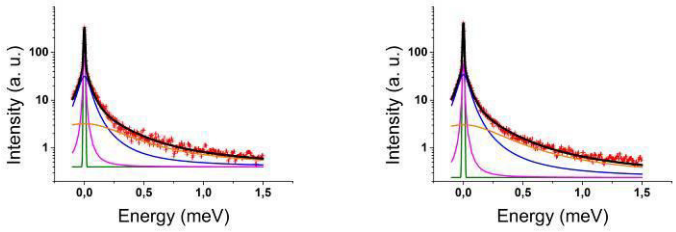
Intensity (a. u.)
Energy (meV)
Intensity (a. u.)
Energy (meV)

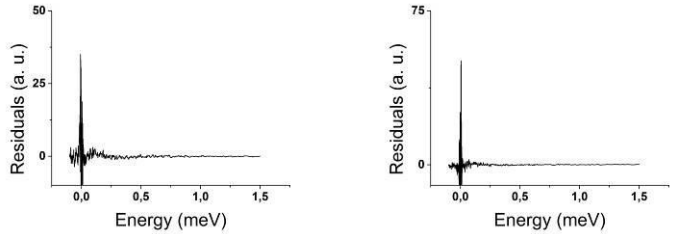
Residuals (a. u.)
Energy (meV)
Residuals (a. u.)
Energy (meV)

0.68

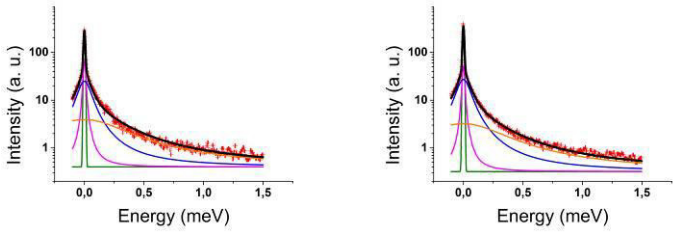
Intensity (a. u.)
Energy (meV)
Intensity (a. u.)
Energy (meV)

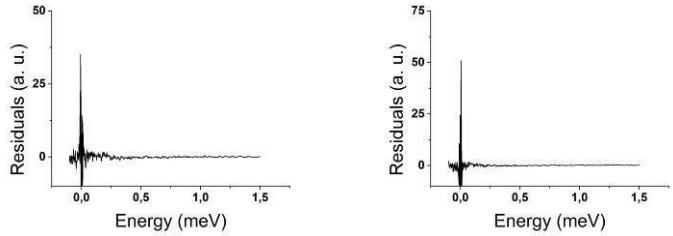
Residuals (a. u.)
Energy (meV)
Residuals (a. u.)
Energy (meV)

0.75	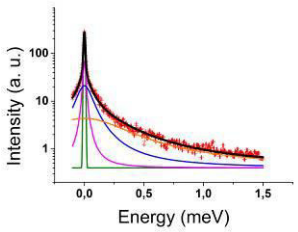	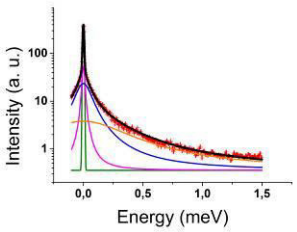
	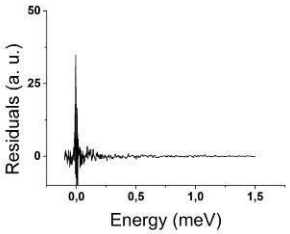	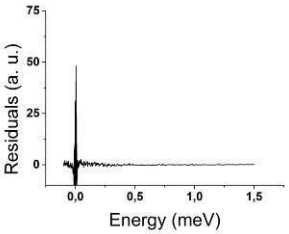
0.80	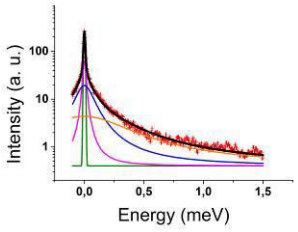	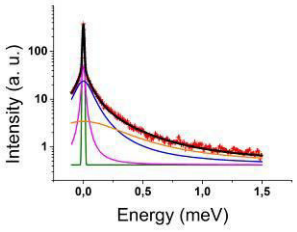
	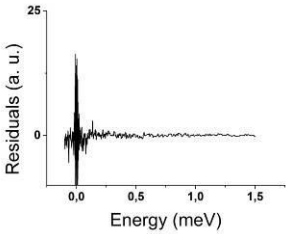	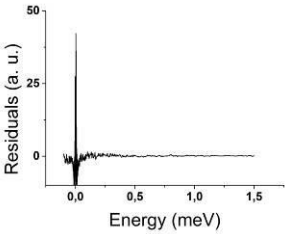
0.86	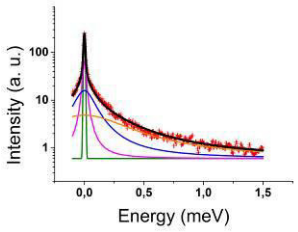	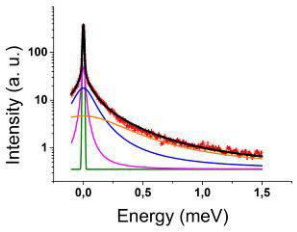
	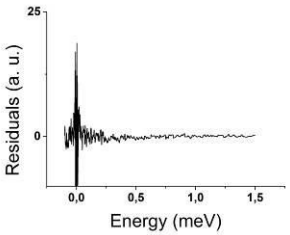	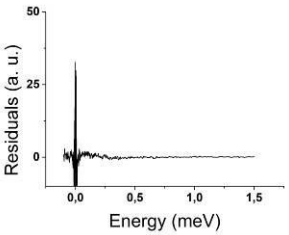
0.91	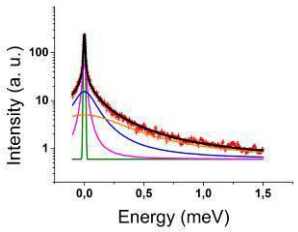	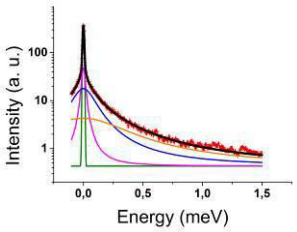

	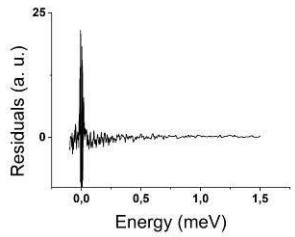	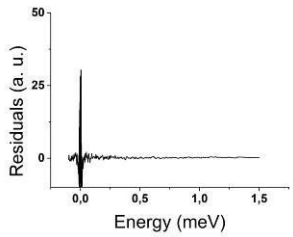
0.96	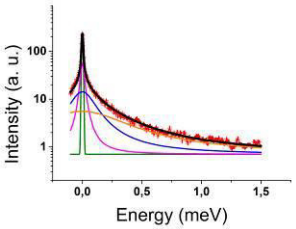	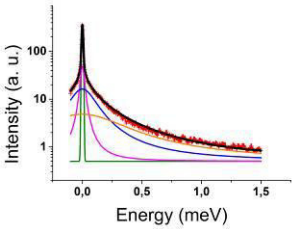
	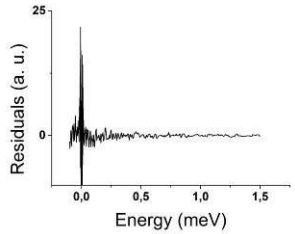	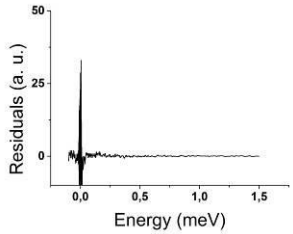
1.00	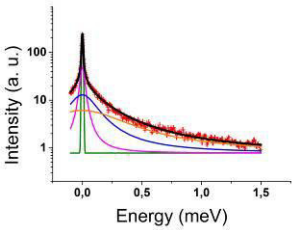	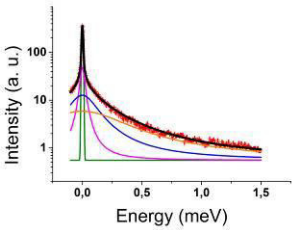
	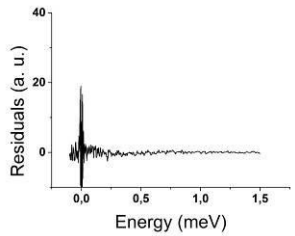	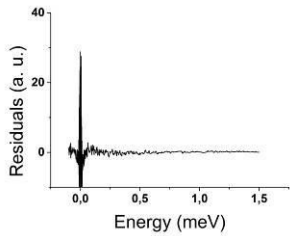

IN6: TG-LDL sample

Q ($Å^{-1}$)	20 bar	3000 bar
0.37	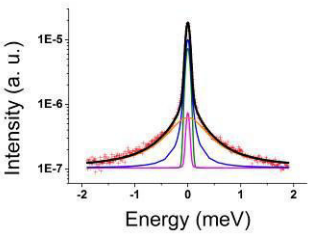	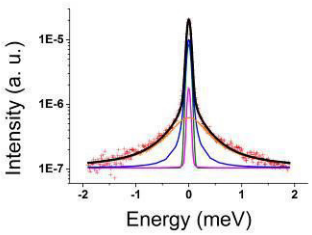
	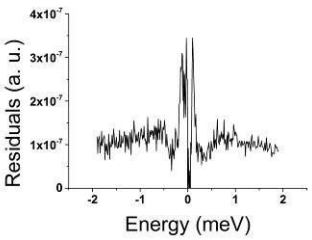	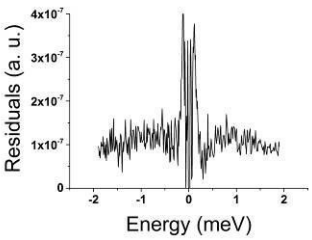

0.55	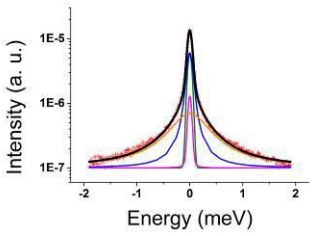	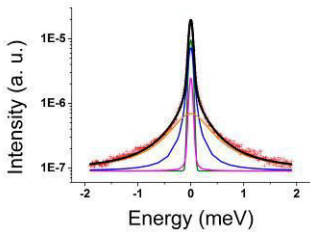
	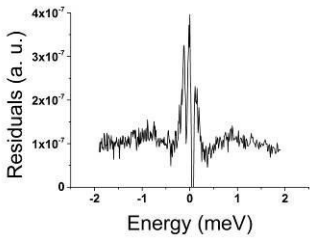	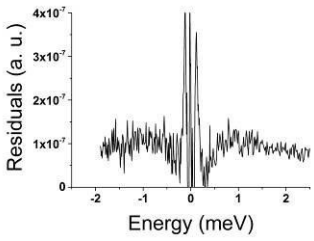
0.73	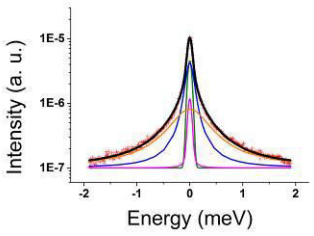	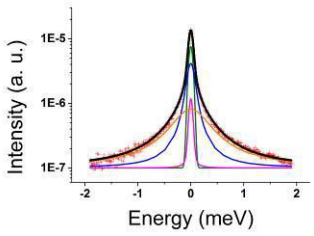
	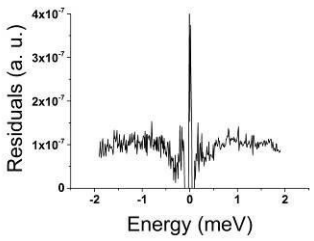	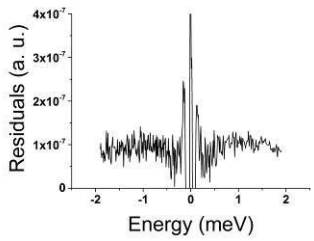
0.90	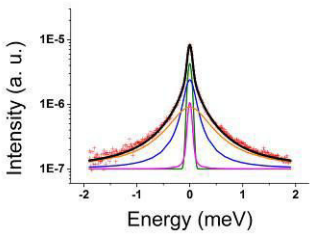	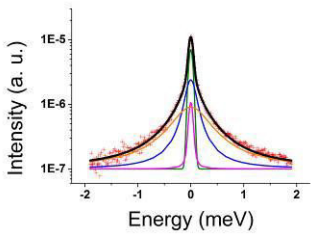
	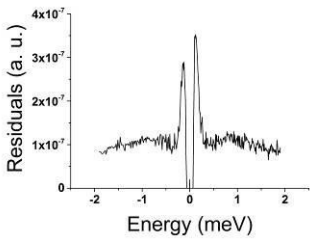	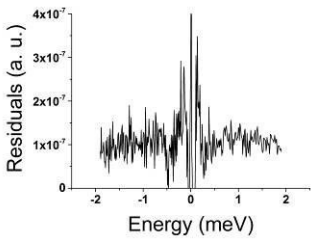
1.07	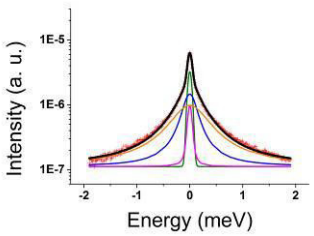	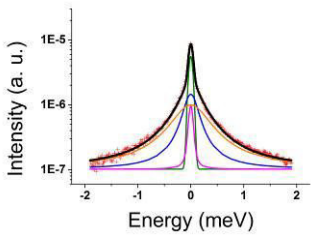

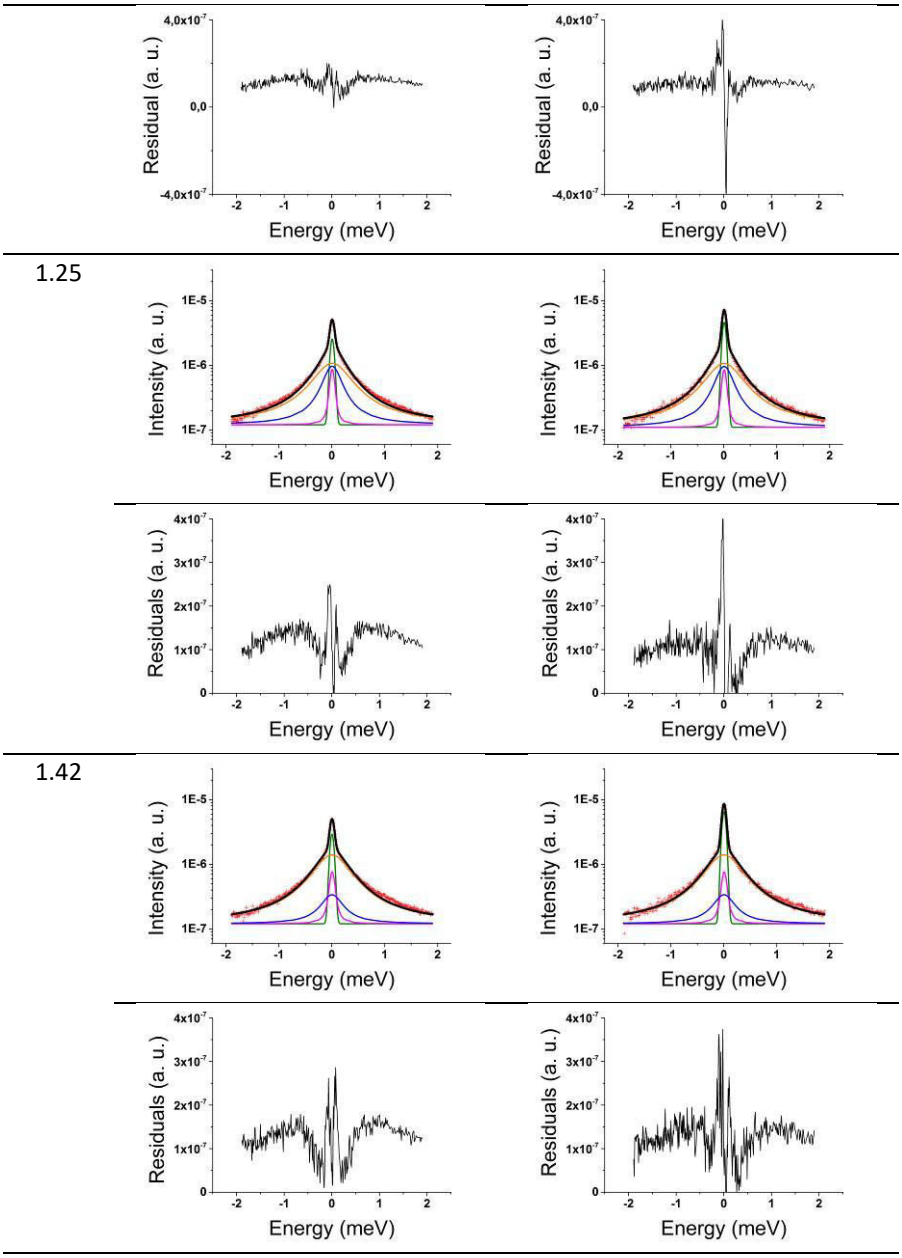

Figure S1: IN5 and IN6 QENS fits of TG-LDL at 20 bar and 3000 bar including fit residuals. The curves are only shown for TG-LDL as they are virtually identical for N-LDL.

Table S1: FWHM values evaluated from data taken on IN5 (a) and IN6 (b) (see also Figure 2b). The estimated error is ± 2 on the last given digit.

(a)

Q^2 (Å^{-2})	Γ_{small} (meV)	$\Gamma_{intermediate}$ (meV)	Γ_{big} (meV)
0.07	0.001	0.025	0.72
0.11	0.003	0.037	0.72
0.17	0.006	0.046	0.72
0.23	0.008	0.062	0.72
0.31	0.011	0.084	0.72
0.38	0.012	0.105	0.72
0.47	0.017	0.128	0.72
0.56	0.020	0.145	0.72

0.65	0.023	0.165	0.72
0.74	0.026	0.185	0.72
0.83	0.029	0.208	0.72
0.92	0.033	0.231	0.72
1.02	0.038	0.252	0.72

(b)

Q^2 (Å^{-2})	Γ_{small} (meV)	$\Gamma_{intermediate}$ (meV)	Γ_{big} (meV)
0.14	0.0048	0.034	0.72
0.30	0.0106	0.080	0.72
0.53	0.0187	0.138	0.72
0.81	0.0285	0.200	0.72
1.14	0.0400	0.275	0.72
1.55	0.0542	0.355	0.72
2.02	0.0709	0.430	0.72

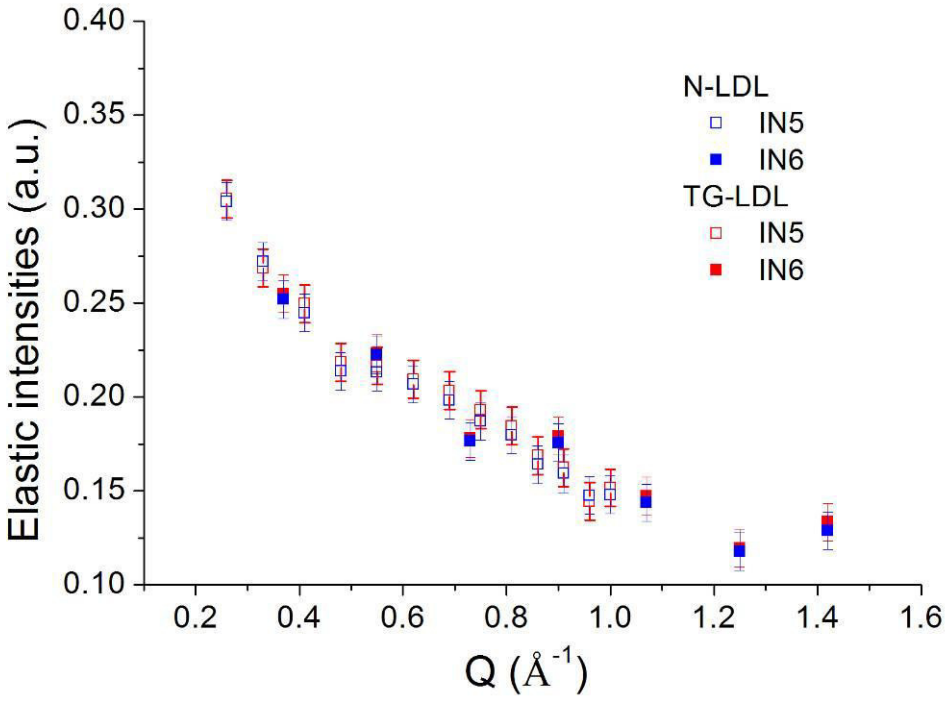

Figure S2: Elastic intensities extracted from QENS data as function of Q: N-LDL (blue) and TG-LDL (red) at 20 bar. All data were measured at 310 K on IN5 and IN6.

Table S2: MSD values evaluated from data taken on IN13 (see Figure 4a).

	MSD (Å^2)	Error (Å^2)
N-LDL 20 bar	2.83	0.21
N-LDL 3000 bar	3.10	0.26
TG-LDL 20 bar	2.26	0.11
TG-LDL 3000 bar	1.17	0.05

Table S3: Elastic intensities evaluated from QENS data taken on IN5 (a) and IN6 (b) (see also Figure S2) at 20 bar and on IN5 (c) and IN6 (d) (see also Figure 4b) at 3000 bar. The estimated error is 5%.

(a)

Q ($Å^{-1}$)	N-LDL	TG-LDL
0.26	0.30388	0.30539
0.33	0.27211	0.26853
0.41	0.2447	0.24964
0.48	0.21363	0.21842
0.55	0.21308	0.21666
0.62	0.20669	0.20942
0.69	0.19823	0.20328
0.75	0.18705	0.19312
0.81	0.17969	0.18444
0.86	0.16403	0.16868
0.91	0.1592	0.16234
0.96	0.14766	0.14444
1.00	0.14782	0.15161

(b)

Q ($Å^{-1}$)	N-LDL	TG-LDL
0.37	0.25182	0.25498
0.55	0.22249	0.22328
0.73	0.17632	0.17801
0.90	0.17564	0.17914
1.07	0.14371	0.14724
1.25	0.11767	0.11951
1.42	0.12873	0.13339

(c)

Q ($Å^{-1}$)	N-LDL	TG-LDL
0.26	0.31	0.31
0.33	0.27	0.30
0.41	0.25	0.27
0.48	0.22	0.26
0.55	0.22	0.26
0.62	0.21	0.26
0.69	0.20	0.27
0.75	0.19	0.26
0.81	0.18	0.27
0.86	0.17	0.26
0.91	0.16	0.25

0.96	0.14	0.23
1.00	0.15	0.23

(d)

Q ($Å^{-1}$)	N-LDL	TG-LDL
0.37	0.26	0.29
0.55	0.22	0.26
0.73	0.18	0.27
0.90	0.18	0.26
1.07	0.15	0.23
1.25	0.12	0.20
1.42	0.13	0.23

Table S4: Fitted radii of a triaxial ellipsoid extracted from the SANS curves. The error of the radii was estimated to ± 1 Å. For technical reasons we could not measure TG-LDL at 20 bar.

N-LDL				
313 K				
Pressure (bar)	R_3 (Å)	R_2 (Å)	R_1 (Å)	Rg (Å)
20	78	101	123	79
300	77	101	123	79
600	77	101	123	79
1200	75	101	121	78
2000	74	100	121	78
3000	72	99	120	77
TG-LDL				
313 K				
Pressure (bar)	R_3 (Å)	R_2 (Å)	R_1 (Å)	Rg (Å)
20	N.D.*	N.D.*	N.D.*	N.D.*
600	82	99	117	78
1200	78	99	118	77
2000	79	98	118	77
3000	77	98	120	76

* not determined

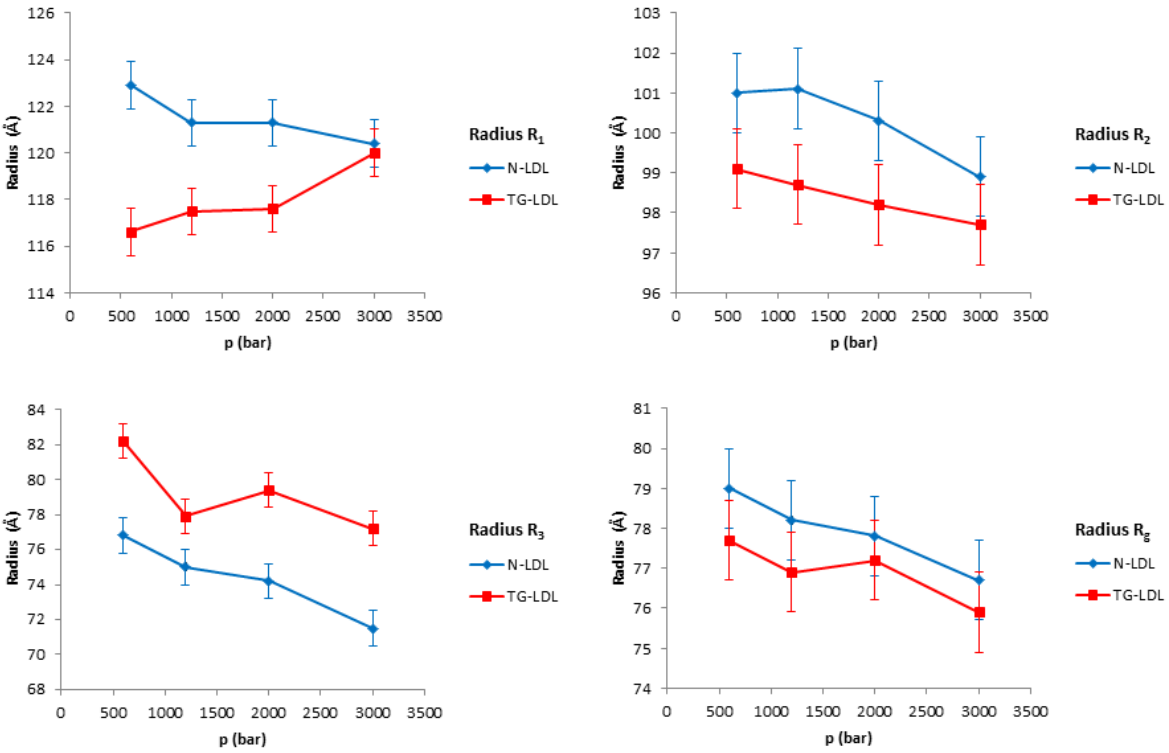

Figure S3: Separate graphs for the changes of the individual radii (R1, R2 and R3) derived by fitting the SANS curves with an ellipsoidal model as well as the R_g are shown.

Table S5: Chemical compositions (wt%) of normolipidemic N-LDL and triglyceride-rich TG-LDL. Values are means ± SD of duplicate or triplicate determinations of each component.

Component	QENS		EINS		SANS	
	N-LDL	TG-LDL	N-LDL	TG-LDL	N-LDL	TG-LDL
Protein	21.1 ± 0.8	19.3 ± 0.8	20.5 ± 3.2	16.6 ± 0.2	19.7 ± 0.2	19.2 ± 0.8
Phospholipids	22.0 ± 0.1	19.9 ± 0.4	20.9 ± 2.3	21.9 ± 1.7	22.6 ± 1.1	20.9 ± 2.0
Unesterified cholesterol	8.3 ± 0.1	6.1 ± 0.3	9.3 ± 0.7	7.0 ± 0.8	7.4 ± 0.3	5.9 ± 0.6
Cholesteryl esters	43.9 ± 1.3	43.6 ± 0.8	41.9 ± 1.1	44.4 ± 0.7	44.0 ± 0.5	43.0 ± 1.2
Triglycerides	4.7 ± 0.1	11.2 ± 0.1	7.4 ± 0.5	10.1 ± 0.8	6.4 ± 0.1	11.0 ± 0.2

Table S6: Protein concentrations (mg/mL) of the measured LDL samples. Values are means ± SD of duplicate or triplicate determinations. All samples were in the buffer system 10 mM NaPi (1.44 g/L $Na_2HPO_4 \cdot 2H_2O$, 0.26 g/L KH_2PO_4), 0.1 % EDTA, pH 7.4 in D_2O. A remaining amount of approximately 5-10 % of H_2O was in the buffer system due to the isolation procedure from a natural source.

Method	N-LDL	TG-LDL
QENS	17.4 ± 1.3	23.0 ± 1.8
EINS	12.2 ± 0.4	24.7 ± 1.7
SANS	2.9 ± 0.13	2.9 ± 0.19

Table S7: Instrumental characteristics of the spectrometers IN5, IN6 and IN13 at the ILL.

Spectrometer	IN5	IN6	IN13
Wavelength [Å]	10	5.1	2.23
Accessible Q-range [$Å^{-1}$]	0.3 – 1.0	0.4 - 2.0	0.2 - 4.9
Length scale [Å]	6 - 21	3 – 16	1 - 30
Energy resolution [μeV]	10	75	10
Time scale [ps]	100	15	100

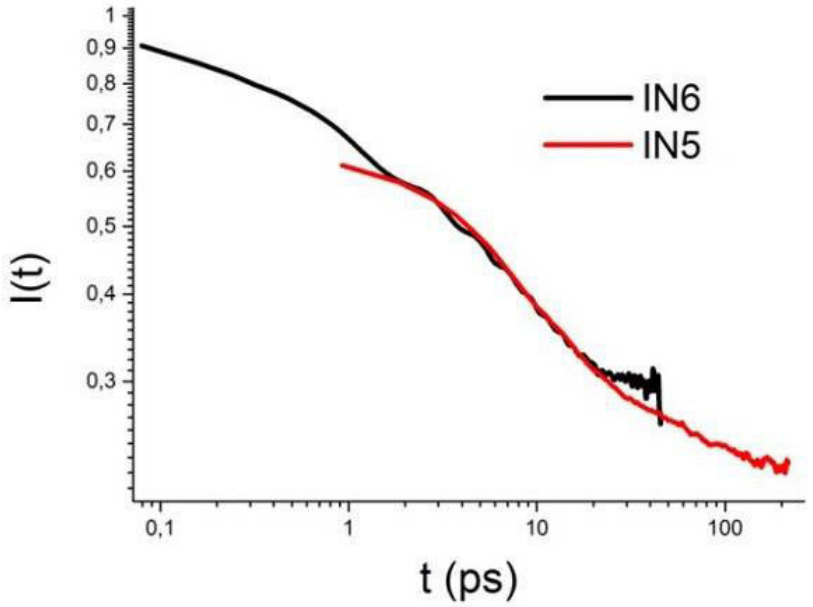

Figure S4. Indirect Fourier Transformation for Q = 0.73 $Å^{-1}$, processed with the program Dave[S1], for the QENS spectra of N-LDL, measured at 3000 bar on IN5 (red line) and IN6 (black line) spectrometers.

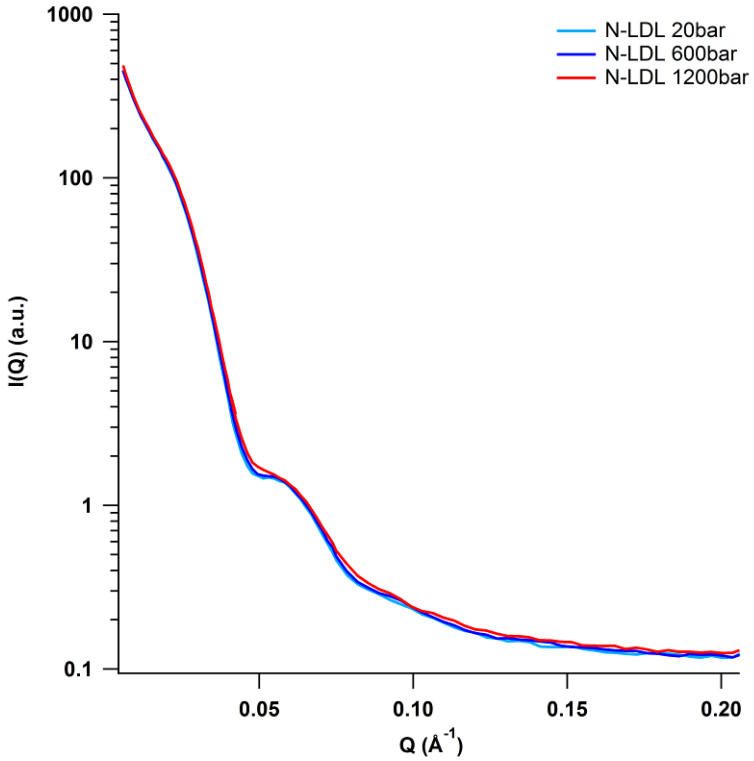

Figure S5. The measured SANS curves for N-LDL at pressure points 20 bar (light blue), 600 bar (dark blue) and 1200 bar (red).

Reference

S1. Azuah, R.T, Kneller, L.R., Qiu, Y., Tregenna-Piggott, P.L.W., Brown, C.M., Copley, J.R.D., and Dimeo, R.M. DAVE: A comprehensive software suite for the reduction, visualization, and analysis of low energy neutron spectroscopic data, *J. Res. Natl. Inst. Stan. Technol.* **114**, 341 (2009).

5. Results Part II

Results part II extends the investigations about the dynamical behavior of different forms of LDL applying neutron scattering. A normolipidemic, triglyceride-rich and oxidized form were compared as a function of temperature and pressure. The influence of lipid composition and oxidation state on motions is presented.

Low-density lipoproteins investigated under high hydrostatic pressure by elastic incoherent neutron scattering

J. Peters[1,2], N. Martinez[2,3,†], B. Lehofer[4], R. Prassl[4,*]

[1] Univ. Grenoble Alpes, LiPhy, F-38044 Grenoble, France
[2] Institut Laue Langevin, F-38000 Grenoble, France
[3] Univ. Grenoble Alpes, IBS, F-38000 Grenoble, France
[4] Institute of Biophysics, Medical University of Graz, A-8010 Graz, Austria

**Corresponding author: Ruth Prassl, ruth.prassl@medunigraz.at*

† Present address: SyMMES 5819, CEA-CNRS-UJF Grenoble 1, France

Abstract

Human low-density lipoprotein (LDL) is a highly complex nanoparticle built up of various lipid classes and a single large protein moiety (apoB-100) owning essential physiological functions in the human body. Besides its vital role as a supplier of cholesterol and fat for peripheral tissues and cells, it is also a known key player in the formation of atherosclerosis. Due to these important roles in physiology and pathology the elucidation of structural and dynamical details is of great interest. In the current study we drew a broader picture of LDL dynamics using elastic incoherent neutron scattering (EINS) as a function of specified temperature and pressure points. We not only investigated a normolipidemic LDL sample, but also a triglyceride-rich and an oxidized one to mimic pathologic conditions as found under hyperlipidemic conditions or in atherosclerotic plaques, respectively. We could show that pressure has a significant effect on atomic motions in modified forms of LDL, whereas the normolipidemic sample seems to cope much better with high pressure conditions irrespective of temperature. These findings might be explained by the altered lipid composition, which is either caused through elevated triglyceride content or modifications through lipid peroxidation.

Published in: *The European Physical Journal E* **2017**, *40*, 68.
DOI: 10.1140/epje/i2017-11558-8

Introduction

Low-density lipoproteins (LDL) are naturally occurring macromolecular assemblies of various lipids and a single protein component, named apolipoprotein B-100 (apoB-100). ApoB-100 stabilizes the structure of the lipid nano-assembly and triggers the function of LDL in human blood circulation. The major role of LDL in humans is the transport of cholesterol and fat to tissues and cells. Apart from its vital role in physiology, LDL is intimately involved in the progression of cardiovascular diseases, in particular atherosclerosis. Chemical modifications of LDL, e.g. through oxidation cause an accumulation and retention of oxidized LDL in the subendothelial space for ingestion by macrophages, which are subsequently transformed into foam cells. In combination with inflammatory reactions LDL retention in the arterial wall constitutes the first stage of atherosclerosis. Atherosclerosis dramatically increases the risk for myocardial infarction and stroke, which are amongst the major causes of morbidity and mortality in Western civilization resulting in substantial economic burden imposed on health care systems [1]. The interaction of surface-located apolipoproteins with specific cellular receptors indeed determines whether triglycerides and cholesterol will be added or removed from the lipoprotein transport particles [2]. According to these functionalities, it is a common use to distinguish between “bad” and “good” cholesterol when designating LDL cholesterol and high-density lipoprotein (HDL) cholesterol, respectively. However, certain blood levels of both HDL and LDL are essential to maintain health. LDL’s structure was investigated exhaustively by small-angle scattering techniques and cryo-electron microscopy [3 4 5 6 7], giving rise to a rough representation of the nano-particle. It has an ellipsoidal shape with radii varying between 87 and 123 Å for the different axes [8]. Contrary to a cell bilayer membrane, its surface is formed by a phospholipid monolayer, and the hydrophobic core is filled with cholesteryl esters and triglycerides. According to the environmental temperature and the actual core composition, the core is more or less ordered in layers [7]. Indeed, LDL nano-particles exhibit phase transitions, whose exact temperature T_m depends on the samples’ core composition [9 10].

The molecular dynamics of biological systems is as important as the structure for the proper functioning of bio-systems [11]. Lipoproteins have shown a distinct dynamical behavior as a function of temperature [12]. However, temperature is only one important thermodynamical variable, therefore to completely describe a system its dependence on pressure has to be taken into account as well [13]. Such pressure experiments are still scarce, especially in

combination with neutron scattering techniques, mainly due to technological challenges. Recently, we investigated LDL particles under high hydrostatic pressure (HHP) conditions by quasi-elastic and elastic incoherent neutron scattering [8] and found significant differences in dynamics and shape of LDL according to the actual core composition. These studies were performed at body temperature (310 K), only. Here, we present elastic incoherent neutron scattering (EINS) results as a function of temperature at the two extreme pressure points investigated before, i.e. 20 bar and 3000 bar. Temperature and pressure are expected to have opposing effects. In fact, temperature increases the thermal energy and the volume of a system and thus its mobility, whereas pressure decreases the available volume and thus the flexibility according to Le Châtelier's principle [14]. We compared the dynamics of LDL samples having a normolipidemic core composition (N-LDL) to LDL particles with a triglyceride-rich core composition (TG-LDL) mimicking LDL particles usually found in patients with hyperlipidemia and a proatherogenic oxidatively modified LDL sample (Ox-LDL).

Experimental details

Sample preparation and characterization

LDL was isolated from human blood plasma by applying a multiple-step density gradient ultracentrifugation [12]. Blood plasma was obtained from the Department of Blood Group Serology and Transfusion Medicine of the University Hospital Graz (Graz, Austria) after written informed consent, according to a protocol approved by the Institutional Review Board of the Medical University of Graz. The blood plasma was free of pathogens (HBV, HCV, HIV). The isolated LDL was extensively dialyzed against buffer solution (10 mM NaPi buffer (1.44 g/L $Na_2HPO_4 \cdot 2\ H_2O$, 0.26 g/L KH_2PO_4), 0.1 % EDTA, pH 7.4), concentrated with Amicon Ultra-15 centrifugal filter units (cut-off 100 kDa) and characterized for its protein and lipid composition. Protein concentration was determined with BCA protein assay kit (Thermo Fisher Scientific, Waltham, MA, USA). The further biochemical composition was determined with colorimetric enzymatic assay kits (DiaSys Diagnostic Systems, Holzheim, Germany) as described previously [15]. Protein integrity was checked with SDS-PAGE.

For the oxidation process LDL was rebuffered in an oxidation buffer (10 mM NaPi, 0.9 % NaCl, pH 7.4) which did not contain EDTA to enable the oxidation with $CuCl_2$. 34 nmol $CuCl_2$/mg apoB-100 protein were used to oxidize the sample at 310 K. The oxidation was monitored simultaneously at a spectrophotometer through the increase of absorption from conjugated dienes at 234 nm as described in [16]. The process was stopped after 135 min in

the middle of the propagation phase through the addition of EDTA. Finally, the samples (N-LDL, TG-LDL and Ox-LDL) were rebuffered to the measurement buffer (10 mM NaPi, 0.1% EDTA, pH* 7.4 (pD 7.8) in D_2O). The pH was measured with an electrode in the D_2O solution and adjusted to pH* 7.4. The pH* value is a pH related quantity representing a direct reading in a D_2O solution of a H_2O-calibrated pH-meter. The conversion of pH* into pD is then accomplished by adding a constant of 0.4 pH units [17]. The chemical compositions of the investigated LDL samples are provided in Table 1.

Table 1: Chemical compositions (% w/w of total LDL mass) of normolipidemic N-LDL, triglyceride-rich TG-LDL and oxidized Ox-LDL. Values are means ± SD of duplicate or triplicate determinations of each component.

Component	N-LDL	TG-LDL	Ox-LDL
Protein	21.0 ± 3.1	16.6 ± 0.2	16.1 ± 1.0
Phospholipids	20.6 ± 2.3	21.9 ± 1.7	22.5 ± 3.6
Unesterified cholesterol	9.2 ± 0.7	7.0 ± 0.8	9.1 ± 0.7
Cholesteryl esters	41.4 ± 1.0	44.4 ± 0.7	44.8 ± 1.3
Triglycerides	7.8 ± 0.5	10.1 ± 0.8	7.5 ± 0.1

To determine the transition temperatures T_m corresponding to the reversible lipid phase transition, and the protein denaturation temperature of apoB-100, differential scanning calorimetry (DSC) scans were performed with a scan rate of 60 °C/h. Figure 1 shows the buffer-subtracted scans converted into heat capacity C_p as a function of temperature. We found transition temperatures of T_m = 23.5 °C for N-LDL, T_m = 19.1 °C for TG-LDL and T_m = 25.6 °C for Ox-LDL. Note, that T_m varies with the lipid composition of the LDL particles. Usually T_m is found around 25°C or higher [10] as was the case for N-LDL and Ox-LDL, while the lower T_m of TG-LDL is typical for LDL with a high TG content. The endothermic protein denaturation peaks were around 80°C for N-LDL and TG-LDL. For Ox-LDL the protein denaturation peak was diminished and shifted to lower temperatures, reflecting protein damage during the oxidation process [18]. The exothermic transition seen as drop in the heat capacity curve at higher temperature is due to particle aggregation and sedimentation. Again, the temperature is lower for oxidized LDL.

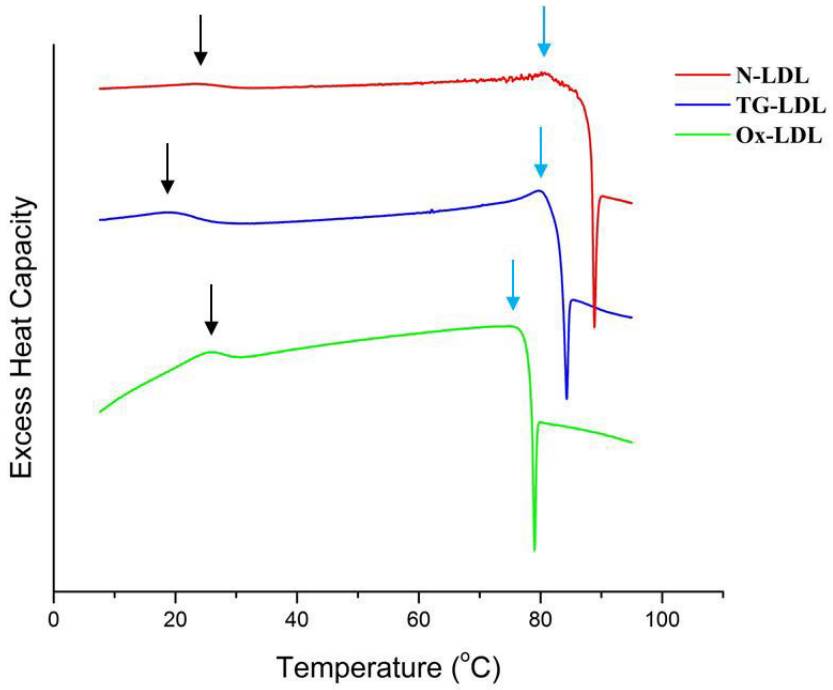

Figure 1: Buffer subtracted DSC curves (shifted vertically for better visibility) with lipid phase transition temperatures T_m (indicated through black arrows) and the endothermic protein denaturation peak (indicated through blue arrows).

Neutron scattering experiments

The EINS experiments, which permit to follow averaged atomic motions, were operated on the thermal backscattering spectrometer IN13 [19] at the Institut Laue Langevin (ILL) in Grenoble/France. The instrument has an energy resolution of 8 μeV, corresponding to a time window of about 100 ps. It therefore allows to see internal motions of macromolecules. Elastic scattering data, corresponding to the situation where no energy is exchanged but the neutrons are deviated from their initial direction giving rise to a variation of momentum (designated as Q) were analyzed through the scattering function S(Q, 0 ± ΔE), where ΔE designates the instrumental resolution. Assuming a normal distribution of the atoms around their equilibrium position it reduces in terms of the Gaussian approximation [20] to:

$$S(Q,0 \pm \Delta E) \approx \exp\left(-\frac{1}{3}Q^2\left\langle u^2\right\rangle\right). \qquad (1)$$

Here $\langle u^2 \rangle$ are the average atomic mean-square displacements (MSD). The MSD values are obtained for each temperature/pressure point from the slope of the logarithm of the scattered intensities S(Q, 0 ± ΔE) plotted versus Q^2 according to

$$\left\langle u^2\right\rangle = -3\frac{\partial \ln S(Q,0 \pm \Delta E)}{\partial Q^2}. \qquad (2)$$

This approximation is strictly speaking only valid for $Q \rightarrow 0$, but can be extended to $\langle u^2 \rangle Q^2 < 1$ [21]. Accordingly, in this study the fit range was restricted to the low Q-range between 0.5 $Å^{-1}$ and 2.0 $Å^{-1}$. The incoherent neutron scattering intensity is dominated by the signal arising from hydrogen. This is due to the hydrogen incoherent scattering cross section, which is one order of magnitude larger than that of all other atoms usually occurring in biological matter, and also of its isotope deuterium [22]. The technique thus probes average dynamics, because hydrogen atoms are almost uniformly distributed in the sample and representative for the molecular subgroups to which they are bound. Thus when using D_2O for the surrounding water, as done in our case, its signal is negligible compared to the signal arising from the sample itself.

A high pressure equipment dedicated to neutron scattering experiments of biological samples in solution has been developed over the last years at the ILL [23]. It consists of a high pressure stick, which can be placed in the cryostats or cryofurnaces of the instruments, a pressure controller, which allows a remote control and permanent adjustment of pressure, and a cylindrical pressure container built of a high-tensile aluminum alloy withstanding pressures up to 6 kbar (600 MPa). The HHP sample holder has an outer diameter of 15 mm and an inner diameter of 6 mm, thus the thick Al walls absorb much more neutrons than standard flat sample holders. Accordingly, each pressure and temperature point was measured for at least 10 hours to ensure a sufficient signal-to-noise ratio. We probed the samples at pressure points of 20 bar and 3 kbar and at temperatures of 280 and 310 K. Moreover, we recorded a temperature point close to the lipid phase transition, that is to say at 297 K (24 °C) for N-LDL, at 292 K (19 °C) for TG-LDL and 300 K (27 °C) for Ox-LDL. For correction and normalization purposes, the empty cell, the buffer (10 mM NaPi, 0.1 % EDTA in D_2O) and a vanadium rod (a completely incoherent scatterer) were probed under similar conditions. Absorption corrections based on the formula of Paalman-Pings [24] were applied and the data reduction was carried out using the LAMP software available at the ILL [25]. All samples were normalised in the same way to give comparable absolute intensities.

Results and Discussion

We first summed the neutron intensities over all scattering angles corresponding to Q-values from 0.2 to 4.5 $Å^{-1}$. This operation is not restricted by any approximation and gives lower error bars (see Figure 2). We showed that the summed intensities are inversely proportional to the square root of the MSD [26]. Here we distinguish two effects: (i) the summed intensities

decrease almost linearly with temperature and (ii) they increase with pressure except for N-LDL, for which the intensities remain constant within error bars. The intensity increases when the atomic motions are slowed down and thus more neutrons are scattered within the instrumental time window. On the contrary a lower intensity is an indication for a higher flexibility of the sample.

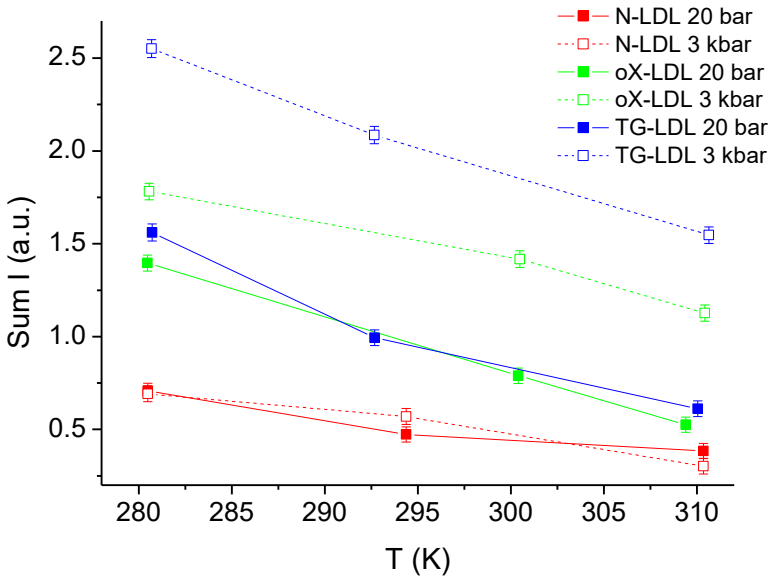

Figure 2: Neutron intensities summed over all scattering angles as function of temperature for both pressure points. Lines are guides to the eyes.

Similar results can be extracted from the MSD (see Figure 3): (i) the MSD values are all increasing with temperature and (ii) they are decreasing at higher pressure, again except for N-LDL for which the MSD values are even slightly increasing with pressure. Therefore, temperature and pressure have clearly different effects: temperature raise increases the thermal energy within the sample, which seems to be roughly homogeneously distributed over all atoms and increases their motions almost equally. In contrast, high pressure specifically affects the different samples, sometimes increasing and sometimes decreasing the flexibility. It seems that the dynamic behavior under pressure of the two LDL particles mimicking pathological conditions is similar and is in clear contrast to the normolipidemic form. This means that temperature has a comparable effect on all samples, whereas pressure seems to specifically induce some structural rearrangements in the modified samples. These effects might be caused by an altered compressibility of surface and core lipids as well as a conformational change of the protein moiety apoB-100 induced by either peroxidation processes or a different core fluidity due to an elevated TG level.

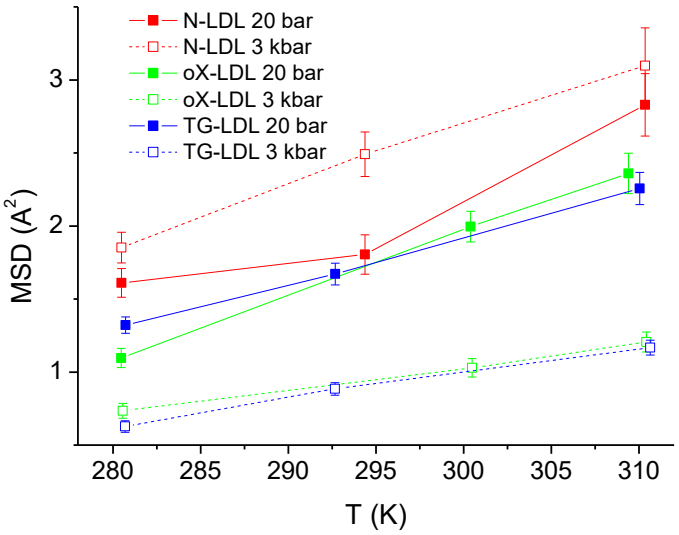

Figure 3: Atomic MSD extracted in the Q-range between 0.5 Å^{-1} and 2.0 Å^{-1} as a function of temperature for both pressure points. Lines are guides to the eyes.

Overall, the MSD of N-LDL are very high compared to other biological macro-molecules [27] and to the MSD of LDL hydrated powder as described in [12] (N.B.: We used a different convention in the two cited publications taking into account a factor 6 in eqs. (1) and (2) instead of 3 as done here, which enhances the differences even more.). Indeed, lipids are known for their high flexibility (about 2.8 Å^2 at 305 K for DMPC membranes when accounting for the factor 3 instead of 6, see [28]) and in the current experiment the sample was in solution, which increases the flexibility even more as whole molecule's diffusion could be added [29]. Below and above the phase transition temperature, the MSD of N-LDL at low and high pressure are almost within error bars, but they differ significantly at the phase transition temperature. This is not surprising as fluctuations of any size occur close to a phase transition [30]. However, it is rather surprising that the normolipidemic particle resists so well to HHP application and becomes even slightly more mobile at higher pressure as all MSD points lie above the corresponding value at ambient pressure in contrast to the two other samples. A similar behavior was already detected in our earlier work [8], that is to say that N-LDL coped very well with pressure with respect to its molecular dynamics and its structure.

The modified forms, Ox-LDL and TG-LDL, seem to be much more sensitive to pressure application, which tends to reduce the atomic motions in accordance with Le Châtelier's principle by a factor of at least two. Triglycerides are indeed much softer than cholesteryl esters and their quantity is enhanced in the lipid core of TG-LDL (see Table 1). This

hydrophobic core undergoes a phase transition from an ordered smectic-like phase to a more disordered isotropic phase at a certain T_m defined by its exact core composition. This phase transition temperature is highly sensitive to very small changes in the core composition, more precisely to changes of the TG content in the core. Higher TG contents lead to lower transition temperatures. This could also be shown in our study (see Figure 1), where the higher TG content lead to a lower T_m. Therefore it is quite evident, that such small changes in the core composition also have significant effects on the dynamical behavior, especially under high pressure conditions. This might be the reason why the atomic motions in TG-LDL are reduced by pressure more intensively, when a higher amount of triglycerides is present in the lipid core.

The modifications occurring during oxidation might have a similar effect. In the propagation phase of LDL oxidation lipid radicals are generated and start a chain reaction of lipid peroxidation, which leads to the formation of lipid peroxyl and lipid alkoxyl radicals resulting in the formation of conjugated dienes and lipid hydroperoxides [31] [32]. While the core lipid organization is less affected by oxidation the protein moiety becomes destabilized [18]. Conformational changes of apoB-100 already occur at early stages of oxidation. It could be shown that changes occur predominantly in the β-sheet regions of the protein and even before LDL peroxidation is initiated [31]. Such changes certainly influence flexibility and compressibility and consequently the dynamical behavior. Likewise, the oxidatively modified acyl chains of the phospholipids in the surface monolayer are less densely packed and ordered. Hence, it is reasonable to assume that the outer layer of LDL becomes softer leading to a higher compressibility at high pressure. However, neutron scattering averages over all H-atoms within the sample, so the various contributions cannot be distinguished further in more detail.

This is the first study that gives insight into the dynamical behavior of normolipidemic LDL compared to the modified forms using EINS. At the present state, we are not able to draw medical conclusions from our findings. We want to remind that the two modified forms of LDL only mimic pathologies, but are not derived from real patients. Therefore, we can only suggest some very tentative statements: It appears that the normolipidemic form of LDL resists very well to HHP application and its mobility is by trend even higher under pressure than without. Both modified forms of LDL have reduced MSD under HHP application and their thermal behavior is very similar to each other. However, the slope of the MSD as a

function of temperature is reduced under high pressure. This means that pressure damps the effect that thermal energy has on the MSD.

Conclusions

Here we report on dynamic data of lipoproteins as a function of temperature and pressure using elastic incoherent neutron scattering. We chose LDL with a normolipidemic composition and two modified forms of LDL to mimic pathological conditions. Triglyceride-rich LDL characteristic for hyperlipidemia and oxidatively modified pro-atherogenic LDL were investigated. As LDL particles show a lipid phase transition, we measured the samples below, at and above the phase transition temperature at two extreme pressure points of 20 and 3000 bar. In accordance with our recent findings [8], normolipidemic LDL seems therefore to be the optimized form of LDL, coping well with harsh external conditions and staying flexible. On the contrary, for both modified forms of LDL the MSD is strongly reduced under pressure and the expected increase of MSD with increasing temperature is also damped under pressure. These modified particles are therefore much less adapted to external extreme conditions and partly lose their flexibility. We assume that this behavior is due to the altered lipid profile which might be correlated with LDL functionality.

Acknowledgements

We are grateful to ILL for the allocation of beam-time. We would like to thank Hanna Lindermuth for excellent technical assistance. This work has been supported by the Austrian Science Fund (FWF Project No. I 1109-N28 to R. P.) and by the Agence Nationale de la Recherche (ANR; project number ANR-12-ISV5-0002-01 LDLPRESS to J.P.).

Author contribution statement

J.P. and R.P. proposed experiments. B.L. prepared samples. N.M., B.L. and J.P. performed neutron scattering experiments. J.P. analysed neutron data and J.P., R.P. and B.L. wrote the manuscript, with input from all authors.

References

1. Benjamin, E. J.; et al., Heart Disease and Stroke Statistics—2017 Update: A Report From the American Heart Association. *Circulation* **2017**, *135*, e146-e603.

2. Krieger, M., The ''best'' of cholesterols, the ''worst'' of cholesterols: a tale of two receptors. *Proc Natl Acad Sci USA* **1998,** *95*, 4077-4080

3. Muller, K.; Laggner, P.; Glatter, O.; Kostner, G., The structure of human-plasma low-density lipoprotein B. An X-ray small-angle scattering study. *Eur J Biochem* **1978,** *82*, 73-90

4. Maric, S.; Lind, T. K.; Lyngso, J.; Cardenas, M.; Pedersen, J. S., Modeling Small-Angle X-ray Scattering Data for Low-Density Lipoproteins: Insights into the Fatty Core Packing and Phase Transition. *ACS Nano* **2017,** *11*, 1080-1090.

5. Orlova, E. V.; Sherman, M. B.; Chiu, W.; Mowri, H.; Smith, L. C.; Gotto, A. M., Three-dimensional structure of low density lipoproteins by electron cryomicroscopy. *Proc Natl Acad Sci U S A* **1999,** *96*, 8420-8425.

6. Liu, Y. H.; Atkinson, D., Immuno-electron cryo-microscopy imaging reveals a looped topology of apoB at the surface of human LDL. *Journal of Lipid Research* **2011,** *52*, 1111-1116.

7. Kumar, V.; et al., Three-Dimensional cryoEM Reconstruction of Native LDL Particles to 16 angstrom Resolution at Physiological Body Temperature. *PLoS One* **2011,** *6*, e18841.

8. Golub, M.; Lehofer, B.; Martinez, N.; Ollivier, J.; Kohlbrecher, J.; Prassl, R.; Peters, J., High hydrostatic pressure specifically affects molecular dynamics and shape of low-density lipoprotein particles. *Sci. Rep.* **2017,** *7*, 46034.

9. Deckelbaum, R. J.; Shipley, G. G.; Small, D. M.; Lees, R. S.; George, P. K., Thermal transitions in human plasma low density lipoproteins. *Science* **1975,** *190,* 392-394.

10. Pregetter, M.; Prassl, R.; Schuster, B.; Kriechbaum, M.; Nigon, F.; Chapman, J.; Laggner, P., Microphase separation in low density lipoproteins - Evidence for a fluid triglyceride core below the lipid melting transition. *J. Biol. Chem.* **1999,** *274* (3), 1334-1341.

11. Doster, W.; Cusack, S.; Petry, W., Dynamical transition of myoglobin revealed by inelastic neutron scattering. *Nature* **1989,** *337* (6209), 754-6.

12. Mikl, C.; Peters, J.; Trapp, M.; Kornmueller, K.; Schneider, W. J.; Prassl, R., Softness of Atherogenic Lipoproteins: A Comparison of Very Low Density Lipoprotein (VLDL) and Low Density Lipoprotein (LDL) Using Elastic Incoherent Neutron Scattering (EINS). *Journal of the American Chemical Society* **2011,** *133* (34), 13213-13215.

13. Kauzmann, W., Protein Stabilization - Thermodynamics of Unfolding. *Nature* **1987,** *325* (6107), 763-764.

14. Le Chatelier, H. L., Sur un énoncé général des lois d'équilibres chimiques. *C.R. Acad. Sci.* **1884,** *99*, 786 - 789.

15. Prassl, R.; Pregetter, M.; Amenitsch, H.; Kriechbaum, M.; Schwarzenbacher, R.; Chapman, J. M.; Laggner, P., Low density lipoproteins as circulating fast temperature sensors. *PLoS ONE* **2008,** *3* (12), e4079.

16. Schuster, B.; Prassl, R.; Nigon, F.; Chapman, M. J.; Laggner, P., Core lipid structure is a major determinant of the oxidative resistance of low density lipoprotein. *Proc. Natl. Acad. Sci. USA* **1995,** *92* (7), 2509-2513.

17. Krężel, A.; Bal, W., A formula for correlating pKa values determined in D2O and H2O. *J. Inorg. Biochem.* **2004,** *98* (1), 161-166.

18. Prassl, R.; Schuster, B.; Laggner, P.; Flamant, C.; Nigon, F.; Chapman, M. J., Thermal stability of apolipoprotein B100 in low-density lipoprotein is disrupted at early stages of oxidation while neutral lipid core organization is conserved. *Biochemistry* **1998,** *37* (3), 938-944.

19. Natali, F.; Peters, J.; Russo, D.; Barbieri, S.; Chiapponi, C.; Cupane, A.; Deriu, A.; Di Bari, M. T.; Farhi, E.; Gerelli, Y.; Mariani, P.; Paciaroni, A.; Rivasseau, C.; Schirò, G.; Sonvico, F., IN13 Backscattering Spectrometer at ILL: Looking for Motions in Biological Macromolecules and Organisms. *Neutron News* **2008,** *19* (4), 14-18.

20. Rahman, A.; Singwi, K. S.; Sjolander, A., Theory of Slow Neutron Scattering by Liquids .1. *Physical Review* **1962,** *126* (3), 986-996.

21. Réat, V.; Zaccai, G.; Ferrand, C.; Pfister, C. in *Biological Macromolecular Dynamics, Proceedings of a Workshop on Inelastic and Quasielastic Neutron Scattering in Biology, Institut Laue-Langevin, Grenoble France, 1996* (Book News, Inc., Portland, OR, 1999)

22. Sears, V. F., Neutron scattering lengths and cross sections. *Neutron News* **1992,** *3*, 26-37.

23. Peters, J.; Trapp, M.; Hughes, D.; Rowe, S.; Demé, B.; Laborier, J.-L.; Payre, C.; Gonzales, J.-P.; Baudoin, S.; Belkhier, N.; Lelievre-Berna, E., High hydrostatic pressure equipment for neutron scattering studies of samples in solutions. *High Pressure Research* **2011,** *32* (1), 97-102.

24. Paalman, H. H.; Pings, C. J., Numerical Evaluation of X-Ray Absorption Factors for Cylindrical Samples and Annular Sample Cells. *Journal of Applied Physics* **1962,** *33* (8), 2635-&.

25. Richard, D.; Ferrand, M.; Kearley, G. J., Analysis and visualisation of neutron-scattering data. *Journal of Neutron Research* **1996,** *4* (1), 33-39.

26. Peters, J.; Martinez, N.; Trovaslet, M.; Scannapieco, K.; Koza, M. M.; Masson, P.; Nachon, F., Dynamics of human acetylcholinesterase bound to non-covalent and covalent inhibitors shedding light on changes to the water network structure. *Phys Chem Chem Phys* **2016,** *18* (18), 12992-3001.

27. Peters, J.; Giudici-Orticoni, M. T.; Zaccai, G.; Guiral, M., Dynamics measured by neutron scattering correlates with the organization of bioenergetics complexes in natural membranes from hyperthermophile and mesophile bacteria. *European Physical Journal E* **2013,** *36* (7), 78.

28. Trapp, M.; Juranyi, F.; Tehei, M.; van Eijck, L.; Deme, B.; Gutberlet, T.; Peters, J., Elastic scattering studies of aligned DMPC multilayers on different hydrations. *Spectroscopy-an International Journal* **2010,** *24* (5), 461-466.

29. Zaccai, G.; Tehei, M.; Scherbakova, I.; Serdyuk, I.; Gerez, C.; Pfister, C., Incoherent elastic neutron scattering as a function of temperature: A fast way to characterise in-situ biological dynamics in complex solutions. *J. Phys. IV France* **2000,** *10*, Pr7-283 - 287.

30. Le Bellac, M., *Des phénomènes critiques aux champs de jauge*. InterEditions/Editions du CNRS: 1988.

31. Krisko, A.; Stjepanovic, G.; Pifat, G.; Ruysschaert, J. M.; Goormaghtigh, E., Detection of apolipoprotein B100 early conformational changes during oxidation. *Biochim. Biophys. Acta* **2007,** *1768* (11), 2923-30.

32. Esterbauer, H.; Gebicki, J.; Puhl, H.; Jurgens, G., The role of lipid peroxidation and antioxidants in oxidative modification of LDL. *Free Radic. Biol. Med.* **1992,** *13* (4), 341-90.

6. Results Part III

The third results chapter presents diverse aspects of structural changes of LDL under high hydrostatic pressure. Small-angle scattering techniques were applied to study various forms of LDL on a molecular basis. Through the application of various model-independent analyses it was possible to get a more detailed understanding of the structural processes happening in LDL under high pressure stress conditions.

High Hydrostatic Pressure Induces Lipid Phase Transition and Complex Molecular Rearrangement in Low-Density Lipoprotein Nanoparticles

B. Lehofer[1,*], M. Golub[2,3,*], K. Kornmueller[1], M. Kriechbaum[4], N. Martinez[2,3], H. Amenitsch[4], J. Peters[2,5] and R. Prassl[1,§]

[1] Institute of Biophysics, Medical University of Graz, Neue Stiftingtalstraße 6/IV, 8010 Graz, Austria
[2] Institut Laue-Langevin, 71 avenue des Martyrs, 38044 Grenoble, France
[3] Institut de Biologie Structurale IBS, Université Grenoble Alpes, 71 avenue des Martyrs, 38044 Grenoble, France
[4] Institute of Inorganic Chemistry, Graz University of Technology, Stremayrgasse 9, 8010 Graz, Austria
[5] Laboratoire Interdisciplinaire de Physique LiPhy, Université Grenoble Alpes, 140 Rue de la Physique, 38402 Saint-Martin-d'Hères, France

These authors contributed equally to this work.
[§] Corresponding author: Ruth Prassl, Institute of Biophysics, Medical University of Graz, Neue Stiftingtalstraße 6/IV, 8010 Graz, Austria, e-mail: ruth.prassl@medunigraz.at

Abstract

Low-density lipoprotein (LDL) is a physiological nanoparticle and a well-known key player in the progression of atherosclerosis, a process responsible for various cardiovascular diseases (CVD). These CVDs account for a vast majority of deaths in westernized civilizations. It is therefore of great interest to gain a detailed understanding of the LDL particle on a molecular basis and further facilitate treatment options or preventive measures. Various forms of LDL, namely normolipidemic, triglyceride-rich and oxidized forms were compared in this study. Through the application of small-angle scattering techniques combined with high hydrostatic pressure equipment it was possible to investigate these nanoparticles under various defined conditions. By means of independent pressure and temperature variations it was possible to detect a core lipid phase transition induced by pressure increase and an interrelated flattening of the particle shape. Moreover it was observed that only pressure values higher than 1200 bar seem to induce detectable structural rearrangements. Altogether the LDL nanoparticle maintains its structural integrity even under the highest investigated pressure condition and is able to adapt the structural arrangement of its components flexibly to external stress conditions.

Manuscript in preparation for: *Small*

Introduction

Human low-density lipoprotein (LDL) nanoparticles are complex biological assemblies consisting of an enormous variety of physiologically highly relevant molecules. Its main purpose is to provide sufficient cholesterol supply for various tissues throughout the human body.[1] The quasi-spherical LDL nanoparticles (~20 nm in diameter) are made up of a combination of various lipids and a large single amphipathic protein moiety, named apolipoprotein B-100 (apoB-100). LDL has a hydrophobic core and an amphiphilic shell. The core is basically built up of cholesteryl esters (CE), triglycerides (TG) as well as free cholesterol (FC). The shell consists of a phospholipid (PL) monolayer and the amphipathic apoB-100 embedded in the surface area. With this complex arrangement it is able to transport highly hydrophobic lipid molecules (CE and TG) in an aqueous environment like the blood circulation. Each LDL nanoparticle has a specific phase transition temperature (T_m) corresponding to the melting of the core lipids from a smectic liquid crystalline phase to a disordered fluid phase and strongly depending on the exact core lipid ratio.[2-3]

As a known key player in atherosclerosis and thereby a main cause for various cardiovascular diseases[4], LDL has been in the focus of medical research for almost sixty years.[5] Beyond that, the very complex arrangement of the particle's constituents has caught the interest of structural biologists and physicists.[6-17] Orlova et al.[10] showed the first low-resolution (27 Å) cryo-electron micrographs with structural details about the particle's inner organization. For the first time they revealed the LDL's three-layered structure of the neutral lipid core, which can be observed below the particle's T_m. These important features as well as many other structural details about LDL, like the approximate position of apoB-100 on the surface or the LDL-receptor (LDLR) binding site, have been repeatedly shown with cryo-electron microscopy by different working groups. [12-13, 15-16, 18-20] Besides this basic structural perspective, there has also been extensive research on the oxidative behavior of LDL [9, 17, 21-26] as well as on the influence of a triglyceride-rich lipid core on LDL particles of hypertriglyceridemic patients [12, 27-30]. Both aforementioned populations seem to have a major influence on the development of cardiovascular diseases and are therefore of great pathophysiological interest.

The use of high hydrostatic pressure (HHP) as a probing tool in biophysical research has become a state-of-the-art technique for various applications.[31] A large number of studies have been carried out on proteins, lipid phases, biomembranes and piezophilic prokaryotes

under HHP to investigate the effect of this thermodynamic parameter on the particular system.[32-37] Nowadays HHP equipment can be combined with an increasing number of biophysical techniques (e.g. small-angle X-ray scattering (SAXS), small-angle neutron scattering (SANS), nuclear magnetic resonance spectroscopy (NMR), Fourier-transform infrared spectroscopy (FTIR) or optical microscopy).[33, 38] These manifold options of structural methods made it possible to investigate the LDL particle under HHP and to gain a deeper understanding of structural changes and molecular mechanisms involved in HHP adaptation of LDL.

Based on the existing information about LDL structure and pressure effects on proteins and lipids, we carried out a systematic study of LDL with different molecular conditions (normolipidemic, TG-rich, oxidized) under HHP by applying SAXS and SANS techniques to elucidate structural changes.

Results and Discussion

High hydrostatic pressure SAXS measurements

SAXS data were measured for different forms of LDL including normolipidemic (N-LDL), triglyceride-rich (TG-LDL) and oxidized forms (Ox-LDL). The normolipidemic samples (N-LDL1, N-LDL2, and N-LDL3) and the triglyceride-rich sample (TG-LDL) were directly isolated from individual plasma donors in its native state. The Ox-LDL samples were prepared through *in vitro* oxidation of native samples (N-LDL1 and N-LDL2) with Cu^{2+} ions and subsequent inhibition of the oxidation at different stages of the oxidation process (for details see Materials & Methods). One minimally oxidized sample was produced, where the oxidation was stopped after 60 minutes (Ox-LDL1 prepared from N-LDL1) in the lag-phase of the oxidation process. For another sample the oxidation was stopped after 115 minutes (Ox-LDL2.1 prepared from N-LDL2) in the middle of the propagation phase. A third sample was prepared with the oxidation process stopped after 195 minutes (Ox-LDL2.2 prepared from N-LDL2) at the end of the propagation phase (see Figure 1).

The chemical composition of the applied samples can be taken from Table 1. Differential Scanning Calorimetry (DSC) curves were measured to get information about the lipid core phase transition temperatures (see Figure 2 and Figure 3). The according results of phase transition temperature (T_m), transition half width ($\Delta T_{1/2}$) and calorimetric transition enthalpy (ΔH_{cal}) are summarized in Table 2.

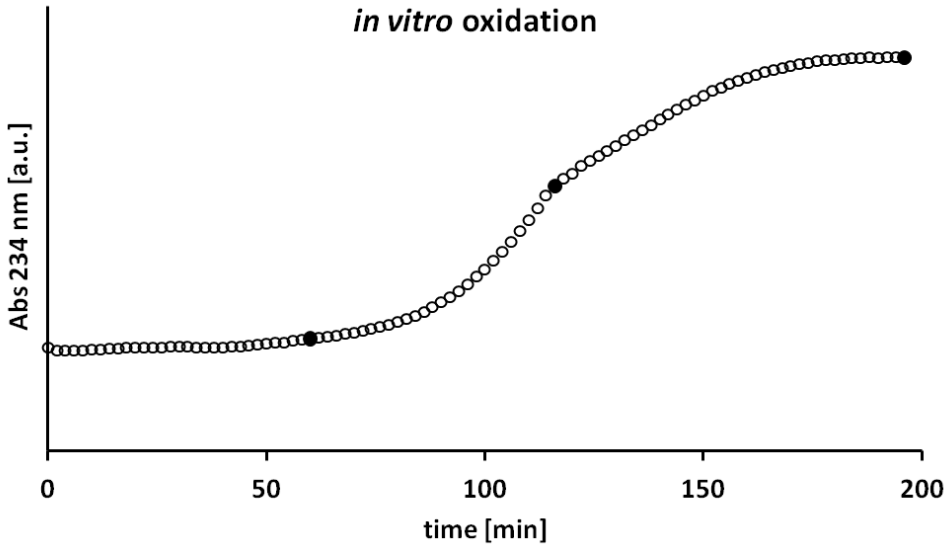

Figure 1: Spectrophotometric monitoring of the *in vitro* oxidation of N-LDL2 through the absorption of conjugated dienes at 234 nm. Data points measured during oxidation (open circles) and time points where the oxidation was stopped (full circles). One sample (Ox-LDL1) stopped after 60 min (indicated in this diagram for N-LDL2), another sample (Ox-LDL2.1) stopped after 115 min, and the third sample (Ox-LDL2.2) stopped after 195 min.

Table 1: Chemical compositions (wt%) of LDL samples used for SAXS measurements. Values are means ± SD of duplicate or triplicate determinations of each component. The CE/TG ratio is provided in the last column.

Sample	Protein	Phospholipids	Unesterified cholesterol	Cholesteryl esters	Triglycerides	CE/TG ratio
N-LDL1	19.2 ± 1.1	22.7 ± 0.3	8.6 ± 0.1	44.3 ± 2.1	5.2 ± 0.1	8.5
TG-LDL	18.2 ± 0.6	22.2 ± 0.3	7.8 ± 0.2	40.3 ± 0.3	11.5 ± 0.1	3.5
N-LDL2	21.3 ± 3.9	17.8 ± 1.0	9.8 ± 0.7	45.5 ± 1.5	5.7 ± 0.2	8.0
N-LDL3	20.6 ± 2.9	18.9 ± 1.7	11.1 ± 1.0	44.3 ± 0.7	5.1 ± 0.2	8.7

Table 2: Calorimetric data derived from DSC measurements of LDL samples used for SAXS measurements. Lipid core transition temperature (T_m), transition half width ($\Delta T_{1/2}$) and calorimetric transition enthalpy (ΔH_{cal}) were determined. Values are means ± SD of triplicate determinations.

Sample	T_m (°C)	$\Delta T_{1/2}$ (°C)	ΔH_{cal} [kJ/mol of CE]
N-LDL1	28.5 ± 0.2	6.5 ± 0.1	1.62 ± 0.08
Ox-LDL1	29.1 ± 0.1	7.1 ± 0.4	1.65 ± 0.12
TG-LDL	14.3 ± 0.3	8.9 ± 0.3	0.84 ± 0.09[1]
N-LDL2	26.3 ± 0.1	7.0 ± 0.2	1.86 ± 0.13
Ox-LDL2.1	27.4 ± 0.1	6.8 ± 0.2	1.43 ± 0.09
Ox-LDL2.2	27.5 ± 0.1	6.5 ± 0.1	1.91 ± 0.03
N-LDL3	29.0 ± 0.2	6.0 ± 0.3	2.02 ± 0.15

[1]note: The endothermic peak of the core lipid phase transition was not fully detected by the calorimetric diagram due to the early onset of the endothermic peak below the lowest measured temperature. Therefore the precise area under the curve might not have been fully detected and the value for the calorimetric enthalpy might be slightly underestimated.

As was already shown in previous studies[28] the CE/TG ratio directly correlates with the occurring transition temperature T_m of LDL. In the applied samples the CE/TG ratio was at 8.0 or higher for the normolipidemic samples and at 3.5 for the triglyceride-rich sample (see Table 1). This was directly reflected by the measured transition temperatures, which were at 28.5°C (N-LDL1), 26.3°C (N-LDL2) and 29.0°C (N-LDL3) for the normolipidemic samples and at 14.3°C for the triglyceride-rich sample (TG-LDL). The transition temperatures for the oxidized samples were slightly increased compared to their native counterparts, which has also been shown in previous studies[23].

The transition half width ($\Delta T_{1/2}$) was comparable for all normolipidemic and oxidized samples in a range from 6.0°C to 7.1°C. The TG-LDL sample had a slightly higher $\Delta T_{1/2}$ of 8.9°C, which is reflected by the broader phase transition peak (see Figure 2). The same is true for the calorimetric transition enthalpies (ΔH_{cal}), which were in a comparable range for all samples (1.43 – 2.02 kJ/mol of CE), except for TG-LDL. The value determined for the TG-LDL sample is significantly lower, which is probably due to the incomplete detection of the endothermic peak due to the early onset of the phase transition and less ordered core lipids (see note in Table 2).

The SAXS experiments were performed at different pressure and temperature points. HHP was altered from 50 bar (lowest pressure) to 3000 bar (highest pressure) at two temperatures, well below and above T_m for each sample (see Figures 4, 5 and 6).

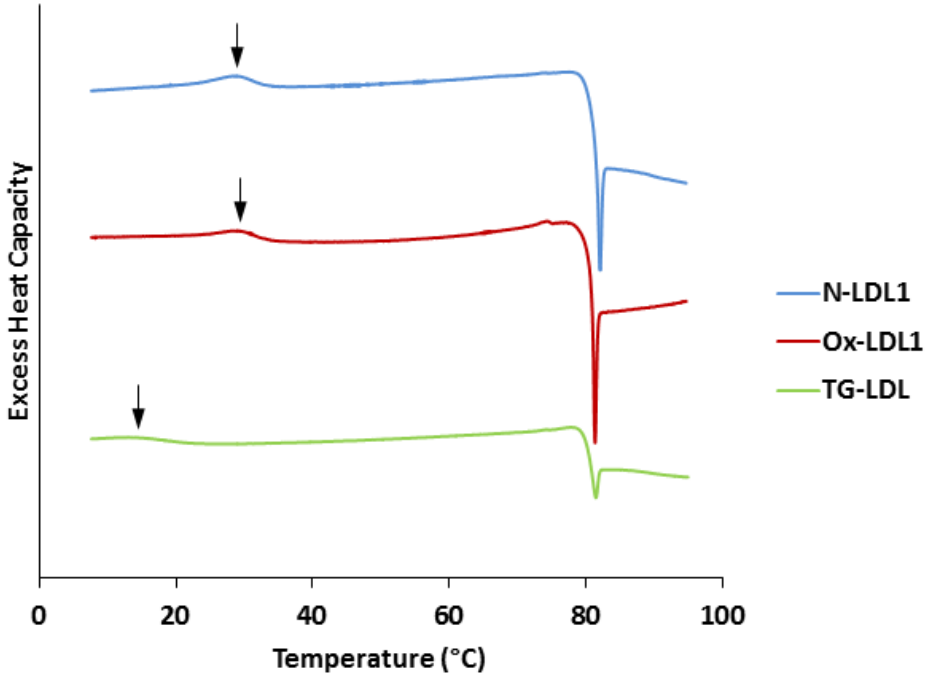

Figure 2: Buffer-subtracted and normalized DSC curves (shifted vertically for better visibility) measured for the LDL samples N-LDL1, Ox-LDL1 and TG-LDL used in SAXS experiments. The lipid core phase transition is marked with a black arrow.

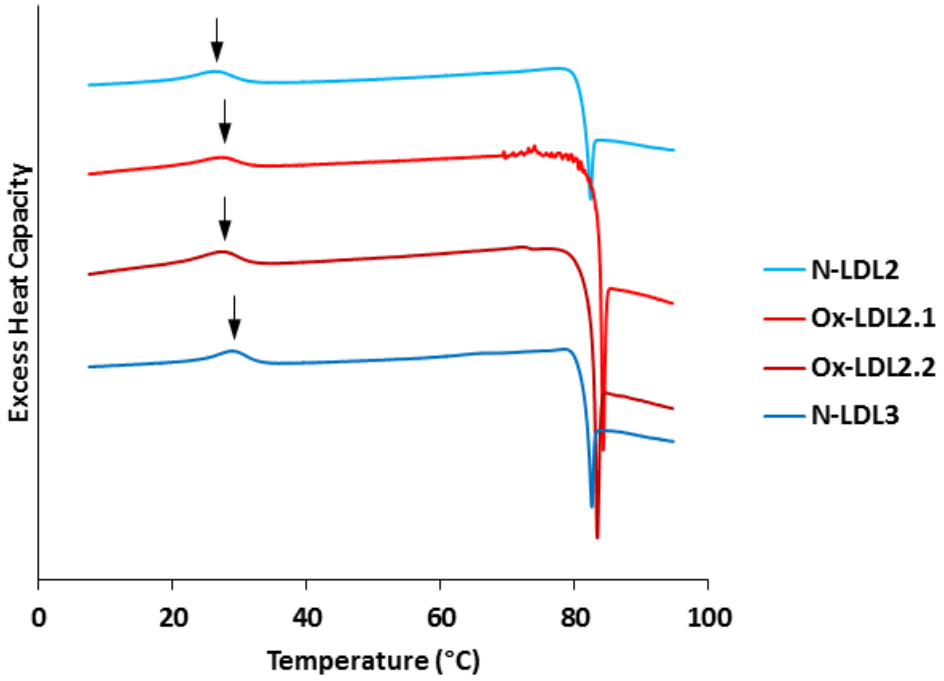

Figure 3: Buffer-subtracted and normalized DSC curves (shifted vertically for better visibility) measured for the LDL samples N-LDL2, Ox-LDL2.1, Ox-LDL2.2 and N-LDL3 used in SAXS experiments. The lipid core phase transition is marked with a black arrow.

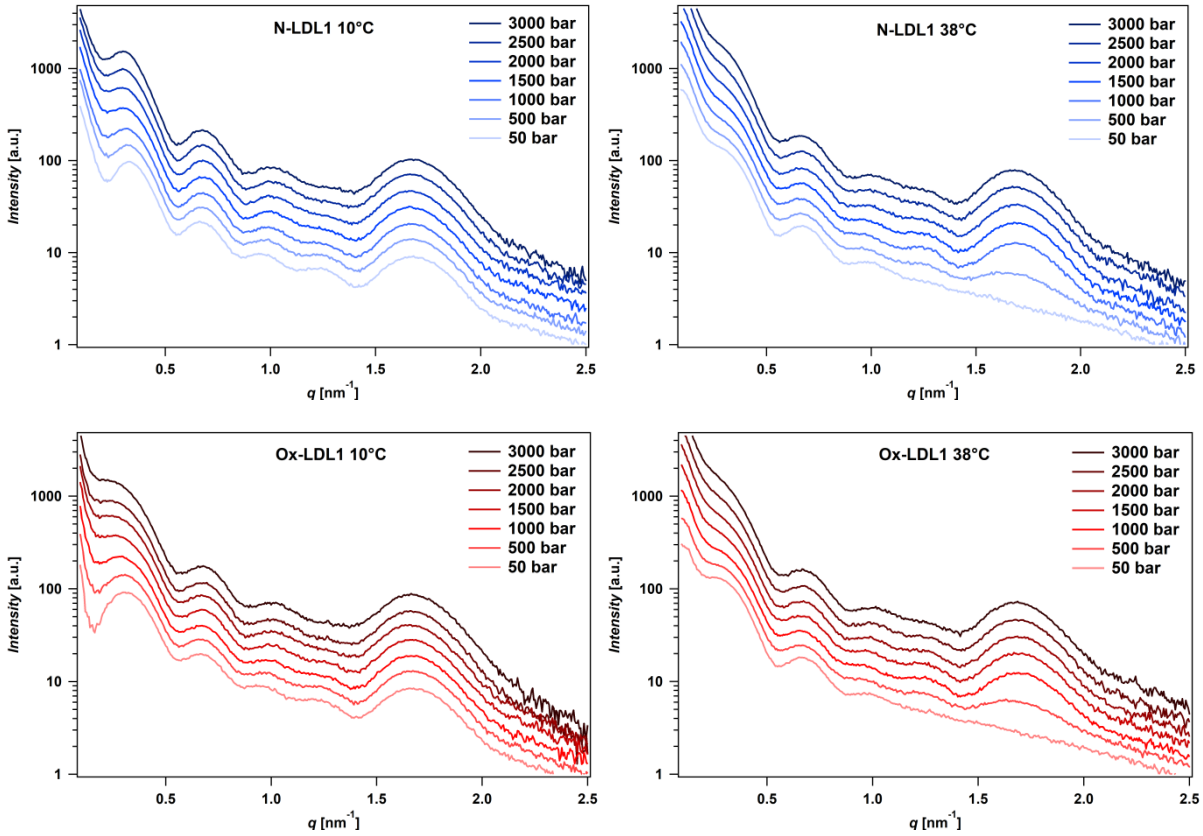

Figure 4: SAXS curves of N-LDL1 (first row) and Ox-LDL1 (second row) measured at increasing pressure points (50, 500, 1000, 1500, 2000, 2500, 3000 bar). The samples were measured below T_m (left column) and above T_m (right column). The curves at the varying pressure points are shown in a continuous order from the lowest pressure point (bottom curve) to the highest pressure point (top curve). The SAXS curves were shifted vertically for better visibility.

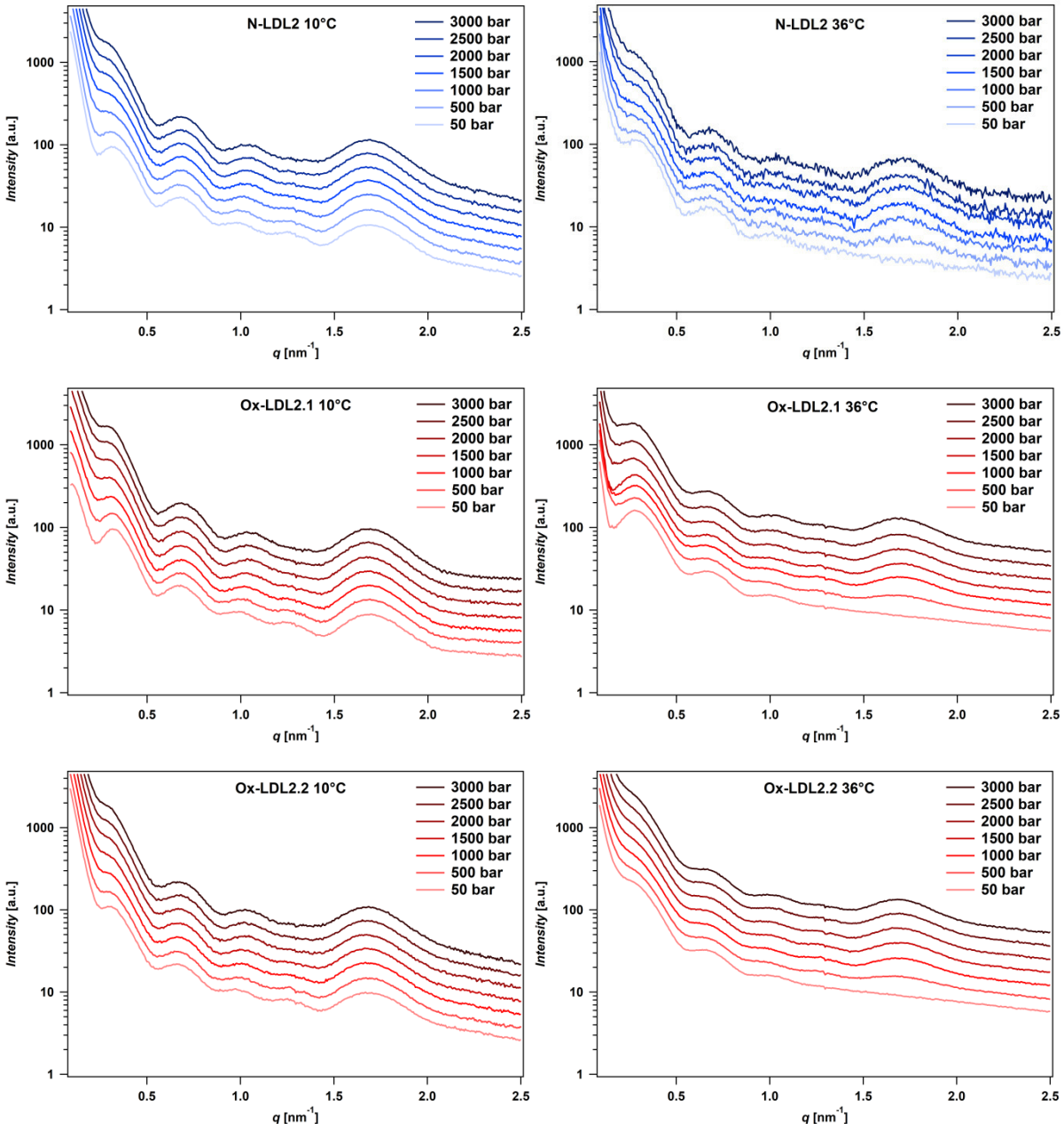

Figure 5: SAXS curves of N-LDL2 (first row), Ox-LDL2.1 (second row) and Ox-LDL2.2 (third row) measured at increasing pressure points (50, 500, 1000, 1500, 2000, 2500, 3000 bar). The samples were measured below T_m (left column) and above T_m (right column). The curves at the varying pressure points are shown in a continuous order from the lowest pressure point (bottom curve) to the highest pressure point (top curve). The SAXS curves were shifted vertically for better visibility.

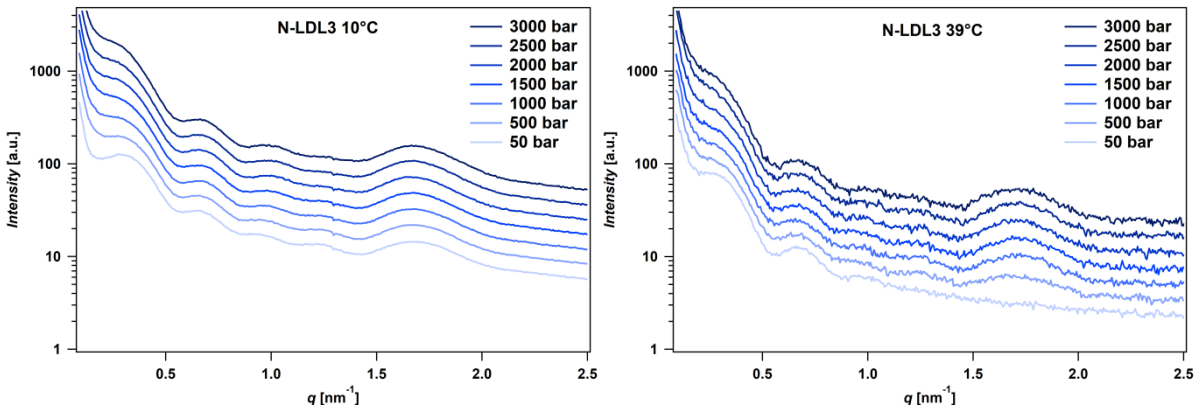

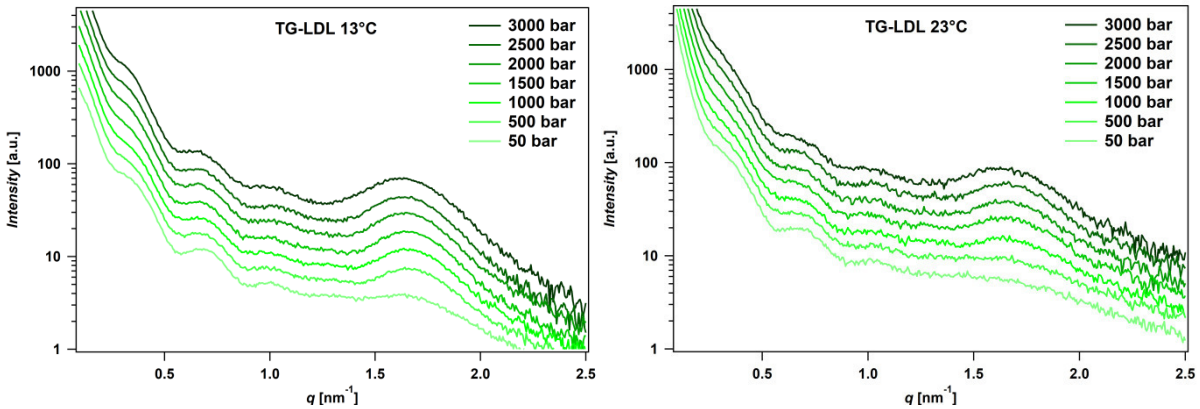

Figure 6: SAXS curves of N-LDL3 (first row) and TG-LDL (second row) measured at increasing pressure points (50, 500, 1000, 1500, 2000, 2500, 3000 bar). The samples were measured below T_m (left column) and above T_m (right column). The curves at the varying pressure points are shown in a continuous order from the lowest pressure point (bottom curve) to the highest pressure point (top curve). The SAXS curves were shifted vertically for better visibility.

One of the most significant effects, which can be directly observed in the small-angle scattering curves, is the emergence of a major peak at q = 1.7 nm^{-1} with increasing pressure for all samples above T_m. This peak correlates with the ordered cholesteryl esters in the lipid core of LDL. Below T_m the lipid core of LDL is organized in three layers of cholesteryl esters with a repeat distance of 3.7 nm. This repeat distance corresponds exactly to q = 1.7 nm^{-1} in reciprocal space. Above T_m the lipid core exists in a liquid disordered state. This is reflected by a missing peak at q = 1.7 nm^{-1}, which is also the case in the measured samples above T_m at the lowest pressure point. Interestingly, with increasing pressure the peak at q = 1.7 nm^{-1} grows and indicates a pressure-induced ordering of the lipid core above T_m.

All measured scattering curves below T_m already show the peak at q = 1.7 nm^{-1} at the lowest pressure point and are not further affected at 1.7 nm^{-1} by increasing pressure. This means that the ordered lipid core arrangement is already formed below T_m and is not influenced by HHP application. One interesting exception is the TG-LDL sample below T_m, where the peak at q = 1.7 nm^{-1} is present at the lowest pressure point (50 bar), but gets more pronounced with increasing pressure (see Figure 6). However, it has to be mentioned that the T_m of TG-LDL is at 14.3°C and so the measured temperature is not far below T_m and therefore the ordered lipid core might not be fully developed at this temperature and so pressure seems to induce a more pronounced ordering, similar to that expected for a further decrease in temperature.

It has already been shown[23] that the peak at q = 1.7 nm^{-1}, which is caused by the ordered lipids in the core of LDL, is a highly conserved feature even at the end of the propagation phase of Cu^{2+}-induced oxidation. This behavior could also be observed in our study, where

the transition peak is preserved after the end of the propagation phase below T_m (see Ox-LDL2.2 sample) and can also be induced by pressure increase in the same sample, when it is heated above T_m (see Figure 5). Other studies[17, 21] could even show that the ordered core lipid arrangement is still preserved after an oxidation time of 18 hours. This indicates that the core lipid phase transition from a disordered fluid phase above T_m to a layered structure below T_m is a highly conserved feature, which is present in native, oxidized and triglyceride-rich LDL particles.

Another feature directly extracted from the scattering curves is a significant flattening of the 1st side maximum with increasing pressure, which is observable for all measured samples at all temperatures (see Figures 4, 5 and 6). The peak maximum is shifted to lower q-values (e.g. from 0.32 nm^{-1} to 0.30 nm^{-1} for N-LDL1 at 10°C) for all measured samples. On the contrary the 2nd side maximum does not shift along the q-axis for none of the samples. The 3rd side maximum, however, shifts to higher q-values with increasing pressure (e.g. from 0.97 nm^{-1} to 1.02 nm^{-1} for N-LDL1 at 10°C). The precise q-values of the shifts slightly differ among the different samples.

Interestingly, the 4th side maximum is only present in the samples below T_m and only at the lower pressure points and disappears with increasing pressure in all samples below T_m. Above T_m the 4th side maximum is not present in the scattering curves at 50 bar. Surprisingly, the peak appears at 500 bar, with a maximum height at 1000 bar, before it disappears again with further increasing pressure. This effect can be best observed in the samples N-LDL1 and Ox-LDL1 at 38°C (see Figure 4).

Reversibility of high pressure effects on LDL samples

All LDL samples measured in SAXS high pressure experiments were examined both upwards and downwards the high pressure range (50 bar -> 3000 bar -> 50 bar) to verify the reversibility of the high pressure effects. It could be shown that all LDL samples possessed a fully reversible behavior concerning high pressure effects at the temperature range used for the pressure scans and the exposure time of approximately one minute per pressure point. The SAXS curves at the lowest pressure point (50 bar) almost perfectly superimposed before and after the high pressure scan up to 3000 bar (see Figure 7). For the pressure scans (Figure 4, 5 and 6) the temperatures were set to a fixed value either below T_m (10°C/13°C) or above T_m (23°C/36°C/38°C/39°C).

Additionally to these isothermal pressure scans (50 to 3000 bar), isobaric temperature scans were carried out (see Figure 8). The pressure was set to 2000 bar and the temperature was continuously increased from 10°C to 50°C (heating rate 1°C/min). The sample was held at 50°C for 10 minutes and cooled back to 10°C with a cooling rate of 1°C/min. In that way the effect of a longer high pressure exposure in combination with higher temperature could be checked.

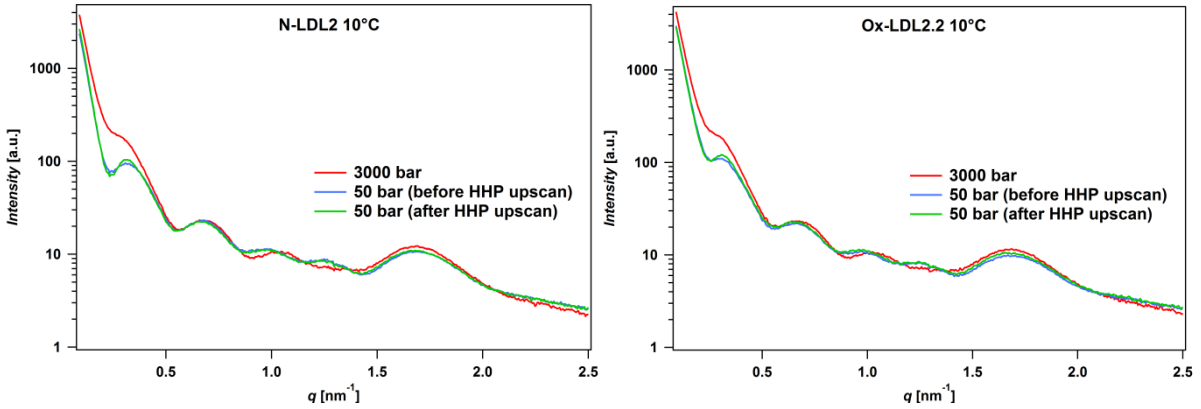

Figure 7: All investigated LDL samples showed a fully reversible behavior concerning the occurring high pressure effects in the isothermal pressure scans. Two samples are exemplarily illustrated in this figure, namely N-LDL2 at 10°C (left) and Ox-LDL2.2 at 10°C (right) to show the reversibility of the measurements. The other samples showed the same behavior.

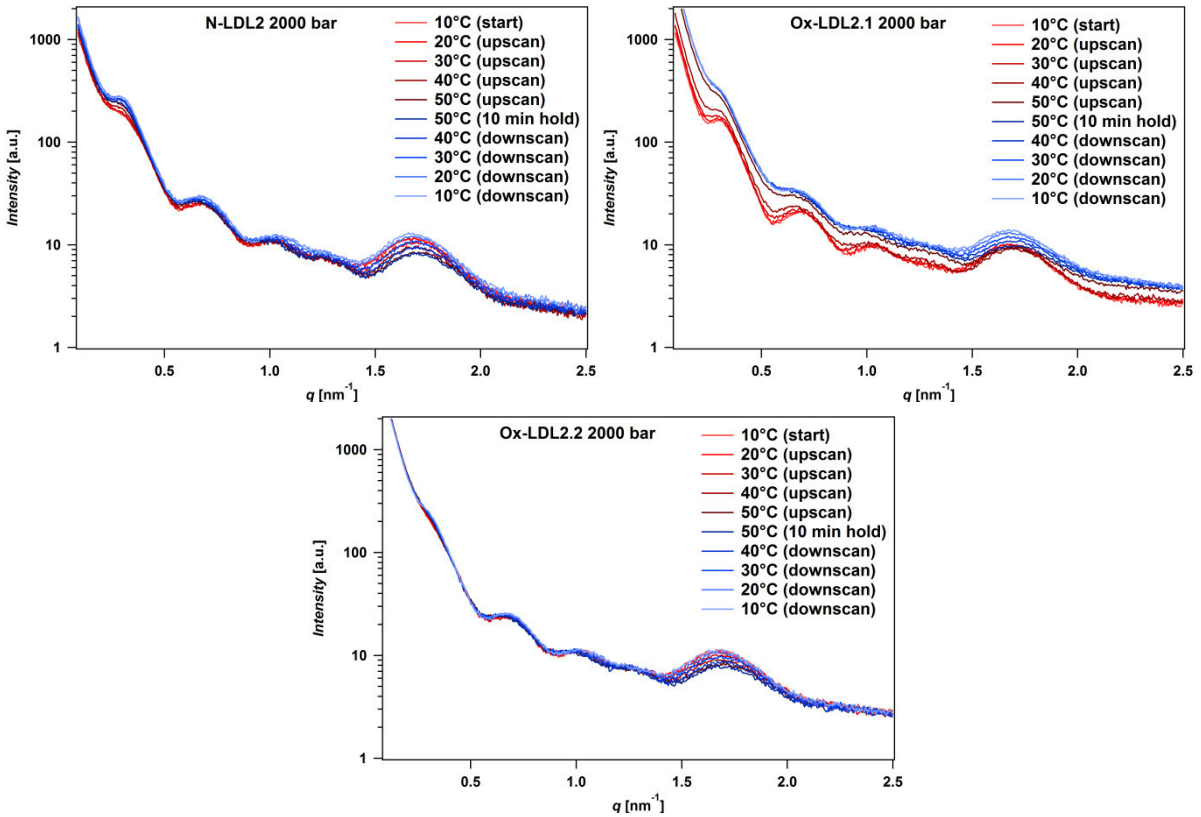

Figure 8: Isobaric temperature scans were measured for N-LDL2 (2000 bar), Ox-LDL2.1 (2000 bar) and Ox-LDL2.2 (2000 bar), where the isobaric condition is indicated in brackets. The temperature scans were performed from 10°C to 50°C with a heating rate of 1°C/min and a temperature hold time of 10 min at 50°C. After this hold time the temperature was decreased back to 10°C with a cooling rate of 1°C/min.

Unexpectedly, the measured samples showed a non-reversible behavior in the scattering curves of the isobaric temperature scans. The upscan and downscan measurements do not fully correspond to each other and show differences at the same temperature. Especially the N-LDL2 and Ox-LDL2.1 sample at 2000 bar clearly differ at the low temperature curves (see Figure 8). The isobaric temperature scans started at 10°C (light red) and ended at the same temperature (light blue), but show a different behavior. This indicates that HHP (2000 bar) in combination with a temperature of 50°C has an irreversible effect on LDL particles. This effect could be observed both in the scattering behavior of the LDL samples (Figure 8) and in the LDL sample condition before and after temperature scans at 2000 bar. The samples for this isobaric scans (N-LDL2, Ox-LDL2.1 and Ox-LDL2.2) were clear and without any precipitation before the scans, but showed a turbidity and precipitation after the scan. This is another clear indication that the applied experimental conditions (2000 bar and 50°C for 10 minutes) had an effect on the structural integrity and stability of the LDL samples.

Model-independent analyses of SAXS data

As a first model-independent analysis the radius of gyration (R_g) for each experimental condition was determined through the Guinier approximation in a q-range from 0.078 nm^{-1} to 0.169 nm^{-1}. The analyzed q-range was held constant for a whole pressure scan (50 to 3000 bar) of the same sample and the exact q-range for each set of samples can be taken from Table 3. The validity range of $q R_g < 1.3$, which is the limit for small globular proteins, can be extended for very large macromolecules and large R_g values, which is also the case for LDL (see Figure 9).

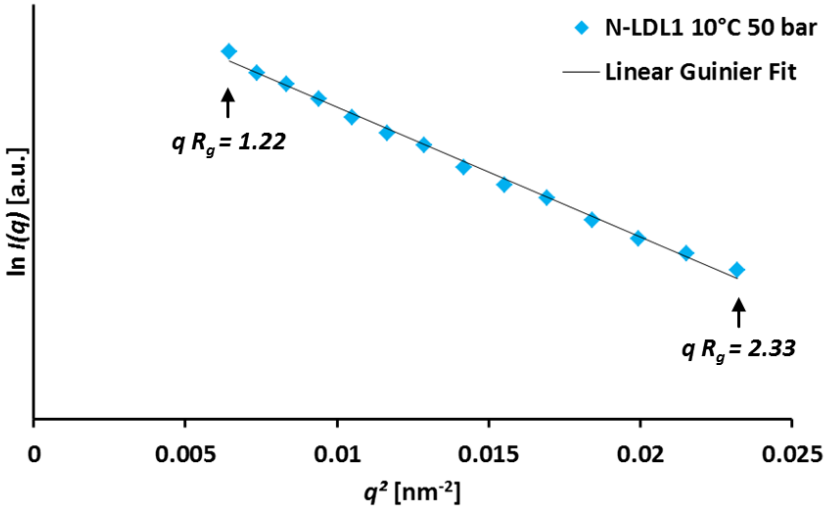

Figure 9: Exemplary depiction of a Guinier plot in the low-q region of N-LDL1 at 10°C and 50 bar with the according linear Guinier fit for the determination of R_g. The corresponding q R_g limits are shown in the diagram.

Table 3: List of the applied q-ranges for the Guinier fit analyses of the pressure scans (50 to 3000 bar).

LDL sample	q-range [nm^{-1}]
N-LDL1 10°C	0.080 - 0.152
N-LDL1 38°C	0.102 - 0.152
Ox-LDL1 10°C	0.080 - 0.136
Ox-LDL1 38°C	0.108 - 0.169
N-LDL2 10°C	0.078 - 0.150
N-LDL2 36°C	0.095 - 0.145
Ox-LDL2.1 10°C	0.100 - 0.161
Ox-LDL2.1 36°C	0.089 - 0.134
Ox-LDL2.2 10°C	0.095 - 0.145
Ox-LDL2.2 36°C	0.095 - 0.145
N-LDL3 10°C	0.095 - 0.134
N-LDL3 39°C	0.089 - 0.139
TG-LDL 13°C	0.086 - 0.152
TG-LDL 23°C	0.086 - 0.147

The obtained R_g-values were plotted as a function of pressure for each pressure scan to evaluate a possible influence of HHP on the R_g-value (see Figure 10). Surprisingly, no clear tendency for R_g could be found.

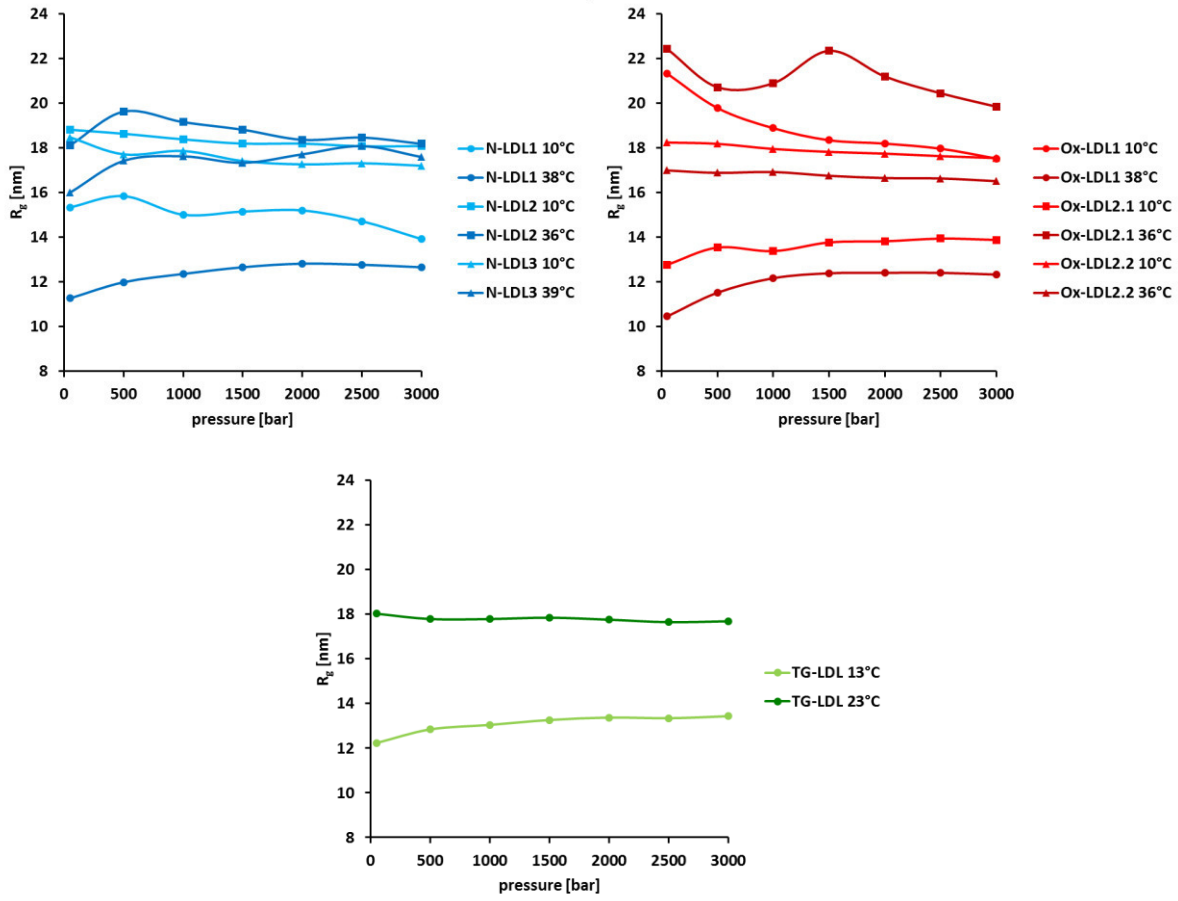

Figure 10: Radii of gyration derived from Guinier plots for all measured SAXS curves. N-LDL samples (blue), Ox-LDL samples (red) and TG-LDL sample (green) are shown for the two measured temperature points below T_m (light color) and above T_m (dark color) for all pressure points. Lines are guides to the eyes.

The R_g-values found in previous SAXS studies[6, 21, 39] were in the range of 12 nm to 18 nm and correlate well with the values found in this study. However, no clear pressure dependency could be extracted from the R_g-values (see Figure 10). The N-LDL samples below T_m showed a minor decrease of the R_g with increasing pressure, whereas the samples above T_m showed a slight increase of the R_g as a function of increasing pressure. For the Ox-LDL samples opposing effects for the R_g could be observed as a function of pressure. The R_g-values of the TG-LDL sample showed almost no change with increasing pressure. Therefore, pressure seems to have no clear effect on the R_g-values, which is a measure for the overall particle size. However, it has to be mentioned at this point, that the low q-region of the SAXS curves is highly sensitive to aggregation which in turn influences the slope of the curve in the low q-region. This slope is the basis for the Guinier fit (see Figure 9) and for the calculation of the Radius of gyration. An influence of aggregation on the slope of the measured SAXS curves in the low q-region cannot be excluded and might have affected the results for the R_g-values.

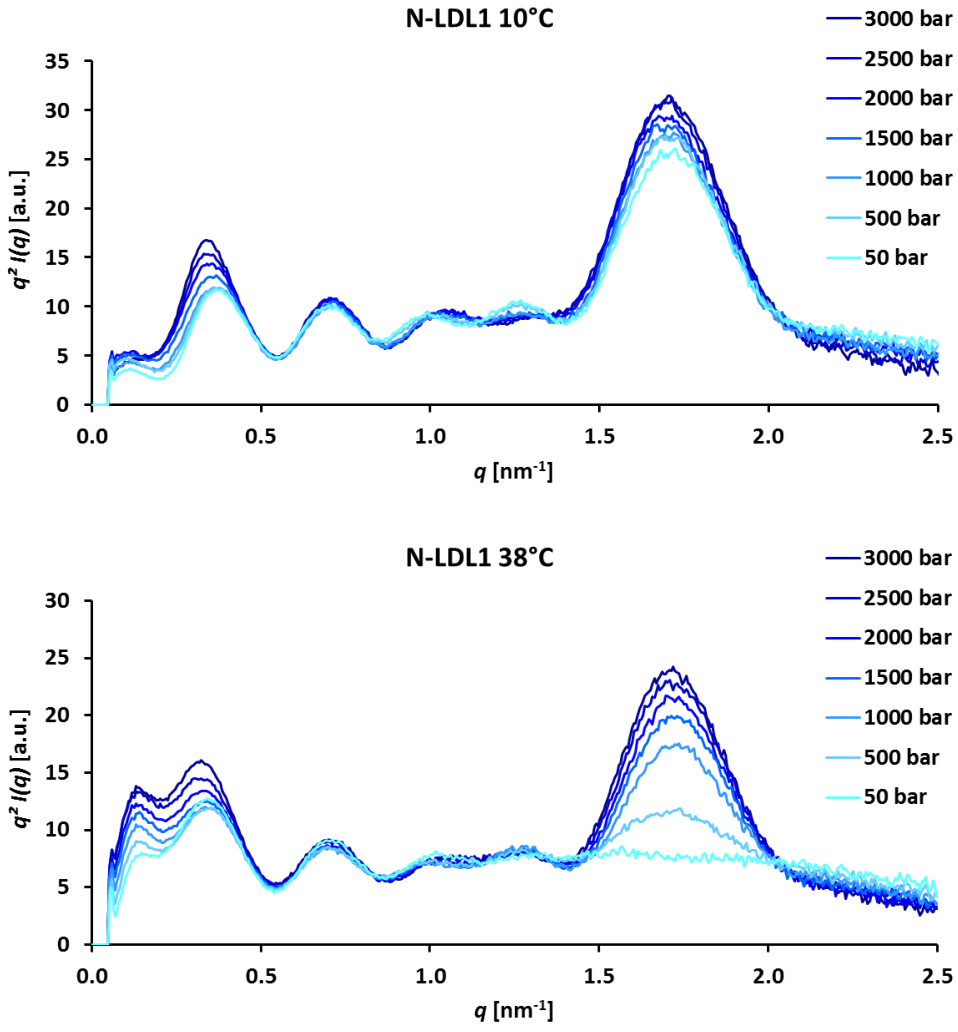

Figure 11: Exemplary Kratky plots are shown for N-LDL1 at 10°C (top) and 38°C (bottom) for all measured pressure points.

As a next step the Kratky plots were drawn for all measured SAXS samples as a function of pressure. Two exemplary Kratky plots are shown for N-LDL1 at 10°C and 38°C with all measured pressure points (see Figure 11). The Kratky plots for all other samples showed a comparable behavior. Based on these plots it can be stated that LDL has a globular-like overall shape according to the bell-shaped curves and keeps its folded integrity over the whole pressure range. A partially unfolded or completely unfolded sample would lead to an increase or a plateau in the higher q-region. Nevertheless, there are major changes in the core region of LDL (1.7 nm^{-1} ≙ 3.7 nm) and in the very low q-region (0.35 nm^{-1} ≙ 18.0 nm) with increasing pressure. The core region of LDL is strongly influenced by pressure at temperatures above T_m, whereas below T_m only a minor effect is observable. For the first side maximum a shift from 0.37 nm^{-1} at 50 bar to 0.33 nm^{-1} at 3000 bar can be observed for all samples. This corresponds to a modification in real space from 17.0 nm (50 bar) to 19.0 nm (3000 bar). Moreover the 4th side maximum (1.27 nm^{-1} ≙ 4.9 nm) disappears under increased pressure conditions for samples below the T_m. The samples above T_m do not show the 4th side maximum at the lowest pressure point (50 bar), but the peak is induced through increasing pressure with a maximum at 1000 bar, in accordance with the effects on the SAXS curves.

Another important model-independent analysis is the calculation of the pair distance distribution function *p(r)*. This function holds great importance for data analysis since it contains the entire real space information that can be directly obtained from an experimental scattering curve[6]. The Indirect Fourier Transformation (IFT) method was used to obtain the *p(r)* functions.

The *p(r)* functions were calculated with the program GIFT in the q-range 0.13-3.00 nm^{-1}. The D_{max} value was set to 26 nm for all calculations, as this was the best value for gaining optimum results for both the *p(r)* functions and the approximated curves. Other D_{max} values were also tested for the calculations (e.g. 24 nm, 25 nm, 27 nm, 28 nm) but did not lead to optimum results. The applied value of 26 nm for D_{max} is in a plausible range as was already shown by other studies[21, 40, 41].

An example for an approximated curve of a calculated *p(r)* function fitted to experimental scattering data (N-LDL1 at 10°C and 50 bar) is shown in Figure 12. The approximated curve perfectly fits the experimental data, except for the very low q-region where a small deviation is observable, most probably caused by a steeper slope of the experimental data due to the influence of a structure factor at high LDL concentrations.

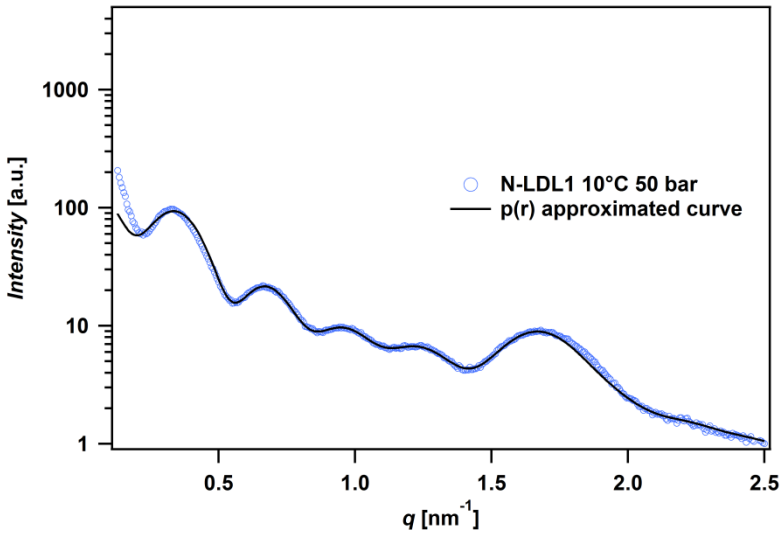

Figure 12: Exemplary depiction of the approximated curve of the calculated *p(r)* function for the sample N-LDL1 at 10°C and 50 bar.

The calculated *p(r)* functions of LDL show several characteristic features, which are exemplarily numbered from 1 to 6 in Figure 13. According to previous studies[21] the peaks 1, 2, and 3 represent the ordered cholesteryl ester lamellae in the lipid core, the negative peak 5 is caused by the hydrocarbon chains of the phospholipid monolayer and the peak with number 6 represents the protein and phospholipid headgroups at the surface. The applied numbering shown in Figure 13 will be also used in the following discussion.

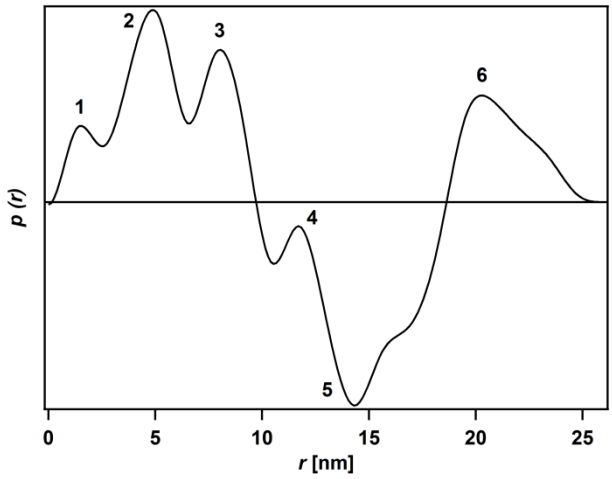

Figure 13: Characteristic features of the calculated *p(r)* functions are shown using the example of N-LDL1 at 10°C and 3000 bar. The characteristic peaks are numbered from 1 – 6 and are used for the discussion.

The *p(r)* functions for all samples below and above T_m and for all investigated pressure points are shown in Figures 14, 15, and 16. The normolipidemic (N-LDL), oxidized (Ox-LDL) and triglyceride-rich (TG-LDL) samples are clustered in the Figures 14, 15 and 16 to pronounce special features of each of the sample groups. In general, the *p(r)* functions reveal similar features for all samples as already depicted in Figure 13.

According to the peak positions and the corresponding distances between the peaks it can be stated that peaks 1 to 4 correlate with the CE lamellae in the lipid core of LDL. The peak positions for peaks 1 to 4 are very similar for all shown *p(r)* functions. The position of peak 1 is at 1.6 ± 0.1 nm, for peak 2 at 5.0 ± 0.1 nm, for peak 3 at 8.1 ± 0.1 nm and for peak 4 at 11.6 ± 0.1 nm. This makes clear that these four peaks represent the LDL core distances in a radius range from 0 to 15 nm as also found in another study[21].

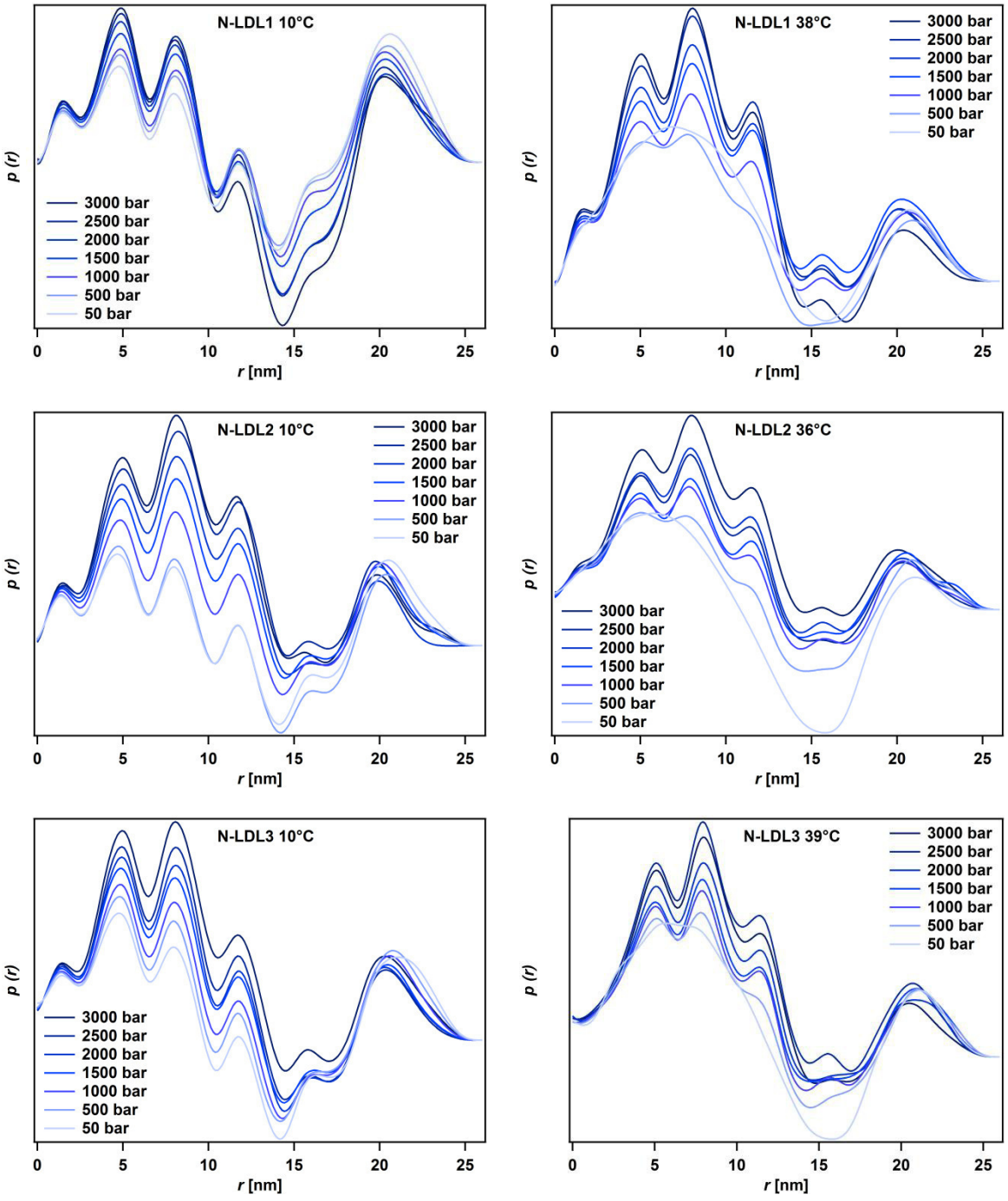

Figure 14: Calculated *p(r)* functions for the normolipidemic samples N-LDL1 (first row), N-LDL2 (second row) and N-LDL3 (third row) for all measured pressure points and at the two measured temperatures below T_m (left) and above T_m (right).

Another fact indicates that peaks 1 to 4 are correlated with the core structure of LDL. At a temperature below T_m, where the LDL core is the ordered state, the peaks 1 to 4 are already present at the lowest pressure point (see Figures 14, 15 and 16, left column). At a temperature above T_m these characteristic peaks are not present at the lowest pressure point, which correlates with a disordered LDL core without the characteristic lamellar ordering. Only one major peak in the radius range from 0 to 15 nm is visible above T_m (see Figures 14, 15 and 16, right column).

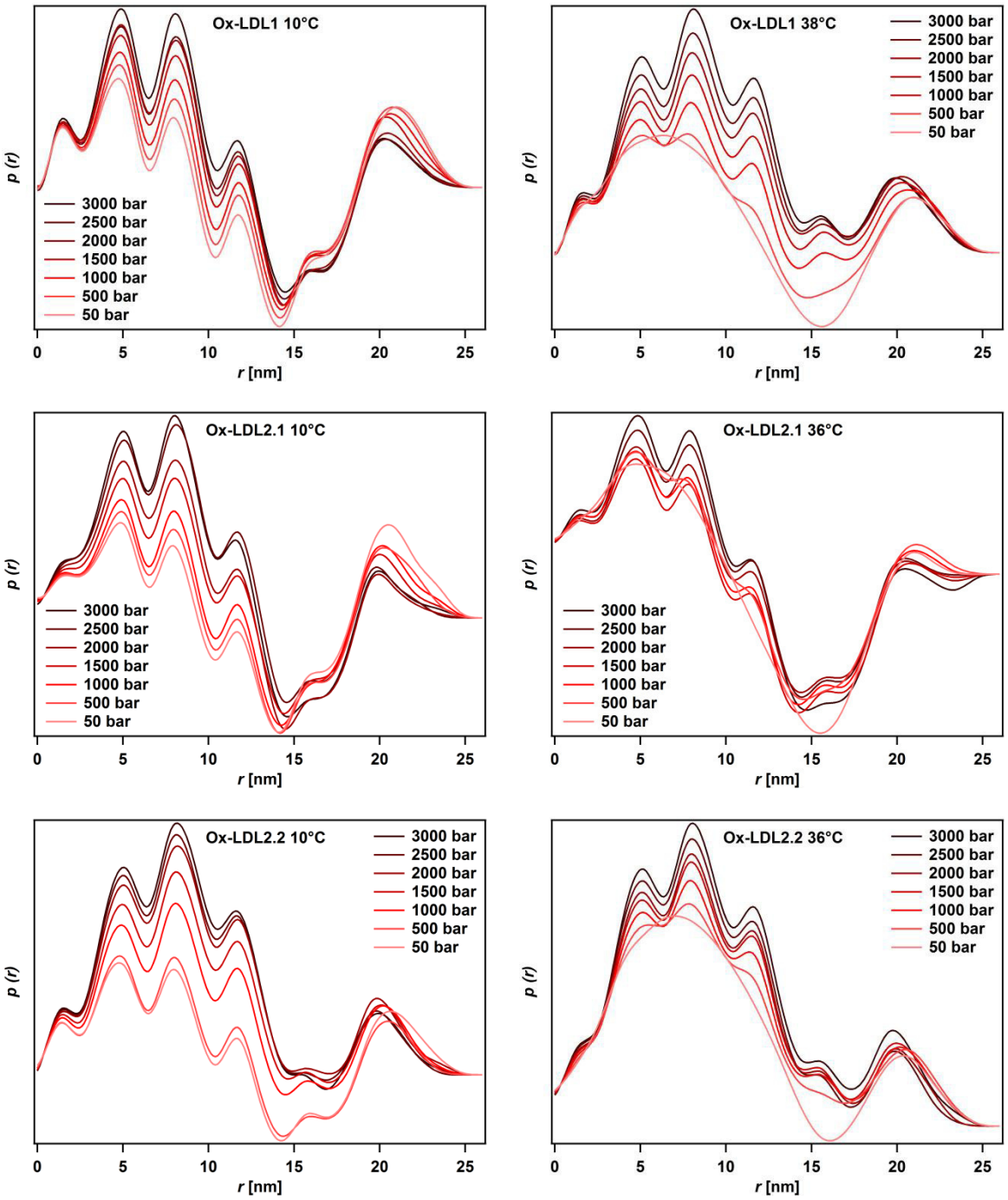

Figure 15: Calculated *p(r)* functions for the oxidized samples Ox-LDL1 (first row), Ox-LDL2.1 (second row) and Ox-LDL2.2 (third row) for all measured pressure points and at the two measured temperatures below T_m (left) and above T_m (right).

With increasing pressure, however, the peaks 1 to 4 are induced above T_m, correlating with the interpretation of the SAXS curves and the occurrence of the peak at 1.7 nm^{-1}.

Interestingly, peak number 1 is sometimes not or only slightly induced by increasing pressure above T_m (see Figure 14 and 15, right column), whereas peaks number 2 to 4 are much more intensively pronounced through pressure increase.

Another very important feature of the curves is the fact that the peak positions of the peaks number 1 to 4 are not shifted under pressure. The positions are identical for the whole pressure scan and for all investigated samples. This indicates that the position of the lamellae in the core, either naturally present through a low temperature or induced by HHP applied to LDL samples heated above T_m, is not altered through HHP application. The distances among these lamellae stay constant throughout the applied pressure range.

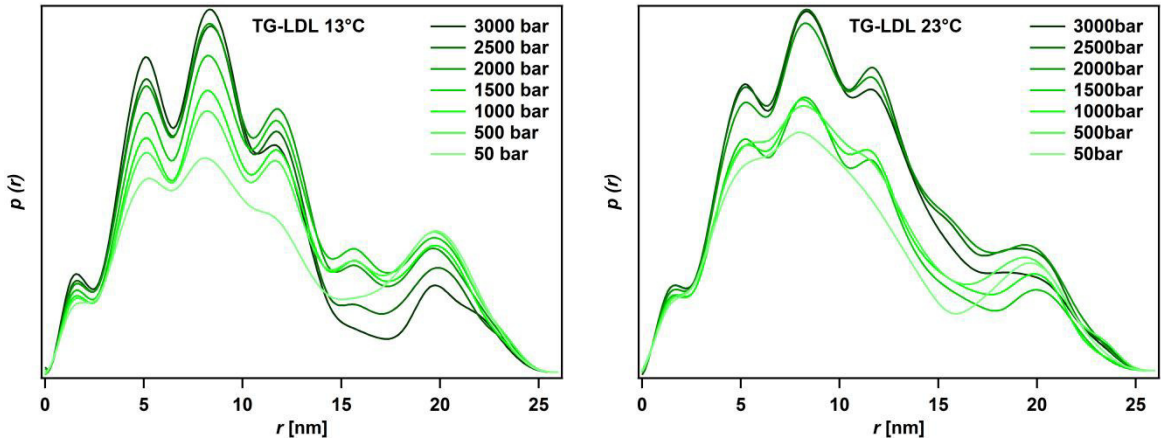

Figure 16: Calculated *p(r)* functions for the triglyceride-rich sample TG-LDL for all measured pressure points and at the two measured temperatures below T_m (left) and above T_m (right).

In contrast to peaks number 1 to 4, peak number 6 is clearly shifted towards lower r-values with increasing pressure. It is a continuous shift from the lowest pressure point (50 bar) to the highest pressure point (3000 bar) with a mean value of 0.7 ± 0.2 nm (N-LDL and Ox-LDL samples). The exact r-values taken from the *p(r)* functions for the lowest and highest pressure point are listed in Table 4. Interestingly, there is one exception for the shift to lower r-values, namely the TG-LDL sample. All normolipidemic and oxidized samples show a similar behavior concerning the shift of peak 6 to lower r-values, whereas the triglyceride-rich sample does not show this behavior (see Table 4). The shift of the maximum of peak 6 would indicate that the distance distribution for the longest distance around a length of 20 nm is shifted to shorter distances. This might be a sign of a structural rearrangement of the LDL particle or might indicate changes in the electron density profile of LDL in this region[17]. As the TG-LDL sample does not show this kind of peak shift under HHP, it could indicate a

different arrangement of the structural components in triglyceride-rich LDL particles. This could be the reason for a different structural rearrangement under HHP and could explain the difference in the peak shifts compared to the other investigated samples.

Table 4: Peak maxima of peak number 6 derived from the *p(r)* functions observed at the pressure scans from 50 to 3000 bar with the corresponding shift between the r-values.

Sample	Peak maximum at 50 bar [nm]	Peak maximum at 3000 bar [nm]	Shift of r [nm]
N-LDL1 10°C	20.7	20.3	0.4
N-LDL1 38°C	20.7	20.3	0.4
N-LDL2 10°C	20.6	19.8	0.8
N-LDL2 36°C	21.1	20.2	0.9
N-LDL3 10°C	21.1	20.4	0.7
N-LDL3 39°C	21.1	20.5	0.6
Ox-LDL1 10°C	21.1	20.3	0.8
Ox-LDL1 38°C	20.9	19.9	1.0
Ox-LDL2.1 10°C	20.5	19.9	0.6
Ox-LDL2.1 36°C	21.1	20.4	0.7
Ox-LDL2.2 10°C	20.7	19.9	0.8
Ox-LDL2.2 36°C	20.4	19.8	0.6
TG-LDL 13°C	19.8	19.8	0.0
TG-LDL 23°C	19.6	19.6	0.0

Another feature of the *p(r)* functions that differs for the TG-LDL compared to the other samples is the peak intensity of peaks 5 and 6. Those are much less pronounced in the *p(r)* function of TG-LDL than compared to all the other samples. Especially the negative peak 5 is significantly less pronounced for the TG-LDL sample. The negative peak 5 correlates with the less electron dense hydrocarbon chains of the phospholipid monolayer on the surface of LDL. As this negative region is less pronounced in the *p(r)* functions of TG-LDL, this could mean that more electron dense regions (e.g. PL headgroups, protein, CE headgroups) are intermixed with this region and raise the average electron density in this part of the particle. This theory would also support the difference in the shift of peak number 6 as discussed before. If the apoB-100 protein or the PL headgroups are intermixed more intensively with the lipid core region in TG-LDL, this could be an explanation why the electron dense region at around 20 nm (peak 6) does not further shift to smaller r-values under HHP.

High hydrostatic pressure SANS measurements

SANS data were measured for three different forms of LDL, namely a normolipidemic (N-LDL), a triglyceride-rich (TG-LDL) and a minimally oxidized (Ox-LDL) form. The Ox-LDL sample was prepared through the *in vitro* oxidation of a native sample with Cu^{2+} ions and subsequent inhibition of the oxidation after 30 min in the lag-phase of the oxidation process (for details see Materials & Methods). The chemical composition of the applied samples can be taken from Table 5. DSC curves were measured to get information about the lipid core phase transition temperature (see Figure 17). The according results of phase transition temperature (T_m), transition half width ($\Delta T_{1/2}$) and calorimetric transition enthalpy (ΔH_{cal}) are summarized in Table 6.

Table 5: Chemical compositions (wt%) of LDL samples used for SANS measurements. Values are means ± SD of duplicate or triplicate determinations of each component. The CE/TG ratio is provided in the last column.

Sample	Protein	Phospholipids	Unesterified cholesterol	Cholesteryl esters	Triglycerides	CE/TG ratio
N-LDL	19.7 ± 0.2	22.6 ± 1.1	7.4 ± 0.3	44.0 ± 0.5	6.4 ± 0.1	6.9
TG-LDL	19.2 ± 0.8	20.9 ± 2.0	5.9 ± 0.6	43.0 ± 1.2	11.0 ± 0.2	3.9
Ox-LDL	19.7 ± 1.9	22.9 ± 3.1	8.2 ± 0.7	44.2 ± 3.5	4.9 ± 0.1	9.0

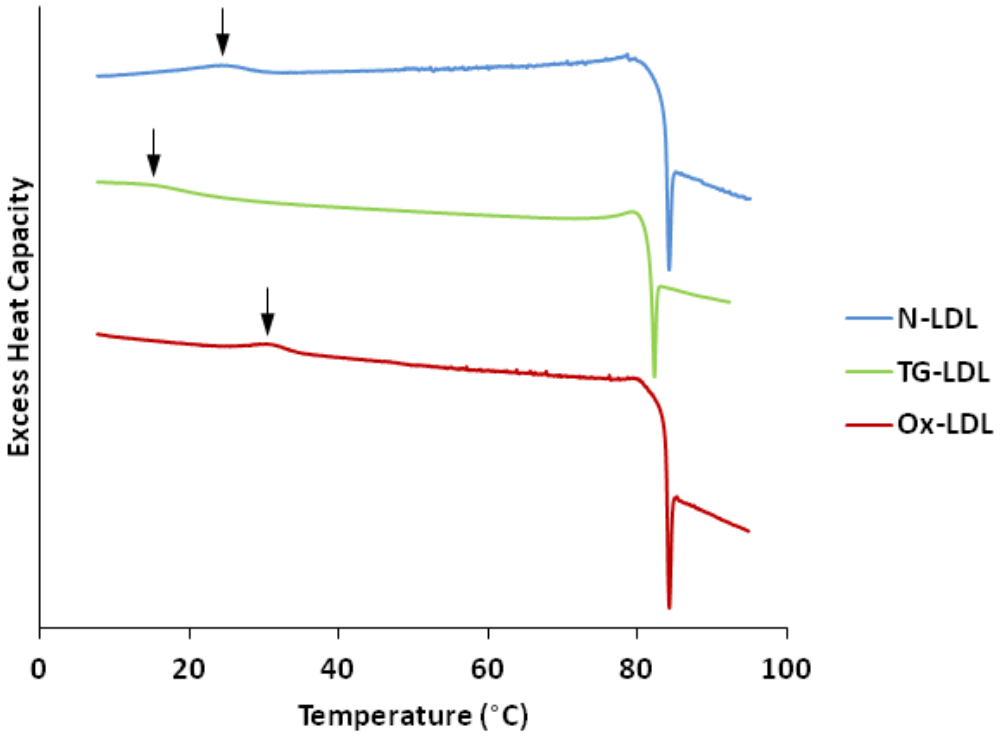

Figure 17: Buffer-subtracted and normalized DSC curves (shifted vertically for better visibility) measured for the LDL samples used in SANS experiments. The lipid core phase transition is marked with a black arrow.

Table 6: Calorimetric data derived from DSC measurements of LDL samples used for SANS measurements. Lipid core transition temperature (T_m), transition half width ($\Delta T_{1/2}$) and calorimetric transition enthalpy (ΔH_{cal}) were determined. Values are means ± SD of triplicate determinations.

Sample	T_m (°C)	$\Delta T_{1/2}$ (°C)	ΔH_{cal} [kJ/mol of CE]
N-LDL	24.1 ± 0.3	8.5 ± 0.5	1.59 ± 0.11
TG-LDL	15.3 ± 0.1	8.9 ± 0.3	0.95 ± 0.08
Ox-LDL	30.6 ± 0.2	5.7 ± 0.1	1.10 ± 0.11

SANS data were measured at several pressure points (20, 300, 600, 1200, 2000, 3000 bar) and at two different temperatures (10°C, 40°C) and are depicted in Figure 18. The temperatures were chosen in a way that one temperature point lies below the phase transition temperature (10°C), where the lipid core is in its smectic-like ordered phase and one temperature point is above the phase transition temperature (40°C), where the lipid core is in the disordered fluid phase. The SANS curves indicate that the higher the applied pressure was, the more significant was the influence on the shape of the curve (see Figure 18).

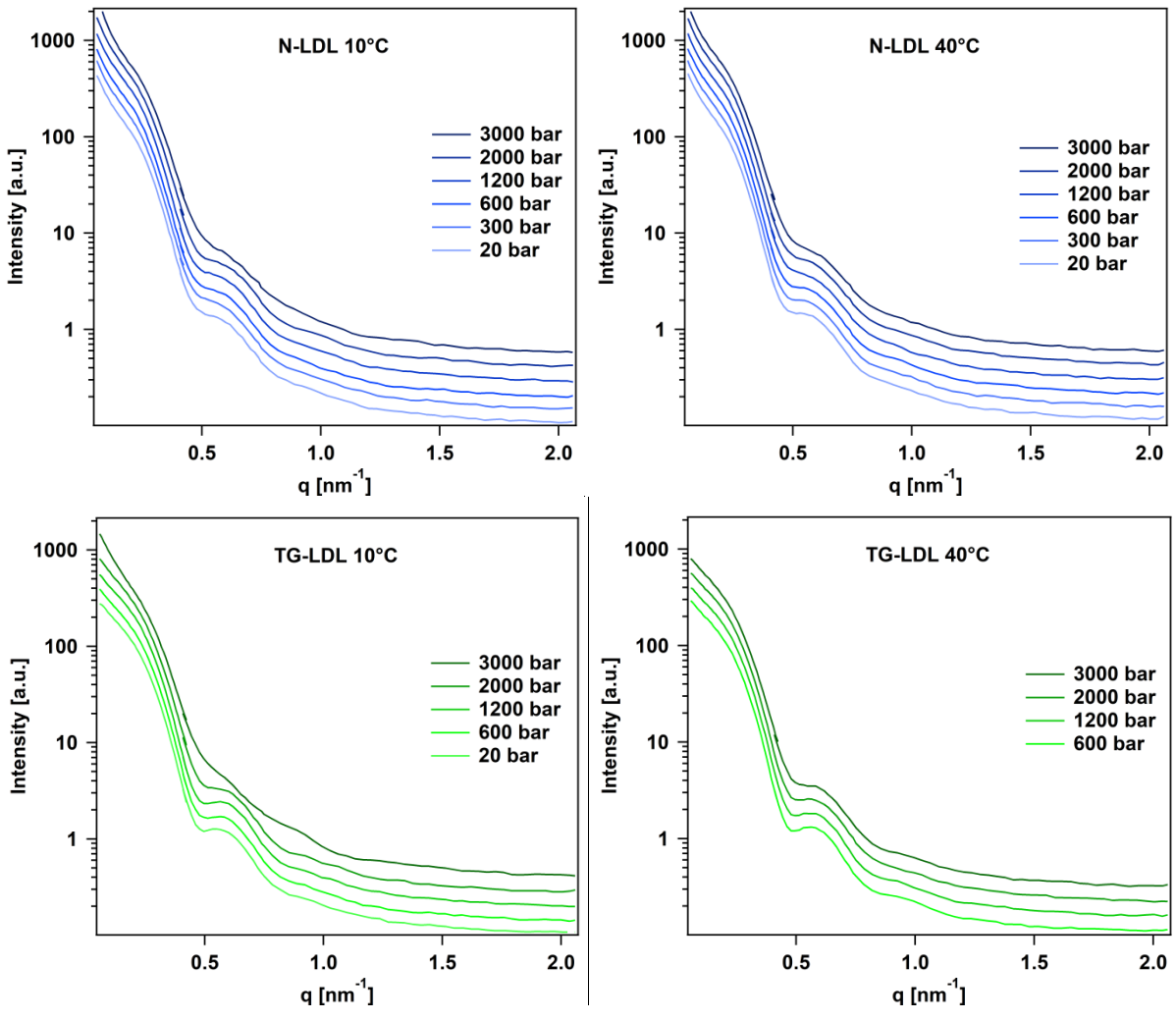

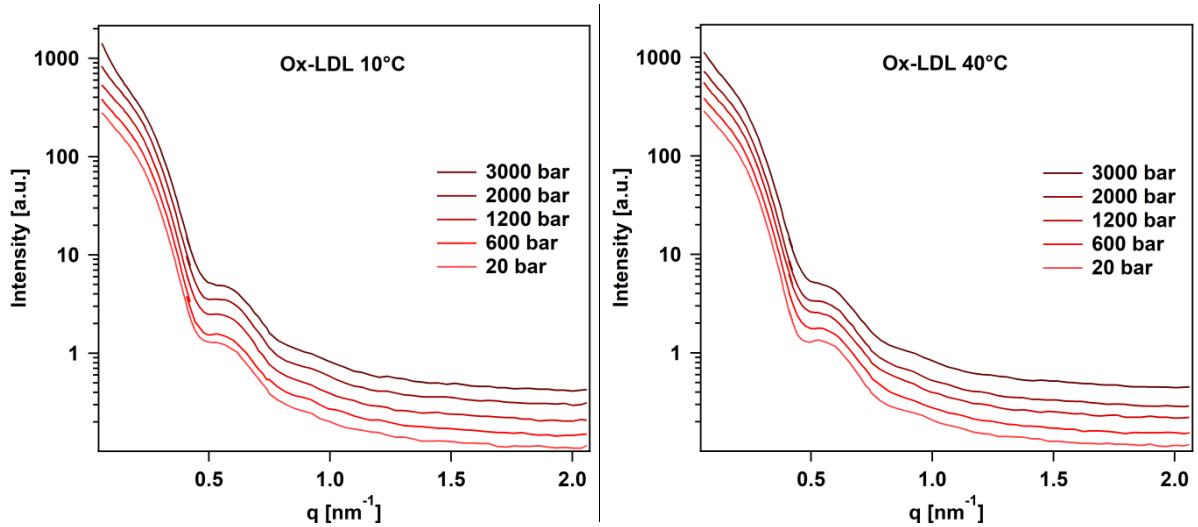

Figure 18: SANS curves measured for N-LDL (first row), TG-LDL (second row) and Ox-LDL (third row) at varying pressure and temperature points. The applied pressure points were 20, 300, 600, 1200, 2000 and 3000 bar (see legend for actual pressure points in each diagram), each at the two temperature points of 10°C (left) and 40°C (right). Curves at varying pressure points are shown in a continuous order from the lowest pressure point (bottom curve) to the highest pressure point (top curve). The curves are shifted vertically for better visibility. The discontinuous curve shape appearing at some positions is caused by the necessity of merging the measurements at three different sample-to-detector distances (1.5 m, 3.0 m and 6.0 m) to enable a broad q-range (0.06 – 2.06 nm^{-1}).

Model-independent analyses of SANS data

The radius of gyration (R_g) for each experimental condition was determined with the Guinier approximation in a q-range from 0.092 nm^{-1} to 0.197 nm^{-1}. The principle of q R_g < 1.3 can be extended for very large macromolecules and large R_g values, which is also the case for LDL. Therefore the q R_g range from 0.86 to 1.83 was used (see Figure 19).

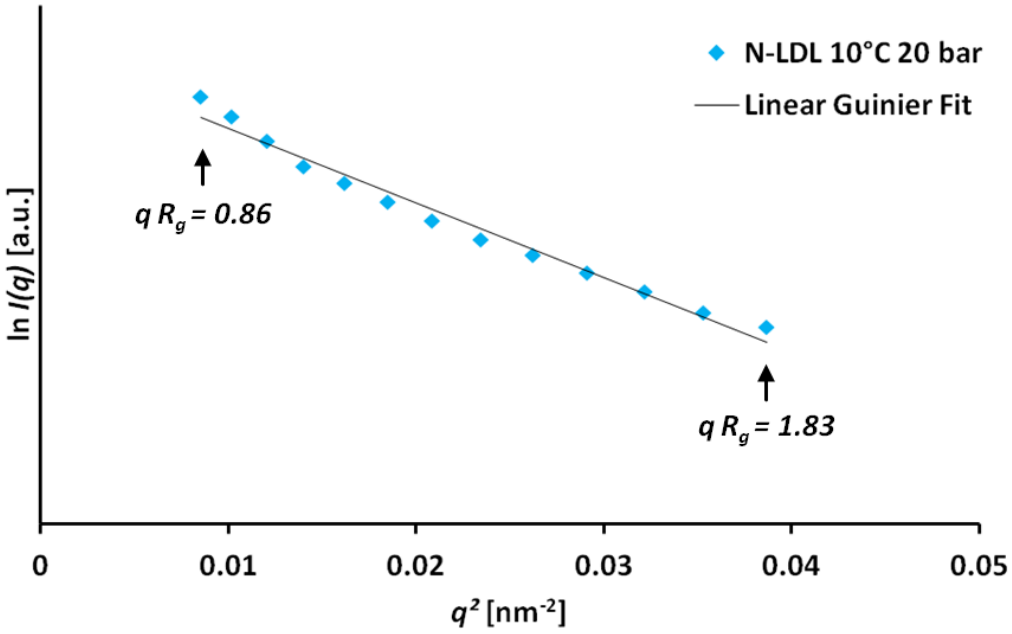

Figure 19: Exemplary depiction of a Guinier plot in the low-q region of N-LDL at 10°C and 20 bar with the according linear Guinier fit for the determination of R_g. The corresponding q R_g limits are shown in the diagram.

The radii of gyration as a function of pressure yield an interesting picture (see Figure 20). There is almost no change in the R_g values for the lower pressure points from 20 to 1200 bar for all investigated samples. However, there is a notable change for the pressure points at 2000 and 3000 bar. For all samples the R_g values increase above 1200 bar. More precisely, the samples measured below the transition temperature at 10°C show an even more prominent increase, especially for the pressure point at 3000 bar, than the samples measured above the phase transition at 40°C. As the radius of gyration can be seen as a measure of the distance between the center of mass of a particle to its termini, the increase of the R_g in these experiments can be interpreted as a deformation of the overall shape leading to the increase of the aforementioned distance. The strikingly higher increase of R_g values for the samples measured below T_m might be explained by a less flexible and more constrained particle at this temperature. Below T_m the LDL particle features a characteristic core lipid arrangement with a smectic-like three layered structure. Due to this arrangement the LDL particles show the characteristic shape of a flattened ellipsoid below T_m at ambient pressure. LDL particles above T_m, however, do not have this layered core organization and might therefore be much more flexible if needed. Consequently, the increase of pressure seems to have a more pronounced effect on the overall shape of the low temperature samples due to a more rigid particle organization and less adaptation possibilities.

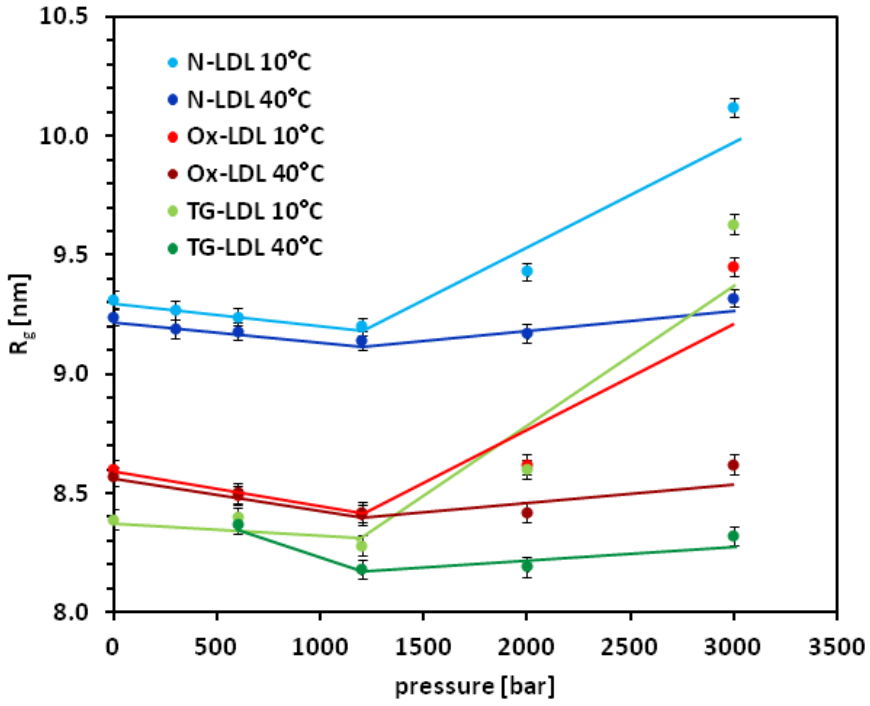

Figure 20: Radii of gyration derived from Guinier plots for all measured SANS curves. N-LDL (blue), TG-LDL (green) and Ox-LDL (red) are shown for the two measured temperature points 10°C (light color) and 40°C (dark color) for all pressure points. Lines are guides to the eyes.

Kratky plots were drawn to monitor the degree of compactness of the particles (see Figure 21). The bell-shaped curves of the Kratky plots indicate globular shaped particles. A plateau or increase in the high q-region, however, would indicate extended molecules or unfolded particles. In our experiments it can be clearly seen that a globular shaped particle is present over the whole range of experimental conditions. The structural integrity could be preserved for all samples even at the highest pressure point.

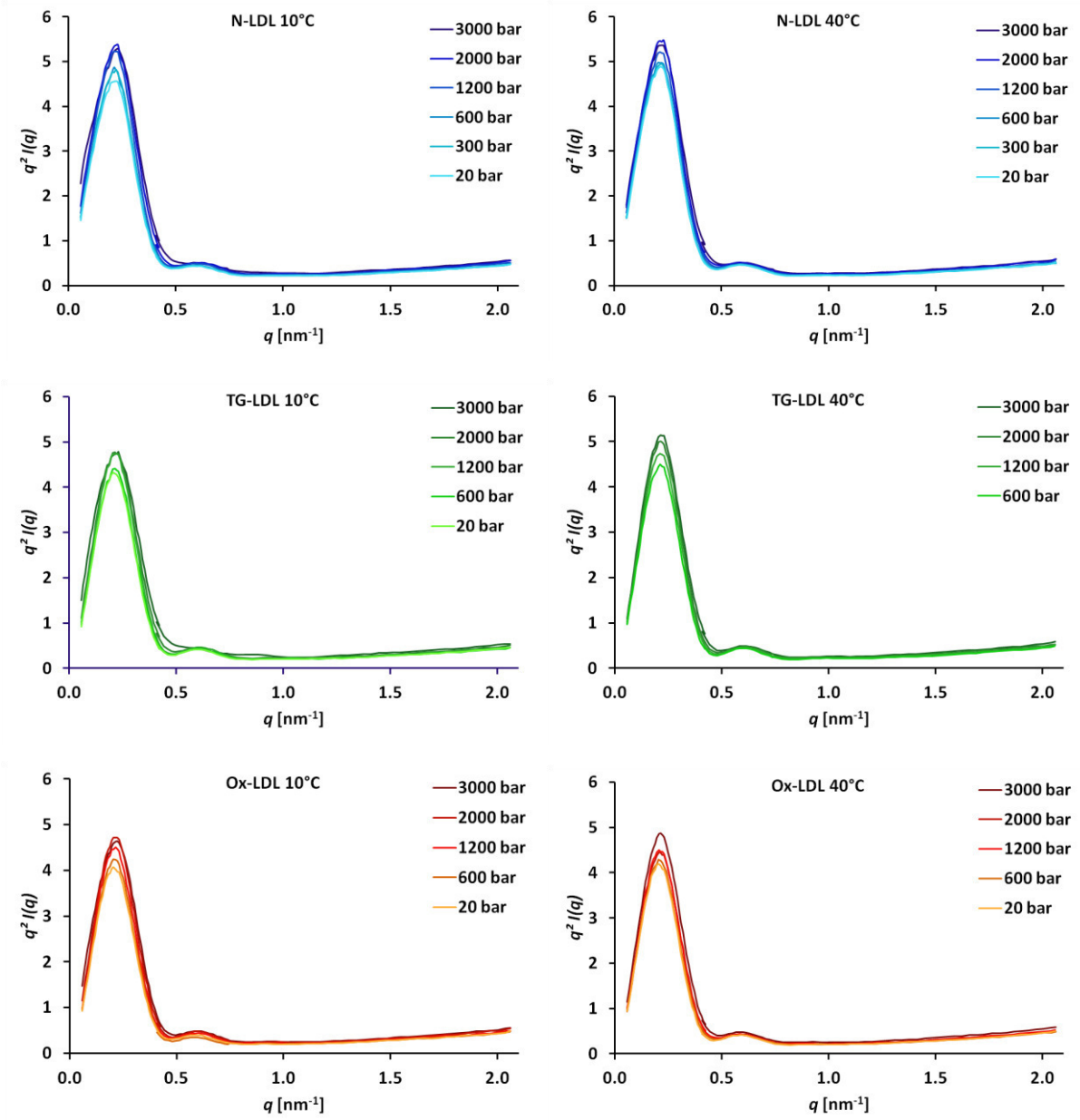

Figure 21: Kratky plots calculated for the measured SANS curves. N-LDL (blue), TG-LDL (green) and Ox-LDL (red) are shown for the two measured temperature points 10°C (left) and 40°C (right) for all pressure points.

As a next step, the pair distance distribution functions *p(r)* were drawn for all experimental conditions (see Figure 22). The *p(r)* functions describe the set of all paired-distances within a structure. Already very small changes in the relative positions of a few residues can lead to

detectable changes in the *p(r)* function. Globular macromolecules have a single peak *p(r)* function. The maximal length within the investigated structure (D_{max}) is the position where the *p(r)* function returns to zero at high values of *r*. In all measured samples D_{max} has a value of 24 nm according to the *p(r)* functions. No differences could be detected here and the maximal length within the particles seems to be stable within the investigated temperature and pressure range. The shapes of the *p(r)* functions, however, show differences with increasing pressure for all samples, which suggests that there is some kind of structural adaptation occurring during pressure increase. Again, the effects are more pronounced for the higher pressure points.

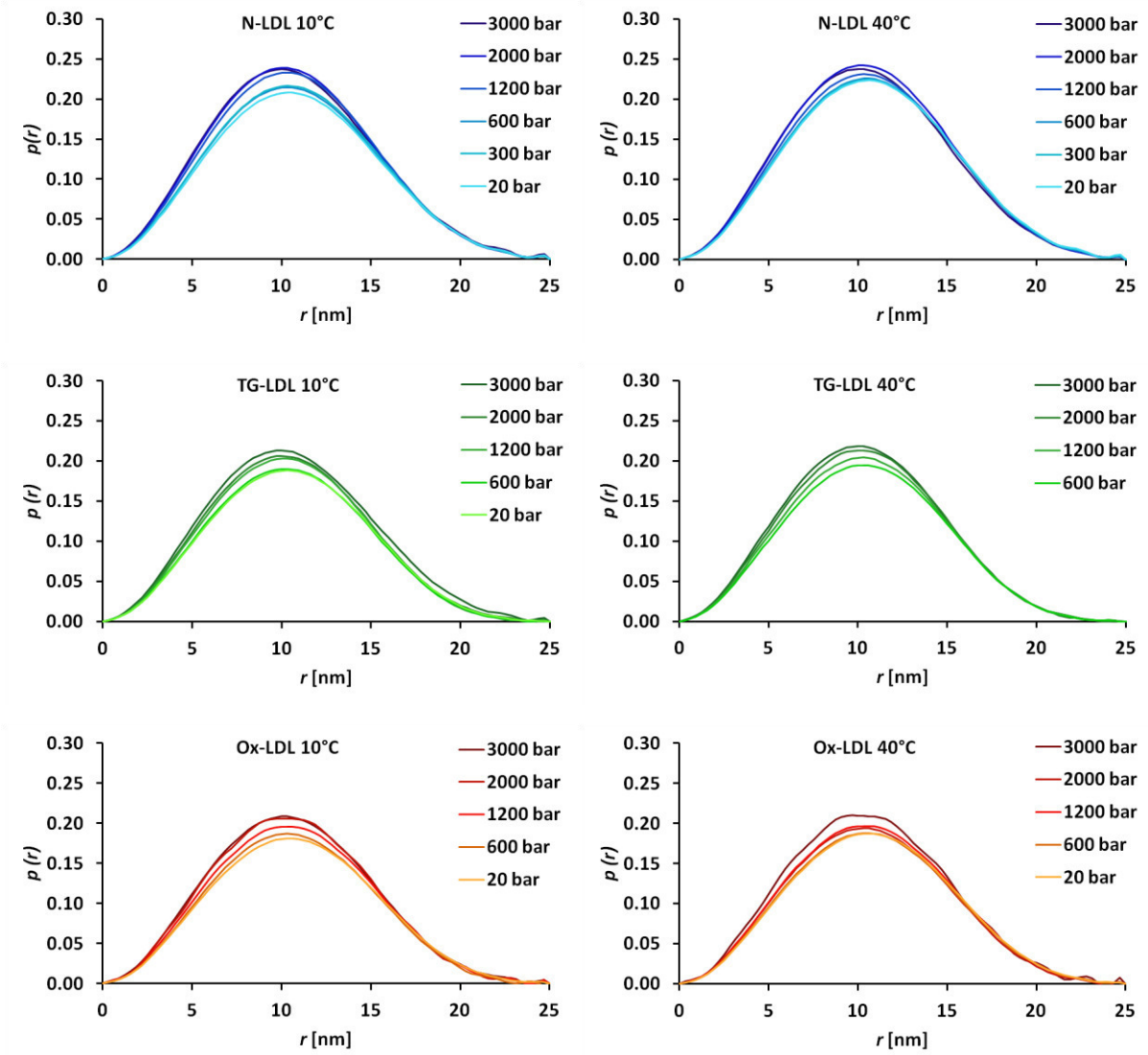

Figure 22: Pair distance distribution functions *p(r)* calculated for the measured SANS curves. N-LDL (blue), TG-LDL (green) and Ox-LDL (red) are shown for the two measured temperature points 10°C (left) and 40°C (right) for all pressure points.

Ab initio shape determination of LDL under HHP

Ab initio low resolution shapes of the measured small-angle neutron scattering data were calculated with the program DAMMIN[42]. A predefined search volume is filled with densely packed spheres (also referred to as dummy atoms) of defined radius to find a configuration which approximates the goal function (in this case a measured small-angle scattering curve) best. Simulated annealing is used to accomplish the global minimization of the target function (see Materials & Methods for details). The search volume was predefined as a sphere with 240 Å diameter, according to the results obtained from the *p(r)* functions. This search volume was filled with densely packed dummy atoms of 10 Å packing radius.[42] The fitting procedure was carried out for the N-LDL, TG-LDL and Ox-LDL sample at the two measured temperature points (10°C and 40°C) and at the two extreme pressure points of 20 bar and 3000 bar. For each sample 10 independent runs of DAMMIN were carried out. This is necessary to produce a variety of possible structures, as the final DAMMIN structure may vary for each independent fitting procedure. Through the production of several possible structures and a subsequent averaging process, the most plausible configuration may result. The final result of a DAMMIN fit to experimental SANS data is shown in Figure 23. The goodness of fit parameters for all DAMMIN fits are presented in Table 7.

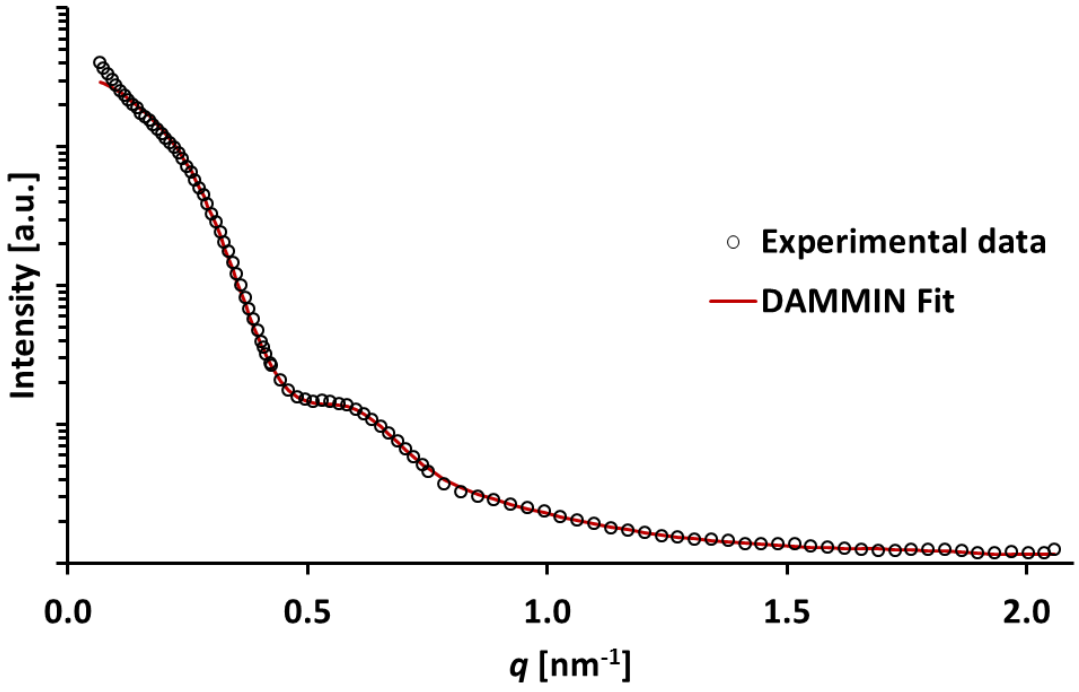

Figure 23: Exemplary depiction of a DAMMIN fitting procedure result. The experimental SANS data (black circles) and the final fit (red line) for a DAMMIN run with N-LDL at 40°C and 20 bar.

Table 7: Goodness of fit parameters obtained from the program DAMMIN averaged for 10 independent runs of each sample. *Rf* describes the goodness of fit of the simulated data versus the experimental data, not taking Penalties into account. The chi-squared value is the final χ^2 against the raw data. Values are means ± SD of 10 independent fitting procedures.

Sample		*Rf*	χ^2
N-LDL	10°C 20 bar	0.00313 ± 0.00016	34.15 ± 0.25
	10°C 3000 bar	0.00320 ± 0.00014	92.03 ± 0.22
	40°C 20 bar	0.00323 ± 0.00023	29.80 ± 0.31
	40°C 3000 bar	0.00254 ± 0.00014	51.06 ± 0.28
TG-LDL	10°C 20 bar	0.00190 ± 0.00030	24.61 ± 0.48
	10°C 3000 bar	0.00279 ± 0.00014	51.48 ± 0.26
	40°C 600 bar	0.00163 ± 0.00027	29.85 ± 0.53
	40°C 3000 bar	0.00179 ± 0.00026	40.78 ± 0.59
Ox-LDL	10°C 20 bar	0.00227 ± 0.00019	14.96 ± 0.34
	10°C 3000 bar	0.00246 ± 0.00024	59.58 ± 0.31
	40°C 20 bar	0.00216 ± 0.00015	15.81 ± 0.41
	40°C 3000 bar	0.00194 ± 0.00025	28.23 ± 0.53

After the generation of ten independent DAMMIN models for each sample, several further processing steps have to follow. These further steps were done with the program suite DAMAVER[43] from the ATSAS package. The program suite contains five independent programs, which are usually run consecutively and have the aim to align and average the produced DAMMIN models from the independent runs of the same SANS curve. The first program in the package is “damsel”, which compares all models and detects possible outliers. The second one is “damsup”, which aligns all models with the most probable one. The third program is “damaver”, which makes an average of all aligned models. The fourth program is “damfilt”, which filters the averaged model at a given cut-off value and the fifth program is “damstart”, a program to generate a modification of the averaged model with a fixed core for further use in DAMMIN. The DAMAVER program suite was applied for each group of samples to align and average the corresponding DAMMIN models. The aligned and averaged models were used to determine the overall model dimensions. The models were loaded in PyMOL and measured with the help of two PyMOL scripts (see Materials & Methods for details). The Inertia Axis Aligned Bounding Box (IABB box) is used to measure the overall dimensions for all averaged models. For this reason each model is aligned along its axes of inertia and the maximal dimensions of these axes are measured. The diameters are named D1 (longest axis), D2 (middle axis) and D3 (shortest axis). An example of an IABB box is shown in Figure 24.

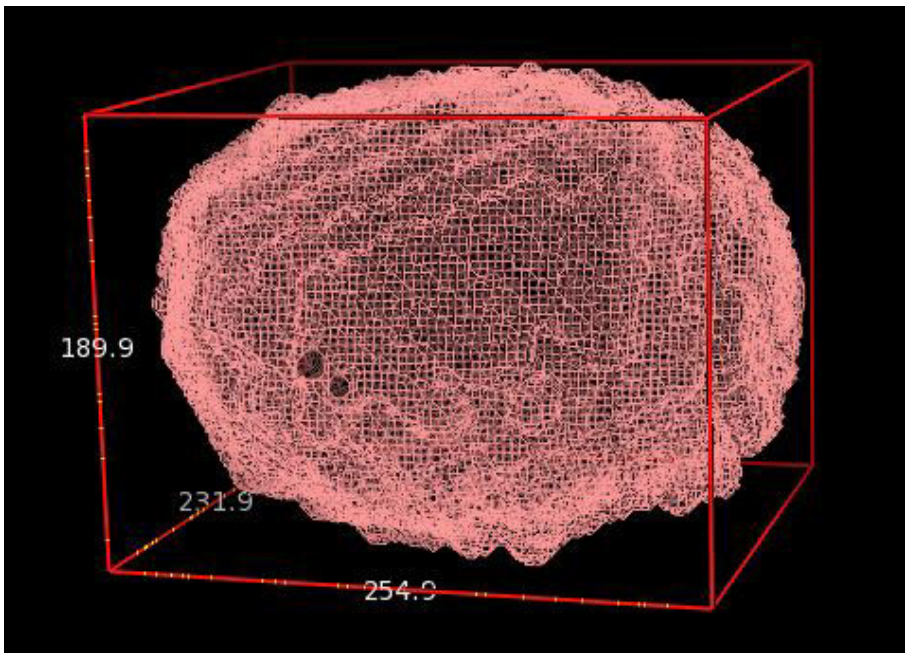

Figure 24: Dimensions derived from the Inertia Axis Aligned Bounding Box (IABB) in PyMOL for N-LDL at 10°C and 20 bar.

The applied SANS curves, the final averaged DAMMIN models and the particle dimensions derived from the IABB box are shown in Figure 25. The final DAMMIN models are depicted from three perpendicular perspectives. The top view shows the particle with the viewer's perspective along the shortest axis. The front and side view correspond to rotations by 90 degrees and viewpoints along the other two axes. The diameters are depicted as a function of pressure and are also listed in Table 8. The relative changes of the measured diameters from the low pressure point to the high pressure point are listed in percent change in Table 9.

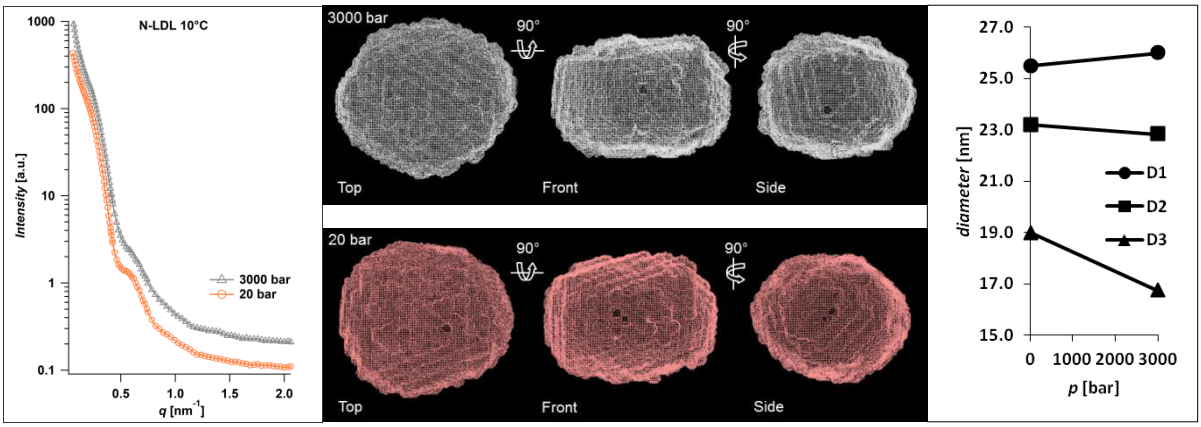

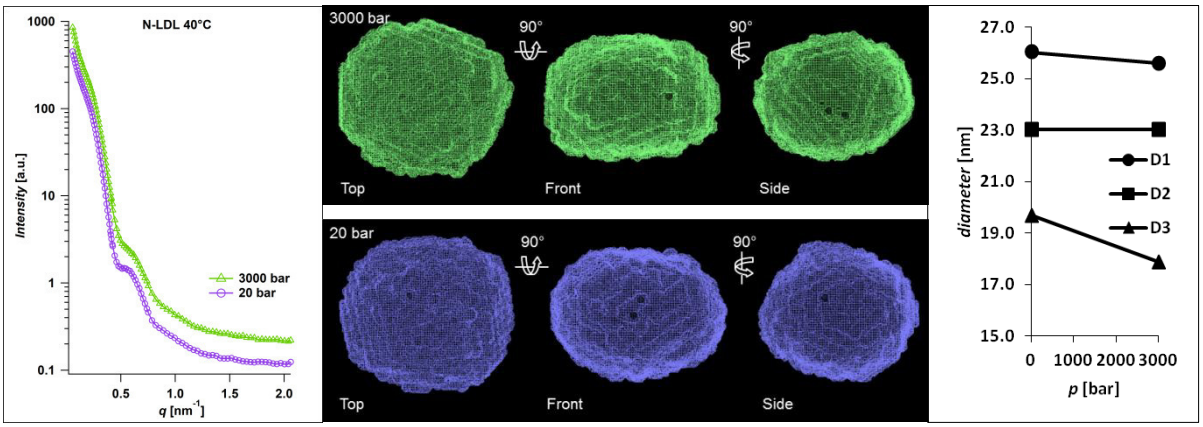
N-LDL 40°C
Intensity [a.u.]
q [nm-1]
3000 bar
20 bar
3000 bar
20 bar
90°
90°
Top
Front
Side
diameter [nm]
p [bar]
D1
D2
D3

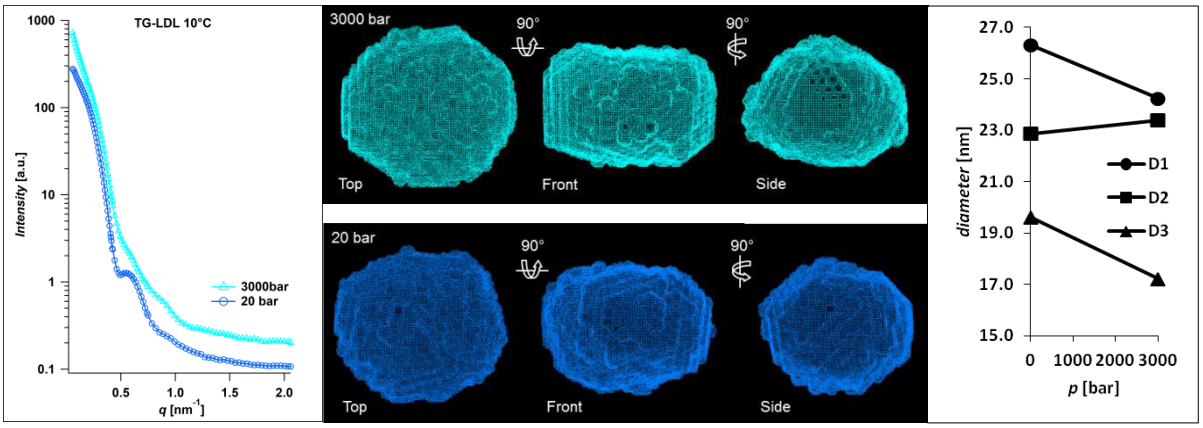
TG-LDL 10°C
Intensity [a.u.]
q [nm-1]
3000bar
20 bar
3000 bar
20 bar
90°
90°
Top
Front
Side
diameter [nm]
p [bar]
D1
D2
D3

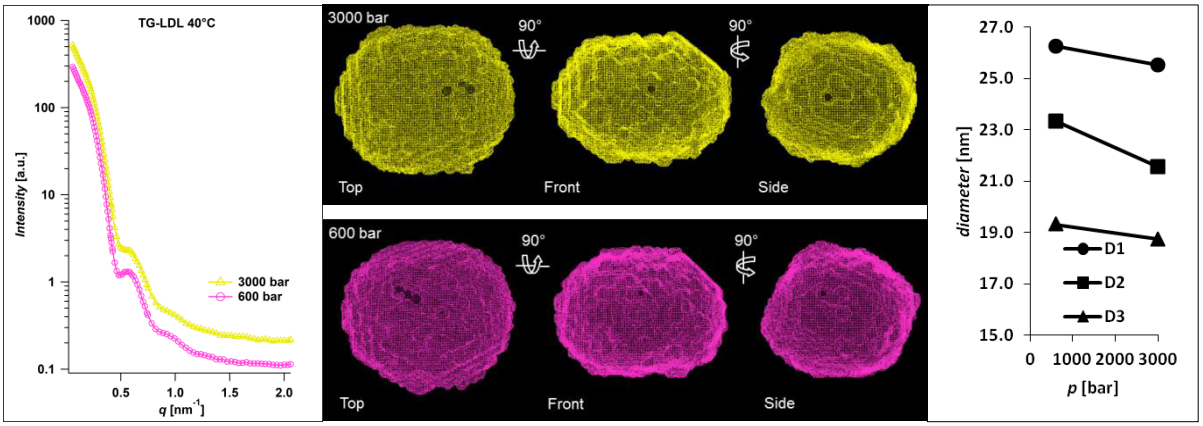
TG-LDL 40°C
Intensity [a.u.]
q [nm-1]
3000 bar
600 bar
3000 bar
600 bar
90°
90°
Top
Front
Side
diameter [nm]
p [bar]
D1
D2
D3

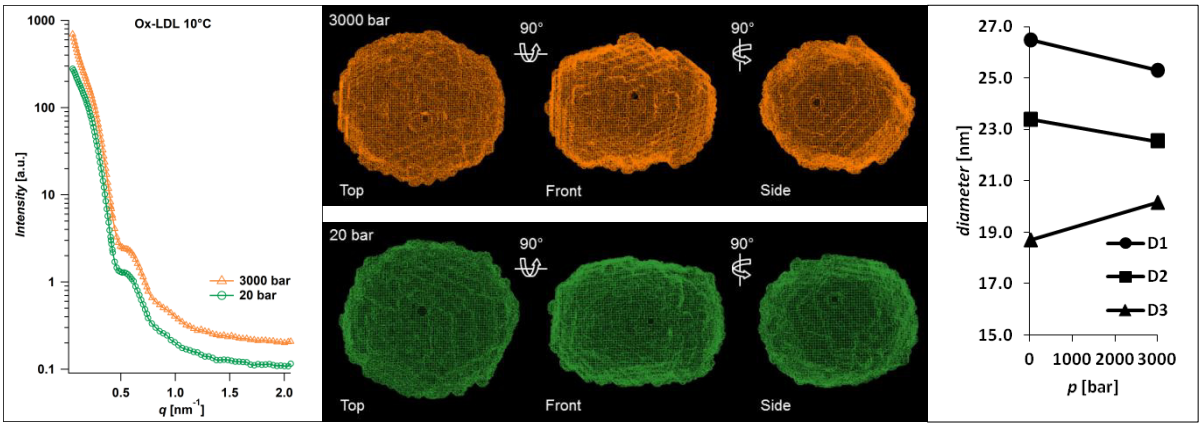
Ox-LDL 10°C
Intensity [a.u.]
q [nm-1]
3000 bar
20 bar
3000 bar
20 bar
90°
90°
Top
Front
Side
diameter [nm]
p [bar]
D1
D2
D3

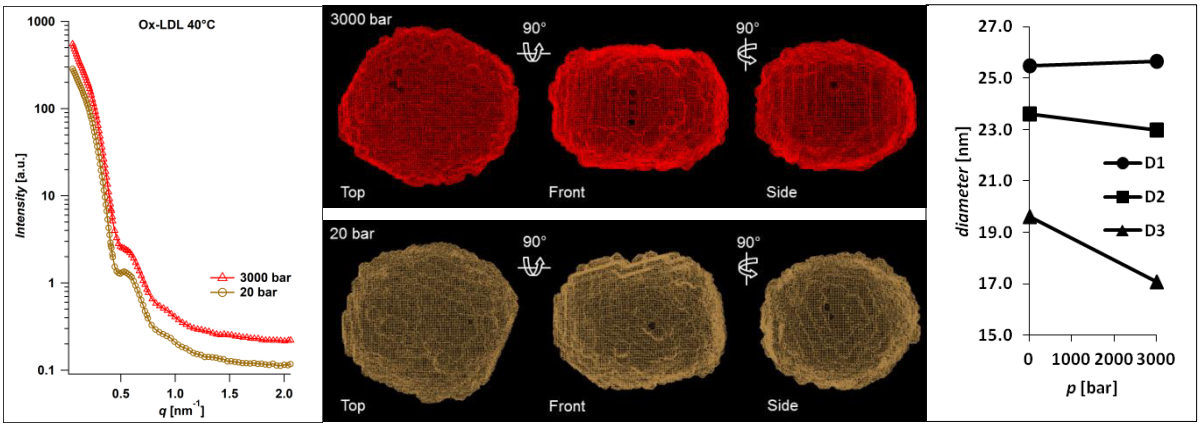

Figure 25: Averaged ab initio shape models of SANS data determined with the program DAMMIN[42] from 10 independent runs. The applied SANS curves (left) and the averaged ab initio shapes of LDL particles are shown from three perpendicular perspectives at 20 bar (lower center) and 3000 bar (upper center). The SANS curves were shifted vertically for better visibility. The models are aligned to each other along the main axes and rotated by 90° for each perspective. The corresponding particle dimensions measured through the IABB box as a function of pressure are also shown (right), where D1 describes the diameter of the particle of the longest axis, D2 the diameter of the middle axis and D3 the diameter of the shortest axis. The diagrams are depicted for the three different samples N-LDL, TG-LDL and Ox-LDL at the two measured temperature points of 10°C and 40°C.

A closer inspection of these results offers some interesting findings. First, D1 and D2 are generally much less affected by pressure than the smallest diameter D3 (see Table 9). The diameter D3 strongly reacts to pressure and (almost) always exhibits a significant decrease of diameter. In one case, namely the Ox-LDL sample at 10°C, the diameter D3 increases. This fact, however, is caused by a small protrusion on the top surface of the particle model (compare Figure 25), which emerges at the transition from 20 bar to 3000 bar and therefore causes the diameter increase. Interestingly this small protrusion was present in some of the independent DAMMIN models for Ox-LDL (10°C and 3000 bar) and was included in the aligned and averaged final DAMAVER model. However, the protrusion might not represent a real particle modification but might be some kind of artifact from the fitting process. The second case, namely the TG-LDL sample at 40°C only shows a minor change of D3, but here it has to be noted that the low pressure point was 600 bar instead of 20 bar as for the other samples. Consequently, the occurring change might be smaller compared to the other samples. Second, N-LDL shows the smallest changes for D1 and D2 compared to the other models. Third, a characteristic flattening can be observed in the front view of all shown models (see Figure 25), which correlates with the major diameter changes of the smallest axis D3. On the contrary, the changes in the top view of the shown models are relatively small due to the minimal decrease of the diameters D1 and D2. Consequently a more roundish form remains.

Table 8: Particle dimensions derived from the IABB box for all averaged DAMMIN models. The values are given for the largest (D1), the medium (D2) and the smallest (D3) diameter of the models.

DAMMIN model	Diameter D1 (largest) [Å]	Diameter D2 (medium) [Å]	Diameter D3 (smallest) [Å]
N-LDL 10°C 20 bar	254.9	231.9	189.9
N-LDL 10°C 3000 bar	259.8	228.3	167.4
N-LDL 40°C 20 bar	260.2	230.1	196.8
N-LDL 40°C 3000 bar	255.9	230.2	178.8
TG-LDL 10°C 20 bar	263.0	228.6	195.9
TG-LDL 10°C 3000 bar	242.4	233.8	172.2
TG-LDL 40°C 600 bar	262.5	233.2	193.2
TG-LDL 40°C 3000 bar	255.1	215.6	187.5
Ox-LDL 10°C 20 bar	264.8	233.8	187.1
Ox-LDL 10°C 3000 bar	252.9	225.4	201.7
Ox-LDL 40°C 20 bar	254.8	236.1	196.0
Ox-LDL 40°C 3000 bar	256.6	229.8	170.7

Table 9: Change of the absolute diameter length of the models in percent from the low pressure to the high pressure point. Positive values indicate an increase of the diameter, whereas negative values indicate a decrease of the diameter length from low to high pressure point.

DAMMIN model	Diameter D1 change [%]	Diameter D2 change [%]	Diameter D3 change [%]
N-LDL 10°C 20 bar to 3000 bar	1.9	-1.6	-13.4
N-LDL 40°C 20 bar to 3000 bar	-1.7	0.0	-10.1
TG-LDL 10°C 20 bar to 3000 bar	-8.5	2.2	-13.8
TG-LDL 40°C 600 bar to 3000 bar	-2.9	-8.2	-3.0
Ox-LDL 10°C 20 bar to 3000 bar	-4.7	-3.7	7.2
Ox-LDL 40°C 20 bar to 3000 bar	0.7	-2.7	-14.8

Conclusion

The herein presented analyses are direct and model-independent evaluations of the scattering data from small-angle scattering experiments. The results gained from these analyses provide a direct interpretation of the measured data without a biased influence from preexisting knowledge of the investigated LDL system.

The SAXS experiments applying HHP indicate that a lipid phase transition in the core of the LDL particles can be induced by hydrostatic pressure. Already at pressures of 500 bar a pressure-induced ordering of the disordered lipid core above T_m is initiated. The higher the applied pressure, the more pronounced is the ordering in the lipid core. If the LDL core structure is already in the ordered state below T_m, no further influence on the core structure is caused by pressure. The position and distance of the lamellar ordering in the core seems to be very stable, as the lattice parameters are not influenced by HHP even at the highest investigated pressure point of 3000 bar. Moreover the pressure-induced phase transition effect is a highly conserved feature which even occurs in oxidatively stressed particles.

The shift of a peak in the *p(r)* functions, corresponding predominantly to the protein and PL headgroups, gives a hint to an altered molecular arrangement in this area of the particle due to the application of HHP. Generally speaking the LDL samples kept their structural integrity over the whole investigated pressure range and exhibited a fully reversible behavior in the temperature range up to 39°C and under a short-time exposure to high pressure. However, an exposure time of 10 min at 50°C and 2000 bar led to irreversible structural damage and precipitation of the sample.

From the SANS data analysis it can be clearly seen that there is a structural rearrangement happening in LDL particles due to HHP stress conditions. The ab initio shape reconstructions indicate, for all investigated samples, that there is some kind of flattening effect under HHP conditions, which is both visible in the 3D shapes and measurable through the maximum diameters of the axes of inertia. This correlates with the *p(r)* functions, which indicate that there is a rearrangement of paired distances within the particle, due to the shifted shape of the *p(r)* functions. At the same time, the Kratky plots and the *p(r)* functions point out that no major changes of the overall integrity are caused through HHP conditions. This could be also shown in the ab inito shape models. The overall ellipsoidal shape is conserved even under 3000 bar. The R_g values suggest that a pronounced influence on the overall shape of the LDL

particles is caused by hydrostatic pressures above 1200 bar and that the effects are more pronounced for samples below the transition temperature.

Another thing to mention is that the comprehensive structural knowledge about the LDL particle, which already exists from numerous cryoEM studies, should be also utilized for SAS data analysis. Through such an approach it should be possible to extract more detailed information from the SAS data, especially about structural adaptations and changes of compositionally different LDL samples as well as samples under extreme external stress conditions, such as HHP. An example for an approach exploiting preexisting structural data is outlined in the next results chapter.

Materials and Methods

Ethical statement

Anonymized human blood plasma was obtained from the Department of Blood Group Serology and Transfusion Medicine of the University Hospital Graz (Graz, Austria) after written informed consent, according to a protocol approved by the Institutional Review Board of the Medical University of Graz. The blood plasma was free of pathogens (HBV, HCV, HIV) and designated for research purposes only.

Isolation, purification and characterization of LDL from human blood plasma

The single-donor plasma bags were stored at -80 °C until used for isolation and purification of LDL. To prevent oxidation, microbial degradation, and enzymatic cleavage, EDTA (3.4 mM), 0.05 % (w/w) gentamicin sulfate and a protease inhibitor mixture (Roche Diagnostics, Basel, Switzerland) were added to the thawed plasma. LDL was isolated and purified through multiple-step density-gradient ultracentrifugation (180,000 g, 4 °C, 24 h) in the density range 1.019-1.063 g mL^{-1} as described previously.[44] The purified LDL fraction was extensively dialyzed against buffer solution (10 mM sodium phosphate buffer (NaPi), 3.4 mM EDTA, pH 7.4). The samples were concentrated with Amicon Ultra-15 100K centrifugal filter devices (Merck Millipore Ltd., Cork, Ireland) until they reached the desired concentration. The samples were stored in the dark at 4 °C in an argon atmosphere until used for further measurements. Protein concentration was determined with BCA protein assay kit (Thermo Fisher Scientific, Waltham, MA, USA). The further biochemical composition was determined with colorimetric enzymatic assay kits (DiaSys Diagnostic Systems, Holzheim, Germany) and sample purity was checked with SDS-PAGE. D_2O buffers were used for samples intended for neutron scattering experiments, all other samples were in H_2O buffers. All additional chemicals were of analytical grade and purchased from Carl Roth (Karlsruhe, Germany).

Differential Scanning Calorimetry (DSC)

The core lipid transition temperature was determined on a Microcal VP-DSC differential scanning calorimeter (Malvern Instruments Ltd., Malvern, UK). Each sample (approx. 2 mg apoB-100 per mL) was scanned reversibly for three times from 5 °C to 50 °C (preequilibrated at 5 °C for 30 min before each heating scan) and subsequently up to 95°C with a scanning rate of 1 °C/min. The collected data were baseline subtracted and mass normalized to obtain heat capacity (kJ mol^{-1} of CE) vs. temperature curves. Calorimetric data was processed with

the data analysis software Microcal LLC DSC (OriginLab Corporation, Northampton, MA, USA). The curves were interpreted in terms of the core lipid phase transition temperature (T_m), observable as the maximum of change in heat capacity, as well as the calorimetric enthalpy (ΔH_{cal}) calculated by integration of peak areas using baseline extrapolation. The detailed information about T_m was used for temperature adjustments during scattering experiments.

***In vitro* oxidation of LDL**

Prior to the oxidation process the sample buffer was changed to a buffer system without EDTA (10 mM NaPi, 154 mM NaCl, pH 7.4) to enable nonenzymatic oxidation utilizing Cu^{2+} ions. The samples were equilibrated to a temperature of 37 °C. The *in vitro* oxidation of LDL was induced by the addition of $CuCl_2$ (34 µM Cu^{2+} ions per 1 mg mL^{-1} apoB-100). The process was monitored by spectrophotometric detection of conjugated diene formation (absorption at 234 nm) at 37 °C, which allowed to evaluate the time course of LDL oxidation.[45] The process was stopped at different stages through the addition of EDTA (1 mM).

Small-angle neutron scattering (SANS)

SANS experiments were performed at the SANS-II beamline at the Paul-Scherrer Institut (Villigen, Switzerland).[46] To enable data collection over a broad q-range (0.06 – 2.06 nm^{-1}, λ = 0.531 nm) three different sample-to-detector distances (1.5 m, 3.0 m and 6.0 m) were applied for each sample. All measurements were performed with D_2O buffer (10 mM NaPi, 3.4 mM EDTA, pH 7.4). Reference measurements (detector efficiency, empty cell, buffer, cadmium) were carried out with the same adjustments and were used for primary data treatment with $GRAS_{ans}P$, a Matlab™ script application designed for the graphical inspection, analysis and reduction of SANS data. Appropriate high hydrostatic pressure equipment including a temperature control unit was available at the beamline.[47] The LDL samples were probed at several pressure points (ranging from 20 bar to 3000 bar) and two temperature points (below and above T_m).

Small-angle X-ray scattering (SAXS)

Synchrotron SAXS experiments were performed at the SAXS beamline[48] at ELETTRA (Trieste, Italy). Scattering patterns were recorded with the two-dimensional photon counting detector system Pilatus 1M (DECTRIS Ltd, Baden-Daettwil, Switzerland). The scattering intensity was measured as a function of the scattering vector q ($q = 4\pi \sin\theta/\lambda$, where 2θ is

the scattering angle and λ is the wavelength), covering a q-range of 0.07-5.35 nm^{-1} (λ = 0.154 nm). The position calibration of the detector was performed using the diffraction pattern of silver behenate. Reference measurements (empty cell, buffer) were carried out with the same adjustments. The exposure time for all measurements was 60 s per image. Calibration and primary data treatment were performed with the Fit2D software.[49-50] For the high hydrostatic pressure experiments we used a high pressure cell available at the beamline with some further adaptations.[51] The equipment consisted of a pressure generator with control unit (SITEC-Sieber Engineering AG, Maur, Switzerland) and a custom-built pressure cell (Resch GmbH, Glojach, Austria). The high pressure cell contained a cylindrical sample capillary (approx. 2 cm x 1.5 mm in diameter), made out of Kapton®, a polymer of very high mechanical and thermal stability, and highly permeable to X-rays. The capillary was sealed with two Teflon plugs. A temperature unit covering the sample cell was attached and provided the possibility to adjust the temperature for the experiments.

Small-angle scattering data analysis procedures

SANS data were reduced with $GRAS_{ans}P$, whereas SAXS data were further processed and reduced in Igor Pro Version 6.2.2.2 (WaveMetrics, Inc., Lake Oswego, OR, USA). The radius of gyration (R_g) for each experimental condition was determined by using the Guinier approximation in the low q-region. According to the equation $\ln\big(I(q)\big) = \ln\big(I(0)\big) - \frac{R_g^2\, q^2}{3}$ the R_g can be determined from the slope of the linear regression of the Guinier plot ($q\,R_g < 1.3$). Kratky Plots were depicted to interpret samples according to their compactness and flexibility. The pair distance distribution function *p(r)*, which gives information about the molecular particle shape and about intra-particle scattering distribution was calculated by indirect Fourier transformation[52] of the scattered intensity *I(q)* by using the programs GNOM[53] and GIFT[54] (PCG Software package, Version 4.05.12). For a particle of uniform electron density the *p(r)* is given by $p(r) = \frac{1}{2\pi^2}\int_0^\infty I(q)\, q\, r \sin(qr)\, dq$.

We applied another model-independent analysis method, namely ab initio low resolution shape reconstruction by simulated annealing. The technique utilizes a single phase dummy atom model to fill a space of predefined size with dummy atoms of specified radius. Through an iterative process the software approximates a theoretical scattering curve to the actually measured data. We processed our SANS curves with the program DAMMIN[42] from the ATSAS software package. For each scattering curve 10 independent runs of DAMMIN with identical parameters were carried out (search volume sphere diameter = 240 Å, dummy

atom packing radius = 10 Å, number of knots = 15, expected shape unknown) resulting in 10 independent low resolution shape reconstructions. As a next step, outliers of these low resolution shapes were identified, the ab initio shapes were aligned and an averaged model was built. These tasks were done with the program suite DAMAVER[43] from the ATSAS package. The dimensions of the averaged models were measured with PyMOL.[55] By applying the script "Draw_Protein_Dimensions.py" it is possible to get the overall dimensions of the aligned models. The script "Draw_Protein_Dimensions.py" (see Appendix) was downloaded from https://github.com/Pymol-Scripts/ (21.11.2016, author Pablo Guardado Calvo). A requirement to run this script is another script called "inertia_tensor.py" (see Appendix), which was also downloaded from https://github.com/Pymol-Scripts/ (21.11.2016, author Mateusz Maciejewski). When PyMOL is started, these scripts have to be loaded first and through the command "draw_Protein_Dimensions <FILE>" the Inertia Axis Aligned Bounding Box (IABB box) cell dimensions are shown for the selected file. It also generates the IABB box and the inertia axis, which can be displayed with the command "show cgo".

Fitting of scattering curves with different form factors was performed in Igor Pro (Version 6.2.2.2, WaveMetrics Inc., USA) using genetic optimization and simulated annealing procedures. Constraints could be directly defined throughout the fitting process. Resulting coefficients and goodness of fit (χ^2) were obtained from the program.

Acknowledgments

This work has been supported by the Austrian Science Fund (FWF Project No. I 1109-N28 to R. P.) and by the Agence Nationale de la Recherche (ANR; project number ANR-12-ISV5-0002-01 LDLPRESS to J.P.). This work is based on experiments performed at Elettra Sincrotrone Trieste, Trieste, Italy. This work is based on experiments performed at the Swiss spallation neutron source SINQ, Paul Scherrer Institute, Villigen, Switzerland. The authors would also like to thank Hanna Lindermuth for excellent technical support. The authors declare no competing financial interest.

References

1. Brown, M. S.; Goldstein, J. L., A receptor-mediated pathway for cholesterol homeostasis. *Science* **1986,** *232* (4746), 34-47.

2. Prassl, R.; Laggner, P., Molecular structure of low density lipoprotein: current status and future challenges. *Eur. Biophys. J.* **2009,** *38* (2), 145-58.

3. Schuster, B.; Prassl, R.; Nigon, F.; Chapman, M. J.; Laggner, P., Core lipid structure is a major determinant of the oxidative resistance of low density lipoprotein. *Proc. Natl. Acad. Sci. U. S. A.* **1995,** *92* (7), 2509-13.

4. Lusis, A. J., Atherosclerosis. *Nature* **2000,** *407* (6801), 233-241.

5. Engelberg, H., Diagnosis of Atherosclerosis .1. Correlation between Clinical Diagnosis, Serum Cholesterol and Low-Density Lipoproteins, and Resting and Exercise Electrocardiograms. *Am. J. Cardiol.* **1958,** *1* (3), 315-322.

6. Muller, K.; Laggner, P.; Glatter, O.; Kostner, G., The structure of human-plasma low-density lipoprotein B. An X-ray small-angle scattering study. *Eur. J. Biochem.* **1978,** *82* (1), 73-90.

7. Laggner, P.; Kostner, G. M.; Degovics, G.; Worcester, D. L., Structure of the cholesteryl ester core of human plasma low density lipoproteins: selective deuteration and neutron small-angle scattering. *Proc. Natl. Acad. Sci. U. S. A.* **1984,** *81* (14), 4389-93.

8. Vanantwerpen, R.; Gilkey, J. C., Cryoelectron Microscopy Reveals Human Low-Density-Lipoprotein Substructure. *J. Lipid Res.* **1994,** *35* (12), 2223-2231.

9. Meyer, D. F.; Mayans, M. O.; Groot, P. H. E.; Suckling, K. E.; Bruckdorfer, R.; Perkins, S. J., Time-Course Studies by Neutron Solution Scattering and Biochemical Assays of the Aggregation of Human Low-Density-Lipoprotein during Cu2+-Induced Oxidation. *Biochem. J.* **1995,** *310*, 417-426.

10. Orlova, E. V.; Sherman, M. B.; Chiu, W.; Mowri, H.; Smith, L. C.; Gotto, A. M., Jr., Three-dimensional structure of low density lipoproteins by electron cryomicroscopy. *Proc. Natl. Acad. Sci. U. S. A.* **1999,** *96* (15), 8420-5.

11. Segrest, J. P.; Jones, M. K.; De Loof, H.; Dashti, N., Structure of apolipoprotein B-100 in low density lipoproteins. *J. Lipid Res.* **2001,** *42* (9), 1346-1367.

12. Sherman, M. B.; Orlova, E. V.; Decker, G. L.; Chiu, W.; Pownall, H. J., Structure of triglyceride-rich human low-density lipoproteins according to cryoelectron microscopy. *Biochemistry* **2003,** *42* (50), 14988-93.

13. Ren, G.; Rudenko, G.; Ludtke, S. J.; Deisenhofer, J.; Chiu, W.; Pownall, H. J., Model of human low-density lipoprotein and bound receptor based on cryoEM. *Proc. Natl. Acad. Sci. U. S. A.* **2010,** *107* (3), 1059-64.

14. Murtola, T.; Vuorela, T. A.; Hyvonen, M. T.; Marrink, S. J.; Karttunen, M.; Vattulainen, I., Low density lipoprotein: structure, dynamics, and interactions of apoB-100 with lipids. *Soft Matter* **2011,** *7* (18), 8135-8141.

15. Liu, Y.; Atkinson, D., Enhancing the contrast of ApoB to locate the surface components in the 3D density map of human LDL. *J. Mol. Biol.* **2011,** *405* (1), 274-83.

16. Kumar, V.; Butcher, S. J.; Oorni, K.; Engelhardt, P.; Heikkonen, J.; Kaski, K.; Ala-Korpela, M.; Kovanen, P. T., Three-dimensional cryoEM reconstruction of native LDL particles to 16A resolution at physiological body temperature. *PLoS One* **2011,** *6* (5), e18841.

17. Oliveira, C. L.; Santos, P. R.; Monteiro, A. M.; Figueiredo Neto, A. M., Effect of oxidation on the structure of human low- and high-density lipoproteins. *Biophys. J.* **2014,** *106* (12), 2595-605.

18. Liu, Y.; Atkinson, D., Immuno-electron cryo-microscopy imaging reveals a looped topology of apoB at the surface of human LDL. *J. Lipid Res.* **2011,** *52* (6), 1111-6.

19. Liu, Y.; Luo, D.; Atkinson, D., Human LDL core cholesterol ester packing: three-dimensional image reconstruction and SAXS simulation studies. *J. Lipid Res.* **2011,** *52* (2), 256-62.

20. van Antwerpen, R., Preferred orientations of LDL in vitreous ice indicate a discoid shape of the lipoprotein particle. *Arch. Biochem. Biophys.* **2004,** *432* (1), 122-7.

21. Meyer, D. F.; Nealis, A. S.; MacPhee, C. H.; Groot, P. H. E.; Suckling, K. E.; Bruckdorfer, K. R.; Perkins, S. J., Time-course studies by synchrotron X-ray solution scattering of the structure of human low-density lipoprotein during Cu2+-induced oxidation in relation to changes in lipid composition. *Biochem. J.* **1996,** *319*, 217-227.

22. Pinchuk, I.; Lichtenberg, D., Continuous monitoring of intermediates and final products of oxidation of low density lipoprotein by means of UV-spectroscopy. *Free Radic. Res.* **1996,** *24* (5), 351-60.

23. Prassl, R.; Schuster, B.; Laggner, P.; Flamant, C.; Nigon, F.; Chapman, M. J., Thermal stability of apolipoprotein B100 in low-density lipoprotein is disrupted at early stages of oxidation while neutral lipid core organization is conserved. *Biochemistry* **1998,** *37* (3), 938-44.

24. Han, C. Y.; Pak, Y. K., Oxidation-dependent effects of oxidized LDL: proliferation or cell death. *Exp. Mol. Med.* **1999,** *31* (4), 165-173.

25. Krisko, A.; Stjepanovic, G.; Pifat, G.; Ruysschaert, J. M.; Goormaghtigh, E., Detection of apolipoprotein B100 early conformational changes during oxidation. *Biochim. Biophys. Acta* **2007,** *1768* (11), 2923-30.

26. Jayaraman, S.; Gantz, D. L.; Gursky, O., Effects of oxidation on the structure and stability of human low-density lipoprotein. *Biochemistry* **2007,** *46* (19), 5790-5797.

27. Deckelbaum, R. J.; Granot, E.; Oschry, Y.; Rose, L.; Eisenberg, S., Plasma triglyceride determines structure-composition in low and high density lipoproteins. *Arteriosclerosis* **1984,** *4* (3), 225-31.

28. Pregetter, M.; Prassl, R.; Schuster, B.; Kriechbaum, M.; Nigon, F.; Chapman, J.; Laggner, P., Microphase separation in low density lipoproteins - Evidence for a fluid triglyceride core below the lipid melting transition. *J. Biol. Chem.* **1999,** *274* (3), 1334-1341.

29. McKeone, B. J.; Patsch, J. R.; Pownall, H. J., Plasma triglycerides determine low density lipoprotein composition, physical properties, and cell-specific binding in cultured cells. *J. Clin. Invest.* **1993,** *91* (5), 1926-33.

30. Coronado-Gray, A.; van Antwerpen, R., Lipid composition influences the shape of human low density lipoprotein in vitreous ice. *Lipids* **2005,** *40* (5), 495-500.

31. Meersman, F.; McMillan, P. F., High hydrostatic pressure: a probing tool and a necessary parameter in biophysical chemistry. *Chem. Commun.* **2014,** *50* (7), 766-775.

32. Winter, R.; Jeworrek, C., Effect of pressure on membranes. *Soft Matter* **2009,** *5* (17), 3157.

33. Brooks, N. J.; Ces, O.; Templer, R. H.; Seddon, J. M., Pressure effects on lipid membrane structure and dynamics. *Chem. Phys. Lipids* **2011,** *164* (2), 89-98.

34. Schroer, M. A.; Paulus, M.; Jeworrek, C.; Krywka, C.; Schmacke, S.; Zhai, Y.; Wieland, D. C. F.; Sahle, C. J.; Chimenti, M.; Royer, C. A.; Garcia-Moreno, B.; Tolan, M.; Winter, R., High-Pressure SAXS Study of Folded and Unfolded Ensembles of Proteins. *Biophys. J.* **2010,** *99* (10), 3430-3437.

35. Russo, D.; Ortore, M. G.; Spinozzi, F.; Mariani, P.; Loupiac, C.; Annighofer, B.; Paciaroni, A., The impact of high hydrostatic pressure on structure and dynamics of beta-lactoglobulin. *Biochimica Et Biophysica Acta-General Subjects* **2013,** *1830* (10), 4974-4980.

36. Barriga, H. M. G.; Law, R. V.; Seddon, J. M.; Ces, O.; Brooks, N. J., The effect of hydrostatic pressure on model membrane domain composition and lateral compressibility. *PCCP* **2016,** *18* (1), 149-155.

37. Peters, J.; Martinez, N.; Michoud, G.; Cario, A.; Franzetti, B.; Oger, P.; Jebbar, M., Deep Sea Microbes Probed by Incoherent Neutron Scattering Under High Hydrostatic Pressure. *Z. Phys. Chem.* **2014,** *228* (10-12).

38. Nishiyama, M., High-Pressure Microscopy for Studying Molecular Motors. *Subcell. Biochem.* **2015,** *72*, 593-611.

39. Laggner, P.; Degovics, G.; Muller, K. W.; Glatter, O.; Kratky, O.; Kostner, G.; Holasek, A., Molecular packing and fluidity of lipids in human serum low density lipoproteins. *Hoppe Seylers Z. Physiol. Chem.* **1977,** *358* (7), 771-8.

40. Hammel, M.; Laggner, P.; Prassl, R., Structural characterisation of nucleoside loaded low density lipoprotein as a main criterion for the applicability as drug delivery system. *Chem. Phys. Lipids* **2003,** *123* (2), 193-207.

41. Laggner, P.; Kostner, G. M.; Rakusch, U.; Worcester, D., Neutron small angle scattering on selectively deuterated human plasma low density lipoproteins. The location of polar phospholipid headgroups. *J. Biol. Chem.* **1981,** *256* (22), 11832-9.

42. Svergun, D. I., Restoring low resolution structure of biological macromolecules from solution scattering using simulated annealing. *Biophys. J.* **1999,** *76* (6), 2879-86.

43. Volkov, V. V.; Svergun, D. I., Uniqueness of ab initio shape determination in small-angle scattering. *J. Appl. Crystallogr.* **2003,** *36*, 860-864.

44. Mikl, C.; Peters, J.; Trapp, M.; Kornmueller, K.; Schneider, W. J.; Prassl, R., Softness of atherogenic lipoproteins: a comparison of very low density lipoprotein (VLDL) and low density lipoprotein (LDL) using elastic incoherent neutron scattering (EINS). *J. Am. Chem. Soc.* **2011,** *133* (34), 13213-5.

45. Esterbauer, H.; Dieber-Rotheneder, M.; Waeg, G.; Striegl, G.; Jurgens, G., Biochemical, structural, and functional properties of oxidized low-density lipoprotein. *Chem. Res. Toxicol.* **1990,** *3* (2), 77-92.

46. Strunz, P.; Mortensen, K.; Janssen, S., SANS-II at SINQ: installation of the former Riso-SANS facility. *Physica B-Condensed Matter* **2004,** *350* (1-3), E783-E786.

47. Kohlbrecher, J.; Bollhalder, A.; Vavrin, R.; Meier, G., A high pressure cell for small angle neutron scattering up to 500 MPa in combination with light scattering to investigate liquid samples. *Rev. Sci. Instrum.* **2007,** *78* (12), 125101.

48. Amenitsch, H.; Rappolt, M.; Kriechbaum, M.; Mio, H.; Laggner, P.; Bernstorff, S., First performance assessment of the small-angle X-ray scattering beamline at ELETTRA. *Journal of Synchrotron Radiation* **1998,** *5*, 506-508.

49. Hammersley, A. P. *FIT2D: An Introduction and Overview*; 1997.

50. Hammersley, A. P.; Svensson, S. O.; Thompson, A., Calibration and Correction of Spatial Distortions in 2d Detector Systems. *Nucl Instrum Meth A* **1994,** *346* (1-2), 312-321.

51. Pressl, K.; Kriechbaum, M.; Steinhart, M.; Laggner, P., High pressure cell for small-and wide-angle x-ray scattering. *Rev. Sci. Instrum.* **1997,** *68* (12), 4588-4592.

52. Glatter, O., New Method for Evaluation of Small-Angle Scattering Data. *J. Appl. Crystallogr.* **1977,** *10* (Oct1), 415-421.

53. Svergun, D. I., Determination of the Regularization Parameter in Indirect-Transform Methods Using Perceptual Criteria. *J. Appl. Crystallogr.* **1992,** *25*, 495-503.

54. Fritz, G.; Glatter, O., Structure and interaction in dense colloidal systems: evaluation of scattering data by the generalized indirect Fourier transformation method. *J. Phys.-Condes. Matter* **2006,** *18* (36), S2403-S2419.

55. Schrodinger, LLC, The PyMOL Molecular Graphics System, Version 1.8. 2015.

7. Results Part IV

Results part IV deals with a novel approach for a comprehensive structural analysis of experimental SAXS data from LDL samples. Through detailed analyses of existing structural information from cryoEM studies of LDL and the combination with new experimental SAXS data a more accurate 3D model was proposed.

Atherogenic low-density lipoprotein: Integration of SAXS and cryoEM data argue for a modified structural model

Bernhard Lehofer[1], Karin Kornmueller[1], Angelika Krebs[2], Manfred Kriechbaum[3], Judith Peters[4,5], Heinz Amenitsch[3] and Ruth Prassl[1,*]

[1] Institute of Biophysics, Medical University of Graz, Neue Stiftingtalstraße 6/IV, 8010 Graz, Austria
[2] Center for Medical Research, Medical University of Graz, Stiftingtalstraße 24, 8010 Graz, Austria
[3] Institute of Inorganic Chemistry, Graz University of Technology, Stremayrgasse 9, 8010 Graz, Austria
[4] Institut Laue-Langevin, 71 avenue des Martyrs, 38044 Grenoble, France
[5] Laboratoire Interdisciplinaire de Physique LiPhy, Université Grenoble Alpes, 140 Rue de la Physique, 38402 Saint-Martin-d'Hères, France

**Corresponding author: Ruth Prassl, Medical University of Graz, Institute of Biophysics, Neue Stiftingtalstraße 6/IV, 8010 Graz, e-mail: ruth.prassl@medunigraz.at*

Abstract

Low-density lipoprotein (LDL) is a well-known key player in the development of atherosclerosis and cardiovascular diseases, however, the structural details of this very complex nanoparticle are still not fully understood and subject of ongoing scientific research. Due to this lack of information we chose a comparative approach to better understand the structural arrangement of LDL. We combined 3D information from cryo-electron microscopy (cryoEM) maps deposited in the Electron Microscopy Data Bank (EMDB) with our experimental synchrotron small-angle X-ray scattering (SAXS) data. We created pdb-files from the cryoEM maps, weighted according to the electron density distribution of the corresponding EM maps and simulated their solution scattering profiles. The simulated scattering curves were compared to the experimental SAXS data. We found a perfect fit to the experimental SAXS curves over a wide range of data, however, distinct differences in the scattering behavior pointing out structural variability existing in individual LDL nanoparticles. Using this knowledge, structural parameters derived from our experimental SAXS data by applying an advanced mathematical 3D model will provide new insights into the different molecular arrangements of LDL particles. This knowledge may be a fundamental component in further understanding the pathological mechanisms of atherosclerosis.

Manuscript in preparation for: *Journal of the American Chemical Society*

Introduction

It is a well-known fact that human low-density lipoprotein (LDL) particles have a complex core-shell structure. Its amphiphilic shell consists of a monolayer of phospholipids (PL) and a single protein moiety named apolipoprotein B-100 (apoB-100), whereas its hydrophobic core primarily contains cholesteryl esters (CE) and triglycerides (TG). Some free unesterified cholesterol molecules are distributed among the surface and core region.[1] Furthermore the LDL particle undergoes a characteristic lipid phase transition at a specific temperature (T_m), which is caused by a smectic to isotropic phase transition of CEs in the core and usually found between 24-30°C.[2]

Besides its essential physiological function as lipid transporter in circulation, the human LDL particle is a well-known key player in the pathological progression of various cardiovascular diseases. Due to accumulation processes of LDL particles in the intima of the vessel wall the development of atherosclerotic plaques in the vasculature is accelerated. Monocytes are attracted to lesions of the endothelial layer and transmigrate to the intima where they proliferate and differentiate into macrophages. Through the uptake of LDL these macrophages subsequently form foam cells and deposit their lipid content in the intima after cell death.[3] The process of plaque formation appears to be accelerated through the presence of small dense LDL particles, which are characterized through a triglyceride-rich core lipid composition.[4-5] Changes in the composition and structure of LDL are directly linked to elevated serum levels of triglycerides. Cholesteryl esters leave the core of LDL and are replaced by TG.[6-7] It could be shown with cryo-electron microscopy (cryoEM) that triglyceride-rich LDL particles (TG-LDL) have a more spherical shape without the characteristic striations seen in normolipidemic LDL (N-LDL) below T_m.[8-9]

To enable detailed structural analysis of different LDL species it is valuable to utilize already existing information as a resource of data and combine it with new experimental data, which are ideally obtained with a complementary biophysical technique. Here we report a novel approach for generating a 3D model for the analysis of experimental small-angle X-ray scattering (SAXS) data. For the first time to our knowledge LDL cryoEM density maps were taken from the EM Data Bank (EMDB)[10] and processed to result in weighted sphere model files, which were subsequently used to simulate solution scattering behavior. The simulated solution scattering pattern was compared to experimental SAXS curves to exploit the

structural information of the EM density maps for development of a new mathematical 3D model of LDL.

Results

Currently three different datasets with structural 3D information from cryoEM studies of LDL are publicly available in the EMDB (EMD-5153[11], EMD-5239[12], EMD-2180[13]). EMD-5153 and EMD-5239 offer particle structures frozen below T_m, at 4°C and 22°C, respectively, whereas EMD-2180 provides a density map of LDL above T_m at 37°C body temperature. Some key parameters of the available LDL density maps are summarized in Table 1. Sphere models were derived from the cryoEM density maps through conversion of the voxel-based structure to a pdb-file format. The spheres were weighted according to the electron density information of the corresponding voxel derived from the cryoEM density maps.

Table 1: Key parameters of the investigated cryoEM maps.

EMD-code	Cryopreservation temperature[a] (°C)	Voxel edge length (Å)	Recommended contour level (σ)[c]	No. of spheres (total model)[d]	Reference
EMD-5153	4	5.34	0.27	41094	Ren et al., 2010[11]
EMD-5239	22	5.80	1.20	23533	Liu et al., 2011[12]
EMD-2180	37	1.40 (original) 5.60 (merged[b])	0.30	14929	Kumar et al., 2011[13]

[a]samples were pre-equilibrated at the corresponding temperature and 100% humidity prior to freezing.
[b]the original deposited voxel size was adjusted by merging four voxels in each direction of space resulting in a voxel edge length comparable to the other two models.
[c]Recommended contour levels were derived directly from the EMDB entries given by the authors.
[d]The cryoEM density maps were converted from a voxel-based structure to pdb-file format composed of weighted spheres.

The electron density distribution of the different LDL sphere models was analyzed using a relative scale ranging from 0 to 100, where 100 represents the recommended threshold contour level from the EMDB for each structure (see Table 1). Figures 1a,b show LDL models derived from the voxel-based cryoEM density maps for particles below T_m, where the typical cross-section structure with ordered CE layers in the core can be seen. Moreover the LDL particles exhibit the typical shape of a flattened ellipsoid below T_m due to the three-layered smectic phase in the core. On the contrary the particle in Figure 1c shows a more spherical shape above T_m, due to a melted core.

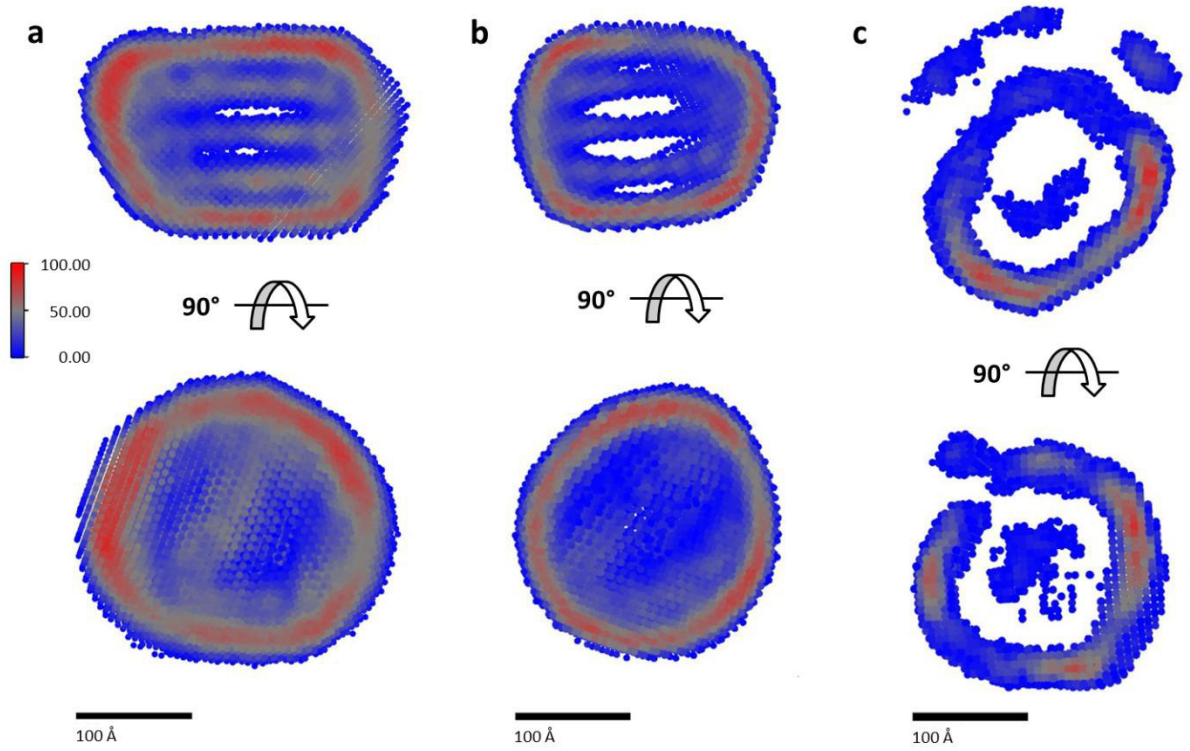

Figure 1: Graphical representation of the LDL sphere models derived from the voxel-based cryoEM density maps. The electron density distribution is scaled in relative values from 0 (blue) to 100 (red), where 100 represents the recommended threshold contour level for each structure. The depicted images are center cuts of the particles shown in frontal perspective (upper row) and top perspective (lower row). (a) EMD-5153, (b) EMD-5239, (c) EMD-2180. (a,b) LDL models were derived from particles equilibrated below the corresponding T_m and (c) was derived from particles at body temperature and therefore above T_m.

The sphere models' small-angle scattering behavior was calculated and compared with experimental SAXS data. The theoretical scattering behavior was calculated using the program CRYSOL[14] from the ATSAS package. CRYSOL automatically takes into account the hydration shell of the particle. The effective width of the simulated border layer is taken to be 0.3 nm to simulate the most ordered first hydration layer, a value which is predefined by the program. The difference of the electron density of the solvent (ρ_s) and the hydration shell (ρ_b) defines the contrast of the border layer $\delta\rho_b = \rho_b - \rho_s$. This contrast of the hydration shell ($\delta\rho_b$) is automatically set to a standard value of 0.03 e/Å³ (= 30 e/nm³), but can be adapted during the calculation process. A typical CRYSOL log-file with the parameters applied for calculation of the scattering behavior is shown in Figure 2. A modification of the average atomic radius from the standard value of 1.47 Å to the voxel size of the original structure (see Table 1) did not change the predicted scattering pattern. On the contrary a change of the solvation shell contrast had an influence on the theoretical scattering behavior. The higher the contrast of the solvation shell (and therefore the higher the

scattering contrast of the particle surface), the larger was the shift of the predicted scattering curve to lower q-values (see Figure 3). The same was observed when the threshold contour levels were altered from the recommended values (see Table 1) to higher values during the conversion from voxel-based cryoEM maps to sphere models. The lower the threshold level (and therefore the larger the converted sphere model), the larger was the shift of the predicted curve to lower q-values (see Figure 4 and 5).

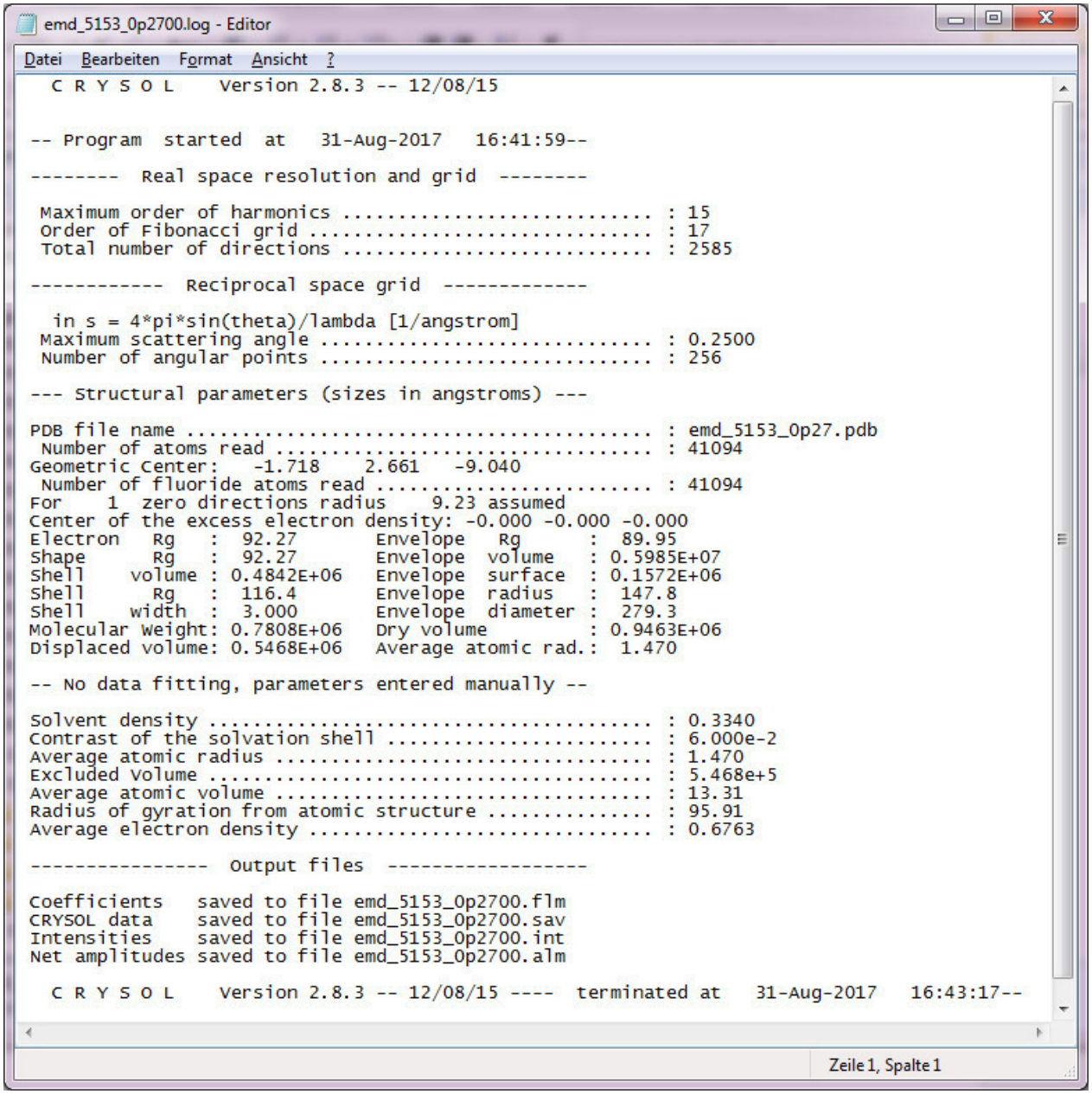

Figure 2: Exemplary log-file of the CRYSOL[14] program after successful calculation of the theoretical scattering behavior of EMD-5153. The maximum scattering angle was set to 0.25 Å^{-1}, contrast of the solvation shell and average atomic radius were altered, the default values were taken for remaining parameters.

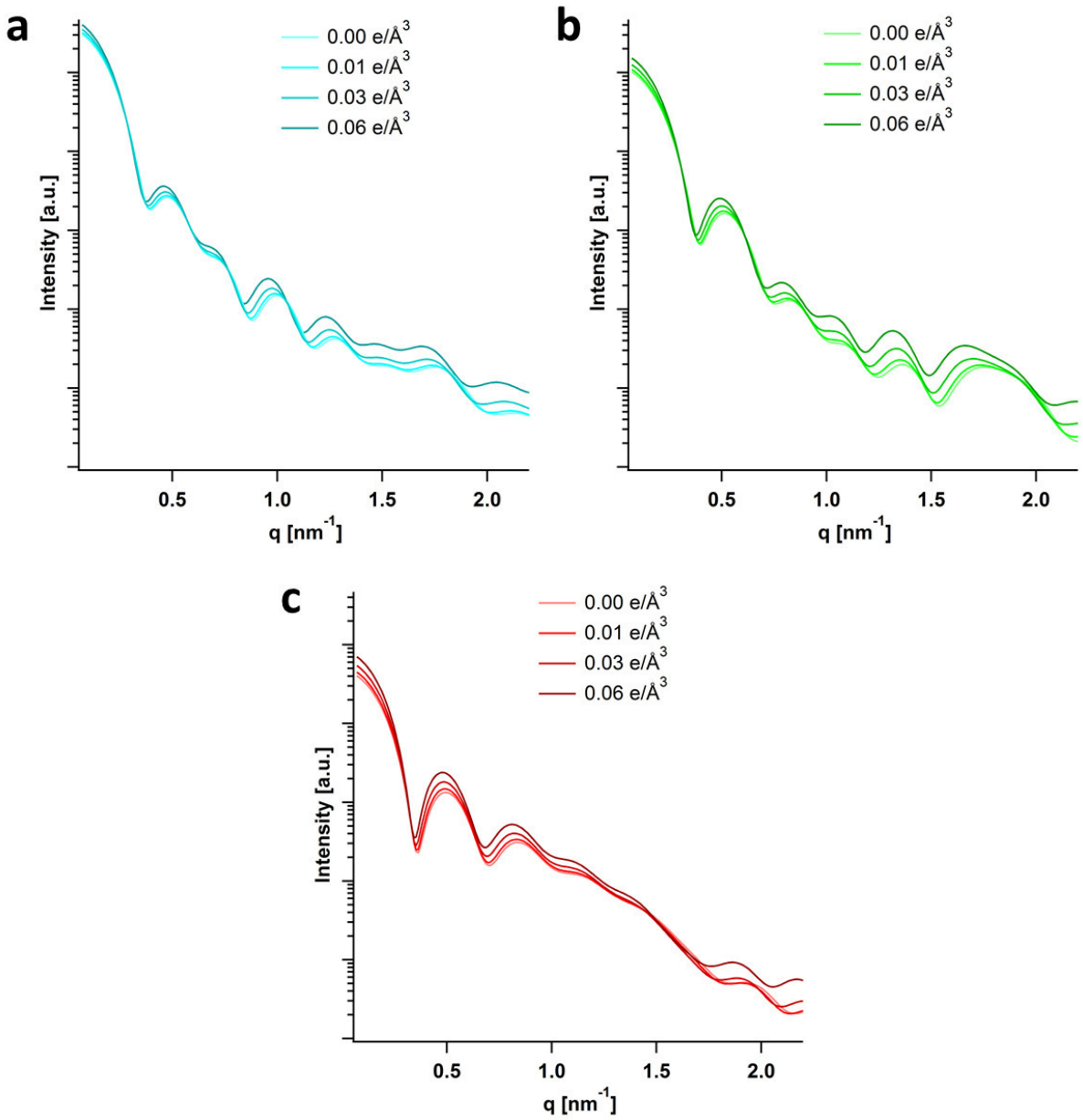

Figure 3: Alteration of the solvation shell contrast ($\delta\rho_b$) influences the theoretical scattering behavior. The calculated curves are shifted towards lower q-values with increasing contrast values. The values for the electron density of the solvation shell contrast were taken between 0.00 electrons/Å³ and 0.06 electrons/Å³ and are shown in (a) EMD-5153, (b) EMD-5239 and (c) EMD-2180.

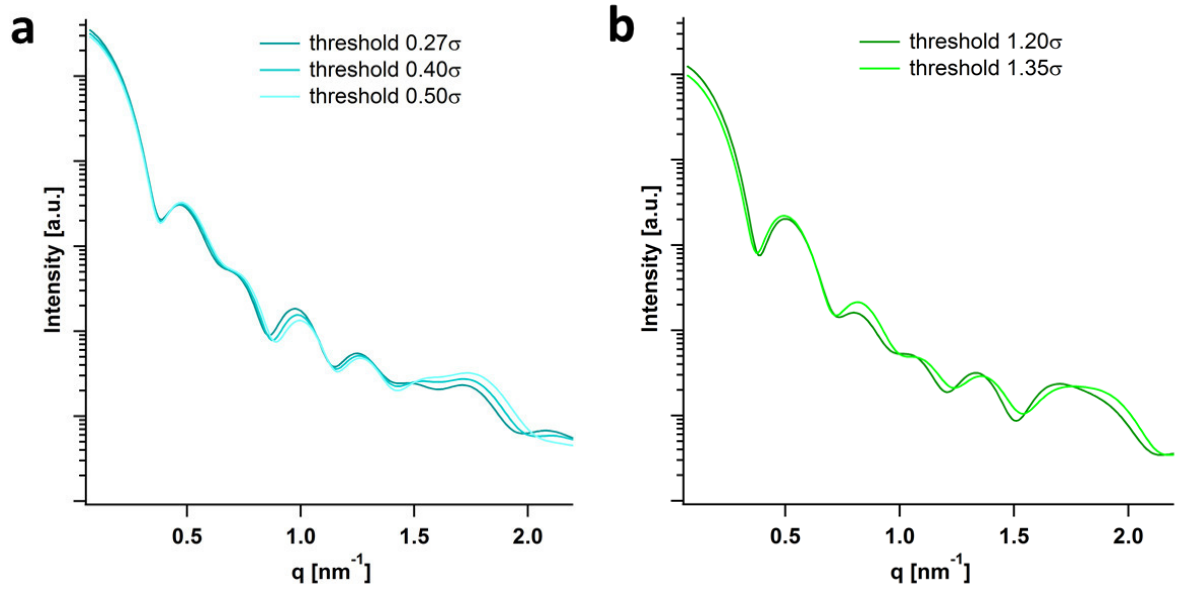

Figure 4: Alteration of the threshold contour level during conversion of cryoEM maps to sphere models influences the theoretical scattering behavior. The lower the threshold level (and the larger the resulting sphere model), the larger was the shift to lower q-values as shown in (a) EMD-5153 and (b) EMD-5239. The threshold level was changed for EMD-5153 from the recommended 0.27σ to 0.40σ and 0.50σ in (a) and for EMD-5239 from the recommended 1.20σ to 1.35σ in (b).

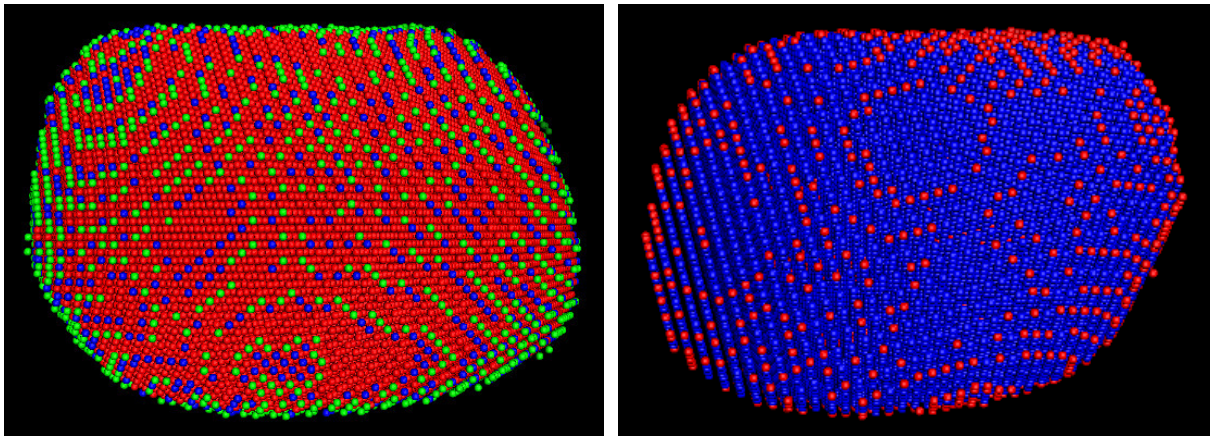

Figure 5: Depiction of the generated LDL sphere models with altered threshold contour levels. The threshold level was changed for EMD-5153 (left) from the recommended 0.27σ (green) to 0.40σ (blue) and 0.50σ (red) and for EMD-5239 (right) from the recommended 1.20σ (red) to 1.35σ (blue). It is seen that the lower the threshold level, the larger the overall size of the sphere model.

As a next step the experimental SAXS curves were compared to the computed scattering patterns of the LDL sphere models. The computed scattering patterns are shown for the recommended threshold levels (see Table 1) and a solvation shell contrast of 0.06 electrons/Å³. The experimental LDL samples show five peaks at characteristic q-values below T_m (see blue curves in Figure 6a,b) similar to the calculated SAXS curves derived from the sphere models of cryoEM data (see cyan and green curves in Figure 6a,b).

The experimental LDL sample above T_m, where the core structure is in the melted state, produces a scattering pattern with only three characteristic peaks (see blue curve in Figure

6c), also comparable to the calculated scattering pattern of the LDL sphere model from above T_m.

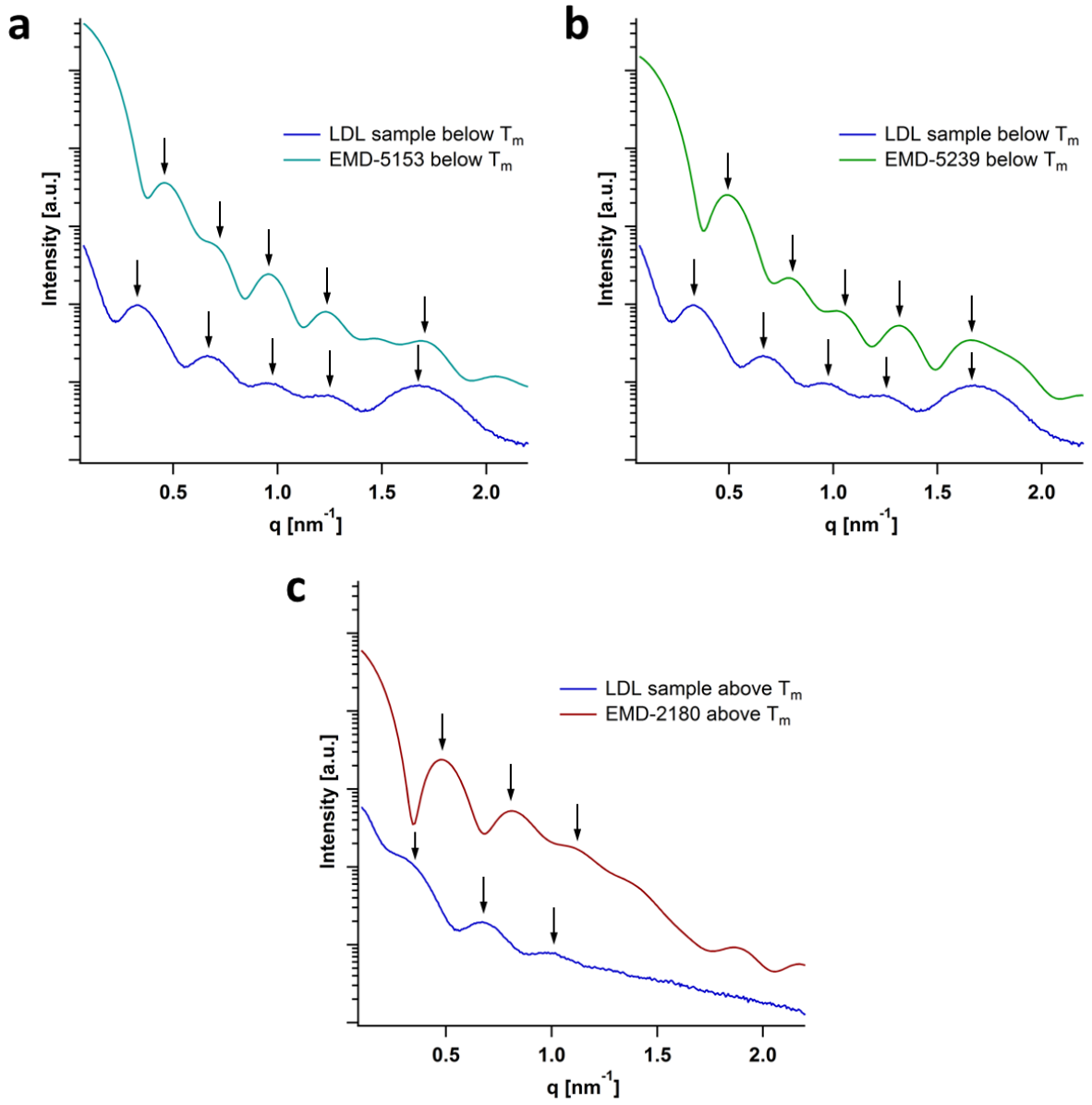

Figure 6: Predicted solution scattering patterns of the LDL sphere models by CRYSOL are depicted in (a) EMD-5153 (cyan), (b) EMD-5239 (green) and (c) EMD-2180 (red) and compared to SAXS measurements of human LDL samples (blue). The characteristic peak positions are marked with arrows in both experimental and simulated curves.

Due to this strong similarity between the experimental SAXS curves and the calculated scattering patterns it can be concluded that the cryoEM reconstructions of the EMDB very closely resemble the native solution structure of LDL in human samples. For this reason the LDL sphere models were evaluated in more detail to get information about the spatial three-dimensional distribution of the electron density. With this information a three-dimensional

model resembling the native electron density distribution can be constructed to enable solution scattering data analysis and interpretation.

Only recently, a superellipsoid shape model of LDL was developed by Maric et al.[15] to describe the LDL particle shape as well as the inner structure below T_m (see Figure 7a). The basic geometrical shape of the model describes a superellipsoid of revolution, with a characteristic radius R_0, an eccentricity ε, which defines the half-height of the superellipsoid (εR_0) and a thickness of the outer layer (*Thick*). Another important parameter is the superellipticity or shape component *t*, responsible for the curvature of the superellipsoid, where a normal ellipsoid of revolution has a shape component $t = 2$ and a cylinder is approached for $t = \infty$. In the developed model the shape component has a value of $t = 3$ for the structure below T_m. The core region is described by another superellipsoid of revolution with the parameters R_1 and εR_1 analogous to the outer superellipsoid. A third hypothetical superellipsoid defines the position of three parallel discs in the core region. This superellipsoid is described by the parameters R_H and $Thick_H$ (which is the distance from the second to the third superellipsoid). The discs themselves have a thickness D_0 and a center to center distance D.[15]

This superellipsoid model is divided into three distinctive electron density regions (see Figure 7a). First, an outer high-density region represents the protein moiety and phospholipid headgroups. Second, a low-density region resembles the inner core molecules, more precisely, the fatty acid chains of the core components (CE and TG) as well as the fatty acid chains of the PL molecules pointing towards the interior. Third, there are three parallel medium-density stripes in the core region, which represent the ordered cholesterol groups of the CEs in the core.[15]

After thorough inspection of the electron density distribution in the LDL sphere models (see Figure 1) we concluded to suggest a novel approach for a detailed LDL model. This new model takes into account that the core structure of LDL particles shows four regions of low electron density surrounded by a medium density area below T_m, rather than three high-density regions (see Figure 7b). The basic structure of this new model, however, resembles the suggestion by Maric et al.[15] and has the same set of parameters. It differs in the core region, where four parallel discs of low-density are surrounded by a medium-density region. In this way the new model is a complementary form of the existing suggestion and might more precisely describe the actual native particle conformation.

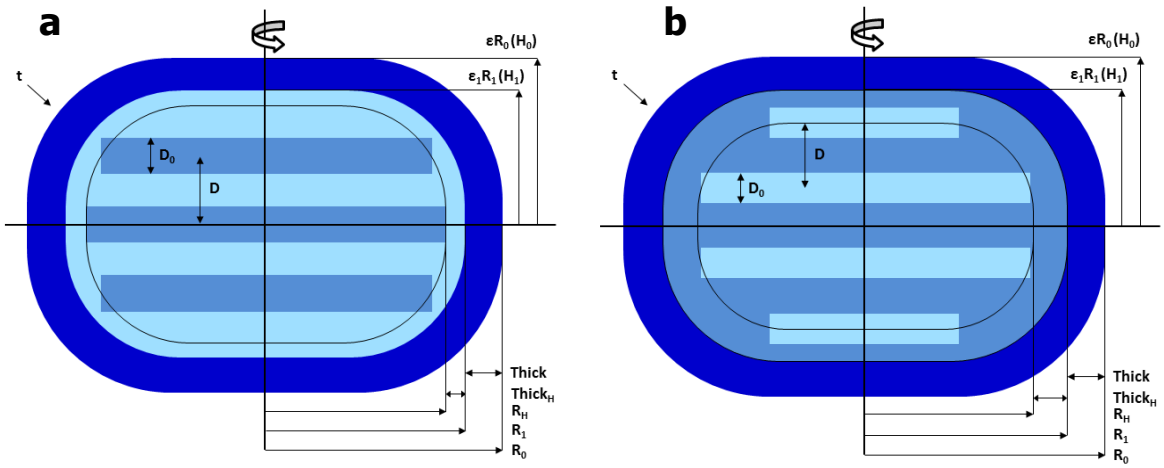

Figure 7: Graphical representation of mathematical LDL models as a potential analysis tool for experimental SAXS data. The LDL model as suggested by Maric et al.[15] (a) shows a high-density outer shell (dark blue) and a low- density inner core (light blue) with three parallel medium-density discs (medium blue). The new model (b) is a complementary approach with four discs of low electron density surrounded by a region of medium density. In both models the symmetry axis goes vertically through the center and is marked with a rotating arrow.

The structural conformation of the LDL particle above T_m, was described by Maric et al.[15] as a transition from the superellipsoid shape to an overall spherical shape with a significant increase of the thickness of the outer shell. The distinction between the electron density of the fatty acid chains and the CE heads in the core region vanished and resulted in an intermediate value of the previous ones.

Similar characteristics are also expected for the new model above T_m, however, the very pronounced increase of the outer shell thickness seems biochemically rather unlikely. Through the significant increase of the outer shell thickness, the volume of this high-density region increases as well and cannot be entirely occupied by the protein moiety and PL headgroups. The fitting process might have resulted in unphysiological results. For that reason it is important to rigorously verify the parameters during the fitting process and to avoid the outcome of implausible parameters. Nevertheless, the disintegration of the ordered CE discs in the core above T_m as well as an overall shape change from a superellipsoid to a spherical shape is physiologically expected and absolutely seems to be plausible.

Discussion

The calculated scattering patterns based on the LDL sphere models from the cryoEM reconstructions show a slight discrepancy to the experimental SAXS curves of native LDL samples. A combination of several factors might be responsible for this effect.

First, the simulation of a theoretical scattering pattern from a given structure has the advantage of getting a precise picture of the scattering behavior of the structure in question. At the same time this is one of the biggest issues in this special investigation. As the scattering behavior is simulated for the exact structure taken from the EMDB, it is the simulation of a completely monodisperse solution of identical particles. But this is not the case for the experimental sample, which is a preparation of particles of human origin and has an inherent polydispersity. Over the applied density range of 1.019-1.063 g mL^{-1} the LDL particles differ in their actual composition and structure. Therefore the effect of polydispersity has to be taken into account and might be responsible for an unspecific background scattering and different slopes of the theoretical and experimental scattering curves (see Figure 6).

Second, the overall size of the particles has a major impact on the scattering behavior and especially on the peak positions at the q-axis. As could be shown by various calculations, both the solvation shell contrasts as well as the threshold contour levels have an impact on the scattering behavior (see Figure 3 and 4). The larger the overall particle size, the higher the shift of the peaks to lower q-values. This implies that the average particle size from the experimental SAXS sample differs from the size of the cryoEM reconstruction and therefore the peaks are shifted in the q-axis. Generally a simple multiplication of all q-values with a defined factor would correlate a size change and q-values. However, a simple multiplication is not sufficient in this case, as the particles structure is much more complicated and other factors than just the overall size are involved (e.g. superellipticity, thickness of the outer shell layer, contrast between core tails and core CE heads electron density, thickness and distance of the core CE head discs, etc.). Due to this multiplicity of factors it is too complicated to exactly identify the origin of the difference.

Third, the temperatures of the cryoEM samples and the experimental samples were different (see Table 1). The experimental samples were measured at 10°C (below T_m) and 38°C (above T_m), respectively. Consequently temperature might also have an impact on the overall conformation of the particles.

However, it has to be stated that despite the aforementioned discrepancies, the scattering patterns have a very high degree of accordance, especially for the samples below T_m. It becomes clear that the structural characteristics given through the cryoEM reconstructions and in detail identified through the LDL sphere models are accurate for the solution structure of LDL as well. Therefore it could be shown that existing structural information can

be applied for the development of a new mathematical model, which will be used for detailed interpretation of scattering data.

According to the cryoEM sphere models the inner core structure below T_m more likely resembles a homogeneously distributed electron density of medium intensity with four parallel layers of low electron density in between, rather than three layers of high electron density. This new model should more accurately fit the measured SAXS data. After development and validation of the new mathematical model, it will be applied for fitting SAXS curves of LDL samples. It will be possible to investigate both native and modified forms of LDL. The derived parameters will provide detailed information about conformational changes under various experimental conditions.

Further knowledge about the detailed structure of LDL will be highly relevant to understand functioning, metabolism and pathological behavior of this vital physiological nanoparticle.

Materials and Methods

Ethical statement

Anonymized human blood plasma was obtained from the Department of Blood Group Serology and Transfusion Medicine of the University Hospital Graz (Graz, Austria) after written informed consent, according to a protocol approved by the Institutional Review Board of the Medical University of Graz. The blood plasma was free of pathogens (HBV, HCV, HIV) and designated for research purposes only.

Sample preparation and characterization

The single-donor plasma bags were stored at -80 °C until used for isolation and purification of LDL. To prevent oxidation, microbial degradation, and enzymatic cleavage, EDTA (3.4 mM), 0.05 % (w/w) gentamicin sulfate and a protease inhibitor mixture (Roche Diagnostics, Basel, Switzerland) were added to the thawed plasma. LDL was isolated and purified through multiple-step density-gradient ultracentrifugation (180,000 g, 4 °C, 24 h) in the density range 1.019-1.063 g mL^{-1} as described previously.[16] The purified LDL fraction was extensively dialyzed against buffer solution (10 mM NaPi (1.44 g/L $Na_2HPO_4 \cdot 2\ H_2O$, 0.26 g/L KH_2PO_4), 3.4 mM EDTA, pH 7.4). The samples were concentrated with Amicon Ultra-15 100K centrifugal filter devices (Merck Millipore Ltd., Cork, Ireland) until they reached the desired concentration. The samples were stored in the dark at 4 °C in an argon atmosphere until

used for further measurements. Protein concentration was determined with BCA protein assay kit (Thermo Fisher Scientific, Waltham, MA, USA). The further biochemical composition (phospholipids, free cholesterol, cholesteryl esters, and triglycerides) was determined with colorimetric enzymatic assay kits (DiaSys Diagnostic Systems, Holzheim, Germany) and sample purity was checked with SDS-PAGE. All additional chemicals were of analytical grade and purchased from Carl Roth (Karlsruhe, Germany).

Differential Scanning Calorimetry (DSC)

The core lipid transition temperature was determined on a Microcal VP-DSC differential scanning calorimeter (Malvern Instruments Ltd., Malvern, UK). Each sample (approx. 2 mg apoB-100 per mL) was scanned reversibly for three times from 5 °C to 50 °C (preequilibrated at 5 °C for 30 min before each heating scan) with a scanning rate of 1 °C/min. The collected data were baseline subtracted and mass normalized with regard to cholesteryl ester (CE) content to obtain heat capacity (kJ mol^{-1} of CE) vs. temperature curves. Calorimetric data was processed with the data analysis software Microcal LLC DSC (OriginLab Corporation, Northampton, MA, USA). The curves were interpreted in terms of the core lipid phase transition temperature (T_m), observable as the maximum of change in heat capacity, as well as the calorimetric enthalpy (ΔH_{cal}) calculated by integration of peak areas using baseline extrapolation. The detailed information about T_m was used for temperature adjustments during scattering experiments.

Small-angle X-ray scattering (SAXS) measurements

Synchrotron SAXS experiments were performed at the SAXS beamline[17] at ELETTRA (Trieste, Italy). Scattering patterns were recorded with the two-dimensional photon counting detector system Pilatus 1M (DECTRIS Ltd, Baden-Daettwil, Switzerland). The scattering intensity was measured as a function of the scattering vector q ($q = 4\pi \sin\theta/\lambda$, where 2θ is the scattering angle and λ is the wavelength), covering a q-range of 0.07-5.35 nm^{-1} (λ = 0.154 nm). The position calibration of the detector was performed using the diffraction pattern of silver behenate. Reference measurements (empty cell, buffer) were carried out with the same adjustments. The exposure time for all measurements was 60 s per image. Calibration and primary data treatment were performed with the Fit2D software.[18-19] A temperature conditioning unit covering the sample cell was attached and provided the possibility to adjust the temperature for the experiments. SAXS data were further processed and reduced in Igor Pro Version 6.2.2.2 (WaveMetrics, Inc., Lake Oswego, OR, USA).

Electron Microscopy Data Bank (EMDB) data processing

Electron density maps of human LDL stored in the electron microscopy data bank were downloaded and inspected. CryoEM electron density maps EMD-5153[11] , EMD-5239[12] and EMD-2180[13] were converted to models composed of spheres reflecting the electron density given in each voxel using the program package Situs[20]. Therefore electron density values of the three-dimensional maps above a certain threshold level were encoded in pdb-files with the density values represented by the occupancy field. Different threshold levels were applied during conversion in order to subsequently assess the influence of particle size and electron density distribution on the theoretical scattering behavior of the LDL particles and on the fit of the cryoEM data with the experimental SAXS data. A mask was necessary in order to remove small areas of positive density which were not connected with the molecules in density maps EMD-2180 and EMD-5239. The created pdb-files were visualized with VMD[21].

Solution scattering simulation of cryoEM 3D models

The theoretical scattering curves of the cryoEM models were calculated using the produced pdb-files and the program CRYSOL[14]. The effect of different threshold values, different atom sizes, and a hydration shell on the scattering behavior was tested with CRYSOL and compared with the experimental SAXS curves. The simulation of a hydration shell is essential to account for the hydration seen by experimental SAXS measurements[22-26].

Development of mathematical 3D fitting model

The development of the mathematical fitting model was based on the preceding analysis of the cryoEM pdb models at the recommended threshold levels (see Table 1). The cross section of the particle as shown in Figure 1 represents a superellipse with a rotation axis through its center; therefore the overall particle shape could be identified as superellipsoid of revolution. Detailed analysis showed that there is an electron dense surface region, presumably harboring the apoB-100 protein moiety as well as the headgroups of the phospholipid surface monolayer. Beneath this high-density region there is an intermediate electron density region, which also spans three parallel layers through the core of the particle. These layers of intermediate density caused by ordered CEs in the core most likely represent the cholesterol ring moiety of CEs. The interstitial space is occupied by four layers

of a low electron dense region, most probably representing the acyl chains of phospholipids and cholesteryl esters.

Fitting of experimental data and derivation of structural parameters

Fitting procedure was done with the software Igor Pro Version 6.2.2.2 (WaveMetrics, Inc., Lake Oswego, OR, USA). The fitting function was implemented in the software and was used for fitting experimental SAXS curves. The Levenberg-Marquardt algorithm, a form of nonlinear, least-squares fitting, is used to search for the coefficient values at minimum chi-square.

References

1. Prassl, R.; Laggner, P. *Eur. Biophys. J.* **2009,** *38*, 145-58.
2. Pregetter, M.; Prassl, R.; Schuster, B.; Kriechbaum, M.; Nigon, F.; Chapman, J.; Laggner, P. *J. Biol. Chem.* **1999,** *274*, 1334-1341.
3. Lusis, A. J. *Nature* **2000,** *407*, 233-241.
4. Diffenderfer, M. R.; Schaefer, E. J. *Curr. Opin. Lipidol.* **2014,** *25*, 221-6.
5. Galeano, N. F.; Al-Haideri, M.; Keyserman, F.; Rumsey, S. C.; Deckelbaum, R. J. *J. Lipid Res.* **1998,** *39*, 1263-1273.
6. Deckelbaum, R. J.; Granot, E.; Oschry, Y.; Rose, L.; Eisenberg, S. *Arteriosclerosis* **1984,** *4*, 225-31.
7. McKeone, B. J.; Patsch, J. R.; Pownall, H. J. *J. Clin. Invest.* **1993,** *91*, 1926-33.
8. Sherman, M. B.; Orlova, E. V.; Decker, G. L.; Chiu, W.; Pownall, H. J. *Biochemistry* **2003,** *42*, 14988-93.
9. Coronado-Gray, A.; van Antwerpen, R. *Lipids* **2005,** *40*, 495-500.
10. Lawson, C. L.; Baker, M. L.; Best, C.; Bi, C. X.; Dougherty, M.; Feng, P. W.; Van Ginkel, G.; Devkota, B.; Lagerstedt, I.; Ludtke, S. J.; Newman, R. H.; Oldfield, T. J.; Rees, I.; Sahni, G.; Sala, R.; Velankar, S.; Warren, J.; Westbrook, J. D.; Henrick, K.; Kleywegt, G. J.; Berman, H. M.; Chiu, W. *Nucleic Acids Res.* **2011,** *39*, D456-D464.
11. Ren, G.; Rudenko, G.; Ludtke, S. J.; Deisenhofer, J.; Chiu, W.; Pownall, H. J. *Proc. Natl. Acad. Sci. U. S. A.* **2010,** *107*, 1059-64.
12. Liu, Y.; Atkinson, D. *J. Mol. Biol.* **2011,** *405*, 274-83.
13. Kumar, V.; Butcher, S. J.; Oorni, K.; Engelhardt, P.; Heikkonen, J.; Kaski, K.; Ala-Korpela, M.; Kovanen, P. T. *PLoS One* **2011,** *6*, e18841.
14. Svergun, D.; Barberato, C.; Koch, M. H. J. *J. Appl. Crystallogr.* **1995,** *28*, 768-773.
15. Maric, S.; Lind, T. K.; Lyngso, J.; Cardenas, M.; Pedersen, J. S. *ACS Nano* **2017,** *11*, 1080-1090.
16. Mikl, C.; Peters, J.; Trapp, M.; Kornmueller, K.; Schneider, W. J.; Prassl, R. *J. Am. Chem. Soc.* **2011,** *133*, 13213-5.

17. Amenitsch, H.; Rappolt, M.; Kriechbaum, M.; Mio, H.; Laggner, P.; Bernstorff, S. *Journal of Synchrotron Radiation* **1998,** *5*, 506-508.

18. Hammersley, A. P. *FIT2D: An Introduction and Overview*; 1997.

19. Hammersley, A. P.; Svensson, S. O.; Thompson, A. *Nuclear Instruments & Methods in Physics Research Section a-Accelerators Spectrometers Detectors and Associated Equipment* **1994,** *346*, 312-321.

20. Wriggers, W. *Acta Crystallogr. Sect. D-Biol. Crystallogr.* **2012,** *68*, 344-351.

21. Humphrey, W.; Dalke, A.; Schulten, K. *J. Mol. Graph. Model.* **1996,** *14*, 33-38.

22. Krebs, A.; Lamy, J.; Vinogradov, S. N.; Zipper, P. *Biopolymers* **1998,** *45*, 289-298.

23. Beavil, A. J.; Young, R. J.; Sutton, B. J.; Perkins, S. J. *Biochemistry* **1995,** *34*, 14449-61.

24. Zipper, P.; Durchschlag, H.; Krebs, A., *Modeling of Biopolymers*. Royal Society of Chemistry: Cambridge, 2005.

25. Zipper, P.; Krebs, A.; Durchschlag, H. *Progress in colloid & polymer science* **2004,** *127*, 126-135.

26. Zipper, P.; Krebs, A.; Durchschlag, H. *Progress in colloid & polymer science* **2002,** *119*, 141-148.

8. Conclusion and Outlook

As cardiovascular diseases are still one of the main causes of death in westernized civilizations, research in this field is of essential importance. It can even be expected that death rates in connection with cardiovascular diseases will increase further in the future, as more and more regions in the world adapt a westernized lifestyle including dietary behavior and lack of exercise. It is a main goal to develop novel types of “theranostics” especially tailored for the treatment and diagnosis of cardiovascular diseases.

This thesis offers a detailed insight into the molecular level of low-density lipoprotein on a dynamical and structural basis. Due to the important role that LDL plays in human pathophysiology of cardiovascular diseases (e.g. coronary artery diseases, stroke, heart failure, aortic aneurysms, etc.) a deeper understanding of the molecular mechanisms is of fundamental importance for the development of novel therapeutics. Through the newly gained knowledge it is possible to better understand the LDL particle on a molecular level and to compare the behavior of physiologically relevant modified forms of LDL. All this newly gained information about LDL further contributes to a global understanding of this highly complex molecular assembly. It is very important to utilize the new information both for the development of novel therapeutics and to emphasize the importance of a healthy lifestyle for the prevention of cardiovascular diseases.

The application of several biophysical techniques in combination with the use of high hydrostatic pressure as a sample probing tool is a novel approach to study such a macromolecular complex on a molecular basis. As we could successfully show, high hydrostatic pressure is a promising tool for the investigation of basic molecular properties of biological molecules and shall be perceived as a viable alternative to other techniques in the future. Through an ever-growing number of techniques and instruments that can be combined with high pressure equipment, it will be possible to further broaden the fields of application for this versatile method.

Different scattering techniques formed the basis for the acquired results in this thesis and provided an insight into a nanoparticle’s behavior on a molecular basis. The comprehensive results about the dynamical behavior of different forms of LDL are complemented by structural analyses of the acquired small-angle scattering curves. These analyses were model-independent and provided unbiased information about the particle’s behavior under high hydrostatic pressure.

Dynamical characteristics of LDL were provided by QENS and EINS measurements and used to compare a normolipidemic and a triglyceride-rich form of LDL at body temperature and at two different pressure points (20 bar vs. 3000 bar). The analyses showed that the types of motions and therefore the motional parameters occurring in the two samples are identical. This is true for the low pressure point as well as for the high pressure point. However, when high hydrostatic pressure was applied to the samples, the quantity of molecular groups participating in these motions was altered. The TG-LDL had a lower proportion of molecular groups participating under HHP as some components of the sample were slowed down. These data are published in Golub, M.; Lehofer, B.; Martinez, N.; Ollivier, J.; Kohlbrecher, J.; Prassl, R.; Peters, J. *Sci. Rep.* **2017,** *7*, 46034.

Further dynamical measurements with EINS on three different forms of LDL, namely a normolipidemic, a triglyceride-rich and an oxidized sample, provided additional information about the dynamical behavior. The samples were also tested at two different pressure points (20 bar and 3000 bar) and additionally at three different temperature points (below, on and above T_m). As expected, the mean square displacements increased for all samples with increasing temperature, due to the thermal energy introduced to the system. In contrast to temperature, the increase of pressure led to a lowering of the mean square displacements. Interestingly, this effect occurred specifically in the modified forms of LDL, whereas the normolipidemic form was not affected in the same way. In agreement with the QENS study, this strongly indicates that the normolipidemic form of LDL is less affected by high hydrostatic pressure with regard to the dynamical properties of the particles. These data are published in Peters, J.; Martinez, N.; Lehofer, B.; Prassl, R. *Eur. Phys. J. E Soft Matter* **2017,** *40*, 68.

To correlate these findings with structural aspects of the highly complex LDL particles, small-angle scattering techniques, namely SAXS and SANS, were applied. It was possible to combine the small-angle scattering techniques with HHP equipment and therefore probe the samples under the same experimental conditions as for the dynamical investigations. From the SAXS data it is clear that high hydrostatic pressure induces the lipid phase transition within the LDL core even at temperatures above T_m. This effect could be observed for all examined samples (normolipidemic, oxidized and triglyceride-rich forms). Below the transition temperature the effect of pressure on the lipid core is much less pronounced. The observation of a pressure-induced phase transition in the LDL core could also explain the before mentioned effects on the dynamical behavior. Modified forms (TG-LDL and Ox-LDL)

showed a significant effect of the MSD values under HHP, whereas normolipidemic LDL did not. Both the Ox-LDL sample and the TG-LDL sample have a distinctively different lipid composition, compared to N-LDL. Through the action of oxygen and free radicals in the oxidation process of Ox-LDL, the polyunsaturated fatty acid chains are transformed to conjugated dienic hydroperoxides, which further decompose to conjugated dienic hydroxyl compounds, enals or dienals. These compounds destabilize the LDL, which in turn might disturb a consistent ordering of lipids in the core. Another effect relevant in TG-LDL comes from triglyceride molecules, which also contain unsaturated lipids and own a more complex sterical structure compared to cholesteryl ester molecules. Therefore a disruption of the lipid ordering in the core is obvious. As HHP seems to induce the lipid ordering in the LDL core in all types of samples, as observed by SAXS, it is reasonable to assume that the pressure-induced phase transition exerts more sterical constraints on the Ox-LDL and TG-LDL samples, due to the different lipid composition. This might be an explanation for the reduced dynamical motions of the modified forms of LDL compared to the normolipidemic form under high hydrostatic pressure.

A further observation by SAXS was that the position of the ordered lipid lamellae in the LDL core stays unchanged under the influence of HHP. Therefore it seems that this lipid ordering is a highly conserved and very characteristic feature of the LDL particles.

The SAXS measurement also showed a fully reversible behavior for a limited temperature range up to 39°C and a short-time pressure exposure of one minute. An exposure of LDL to 50°C and 2000 bar for 10 minutes had irreversible structural effects on the sample.

The same forms of LDL (N-LDL, Ox-LDL, TG-LDL) investigated by SANS showed that pressure values of 1200 bar or higher have a significant effect on the overall shape of the LDL particles according to the radii of gyration. The effect is more pronounced for samples below T_m, than above T_m.

Through ab initio shape reconstruction of SANS data it was additionally possible to get an overall shape from the SANS curves and to detect changes of the corresponding dimensions. This has shown that the shortest axis of the LDL particle, which is perpendicular to the CE lamellae in the core, is much more affected through HHP than the other axes. Therefore a characteristic flattening was observed for all samples.

The combination of SANS and SAXS methods is highly reasonable, since they probe different atomic components (nucleus vs. electrons) and therefore exhibit a different contrast. LDL in D_2O probed with SANS is best described as a sphere with uniform scattering density,

whereas LDL in aqueous buffer probed by SAXS also reveals the inner structure based on electron density differences. The hydration shell around LDL is detectable by X-rays but invisible by neutrons.

A logical approach to extend the model-independent data presented within the scope of this thesis would be the use of a three-dimensional mathematical model describing the features of the LDL particle. A possible approach for such an analysis was shown in the last chapter and could be continued in following studies. A vast majority of previous studies on the LDL particle offers broad and comprehensive knowledge about the three-dimensional structure of LDL and can be a basis for the development of a new fitting model for small-angle scattering data. Through such an approach the model-independent analysis steps would be complemented by model-dependent analyses and would provide more structural details about different forms of LDL under physiological conditions.

The knowledge gained in this thesis provides new molecular details about the physiologically highly relevant LDL particle and might support the development of new concepts for the treatment of cardiovascular diseases.

9. Appendix

PyMOL Script Draw_Protein_Dimensions

```
'''
Calculate and display the dimensions of a protein.

This is a first version, please use at your own risk!

REQUIREMENTS

numpy (http://numpy.scipy.org) that should be built into the newers versions of Pymol

(c) Pablo Guardado Calvo

Based on "inertia_tensor.py" (c) 2010 by Mateusz Maciejewski

License: MIT

'''

#from __future__ import print_function

#__author__  = 'Pablo Guardado Calvo'
#__version__ = '0.1'
#__email__   = 'pablo.guardado (at) gmail.com'
#__date__    = '13/08/2015'

############################################################
############################################################
################################################
# USAGE
#
# The idea behing this script is to calculate an aproximate minimal bounding box to extract the cell dimensions of a protein. To calculate the minimal bounding
# is not trivial and usually the Axis Aligned Bounding Box (AABB) does not show up the real dimensions of the protein. This script calculates the inertia tensor
# of the object, extract the eigenvalues and use them to rotate the molecule (using as rotation matrix the transpose of the eigenvalues matrix). The result is that
# the molecule is oriented with the inertia axis aligned with the cartesian axis. A new Bounding Box is calculated that is called Inertia Axis Aligned Bounding Box
#(IABB), whose volume is always lower than AABB volume, and in many cases will correspond with the lowest volume. Of course, maybe it exists another Bounding Box
# with a lower volume (the minimal Bounding Box).
#
# As always with these type of things, you have to use at your own risk. I did not try all the possible combinations, but if you find a bug, do
# not hesitate to contact me (pablo.guardado (at) gmail.com) or try to modify the code for yourself to correct it.
#
# To load the script just type:
#
# run path-to-the-script/Draw_Protein_Dimensions.py
#
# or if you want something more permanent add the previous line to your .pymolrc file
#
# The script works just typing:
#
# draw_Protein_Dimensions selection
#
# This will draw the cell dimensions of your selection based on a IABB. It also generates the IABB box and the inertia axis, you just need to do "show cgo" to display them.
#
# You could also try:
#
# draw_BB selection
#
# This will draw the AABB and IABB boxes with their cell dimensions and show in the command line their volumes, you can compare both of them.
############################################################
############################################################
################################################

from pymol import cmd, cgo
from pymol.cgo import *
import numpy
from random import randint

def matriz_inercia(selection):
        '''
        DESCRIPTION

        The method calculates the mass center, the inertia tensor and the eigenvalues and eigenvectors
        for a given selection. Mostly taken from inertia_tensor.py
        '''

        model = cmd.get_model(selection)
        totmass = 0.0
        x,y,z = 0,0,0
        for a in model.atom:
                m = a.get_mass()
                x += a.coord[0]*m
                y += a.coord[1]*m
                z += a.coord[2]*m
                totmass += m
        global cM
        cM = numpy.array([x/totmass, y/totmass, z/totmass])


        I = []
        for index in range(9):
                I.append(0)

        for a in model.atom:
                temp_x, temp_y, temp_z = a.coord[0], a.coord[1], a.coord[2]
                temp_x -= x
                temp_y -= y
                temp_z -= z

                I[0] += a.get_mass() * (temp_y**2 + temp_z**2)
                I[1] -= a.get_mass() * temp_x * temp_y
                I[2] -= a.get_mass() * temp_x * temp_z
                I[3] -= a.get_mass() * temp_x * temp_y
                I[4] += a.get_mass() * (temp_x**2 + temp_z**2)
                I[5] -= a.get_mass() * temp_y * temp_z
                I[6] -= a.get_mass() * temp_x * temp_z
                I[7] -= a.get_mass() * temp_y * temp_z
                I[8] += a.get_mass() * (temp_x**2 + temp_y**2)

        global tensor
        tensor = numpy.array([(I[0:3]), (I[3:6]), (I[6:9])])
```

```
        global autoval, autovect, ord_autoval, ord_autovect
        autoval, autovect = numpy.linalg.eig(tensor)
        auto_ord = numpy.argsort(autoval)
        ord_autoval = autoval[auto_ord]
        ord_autovect_complete = autovect[:, auto_ord].T
        ord_autovect = numpy.around(ord_autovect_complete, 3)

        return ord_autoval


def draw_inertia_axis(selection):
        '''
        DESCRIPTION

        This method draw the inertia axis calculated with the method matriz_inercia.
        '''

        matriz_inercia(selection)
        axis1 = ord_autovect[0]
        x1, y1, z1 = cM[0], cM[1], cM[2]
        x2, y2, z2 = cM[0]+50*axis1[0], cM[1]+50*axis1[1], cM[2]+50*axis1[2]
        eje1 = [cgo.CYLINDER, x1, y1, z1, x2, y2, z2, 0.6, 1, 0, 0, 1, 0, 0, 0.0]
        cmd.load_cgo(eje1, 'Inertia_Axis1')
        axis2 = ord_autovect[1]
        x3, y3, z3 = cM[0]+40*axis2[0], cM[1]+40*axis2[1], cM[2]+40*axis2[2]
        eje1 = [cgo.CYLINDER, x1, y1, z1, x3, y3, z3, 0.6, 1, 0.5, 0, 1, 0.5, 0, 0.0]
        cmd.load_cgo(eje1, 'Inertia_Axis2')
        axis4 = ord_autovect[2]
        x4, y4, z4 = cM[0]+30*axis4[0], cM[1]+30*axis4[1], cM[2]+30*axis4[2]
        eje1 = [cgo.CYLINDER, x1, y1, z1, x4, y4, z4, 0.6, 1, 1, 0, 1, 1, 0, 0.0]
        cmd.load_cgo(eje1, 'Inertia_Axis3')

def translacion_cM(selection):
        '''
        DESCRIPTION

        Translate the center of mass of the molecule to the origin.
        '''
        model = cmd.get_model(selection)
        totmass = 0.0
        x,y,z = 0,0,0
        for a in model.atom:
                m = a.get_mass()
                x += a.coord[0]*m
                y += a.coord[1]*m
                z += a.coord[2]*m
                totmass += m
        cM = numpy.array([x/totmass, y/totmass, z/totmass])
        trans_array = ([1, 0, 0, 0, 0, 1, 0, 0, 0, 0, 1, 0, -cM[0], -cM[1], -cM[2], 1])
        model_trans = cmd.transform_selection(selection, trans_array)


def rotacion_orig(selection):
        '''
        DESCRIPTION

        Find the proper rotation matrix, i.e. the transpose of the matrix formed by the eigenvectors of the inertia tensor
        '''

        translacion_cM(selection)
        matriz_inercia(selection)

        global transf, transf_array, ord_autovect_array, transf_array_print
        ord_autovect_array = numpy.array([[ord_autovect[0][0], ord_autovect[0][1], ord_autovect[0][2]],
                                          [ord_autovect[1][0], ord_autovect[1][1], ord_autovect[1][2]],

                                          [ord_autovect[2][0], ord_autovect[2][1], ord_autovect[2][2]]])
        if numpy.linalg.det(ord_autovect_array) == -1:
                ord_autovect_array = numpy.array([[ord_autovect[2][0], ord_autovect[2][1], ord_autovect[2][2]],
                                                  [ord_autovect[1][0], ord_autovect[1][1], ord_autovect[1][2]],

                                                  [ord_autovect[0][0], ord_autovect[0][1], ord_autovect[0][2]]])
        transf = numpy.transpose(ord_autovect_array)
        transf_array = numpy.array([transf[0][0], transf[0][1], transf[0][2], 0,
                                    transf[1][0], transf[1][1], transf[1][2], 0,
                                    transf[2][0], transf[2][1], transf[2][2], 0,
                                    0, 0, 0, 1])


def transformar(selection):
        '''
        DESCRIPTION

        Rotate the molecule and draw the inertia axis.
        '''

        rotacion_orig(selection)
        model_rot = cmd.transform_selection(selection, transf_array, homogenous=0, transpose=1);
        draw_inertia_axis(selection)



def draw_AABB(selection):
    """
    DESCRIPTION
    For a given selection, draw the Axes Aligned bounding box around it without padding. Code taken and modified from DrawBoundingBox.py.

    """

        AA_original = selection + "_original"
        model_orig = cmd.create(AA_original, selection)

    ([min_X, min_Y, min_Z],[max_X, max_Y, max_Z]) = cmd.get_extent(AA_original)

        print("The Axis Aligned Bounding Box (AABB) dimensions are (%.2f, %.2f, %.2f)" % (max_X-min_X, max_Y-min_Y, max_Z-min_Z))
        print("The Axis Aligned Bounding Box (AABB) volume is %.2f A3" % ((max_X-min_X)*(max_Y-min_Y)*(max_Z-min_Z)))


    min_X = min_X
    min_Y = min_Y
    min_Z = min_Z
    max_X = max_X
    max_Y = max_Y
    max_Z = max_Z

    boundingBox = [
        LINEWIDTH, float(2),

        BEGIN, LINES,
        COLOR, float(1), float(1), float(0),
```

```
        VERTEX, min_X, min_Y, min_Z,
        VERTEX, min_X, min_Y, max_Z,
        VERTEX, min_X, max_Y, min_Z,
        VERTEX, min_X, max_Y, max_Z,
        VERTEX, max_X, min_Y, min_Z,
        VERTEX, max_X, min_Y, max_Z,
        VERTEX, max_X, max_Y, min_Z,
        VERTEX, max_X, max_Y, max_Z,
        VERTEX, min_X, min_Y, min_Z,
        VERTEX, max_X, min_Y, min_Z,
        VERTEX, min_X, max_Y, min_Z,
        VERTEX, max_X, max_Y, min_Z,
        VERTEX, min_X, max_Y, max_Z,
        VERTEX, max_X, max_Y, max_Z,
        VERTEX, min_X, min_Y, max_Z,
        VERTEX, max_X, min_Y, max_Z,
        VERTEX, min_X, min_Y, min_Z,
        VERTEX, min_X, max_Y, min_Z,
        VERTEX, max_X, min_Y, min_Z,
        VERTEX, max_X, max_Y, min_Z,
        VERTEX, min_X, min_Y, max_Z,
        VERTEX, min_X, max_Y, max_Z,
        VERTEX, max_X, min_Y, max_Z,
        VERTEX, max_X, max_Y, max_Z,

                END
        ]

        p0 = '_0'  + str(randint(0, 100))
        p1 = '_1' + str(randint(0, 100))
        p2 = '_2' + str(randint(0, 100))
        p3 = '_3' + str(randint(0, 100))
        cmd.pseudoatom (pos=[min_X, min_Y, min_Z],
object=p0)
        cmd.pseudoatom (pos=[min_X, min_Y, max_Z],
object=p1)
        cmd.pseudoatom (pos=[min_X, max_Y, min_Z],
object=p2)
        cmd.pseudoatom (pos=[max_X, min_Y, min_Z],
object=p3)
        cmd.distance(None, p0, p3)
        cmd.distance(None, p0, p2)
        cmd.distance(None, p0, p1)
        cmd.hide("nonbonded")

        boxName = "box_AABB_"  + str(randint(0, 100))
    cmd.load_cgo(boundingBox,boxName)
    return boxName


def draw_IABB(selection):
    """
    DESCRIPTION
    For a given selection, draw the Inertia Axes Aligned bounding
box around it without padding. Code taken and modified from
DrawBoundingBox.py.

    """

        transformar(selection)

    ([minX, minY, minZ],[maxX, maxY, maxZ]) =
cmd.get_extent(selection)

        print("The Inertia Axis Aligned Bounding Box (IABB)
dimensions are (%.2f, %.2f, %.2f)" % (maxX-minX, maxY-minY,
maxZ-minZ))
        print("The Inertia Axis Aligned Bounding Box (IABB)
volume is %.2f A3" % ((maxX-minX)*(maxY-minY)*(maxZ-minZ)))

    minX = minX
    minY = minY
    minZ = minZ
    maxX = maxX
    maxY = maxY
    maxZ = maxZ

    boundingBox = [
        LINEWIDTH, float(2),

        BEGIN, LINES,
        COLOR, float(1), float(0), float(0),

        VERTEX, minX, minY, minZ,
        VERTEX, minX, minY, maxZ,
        VERTEX, minX, maxY, minZ,
        VERTEX, minX, maxY, maxZ,
        VERTEX, maxX, minY, minZ,
        VERTEX, maxX, minY, maxZ,
        VERTEX, maxX, maxY, minZ,
        VERTEX, maxX, maxY, maxZ,
        VERTEX, minX, minY, minZ,
        VERTEX, maxX, minY, minZ,
        VERTEX, minX, maxY, minZ,
        VERTEX, maxX, maxY, minZ,
        VERTEX, minX, maxY, maxZ,
        VERTEX, maxX, maxY, maxZ,
        VERTEX, minX, minY, maxZ,
        VERTEX, maxX, minY, maxZ,
        VERTEX, minX, minY, minZ,
        VERTEX, minX, maxY, minZ,
        VERTEX, maxX, minY, minZ,
        VERTEX, maxX, maxY, minZ,
        VERTEX, minX, minY, maxZ,
        VERTEX, minX, maxY, maxZ,
        VERTEX, maxX, minY, maxZ,
        VERTEX, maxX, maxY, maxZ,

        END
    ]

        p4 = '_4' + str(randint(0, 100))
        p5 = '_5' + str(randint(0, 100))
        p6 = '_6' + str(randint(0, 100))
        p7 = '_7' + str(randint(0, 100))
        cmd.pseudoatom (pos=[minX, minY, minZ], object=p4)
        cmd.pseudoatom (pos=[minX, minY, maxZ], object=p5)
        cmd.pseudoatom (pos=[minX, maxY, minZ], object=p6)
        cmd.pseudoatom (pos=[maxX, minY, minZ], object=p7)
        cmd.distance(None, p4, p7)
        cmd.distance(None, p4, p6)
        cmd.distance(None, p4, p5)
        cmd.hide("nonbonded")

        boxName = "box_IABB_" + str(randint(0, 100))
    cmd.load_cgo(boundingBox,boxName)
    return boxName


def draw_BB(selection):
        draw_AABB(selection)
        draw_IABB(selection)

def draw_Protein_Dimensions(selection):
        draw_IABB(selection)
        cmd.hide("cgo")

cmd.extend ("draw_Protein_Dimensions",
draw_Protein_Dimensions)
cmd.extend ("draw_BB", draw_BB)
```

PyMOL Script inertia_tensor

```
'''
http://www.pymolwiki.org/index.php/inertia_tensor

(c) August 2010 by Mateusz Maciejewski
matt (at) mattmaciejewski . com

License: MIT

'''

from pymol.cgo import *
from pymol import cmd


def tensor(selection, name="tensor", state=1, scaling=0, quiet=1):
   """
DESCRIPTION

   This script will draw the inertia tensor of the selection.

ARGUMENTS

   selection = string: selection for the atoms included in the tensor
calculation

   name = string: name of the tensor object to be created {default:
"tensor"}

   state = int: state/model in the molecule object used in the
tensor calculation

   scaling = int {0, 1, or 2}: 0 for no scaling of the inertia axes, 1 for
scaling
   according to the molecular shape, 2 for scaling according to the
eigenvalues
   {default: 0}

EXAMPLE

   PyMOL> run inertia_tensor.py
   PyMOL> tensor molecule_object & i. 2-58+63-120 & n. n+ca+c,
"tensor_model5_dom2", 5, 1

NOTES

   Requires numpy.
   """

   import numpy

   def draw_axes(start, ends, cone_ends, radius=.2,
name_obj="tensor"):
      radius = float(radius)
      size = radius * 15.

      obj = [
         CYLINDER, start[0], start[1], start[2], ends[0][0] + start[0],
ends[0][1] + start[1], ends[0][2] + start[2], radius, 1.0, 1.0, 1.0,
1.0, 0.0, 0.,
         CYLINDER, start[0], start[1], start[2], (-1) * ends[0][0] +
start[0], (-1) * ends[0][1] + start[1], (-1) * ends[0][2] + start[2],
radius, 1.0, 1.0, 1.0, 1.0, 0.0, 0.,
         CYLINDER, start[0], start[1], start[2], ends[1][0] + start[0],
ends[1][1] + start[1], ends[1][2] + start[2], radius, 1.0, 1.0, 1.0, 0.,
1.0, 0.,
         CYLINDER, start[0], start[1], start[2], (-1) * ends[1][0] +
start[0], (-1) * ends[1][1] + start[1], (-1) * ends[1][2] + start[2],
radius, 1.0, 1.0, 1.0, 0., 1.0, 0.,
         CYLINDER, start[0], start[1], start[2], ends[2][0] + start[0],
ends[2][1] + start[1], ends[2][2] + start[2], radius, 1.0, 1.0, 1.0, 0.,
0.0, 1.0,
         CYLINDER, start[0], start[1], start[2], (-1) * ends[2][0] +
start[0], (-1) * ends[2][1] + start[1], (-1) * ends[2][2] + start[2],
radius, 1.0, 1.0, 1.0, 0., 0.0, 1.0,
         CONE, ends[0][0] + start[0], ends[0][1] + start[1],
ends[0][2] + start[2], cone_ends[0][0] + start[0], cone_ends[0][1]
+ start[1], cone_ends[0][2] + start[2], 0.5, 0.0, 1.0, 0.0, 0.0, 1.0,
0.0, 0.0, 1.0, 1.0,
         CONE, (-1) * ends[0][0] + start[0], (-1) * ends[0][1] +
start[1], (-1) * ends[0][2] + start[2], (-1) * cone_ends[0][0] +
start[0], (-1) * cone_ends[0][1] + start[1], (-1) * cone_ends[0][2] +
start[2], 0.5, 0.0, 1.0, 0.0, 0.0, 1.0, 0.0, 0.0, 1.0, 1.0,
         CONE, ends[1][0] + start[0], ends[1][1] + start[1],
ends[1][2] + start[2], cone_ends[1][0] + start[0], cone_ends[1][1]
+ start[1], cone_ends[1][2] + start[2], 0.5, 0.0, 0.0, 1.0, 0.0, 0.0,
1.0, 0.0, 1.0, 1.0,
         CONE, (-1) * ends[1][0] + start[0], (-1) * ends[1][1] +
start[1], (-1) * ends[1][2] + start[2], (-1) * cone_ends[1][0] +
start[0], (-1) * cone_ends[1][1] + start[1], (-1) * cone_ends[1][2] +
start[2], 0.5, 0.0, 0.0, 1.0, 0.0, 0.0, 1.0, 0.0, 1.0, 1.0,
         CONE, ends[2][0] + start[0], ends[2][1] + start[1],
ends[2][2] + start[2], cone_ends[2][0] + start[0], cone_ends[2][1]
+ start[1], cone_ends[2][2] + start[2], 0.5, 0.0, 0.0, 0.0, 1.0, 0.0,
0.0, 1.0, 1.0, 1.0,
         CONE, (-1) * ends[2][0] + start[0], (-1) * ends[2][1] +
start[1], (-1) * ends[2][2] + start[2], (-1) * cone_ends[2][0] +
start[0], (-1) * cone_ends[2][1] + start[1], (-1) * cone_ends[2][2] +
start[2], 0.5, 0.0, 0.0, 0.0, 1.0, 0.0, 0.0, 1.0, 1.0, 1.0,
      ]

      cmd.load_cgo(obj, name_obj)

   totmass = 0.0
   x_com, y_com, z_com = 0, 0, 0

   model = cmd.get_model(selection, state)

   for a in model.atom:

      x_com += a.coord[0] * a.get_mass()
      y_com += a.coord[1] * a.get_mass()
      z_com += a.coord[2] * a.get_mass()
      totmass += a.get_mass()

   x_com /= totmass
   y_com /= totmass
   z_com /= totmass

   if not int(quiet):
      print()
      print("Center of mass: ")
      print()
      print(x_com, y_com, z_com)

   I = []

   for index in range(9):
      I.append(0)

   for a in model.atom:

      temp_x, temp_y, temp_z = a.coord[0], a.coord[1], a.coord[2]
      temp_x -= x_com
      temp_y -= y_com
      temp_z -= z_com

      I[0] += a.get_mass() * (temp_y ** 2 + temp_z ** 2)
```

```
        I[4] += a.get_mass() * (temp_x ** 2 + temp_z ** 2)
        I[8] += a.get_mass() * (temp_x ** 2 + temp_y ** 2)
        I[1] -= a.get_mass() * temp_x * temp_y
        I[3] -= a.get_mass() * temp_x * temp_y
        I[2] -= a.get_mass() * temp_x * temp_z
        I[6] -= a.get_mass() * temp_x * temp_z
        I[5] -= a.get_mass() * temp_y * temp_z
        I[7] -= a.get_mass() * temp_y * temp_z

    tensor = numpy.array([(I[0:3]), (I[3:6]), (I[6:9])])
    vals, vects = numpy.linalg.eig(tensor)  # they come out unsorted, so the command below is needed

    eig_ord = numpy.argsort(vals)  # a thing to note is that here COLUMN i corrensponds to eigenvalue i.

    ord_vals = vals[eig_ord]
    ord_vects = vects[:, eig_ord].T

    if not int(quiet):
        print()
        print("Inertia tensor z, y, x eigenvalues:")
        print()
        print(ord_vals)
        print()
        print("Inertia tensor z, y, x eigenvectors:")
        print()
        print(ord_vects)

    if int(scaling) == 0:
        norm_vals = [sum(numpy.sqrt(ord_vals / totmass)) / 3 for i in range(3)]

    elif int(scaling) == 1:
        normalizer = numpy.sqrt(max(ord_vals) / totmass)
        norm_vals = normalizer / numpy.sqrt(ord_vals / totmass) * normalizer
        norm_vals = norm_vals / (max(norm_vals) / min(norm_vals))

    elif int(scaling) == 2:
        normalizer = numpy.sqrt(max(ord_vals) / totmass)
        norm_vals = numpy.sqrt(ord_vals / totmass)

    start = [x_com, y_com, z_com]
    ends = [[(norm_vals[0] - 1) * ord_vects[0][0], (norm_vals[0] - 1) * ord_vects[0][1], (norm_vals[0] - 1) * ord_vects[0][2]],
            [(norm_vals[1] - 1) * ord_vects[1][0], (norm_vals[1] - 1) * ord_vects[1][1], (norm_vals[1] - 1) * ord_vects[1][2]],
            [(norm_vals[2] - 1) * ord_vects[2][0], (norm_vals[2] - 1) * ord_vects[2][1], (norm_vals[2] - 1) * ord_vects[2][2]]]

    cone_ends = [[norm_vals[0] * ord_vects[0][0], norm_vals[0] * ord_vects[0][1], norm_vals[0] * ord_vects[0][2]],
                 [norm_vals[1] * ord_vects[1][0], norm_vals[1] * ord_vects[1][1], norm_vals[1] * ord_vects[1][2]],
                 [norm_vals[2] * ord_vects[2][0], norm_vals[2] * ord_vects[2][1], norm_vals[2] * ord_vects[2][2]]]

    draw_axes(start, ends, cone_ends, name_obj=name)


cmd.extend("tensor", tensor)
```

10. List of Publications

Full Papers

Golub, M*.; **Lehofer, B***.; Martinez, N.; Ollivier, J.; Kohlbrecher, J.; Prassl, R.; Peters, J.,
High hydrostatic pressure specifically affects molecular dynamics and shape of low-density lipoprotein particles.
Sci. Rep. 2017, 7, 46034. (*equally contributed)

Peters, J.; Martinez, N.; **Lehofer, B**.; Prassl, R.,
Low-density lipoproteins investigated under high hydrostatic pressure by elastic incoherent neutron scattering.
Eur. Phys. J. E 2017, 40 (7), 68.

Kornmueller, K.; **Lehofer, B**.; Meindl, C.; Frohlich, E.; Leitinger, G.; Amenitsch, H.; Prassl, R.,
Peptides at the Interface: Self-Assembly of Amphiphilic Designer Peptides and Their Membrane Interaction Propensity.
Biomacromolecules 2016, 17 (11), 3591-3601.

Lehofer, B.; Bloder, F.; Jain, P. P.; Marsh, L. M.; Leitinger, G.; Olschewski, H.; Leber, R.; Olschewski, A.; Prassl, R.,
Impact of atomization technique on the stability and transport efficiency of nebulized liposomes harboring different surface characteristics.
Eur. J. Pharm. Biopharm. 2014, 88 (3), 1076-1085.

Jain, P. P.; Leber, R.; Nagaraj, C.; Leitinger, G.; **Lehofer, B**.; Olschewski, H.; Olschewski, A.; Prassl, R.; Marsh, L. M.,
Liposomal nanoparticles encapsulating iloprost exhibit enhanced vasodilation in pulmonary arteries.
Int. J. Nanomedicine 2014, 9, 3249-61.

Published Abstracts

Kornmueller, K.; **Lehofer, B.**; Leitinger, G.; Amenitsch, H.; Prassl, R.,
Artificial Peptide-Based Membranes and their Interaction with Lipid Systems.
Biophys. J. 2017, 112 (3), 361A-361A.

Lehofer, B.; Golub, M.; Kornmueller, K.; Kriechbaum, M.; Martinez, N.; Amenitsch, H.; Peters, J.; Prassl, R.,
Structural Effects of High Hydrostatic Pressure on Human Low Density Lipoprotein Revealed by Small Angle X-ray and Neutron Scattering.
Biophys. J. 2016, 110 (3), 255A-256A.

Marsh, L.; Jain, P. P.; Leber, R.; **Lehofer, B**.; Bloder, F.; Nagaraj, C.; Egemnazarov, B.; Olschewski, A.; Olschewski, H.; Prassl, R.,
Development Of Inhalable Liposomal Formulations For The Treatment Of Pulmonary Hypertension.
Am. J. Respir. Crit. Care Med. 2014, 189, 1.

Scientific presentations

Lehofer, B; Krebs, A; Kornmueller, K; Kriechbaum, M; Peters, J; Amenitsch, H; Prassl, R
Atherogenic low-density lipoprotein: Integration of SAXS and cryo-EM data argue for a modified structural model.
SAXS excites – International SAXS Symposium; SEP 26-27, 2017; Graz, AUSTRIA. 2017. [Poster]

Golub, M; **Lehofer, B**; Kornmueller, K; Kriechbaum, M; Martinez, N; Amenitsch, H; Prassl, R; Peters, J
Combined SANS-QENS studies of low-density lipoprotein (LDL) under high hydrostatic pressure.
10e Forum de technologie des Hautes Pressions; OCT 10-13, 2016; La Londe-Les-Maures, FRANCE. 2016. [Oral Communication]

Kriechbaum, M; Amentisch, H; **Lehofer, B**; Kornmueller, K; Prassl, R
High-Pressure Cell for the SAXS-Beamline at ELETTRA.
SAXS on Nanosystems: Current trends and perspectives, 20 years of the Austrian SAXS beamline; OCT 10-12, 2016; Triest, ITALY. 2016. [Poster]

Kornmueller, K; **Lehofer, B**; Leitinger, G; Amenitsch, H; Prassl, R
Amphiphilic designer peptides and their propensity to interact with membranes of different complexity.
Symposium: “Future Possible Use of Neutron and Synchrotron Sources by the Austrian User Community”; SEPT 15-16, 2016; Graz, AUSTRIA. 2016. [Poster]

Kriechbaum, M; Amenitsch, H; **Lehofer, B**; Kornmueller, K; Prassl, R
Hydrostatic High-Pressure Cell for the SAXS-Beamline at ELETTRA.
NESY Symposium “Future Possible Use of Neutron and Synchrotron Sources by the Austrian User Community”; SEP 15-16, 2016; Graz, AUSTRIA. 2016. [Poster]

Lehofer, B; Golub, M; Kornmueller, K; Kriechbaum, M; Martinez, N; Amenitsch, H; Peters, J; Prassl, R
Particle shape alterations and lipid phase changes of low density lipoprotein induced by high hydrostatic pressure.
NESY Symposium "Future Possible Use of Neutron and Synchrotron Sources by the Austrian User Community"; SEP 15-16, 2016; Graz, AUSTRIA. 2016. [Poster]

Golub, M; **Lehofer, B**; Kornmueller, K; Kriechbaum, M; Martinez, N; Amenitsch, H; Prassl, R; Peters, J
Combined SANS-QENS studies of low-density lipoprotein under high hydrostatic pressure.
14th International conference on applications of quasielastic neutron scattering (QENS 2016); SEP 5-8, 2016; Potsdam, GERMANY. 2016. [Oral Communication]

Kornmueller, K; **Lehofer, B**; Leitinger, G; Amenitsch, H; Prassl, R
Amphiphilic designer peptides and their membrane-interaction propensity.
BioNanoMed 2016: Nanotechnology enables Personalized Medicine; APR 6-8, 2016; Krems, AUSTRIA. 2016. [Poster]

Lehofer, B; Golub, M; Kornmueller, K; Kriechbaum, M; Martinez, N; Amenitsch, H; Peters, J; Prassl, R
Particle shape alterations and lipid phase changes of human low density lipoprotein induced by high hydrostatic pressure.
7th International Congress Nanotechnology in Medicine & Biology; APR 6-8, 2016; Krems, AUSTRIA. 2016. [Poster]

Lehofer, B; Golub, M; Kornmueller, K; Kriechbaum, M; Martinez, N; Amenitsch, H; Peters, J; Prassl, R
Structural Effects of High Hydrostatic Pressure on Human Low Density Lipoprotein Revealed by Small

Angle X-ray and Neutron Scattering
BIOPHYS J. 2016; 110(3):255A-256A.-60th Annual Meeting of the Biophysical-Society; FEB 27-MAR 02, 2016; Los Angeles, CA. [Poster]

Golub, M; **Lehofer, B**; Kornmueller, K; Kriechbaum, M; Martinez, N; Amenitsch, H; Prassl, R; Peters, J
Combined SANS-QENS Studies of Low-Density Lipoprotein under High Hydrostatic Pressure.
8th International Meeting on Biomolecules under Pressure (IMBP); FEB 15-17, 2016; Dortmund, GERMANY. 2016. [Oral Communication]

Lehofer, B; Kornmueller, K; Kriechbaum, M; Martinez, N; Peters, J; Amenitsch, H; Prassl, R
Lipid core phase transition and shape modification of low density lipoprotein induced by high hydrostatic pressure.
16th International Conference on Small-Angle Scattering, SAS2015; SEP 13-18, 2015; Berlin, GERMANY. 2015. [Poster]

Lehofer, B; Jain, PP; Bloder, F; Leber, R; Leitinger, G; Marsh LM; Olschewski, H; Olschewski, A; Prassl, R
Transport Properties of Liposomes for Pulmonary Drug Delivery depend on the Surface Characteristics of the Liposomes and the Atomization Technique used for Nebulization
42nd Controlled Release Society Annual Meeting ; JUL 25-29, 2015; Edinburgh, UK. 2015. [Oral Communication]

Lehofer, B; Bloder, F; Jain, P.P; Marsh, L.M.; Leitinger, G.; Olschewski, H.; Leber, R.; Olschewski, A.; Prassl, R.
Suitability of Liposomal Nanocarriers for Pulmonary Drug Administration depends on the applied Nebulizer Device and Particle Surface Characteristics
BioNanoMed 2015 6th Congress Nanotechnology in Medicine and Biology; APRIL 8-10, 2015; Graz, AUSTRIA. 2015. [Poster]

Lehofer, B; Jain, PP; Bloder, F; Leber,R; Marsh, LM; Olschewski, H; Olschewski, A; Prassl, R
Nebulization characteristics of surface modified liposomes optimized for pulmonary drug delivery
1st European Conference on Pharmaceutics - Drug Delivery; APRIL 3-4, 2015; Reims, FRANCE. 2015. [Poster]

Peters, J; Prassl, R; **Lehofer, B**
Elastic neutron scattering on low-density lipoprotein under high hydrostatic pressure
9e forum de la technologie des hautes pressions; OCT 13-16, 2014; La Rochelle, FRANCE. 2014. [Poster]

Marsh, LM; Jain, PP; Leber, R; **Lehofer, B**; Bloder, F; Nagaraj, C; Egemnazarov, B; Olschewski, A; Olschewski, H; Prassl, R
Development Of Inhalable Liposomal Formulations For The Treatment Of Pulmonary Hypertension
American Thoracic Society. 2014; 271: A4808-A4808.-American Thoracic Society; May 16-21, 2014; San Diego, USA. [Poster]

Lehofer, B; Martinez, N; Peters, J; Prassl, R
Structural changes under high hydrostatic pressure of native and modified low density lipoprotein particles revealed by small angle neutron scattering (SANS).
11th DocDay NAWI Graz Doctoral School Molekulare Biowissenschaften und Biotechnologie; FEB 7, 2014; Graz, AUSTRIA. 2014. [Poster]